

SYSTEMATIC IMPROVEMENTS OF *AB-INITIO* IN-MEDIUM SIMILARITY  
RENORMALIZATION GROUP CALCULATIONS

By

Titus Dan Morris

A DISSERTATION

Submitted to  
Michigan State University  
in partial fulfillment of the requirements  
for the degree of

Physics - Doctor of Philosophy

2016

## ABSTRACT

### SYSTEMATIC IMPROVEMENTS OF *AB-INITIO* IN-MEDIUM SIMILARITY RENORMALIZATION GROUP CALCULATIONS

By

Titus Dan Morris

The In-Medium Similarity Renormalization Group (IM-SRG) is an *ab initio* many-body method that has enjoyed increasing prominence in nuclear theory, due to its soft polynomial scaling with system size, and the flexibility to target ground and excited states of both closed- and open-shell systems. Despite many successful applications of the IM-SRG to microscopic calculations of medium-mass nuclei in recent years, the conventional formulation of the method suffers a number of limitations. Key amongst these are i) large memory demands that limit calculations in heavier systems and render the calculation of observables besides energy spectra extremely difficult, and ii) the lack of a *computationally feasible* sequence of improved approximations that converge to the exact solution in the appropriate limit, thereby verifying that the IM-SRG is systematically improvable. In this thesis, I present a novel formulation of the IM-SRG based on the Magnus expansion. I will show that this improved formulation, guided by intuition gleaned from a diagrammatic analysis of the perturbative content of different truncations and parallels with coupled-cluster theory, allows one to bypass the computational limitations of traditional implementations, and provides computationally viable approximations that go beyond the truncations used to date. The effectiveness of the new Magnus formulation is illustrated for several many-nucleon and many-electron systems.

## ACKNOWLEDGMENTS

The list of people who I have become indebted to along the way is vast, if I have forgotten anyone in this list, I can only thank them for patience, and hope they understand.

To begin with, I owe my parents everything that I am. They are both special people who supported me along the way in every way imaginable. They have always been there for me with calls when I need encouragement, and occasionally a few bucks when things were tight. There is no way to understate their importance to me.

Before my time at Michigan State, I learned much from Dr. William Oliver III, who mentored me while I earned my Masters degree studying glassy liquids at the University of Arkansas. He taught me patience by having me learn how to load Diamond Anvil Cells. In addition, he helped nurse a love of physics in me, despite being constantly more busy than any single person should be. I will always think fondly of my time in his lab, and Tim Ransom, who worked closely with me my last year in Arkansas.

I would be remiss if I didn't mention the many friends and loved ones that have been there for me for tough times and good. I have never wanted for good friends to go mourn the cold temperatures over a beer inside at Crunchy's, or to celebrate the return of the sun in the spring on a patio. I would like to mention a few people who have come and gone during my time here who I sincerely miss, or will miss upon leaving. Steve Quinn, Zach and Jayda Meisel, Anthony Schneider, Nikki Larson are a few of the first close friends I made in town, and some of my favorite people to see on a dance floor. Oren Yair, Kortney Kooper, and Chris Prokop have come to be close friends that I can always count on seeing at our weekly pool night at the Riv, and count on to listen to my midweek problems. In my last year here I have had the pleasure of getting to know Debra Richman, who introduced me to the joy of

getting thrashed at Seinfeld trivia; she has made my last year here a joy. All of these people I will certainly miss dearly, and will have only fond memories for the rest of my life.

My research group has been a huge blessing. I could not have asked for a better group of friends to work with. Discussions with Nathan Parzuchowski have yielded great inspiration and insight, as well as just generally being fun. His relentless work ethic has certainly set a good example for me to follow, or a little bit of shame when I was not. Fei Yuan's encyclopedic knowledge of all things computers has been invaluable any time a compiler/library error popped up. The frequent group lunches with Justin Lietz, Adam Jones, and Sam Novario have always been fun. Everyone in the group has been amazing.

Most of all, I have to thank my advisors, Scott Bogner and Morten Hjorth-Jensen, who both deserve my deepest thanks. They have always been there to answer questions about a host of issues. Scott and Morten have always had time for all the graduate students in the group, even as the group has grown quite large. Even during their busiest times, they have made time to keep me on track. I have always been encouraged to pursue my own areas of interest, and helped in doing so. Despite their clear leading of the group, I have never felt as anything but a colleague and friend to both. I do not know how they accomplish this, but I feel blessed by it. Hopefully by the time I have students of my own, if that ever happens, I'll have figured out how to create this same atmosphere. And in the last year, with the hiring of Heiko Hergert, I have been blessed with a third deep well of expertise to draw from. These three have my greatest appreciation.

Lastly, I would like to thank my committee. I have had each as a teacher, and can say beyond any doubt that even before serving on my committee, I owed each a thanks for my own better understanding of physics that was crucial to my research. Both for the direction and support they have provided, I am exceedingly thankful.

# TABLE OF CONTENTS

<b>LIST OF TABLES</b> . . . . .	<b>viii</b>
<b>LIST OF FIGURES</b> . . . . .	<b>x</b>
<b>Chapter 1 Introduction</b> . . . . .	<b>1</b>
1.1 Brief History . . . . .	1
<b>Chapter 2 The Many-Body Problem</b> . . . . .	<b>7</b>
2.1 Many-Body Schrödinger Equation . . . . .	7
2.2 Normal Ordering . . . . .	9
2.3 Many Body Perturbation Theory . . . . .	13
2.4 Coupled Cluster Theory . . . . .	16
2.4.1 Exponential Ansatz . . . . .	17
2.5 Approximate Triples . . . . .	20
2.5.1 CCSD(T) . . . . .	20
2.5.2 $\Lambda$ -CCSD[T] . . . . .	22
2.5.3 Completely Renormalized CC Methods . . . . .	23
<b>Chapter 3 In-Medium Similarity Renormalization Group</b> . . . . .	<b>26</b>
3.1 IM-SRG Formalism . . . . .	27
3.1.1 Overview of the SRG . . . . .	27
3.1.2 $M$ -Scheme Flow Equations for IM-SRG(2) . . . . .	29
3.1.3 Symmetries and the Flow Equations . . . . .	31
3.1.4 General Observables . . . . .	33
3.2 Choice of Generator . . . . .	34
3.2.1 Decoupling . . . . .	34
3.2.2 White Generators . . . . .	36
3.2.3 Imaginary-Time Generators . . . . .	38
3.2.4 Wegner Generators . . . . .	39
3.2.5 Decay Scales . . . . .	41
3.3 Numerical Explorations . . . . .	44
3.3.1 Implementation . . . . .	44
3.3.2 Convergence . . . . .	46
3.3.3 Choice of Generator . . . . .	51
3.3.4 Decoupling . . . . .	56
3.3.5 Radii . . . . .	60
3.4 Choice of Reference State . . . . .	63
3.4.1 Overview . . . . .	63
3.4.2 Harmonic Oscillator vs. Hartree-Fock Slater Determinants . . . . .	63
3.5 Perturbative Analysis of the Flow Equations . . . . .	68

3.5.1	Overview . . . . .	68
3.5.2	Power Counting . . . . .	71
3.5.3	$\mathcal{O}(g)$ Flow . . . . .	72
3.5.4	$\mathcal{O}(g^2)$ Flow . . . . .	73
3.5.5	$\mathcal{O}(g^3)$ Flow . . . . .	79
3.5.6	Energy through $\mathcal{O}(g^4)$ . . . . .	82
3.5.7	Discussion . . . . .	86
3.5.8	Perturbative Truncations . . . . .	89
<b>Chapter 4</b>	<b>Magnus Formulation . . . . .</b>	<b>95</b>
4.1	Introduction . . . . .	95
4.2	Formalism . . . . .	96
4.3	Analytical Model . . . . .	98
4.4	MAGNUS(2) Approximation . . . . .	101
4.5	Hamiltonians and Implementation . . . . .	102
4.6	Results . . . . .	105
4.7	MAGNUS(2) Conclusion . . . . .	115
<b>Chapter 5</b>	<b>Approximating the IM-SRG(3) . . . . .</b>	<b>116</b>
5.1	Deficiencies of the IM-SRG(2) in Chemistry . . . . .	117
5.2	The IM-SRG(2*) Approximation . . . . .	118
5.3	The MAGNUS(2*) Approximation . . . . .	120
5.4	Approximations to MAGNUS(3) . . . . .	124
5.5	Applications . . . . .	128
5.5.1	Electron Gas Results . . . . .	129
5.5.2	Nuclear Results . . . . .	132
5.5.3	H <sub>2</sub> O Results . . . . .	134
5.5.4	Neon Results . . . . .	135
5.5.5	C <sub>2</sub> Results . . . . .	136
5.5.6	HF Results . . . . .	137
5.6	Summary . . . . .	138
<b>Chapter 6</b>	<b>Other Work . . . . .</b>	<b>139</b>
6.1	Improving the Reference . . . . .	139
6.2	Brueckner IM-SRG Results . . . . .	142
6.2.1	BMAGNUS(2*) Results for Neon and C <sub>2</sub> . . . . .	143
6.2.2	BMAGNUS(2*) Results for HF and H <sub>2</sub> O . . . . .	144
6.2.3	Brueckner Summary . . . . .	145
6.3	Extensions to MR-IM-SRG . . . . .	145
6.4	Extensions to Excited State Formalism . . . . .	151
<b>Chapter 7</b>	<b>Summary and Conclusions . . . . .</b>	<b>155</b>

<b>APPENDICES</b> . . . . .	<b>157</b>
Appendix A Fundamental Commutators . . . . .	158
Appendix B IM-SRG(3) Flow Equations . . . . .	162
Appendix C Diagram Rules . . . . .	165
 <b>REFERENCES</b> . . . . .	 <b>170</b>

## LIST OF TABLES

Table 3.1:	IM-SRG(2) ground-state energies of selected closed-shell nuclei for the the chiral N <sup>3</sup> LO interaction by Entem and Machleidt [1, 2], with $\lambda = \infty$ and $\lambda = 2.0 \text{ fm}^{-1}$ (cf. Fig. 3.2). $E_{14}$ are the energies obtained for $e_{\text{max}} = 14$ at optimal $\hbar\omega$ , and $E_{\text{ex}}$ are extrapolated to infinite basis size (see text), with extrapolation uncertainties indicated in parentheses. . . . .	46
Table 5.1:	Approximations made in the various MAGNUS(2*)[3] variants. . . .	129
Table 5.2:	<sup>a</sup> FCIQMC results from Ref. [3]. <sup>b</sup> CCD and CCDT results from Ref. [4]. Ground state of 14 electrons calculated in a basis set of M=114 plane waves with various approximations. The Full Configuration Quantum Monte Carlo correlation energy is reported in Hartree. All other energies are reported as a fraction of the correlation energy recovered with respect to quasi-exact FCIQMC results. . . . .	131
Table 5.3:	<sup>a</sup> From Ref. [5]. <sup>b</sup> CCSD and CCSD(T) results obtained with PSI4[6]. <sup>c</sup> From Ref.[7] <sup>d</sup> From Ref. [8] A comparison of various CC ground-state energies obtained for the cc-pVDZ H <sub>2</sub> O molecule at the equilibrium OH bond length $R_e = 1.84345 \text{ bohr}$ and several nonequilibrium geometries obtained by stretching the OH bonds, while keeping the HOH angle fixed at 110.6. The spherical components of the d orbitals were used. In post-RHF calculations, all electrons were correlated. The full CI total energies are given in hartree. The remaining energies are reported in millihartree relative to the corresponding full CI energies. . . . .	135
Table 5.4:	<sup>a</sup> From Ref. [9]. A comparison of CC and Magnus IM-SRG ground-state energies obtained for a Neon atom in a cc-pVDZ basis set. In these post-HF calculations, the 1s orbital was frozen. The full CI total energy is given in Hartree. The remaining energies are reported as a fraction of the correlation energy recovered relative to $\Delta E = E_{\text{HF}} - E_{\text{FCI}}$ . . . . .	136
Table 5.5:	<sup>a</sup> From Ref. [9]. A comparison of CC and Magnus IM-SRG ground-state energies obtained for C <sub>2</sub> at the equilibrium FCI bond length of $r_e = 1.27273 \text{ \AA}$ in a cc-pVDZ basis set, taken from Ref. [9]. In these post-HF calculations, the 1s orbitals was frozen on the C atoms. The full CI total energy is given in Hartree. The remaining energies are reported correlation energy recovered relative to $\Delta E = E_{\text{HF}} - E_{\text{FCI}}$ . . . . .	137

Table 5.6:	<sup>a</sup> From Ref. [10]. <sup>b</sup> CCSD and CCSD(T) results from [6]. <sup>c</sup> From Ref. [8] A comparison of CC and Magnus IMSRG ground-state energies obtained for the equilibrium geometry of $R_e = 1.7328$ bohr and other nuclear separations of HF with a DZ basis set. In these post-HF calculations all electrons were correlated. The full CI total energies are given in hartree. The remaining energies are reported in millihartree relative to the corresponding full CI energy values. . . . .	138
Table 6.1:	<sup>a</sup> From Ref. [9]. A comparison of CC and Magnus IMSRG ground-state energies obtained for a Neon atom. In these post-HF calculations, the 1s orbital was frozen. The full CI total energy is given in Hartree. The remaining energies are reported as a fraction of the correlation energy recovered relative to FCI in mH. . . . .	144
Table 6.2:	<sup>a</sup> From Ref. [9]. A comparison of CC and Magnus IMSRG ground-state energies obtained for C <sub>2</sub> at the equilibrium FCI bond length of $r_e = 1.27273$ Å. In these post-HF calculations, the 1s orbitals was frozen on the C atoms. The full CI total energy is given in Hartree. The remaining energies are reported in millihartree relative to the full CI energy. . . . .	144
Table 6.3:	<sup>a</sup> From Ref. [5]. <sup>b</sup> CCSD and CCSD(T) results obtained with PSI4[6]. <sup>c</sup> From Ref.[7] <sup>d</sup> From Ref. [8] A comparison of various CC ground-state energies obtained for the cc-pVDZ H <sub>2</sub> O molecule at the equilibrium OH bond length $R_e = 1.84345$ bohr and several nonequilibrium geometries obtained by stretching the OH bonds, while keeping the HOH angle fixed at 110.6. The spherical components of the d orbitals were used. In post-RHF calculations, all electrons were correlated. The full CI total energies are given in hartree. The remaining energies are reported in millihartree relative to the corresponding full CI energies. In Ref. [10], the authors noticed that there are two SCF solutions, one of which poorly describes the weak H-O bonding. In the chemistry suite, PSI4[6], we could not force the CCSD routine, and thus the BCCD routine to use the correct SCF starting reference. This is why there are no results reported for $3.0R_e$ . . . . .	146
Table 6.4:	<sup>a</sup> From Ref. [10]. <sup>b</sup> CCSD and CCSD(T) results obtained with PSI4[6]. <sup>c</sup> From Ref. [8] A comparison of CC and Magnus IMSRG ground-state energies obtained for the equilibrium geometry of $R_e = 1.7328$ bohr and other nuclear separations of HF with a DZ basis set. In these post-HF calculations all electrons were correlated. The full CI total energies are given in hartree. The remaining energies are reported in millihartree relative to the corresponding full CI energy values. . . . .	147

## LIST OF FIGURES

Figure 1.1:	Taken from Ref. [11]. The chart of nuclides and the reach of <i>ab initio</i> calculations in (a) 2005 and (b) 2015. Nuclei (including potentially unbound isotopes) for which <i>ab initio</i> calculations based on high-precision nuclear interactions exist are highlighted. Essentially all of the 2015 calculations include 3N forces. We note that the figure is for illustrative purposes only, and is based on the authors' potentially non-exhaustive survey of the literature. . . . .	3
Figure 2.1:	Matrix dimension versus $N_{max}$ for stable and unstable Oxygen isotopes. The vertical red line signals the boundary, beyond which one might expect reasonable convergence with respect to $N_{max}$ . The horizontal lines show the computational power of a facility expected to conduct these diagonalizations. Figure taken from Ref. [12]. . . . .	9
Figure 2.2:	Diagram demonstrating the diagrammatic form of Eq. (2.26). The dashed line indicates the resolvent operator $R_0$ . . . . .	16
Figure 2.3:	Diagrams demonstrating the approximate $T_3$ constructed from converged $T_2$ amplitudes in the CCSD[T] energy correction. The dashed line represents the resolvent operator $R_0$ from perturbation theory. . . . .	21
Figure 3.1:	Schematic representation of the initial and final Hamiltonians, $H(0)$ and $H(\infty)$ , in the many-body Hilbert space spanned by particle-hole excitations of the reference state. . . . .	34
Figure 3.2:	Convergence of ${}^4\text{He}$ , ${}^{16}\text{O}$ , and ${}^{40}\text{Ca}$ IM-SRG(2) ground-state energies w.r.t. single-particle basis size $e_{max}$ , for a chiral $\text{N}^3\text{LO}$ $NN$ interaction with $\lambda = \infty$ (left panels) and $\lambda = 2.0 \text{ fm}^{-1}$ (right panels). Notice the significant differences in the energy scales between the left and right panels. Gray dashed lines indicate energies from extrapolation the $e_{max} \geq 10$ data sets to infinite basis size (see text and Refs. [13, 14]). . . . .	47
Figure 3.3:	Convergence of ${}^{78}\text{Ni}$ , ${}^{100}\text{Sn}$ , and ${}^{132}\text{Sn}$ IM-SRG(2) ground-state energies w.r.t. single-particle basis size $e_{max}$ , for the chiral $\text{N}^3\text{LO}$ $NN$ interaction with $\lambda = 2.0 \text{ fm}^{-1}$ . Gray dashed lines indicate energies from extrapolation the $e_{max} \geq 10$ data sets to infinite basis size (see text and Refs. [13, 14]). . . . .	49

Figure 3.4:	IM-SRG(2) ground-state energies of $^{40}\text{Ca}$ obtained with different choices of the generator, as a function of $\hbar\omega$ and the single-particle basis size $e_{\text{max}}$ . The interaction is the chiral $\text{N}^3\text{LO}$ potential with $\lambda = \infty$ (top panels) and $\lambda = 2.0 \text{ fm}^{-1}$ (bottom panels), respectively. The dashed lines indicate extrapolated energies. For the Wegner generator, the shaded area indicates the variation from using different data sets for the extrapolation (see text). . . . .	52
Figure 3.5:	IM-SRG(2) ground-state energies of $^{40}\text{Ca}$ for the regular (left, as in Fig. 3.4) and restricted Wegner generators (right, see text), as a function of $\hbar\omega$ and the single-particle basis size $e_{\text{max}}$ . The interaction is the chiral $\text{N}^3\text{LO}$ potential with $\lambda = \infty$ (top panels) and $\lambda = 2.0 \text{ fm}^{-1}$ (bottom panels), respectively. The dashed lines indicate extrapolated energies. . . . .	54
Figure 3.6:	Decoupling for the White generator, Eq. (3.23), in the $J^\pi = 0^+$ neutron-neutron interaction matrix elements of $^{40}\text{Ca}$ ( $e_{\text{max}} = 8$ , $\hbar\omega = 20 \text{ MeV}$ , Entem-Machleidt $\text{N}^3\text{LO}(500)$ evolved to $\lambda = 2.0 \text{ fm}^{-1}$ ). Only $hhhh$ , $hhpp$ , $pphh$ , and $pppp$ blocks of the matrix are shown. . . . .	56
Figure 3.7:	IM-SRG(2) ground-state energy of $^{40}\text{Ca}$ as a function of the flow parameter $s$ , compared to MBPT(2), CCSD, and $\Lambda$ -CCSD(T) energies with the IM-SRG-evolved Hamiltonian $H(s)$ . We only show part of the data points to avoid clutter. Calculations were done for $e_{\text{max}} = 10$ and optimal $\hbar\omega = 32 \text{ MeV}$ (top) and $\hbar\omega = 24 \text{ MeV}$ (bottom), respectively, using the chiral NN interaction at different resolution scales. The dashed lines indicate the final IM-SRG(2) energies. . . . .	58
Figure 3.8:	Convergence of $^4\text{He}$ , $^{16}\text{O}$ , and $^{40}\text{Ca}$ IM-SRG(2) charge radii w.r.t. single-particle basis size $e_{\text{max}}$ , for a chiral $\text{N}^3\text{LO}$ NN interaction with $\lambda = \infty$ (left panels) and $\lambda = 2.0 \text{ fm}^{-1}$ (right panels). The gray dashed lines indicate experimental charge radii from [15]. . . . .	61
Figure 3.9:	Top panel: IM-SRG(2) energy of $^{40}\text{Ca}$ with a HF (solid lines and symbols) and a HO reference state (dashed lines, open symbols), obtained with the Wegner generator. Bottom panel: Overlap of the HF and HO reference states. . . . .	64
Figure 3.10:	IM-SRG decoupling of 1p1h excitations for different generator choices, starting from a HO reference state. The figure shows the $^{40}\text{Ca}$ ground-state energy as a function of the value of the flow parameter $s$ . The unit of $s$ is suppressed because it differs with the choice of generator. The gray line indicates the result of the Hartree-Fock calculation with the same interaction and basis parameters. . . . .	65

Figure 3.11:	Schematic illustration of the energy flow equation (3.61) for the White generator with Møller-Plesset energy denominators (Eq. (3.23)) in terms of Hugenholtz diagrams (see text). The grey vertices represent $H(s)$ , and the double lines indicate energy denominators calculated with $f(s)$ . On the second line, the flow equation is expanded in terms of $H(s - \delta s)$ (simple black vertices) and the corresponding energy denominators from $f(s - \delta s)$ (single lines). The braces indicate which term of $H(s)$ is expanded, and dots represent higher order diagrams generated by the integration step $s - \delta s \rightarrow s$ . . . . .	67
Figure 3.12:	Antisymmetrized Goldstone diagrams for the $\mathcal{O}(g^2)$ effective one-body Hamiltonian (see text). Interpretation rules are summarized in Appendix C. . . . .	75
Figure 3.13:	Antisymmetrized Goldstone diagrams for the $\mathcal{O}(g^2)$ effective two-body vertex $\Gamma$ (see text). Interpretation rules are summarized in Appendix C. . . . .	76
Figure 3.14:	Antisymmetrized Goldstone diagrams for the $\mathcal{O}(g^2)$ effective three-body vertex $W$ (see text). Interpretation rules are summarized in Appendix C. . . . .	78
Figure 3.15:	Antisymmetrized Goldstone diagrams for the $\mathcal{O}(g^3)$ effective two-body vertex $\Gamma$ (see text). Black ( $\bullet$ ) and gray vertices ( $\circ$ ) correspond to $\bar{\Gamma}^{[1]}$ (Eq. (3.77)), $\bar{f}^{[2]}$ (Eqs. (3.80)–(3.82)), $\bar{\Gamma}^{[2]}$ (Eqs. (3.85)–(3.90)), and $\bar{W}^{[2]}$ (Eqs. (3.92)–(3.94)), respectively. Interpretation rules are summarized in Appendix C. . . . .	79
Figure 3.16:	Connected Hugenholtz diagrams for the fourth-order energy correction $E^{(4)}$ (Ref. [16]). . . . .	84
Figure 3.17:	Effect of fourth-order quadruples (4p4h) contribution $E_C^{[4]}$ , Eq. (3.120) on the ground-state energies of ${}^4\text{He}$ , ${}^{16}\text{O}$ , and ${}^{40}\text{Ca}$ (see text): Comparison of IM-SRG(2) with and without $E_C^{[4]}$ , calculated with the initial Hamiltonian $H(0)$ , to CCSD and $\Lambda$ -CCSD(T). All calculations used the chiral $\text{N}^3\text{LO}$ Hamiltonian with $\lambda = \infty$ in an $e_{\text{max}} = 14$ single-particle basis. The shown CC values were taken at optimal $\hbar\omega$ . . . . .	88

Figure 3.18:	Comparison of $^{40}\text{Ca}$ ground-state energies of the regular IM-SRG(2) (solid lines) and perturbative IM-SRG(2') truncations (dashed lines). The default White generator $\eta^{\text{IA}}$ , Eq. (3.23), was used in both cases. The interaction is the chiral $\text{N}^3\text{LO}$ potential with $\lambda = \infty$ (left and center panels) and $\lambda = 2.0 \text{ fm}^{-1}$ (right panel), respectively. The dashed lines indicate extrapolated energies. For the IM-SRG(2') truncation, the shaded area indicates the variation from using different data sets for the extrapolation (see text). . . . .	91
Figure 3.19:	Effect of adding the fourth-order singles (1p1h) contribution (cf. Eqs. (3.115), (3.118) and (3.128)) to the IM-SRG(2') ground-state energy of $^{40}\text{Ca}$ (see text). The singles contributions for different $\hbar\omega$ were calculated with the initial Hamiltonian $H(0)$ . All shown results were obtained for the chiral $\text{N}^3\text{LO}$ Hamiltonian with $\lambda = \infty$ . . . . .	93
Figure 3.20:	Effective neutron (left panel) and proton (right panel) single-particle energies of $^{40}\text{Ca}$ from IM-SRG(2) (solid lines) and IM-SRG(2') (dashed lines) calculations using the chiral $\text{N}^3\text{LO}$ interaction with $\lambda = \infty$ in an $e_{\text{max}} = 14$ single-particle basis. . . . .	93
Figure 4.1:	$ H_{11}(s) - E_{\text{gs}} $ versus $s$ for different Euler step sizes calculated via direct integration of the SRG flow equation, Eq. 3.2, and using the Magnus expansion, Eqs. 4.6 and 4.8. Also plotted is the integration of Eq. 3.2 with the Gordon-Shampine integrator. . . . .	100
Figure 4.2:	Relative importance of the $k^{\text{th}}$ term in the Magnus derivative as defined by the lefthand side of Eq. 4.16 evaluated in the NO2B approximation. The top row is for the homogeneous electron gas at Wigner-Seitz radii of a) $r_s = 0.5$ and b) $r_s = 5.0$ . The bottom row is for $^{16}\text{O}$ , starting from the chiral NN potential of Entem and Machleidt [17], softened by a free-space SRG evolution to (c) $\lambda = 2.0 \text{ fm}^{-1}$ and (d) $\lambda = 3.0 \text{ fm}^{-1}$ . The electron gas calculations were done for $N = 14$ electrons in a periodic box with $M = 114$ single particle orbitals. The $^{16}\text{O}$ calculations were done in an $e_{\text{max}} = 8$ model space, with $\hbar\omega = 24 \text{ MeV}$ for the underlying harmonic oscillator basis. . . .	105
Figure 4.3:	Magnitude of the 0-body contributions of the $k^{\text{th}}$ term in Eq. 4.8 evaluated in the NO2B approximation. The top row is for the electron gas at Wigner-Seitz radii of (a) $r_s = 0.5$ and (b) $r_s = 5.0$ . The bottom row is for $^{16}\text{O}$ , starting from the chiral NN potential of Entem and Machleidt [17], softened by a free-space SRG evolution to (c) $\lambda = 2.0 \text{ fm}^{-1}$ and (d) $\lambda = 3.0 \text{ fm}^{-1}$ . The electron gas calculations were done for $N = 14$ electrons in a periodic box with $M = 114$ single particle orbitals. The $^{16}\text{O}$ calculations were done in an $e_{\text{max}} = 8$ model space, with $\hbar\omega = 24 \text{ MeV}$ for the underlying harmonic oscillator basis. . . .	107

Figure 4.4:	Flowing IM-SRG(2) and MAGNUS(2) HEG correlation energy, $E_0(s) - E_{\text{HF}}$ , for Wigner-Seitz radii of a) $r_s = 5.0$ and b) $r_s = 0.5$ . The solid black line corresponds to IM-SRG(2) results using an adaptive solver based on the Adams-Bashforth method, while the other lines correspond to MAGNUS(2) and IM-SRG(2) results using different Euler step sizes. The red circles denote the quasi-exact FCIQMC results of Ref. [3]. . . . .	108
Figure 4.5:	Flowing IM-SRG(2) and MAGNUS(2) ground state energy, $E_0(s)$ , for $^{16}\text{O}$ starting from the $\text{N}^3\text{LO}$ NN interaction of Entem and Machleidt [17] evolved by the free-space SRG to a) $\lambda = 2.7 \text{ fm}^{-1}$ and $\lambda = 2.0 \text{ fm}^{-1}$ . The solid black line corresponds to IM-SRG(2) results using an adaptive solver based on the Adams-Bashforth method, while the other lines correspond to MAGNUS(2) and IM-SRG(2) results using different Euler step sizes. The calculations were done in an $e_{\text{max}} = 8$ model space, with $\hbar\omega = 24 \text{ MeV}$ for the underlying harmonic oscillator basis. . . . .	109
Figure 4.6:	Electron gas momentum distributions calculated in the MAGNUS(2) approximation. The calculations were done for $N = 14$ electrons in a periodic box with $M = 778$ single particle orbitals. . . . .	111
Figure 4.7:	Timing for MAGNUS(2) and IM-SRG(2) HEG calculations as the single particle basis is increased. The two bottom curves are for $r_s = .5$ and the top for $r_s = 5$ . For the MAGNUS(2) timing, this includes the calculations of the momentum distributions. . . . .	112
Figure 4.8:	Center of mass diagnostics for MAGNUS(2) calculations of $^{16}\text{O}$ starting from the $\text{N}^3\text{LO}$ NN interaction of Entem and Machleidt [17] evolved by the free-space SRG to $\lambda = 2.0 \text{ fm}^{-1}$ . See the text for details. The calculations were done in an $e_{\text{max}} = 9$ model space. . .	113
Figure 5.1:	The dark circle and square represent the bare Hamiltonian and generator respectively. The light circles in the first column represent the second order 1-body Hamiltonian originating from $[\eta, H]_{1B}$ . If the second order 1-body vertex is expanded in terms of bare quantities, the 4 asymmetric Goldstone diagrams on the right are the result. . .	121
Figure 5.2:	The dark circle and square represent the bare Hamiltonian and generator respectively. The light circles in the first column represent the second order 3-body Hamiltonian originating from $[\eta, H]_{3B}$ . If the second order induced 3-body vertex is expanded in terms of bare quantities, the 4 asymmetric Goldstone diagrams on the right are the result. . . . .	122

Figure 5.3:	Ground state calculations for 14 electrons confined to a box at densities of $r_s/a_0$ of .5,1,2,and 5 and performed at 3 basis set sizes of 114,186, and 358 with various methods. Although CCSD results are not plotted, correcting the MAGNUS(2) commutator expressions as shown in Eq. (5.4) makes MAGNUS(2*) indistinguishable from CCSD on these scales. Further, the triples correction due to the MAGNUS(2*)[3]-D binds the result back down to agree very well with FCIQMC results from Ref. [3], while the bare denominators found in variant A of MAGNUS(2*)[3] overbind dramatically. . . .	130
Figure 5.4:	MAGNUS(2*) results, with final MAGNUS(2*)[3]-C for the largest basis set for ${}^4\text{He}$ with the chiral $\text{N}^3\text{LO}$ chiral interaction by Entem and Machleidt [1, 2] softened to $\lambda = 2.0 \text{ fm}^{-1}$ . We notice that correcting the commutator as shown in Eq. (5.4) provides repulsion that brings MAGNUS(2*) up to CCSD. Further, the triples correction due to the MAGNUS(2*)[3]-C binds the result back down to agree with ACCSD[T]. CC results from Ref. [18] . . . . .	133
Figure 5.5:	MAGNUS(2*) results, with final MAGNUS(2*)[3]-C for the largest basis set for ${}^{16}\text{O}$ with the chiral $\text{N}^3\text{LO}$ chiral interaction by Entem and Machleidt [1, 2] softened to $\lambda = 2.0 \text{ fm}^{-1}$ . . . . .	133
Figure 6.1:	Ground-state energies of the oxygen isotopes from MR-IM-SRG and other many-body approaches, based on the NN+3N-full interaction with $\Lambda_{3\text{N}} = 400 \text{ MeV}$ , evolved to the resolution scale $\lambda = 1.88 \text{ fm}^{-1}$ ( $\lambda = 2.0 \text{ fm}^{-1}$ for the Green's Function ADC(3) results, cf. [19]). Black bars indicate experimental data [20]. See Ref. [21] for additional details. . . . .	149
Figure 6.2:	MR-IM-SRG results for Ca two-neutron separation energies, for chiral NN+3N interactions with different cutoffs in the 3N sector, and a range of resolution scales from $\lambda = 1.88 \text{ fm}^{-1}$ (open symbols) to $2.24 \text{ fm}^{-1}$ (solid symbols). Black bars indicate experimental data [20, 22]. See Ref. [23] for additional details. . . . .	150
Figure 6.3:	Excited-state spectra of ${}^{22,23,24}\text{O}$ based on chiral NN+3N interactions and compared with experiment. Figures adapted from Ref. [24]. The MBPT results are performed in an extended $sd f_{7/2} p_{3/2}$ space [25] based on low-momentum NN+3N interactions, while the IM-SRG [24] and CC effective interaction (CCEI) [26] results are in the $sd$ shell from the SRG-evolved NN+3N-full Hamiltonian with $\hbar\omega = 20 \text{ MeV}$ (CCEI and dotted IM-SRG) and $\hbar\omega = 24 \text{ MeV}$ (solid IM-SRG). The dashed lines show the neutron separation energy. Figure taken from Ref. [27]. . . . .	153

# Chapter 1

## Introduction

### 1.1 Brief History

The quest to predict and understand the properties of nuclei starting from the underlying nuclear forces goes back nearly 60 years, dating back to the pioneering work of Brueckner, Bethe, and Goldstone [28–30]. In contrast predictive and accurate *ab initio* many-body calculations were commonplace in quantum chemistry by the 1980s [31]. Progress was not slowed there by the challenging aspects of the nuclear problem like the lack of a consistent theory for the strong inter-nucleon interactions, and the need to perform computationally expensive (and uncontrolled) resummations to handle the non-perturbative aspects of the problem. Consequently, for many years nuclear *ab initio* theory languished as a predictive force, and could only explain in semi-quantitative terms how successful phenomenology such as the shell model and Skyrme energy-density functionals are linked to the underlying nuclear interactions.

As experimental efforts have shifted towards exotic nuclei, there has been an increased urgency to develop reliable *ab initio* approaches to counter the inherent limitations of phenomenology. As evidenced by Fig. 1.1, tremendous progress has been made in recent years, where the interplay of different threads, namely rapidly increasing computational power, effective field theory (EFT) descriptions of inter-nucleon interactions, and renormalization group (RG) transformations, have enabled the development of new many-body methods and

the revival of old ones to successfully attack these problems [27, 32–35]. Remarkably, it is now possible to perform quasi-exact calculations including three-nucleon interactions of nuclei up to carbon or oxygen in quantum Monte Carlo (QMC) and no-core shell model (NCSM) calculations, and  $N = Z$  nuclei up through  $^{28}\text{Si}$  in lattice effective field theory with Euclidean time projection [12, 36–38]. Moreover, a host of approximate (but systematically improvable) methods such as Coupled Cluster (CC), self-consistent Green’s functions (SCGF), auxiliary field diffusion Monte Carlo (AFDMC), and the IM-SRG have pushed the frontiers of *ab initio* theory well into the medium-mass region, opening up new directions to the challenging terrain of open-shell and exotic nuclei [21, 23, 24, 26, 39–46], with recent highlights in the calcium isotopes [22, 47].

RG methods have played a prominent role in the resurgence of *ab initio* theory. A key to optimizing calculations of nuclei is a proper choice of degrees of freedom. While Quantum Chromodynamics (QCD) is the underlying theory of strong interactions, the most *efficient* low-energy degrees of freedom for nuclear structure are the colorless hadrons of traditional nuclear phenomenology. But this realization is not enough. For low-energy calculations to be computationally efficient (or even feasible in some cases) we need to exclude or, more generally, to *decouple* the high-energy degrees of freedom in a manner that leaves low-energy observables invariant.

Progress on the nuclear many-body problem was hindered for decades because nucleon-nucleon (NN) potentials that reproduce elastic scattering phase shifts typically have strong short-range repulsion and strong short-range tensor forces. This produces substantial coupling to high-momentum modes, which is manifested as strongly correlated many-body wave functions and highly nonperturbative few- and many-body systems. For many years, the only viable option to handle these features in a controlled manner was to use quasi-exact methods

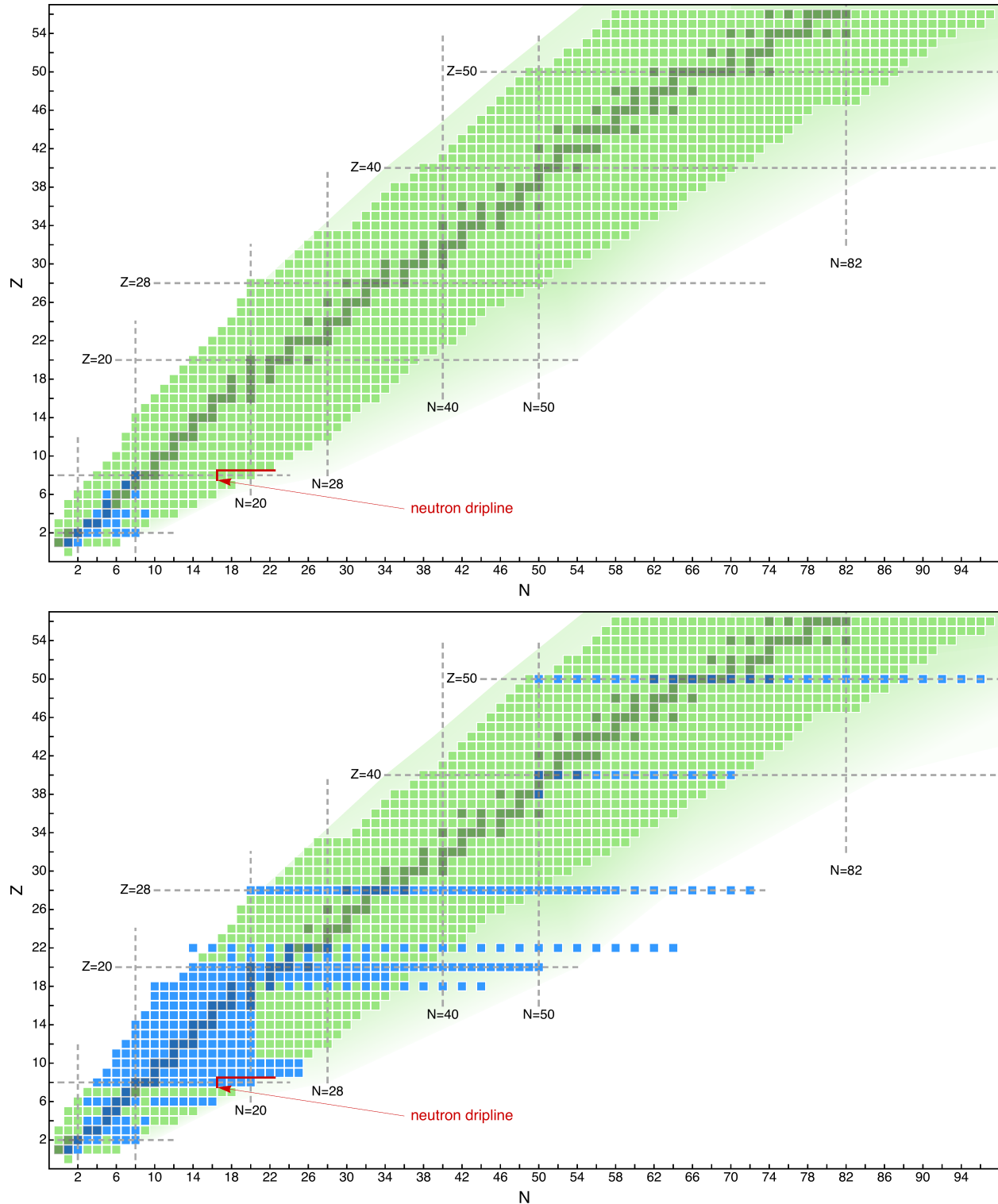


Figure 1.1: Taken from Ref. [11]. The chart of nuclides and the reach of *ab initio* calculations in (a) 2005 and (b) 2015. Nuclei (including potentially unbound isotopes) for which *ab initio* calculations based on high-precision nuclear interactions exist are highlighted. Essentially all of the 2015 calculations include  $3N$  forces. We note that the figure is for illustrative purposes only, and is based on the authors' potentially non-exhaustive survey of the literature.

such as QMC or NCSM, which limited the reach of *ab initio* calculations to light p-shell nuclei. Powerful methods that scale favorably to larger systems like CC and many-body perturbation theory (MBPT) were largely abandoned in nuclear physics, but exported to quantum chemistry, where they enjoyed immediate success and quickly became the gold-standard for *ab initio* calculations[48–50]. The success of CC and related methods in quantum chemistry stems from the fact that Hartree-Fock is a relatively good starting point due to the relatively weak correlations induced by the Coulomb interaction, in stark contrast to the nuclear case. Additionally, the nuclear case is beset with difficulties with the quality of nuclear forces, and other issues that plague self-bound systems like center of mass contamination.

New approaches to nuclear forces grounded in RG ideas and techniques have been developed in recent years that effectively make the nuclear many-body problem look more like quantum chemistry [33, 37, 51–55]. The RG allows continuous changes in “resolution” that decouple the troublesome high-momentum modes and can be used to evolve interactions to nuclear structure energy and momentum scales while preserving low-energy observables. Such potentials, known generically as “low-momentum interactions,” are more perturbative and generate much less correlated wave functions. This has played a major role in expanding the reach of *ab initio* calculations to medium-mass nuclei, since methods that exhibit polynomial scaling can now be converged in manageable model spaces. See Refs. [33, 56, 57] for recent reviews on the use of RG methods in nuclear physics.

As will be shown in the following, the IM-SRG approach extends the RG notion of decoupling to the many-body Hilbert space by formulating “in-medium” flow equations, the solution of which is equivalent to the partial diagonalization or block-diagonalization of the many-body Hamiltonian [21, 24, 33, 39, 58]. Because of its favorable polynomial scaling with system size, and the flexibility to target ground and excited states of both closed-

and open-shell systems, the IM-SRG provides a powerful *ab initio* framework for calculating medium-mass nuclei from first principles that is grounded in modern RG principles.

Despite the inherent strengths of this method, it suffers from several shortcomings. Key amongst these are i) the linear scaling with each additional observable one wishes to calculate, ii) the need to solve a large set of coupled differential equations to high numerical accuracy, iii) and the inability to approximate the effect of omitted terms in the simplest truncations of the IM-SRG equations. The aim of this thesis is to show how a novel reformulation of the IM-SRG using Magnus expansion techniques allows one to circumvent all three of these weaknesses, at least for closed-shell systems. I will show that the IM-SRG, when coupled with a true matrix exponential formalism via the Magnus expansion, provides a controlled, non-perturbative scheme to find the ground states of nuclei and of quantum chemistry systems. Moreover, there are promising indications that the methods laid out in this thesis will provide important tools for deriving effective valence shell model Hamiltonians and operators from the underlying nuclear forces, opening the door to an *ab initio* description of open-shell, medium-mass nuclei.

The rest of this thesis is organized as follows. In Chapter 2, I start with a brief review of many-body perturbation theory (MBPT) and CC theory, as many of the improvements described in this thesis are based on analyzing the perturbative content of the IM-SRG and understanding the similarities and differences from CC theory. In Chapter 3, the basic elements of the IM-SRG method are reviewed in some detail, and a sampling of its successes in nuclei are presented. Note that the diagrammatic analysis of the perturbative content of the IM-SRG in Section 3.5 is especially important. In addition to guiding many of the improvements detailed in Chapter 5, this was my main contribution to the recent review article [11] that much of the material in Chapter 3 is based on. Chapter 4 describes the

crucial reformulation of the IM-SRG equations using the Magnus expansion, and shows how this eliminates many of the computational limitations faced by the conventional formulation due to large memory overhead. Chapter 5 documents how the simplest IM-SRG(2) and MAGNUS(2) truncations fail in certain quantum chemistry systems, and uses the perturbative analysis of Section 3.5 to motivate improved truncations, which are then validated for several electronic and nuclear systems. Chapter 6 highlights some interesting open topics that are presently “in development”, such as a computationally inexpensive method to perform calculations in Brueckner orbitals and extensions to more challenging open-shell and multi-reference problems. Finally, conclusions are presented in Chapter 7.

# Chapter 2

## The Many-Body Problem

In low energy nuclear systems, quantum chemistry, and solid state physics, one wishes to be able to understand emergent phenomena from a microscopic Hamiltonian. Despite the ambiguity in the inter-nucleon interactions arising from scheme and scale dependence, the basic mechanics for solving all three systems are the same once a given interaction is settled on. However, because solving the  $A$ -body Schrödinger equation in an exact and straightforward manner leads to a factorially scaling problem in  $A$ , approximate solutions are the only way to move forward. A variety of different approximate methods have shown promise in recent years, but in order to motivate both the strengths and deficiencies of the IM-SRG method, and the to-be-presented Magnus formulation of it, we will begin by reviewing the basics of the many-body problem and two established methods for approximately solving it. The first, and most well known of these is MBPT, which will be covered in Section 2.3. Further because of the strong relationship between IM-SRG and CC theory, and how CC theory motivates improvements in the IM-SRG method, we will also present the important elements of CC theory in Section 2.4.

### 2.1 Many-Body Schrödinger Equation

The main problem in non-relativistic many-body physics is to find the solution of the Schrödinger equation for a system of  $A$  interacting elementary particles, generally fermions.

One can write down the time-independent ground state solution as

$$H |\Psi_0\rangle = E_0 |\Psi_0\rangle. \quad (2.1)$$

For the purposes of this work, it is useful to start with a Fock-space second quantized Hamiltonian

$$H = \sum_{pq} T_{pq} a_p^\dagger a_q + \frac{1}{4} \sum_{pqrs} V_{pqrs}^{(2)} a_p^\dagger a_q^\dagger a_s a_r + \frac{1}{36} \sum_{pqrst} V_{pqrst}^{(3)} a_p^\dagger a_q^\dagger a_r^\dagger a_u a_t a_s, \quad (2.2)$$

where  $V_{pqrs}^{(2)}$  and  $V_{pqrst}^{(3)}$  are antisymmetrized two- and three-body interaction matrix elements, and a complete basis set of Slater determinants for the  $A$ -body Hilbert space as

$$|\Phi\{p_1 \dots p_A\}\rangle = \prod_{k=1}^A a_{p_k}^\dagger |0\rangle, \quad (2.3)$$

given that the single-particle basis state to which the creation operators refer to are complete in the one-body space. It is clear then that any  $A$ -body state can be written in terms of these Slater determinants, and in particular the true ground state has the form

$$|\Psi_0\rangle = \sum_{p_1 < \dots < p_A} C_{p_1 \dots p_A} |\Phi\{p_1 \dots p_A\}\rangle. \quad (2.4)$$

This expansion demonstrates what was mentioned earlier, that a straightforward variational calculation of the  $C_{p_1 \dots p_A}$ 's becomes intractable with increasing  $A$ . If the single particle basis is truncated at  $n$  orbitals and symmetry is ignored, then there are  $\binom{n}{A}$   $C_{p_1 \dots p_A}$ 's which must be determined. Even for very moderate systems being optimized on a very large computational facility, this procedure is intractable. Figure 2.1 demonstrates the feasibility

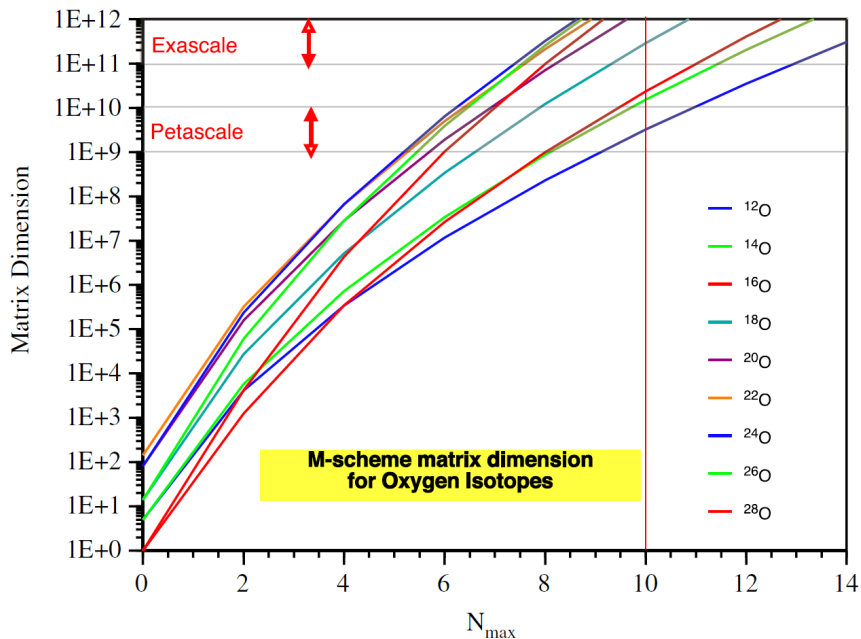


Figure 2.1: Matrix dimension versus  $N_{max}$  for stable and unstable Oxygen isotopes. The vertical red line signals the boundary, beyond which one might expect reasonable convergence with respect to  $N_{max}$ . The horizontal lines show the computational power of a facility expected to conduct these diagonalizations. Figure taken from Ref. [12].

of calculating the oxygen isotopes in a straightforward way taken from [12].

There are some common conventions which will be worthwhile to introduce in order to be able to discuss MBPT, CC theory, and the IM-SRG in the next chapter. First I will introduce the concept of an adequately chosen reference state, which will lead immediately to the concept of normal ordering, which is invaluable for the purposes of bookkeeping for the methods discussed in this work.

## 2.2 Normal Ordering

Reference states are a common ingredient to most many-body methods. Usually, their function is to fix certain characteristics of the system we want to describe, e.g., the proton

and neutron numbers of a nucleus, and to provide a starting point for the construction of a many-body Hilbert space that is superior to the particle vacuum. Describing many-body states as excitations with respect to a suitably chosen reference state allows us to account for the characteristic energy scales of the target nucleus, and introduce systematic truncation schemes based on this information. It also suggests the use of normal-ordering techniques in a natural fashion (cf. 2.2). Using a Slater determinant as the reference state is a suitable choice for systems with a large gap in their excitation spectrum, e.g., closed-shell nuclei. Among the Slater determinants, those that satisfy the Hartree-Fock conditions for a given system are the most natural choices (cf. Sec. 3.3), because they minimize *both* the mean-field energy and the *beyond mean-field correlation energy* in a variational sense.

Once a suitable single reference  $|\Phi\rangle$  is chosen, one can invoke the concept of normal ordering. As mentioned, this leads to a natural organization of the complete  $A$ -body states into their level of excitation away from  $|\Phi\rangle$ . Normal-ordered operators can then be defined by beginning with the most simple of these,

$$a_p^\dagger a_q \equiv : a_p^\dagger a_q : + \overline{a_p^\dagger a_q}, \quad (2.5)$$

where the contraction is related to the reference state  $|\Phi\rangle$ :

$$\overline{a_p^\dagger a_q} \equiv \langle \Phi | a_p^\dagger a_q | \Phi \rangle \equiv \rho_{qp} = \delta_{pq} n_p, \quad (2.6)$$

where  $n_p$  is 1 or 0 depending on occupation in  $|\Phi\rangle$ . This generalizes easily to  $A$ -body

operator:

$$\begin{aligned}
& a_{p_1}^\dagger \dots a_{p_N}^\dagger a_{q_N} \dots a_{q_1} \\
& \equiv : a_{p_1}^\dagger \dots a_{p_N}^\dagger a_{q_N} \dots a_{q_1} : \\
& + \overline{a_{p_1}^\dagger a_{q_1}} : a_{p_2}^\dagger \dots a_{p_N}^\dagger a_{q_N} \dots a_{q_2} : - \overline{a_{p_1}^\dagger a_{q_2}} : a_{p_2}^\dagger \dots a_{p_N}^\dagger a_{q_N} \dots a_{q_3} a_{q_1} : + \text{singles} \\
& + \left( \overline{a_{p_1}^\dagger a_{q_1}} \overline{a_{p_2}^\dagger a_{q_2}} - \overline{a_{p_1}^\dagger a_{q_2}} \overline{a_{p_2}^\dagger a_{q_1}} \right) : a_{p_3}^\dagger \dots a_{p_N}^\dagger a_{q_N} \dots a_{q_3} : + \text{doubles} \\
& + \dots + \text{full contractions.} \tag{2.7}
\end{aligned}$$

It is clear that  $\langle \Phi | : a_p^\dagger a_q : | \Phi \rangle$  must vanish, and a similar finding is true for general normal-ordered operators in the reference state  $|\Phi\rangle$

$$\langle \Phi | : a_{p_1}^\dagger \dots a_{p_1} : | \Phi \rangle = 0. \tag{2.8}$$

It is then possible to invoke Wick's theorem (see e.g. [16]), which is a simple ramification of the definition of normal ordering in Eq. (2.7). This allows for the expansion of products of two or more normal ordered operators:

$$\begin{aligned}
& : a_{p_1}^\dagger \dots a_{p_N}^\dagger a_{q_N} \dots a_{q_1} : : a_{r_1}^\dagger \dots a_{r_M}^\dagger a_{s_M} \dots a_{s_1} : \\
& = (-1)^{M \cdot N} : a_{p_1}^\dagger \dots a_{p_N}^\dagger a_{r_1}^\dagger \dots a_{r_M}^\dagger a_{q_N} \dots a_{q_1} a_{s_M} \dots a_{s_1} : \\
& + (-1)^{M \cdot N} \overline{a_{p_1}^\dagger a_{s_1}} : a_{p_2}^\dagger \dots a_{r_M}^\dagger a_{q_N} \dots a_{s_2} : \\
& + (-1)^{(M-1)(N-1)} \overline{a_{q_1}^\dagger a_{r_1}^\dagger} : a_{p_1}^\dagger \dots a_{r_M}^\dagger a_{q_N} \dots a_{l_1} : \\
& + \text{singles} + \text{doubles} + \dots \tag{2.9}
\end{aligned}$$

The phases appear as the  $a_r^\dagger$  operators are anti-commuted past  $a_q$ . Since  $|\Phi\rangle$  is an  $A$ -body

state and not the true vacua, there is a new type of contraction,

$$\overline{a_p a_q^\dagger} \equiv \langle \Phi | a_p a_q^\dagger | \Phi \rangle = \delta_{pq} - \rho_{pq}, \quad (2.10)$$

as expected from the basic fermionic anti-commutator algebra. This provides a robust framework for evaluating the product of normal ordered operators with the least amount of terms. Also beneficial, is that it motivates a diagrammatic formalism that makes evaluation of terms intuitive. An important finding from Wick's theorem that will be relevant in the formulation of the IM-SRG is that a product of normal-ordered  $M$  and  $N$ -body operators has the general form

$$A^M B^N = \sum_{k=|M-N|}^{M+N} C^{(k)}. \quad (2.11)$$

Exploiting normal ordering, one can exactly rewrite the hamiltonian Eq. (2.2),

$$H = E + \sum_{pq} f_{pq} : a_p^\dagger a_q : + \frac{1}{4} \sum_{pqrs} \Gamma_{pqrs} : a_p^\dagger a_q^\dagger a_s a_r : + \frac{1}{36} \sum_{pqrst} W_{pqrst} : a_p^\dagger a_q^\dagger a_r^\dagger a_u a_t a_s : . \quad (2.12)$$

The individual normal-ordered contributions in Eq. (2.12) are then given by

$$E = \sum_i \langle i | T | i \rangle + \frac{1}{2} \sum_{ij} \langle ij | V^{(2)} | ij \rangle + \frac{1}{6} \sum_{ijk} \langle ijk | V^{(3)} | ijk \rangle, \quad (2.13)$$

$$f_{pq} = \langle p | T | q \rangle + \sum_i \langle pi | V^{(2)} | qi \rangle + \frac{1}{2} \sum_{ij} \langle pij | V^{(3)} | qij \rangle, \quad (2.14)$$

$$\Gamma_{pqrs} = \langle pq | V^{(2)} | rs \rangle + \sum_i \langle pqi | V^{(3)} | rsi \rangle, \quad (2.15)$$

$$W_{pqrst} = \langle pqr | V^{(3)} | stu \rangle. \quad (2.16)$$

I use the convention where  $i, j, \dots$  refer to occupied orbitals in  $|\Phi\rangle$ ,  $a, b, \dots$  refer to

unoccupied orbitals in  $|\Phi\rangle$ , and  $p, q, \dots$  refer to either. In Eqs. (2.13)–(2.15), it is important to note that the zero-, one-, and two-body parts of the normal-ordered hamiltonian all contain contributions from the higher-body free-space interaction. This suggests that the dominant effects of computationally expensive three- and higher-body interactions can be included in two- and lower-body operators via normal ordering.

## 2.3 Many Body Perturbation Theory

Armed with a quality reference state  $|\Phi\rangle$ , it is often possible to expand the full solution and properties around this reference. To do so is to follow the path of many body perturbation theory (MBPT). I present here a brief summary of the material provided in [16].

The Hamiltonian is first partitioned into a diagonal and interaction part

$$H |\Psi_0\rangle = (H_0 + H_I) |\Psi_0\rangle = E_0 |\Psi_0\rangle \quad (2.17)$$

where  $H_I = H - H_0$ , and the zero-order solutions based on  $H_0$  are known

$$H_0 |\Phi\rangle = E_0^{(0)} |\Phi\rangle. \quad (2.18)$$

Multiplying Eq (2.17) on the left with the reference  $\langle\Phi_0|$  one arrives at

$$E_0^{(0)} + \langle\Phi|H_I|\Psi_0\rangle = E_0 \langle\Phi|\Psi_0\rangle. \quad (2.19)$$

Invoking intermediate normalization where  $\langle\Phi|\Psi_0\rangle = 1$ , one arrives at the working expres-

sion for the correlation energy,

$$\Delta E = E_0 - E_0^{(0)} = \langle \Phi | H_I | \Psi_0 \rangle. \quad (2.20)$$

Following the usual prescription to generate the different versions of perturbation theory (e.g. Rayleigh-Schrödinger and Brillouin-Wigner), one arrives at the infinite order solution

$$|\Psi_0\rangle = \sum_{m=0}^{\infty} \{R_0(\zeta)(H_I - E_0 + \zeta)\}^m |\Phi\rangle, \quad (2.21)$$

with the resolvent operator

$$R_0(\zeta) = \frac{Q}{\zeta - H_0} \quad (2.22)$$

where  $Q$  projects onto the orthogonal complement of  $|\Phi\rangle$ . This immediately yields a perturbative expansion for the energy of

$$\Delta E = \sum_{m=0}^{\infty} \langle \Phi | H_I \{R_0(\zeta)(H_I - E_0 + \zeta)\}^m |\Phi\rangle. \quad (2.23)$$

For the remainder of this work we make the choice  $\zeta = E_0^{(0)}$  which corresponds to the size extensive Rayleigh-Schrödinger perturbation theory. We use this decision to rewrite  $R_0(E_0^{(0)})$  as just  $R_0$ .

$$\Delta E = \sum_{m=0}^{\infty} \langle \Phi | H_I \{R_0(H_I - \Delta E)\}^m |\Phi\rangle \quad (2.24)$$

Thus, as long as  $H_0$  and its spectrum can be found, Eq. (2.24) can be solved order by order. The lack of small expansion parameter in this formalism indicates that convergence is not guaranteed. Evaluation of terms in Eq. (2.24) is aided by the help of diagrammatic methods applicable when working with a normal ordered Hamiltonian. The rules for interpreting

diagrams are found both in Appendix C and Ref [16]. For many systems, it is necessary to find non-perturbative methods that resum certain classes of perturbative diagrams to infinite order to achieve adequate accuracy. Size extensivity is guaranteed in Rayleigh-Schrödinger perturbation theory, as all unlinked diagrams appearing in the energy cancel order-by-order [59].

As we will see in Chapter 5, the intuition gleaned from diagrammatic MBPT will be crucial in developing systematically improvable IM-SRG truncations. As an example, the first non-trivial contribution to the energy that arises at second order in MBPT has the form

$$\Delta E^{[2]} = \langle \Phi | \{H_I R_0 H_I\}_C | \Phi \rangle, \quad (2.25)$$

where the subscripted C represents that only connected terms contribute. Plugging in the normal ordered operators in Eqs. (2.14)–(2.16) for  $H_I$ , the expanded version of Eq. (2.25) becomes

$$\Delta E^{[2]} = \sum_{ia} \frac{f_{ia} f_{ai}}{\Delta_{ia}} + \frac{1}{2!^2} \sum_{ijab} \frac{\Gamma_{ijab} \Gamma_{abij}}{\Delta_{ijab}} + \frac{1}{3!^2} \sum_{ijkabc} \frac{W_{ijkabc} W_{abcijk}}{\Delta_{ijkabc}} \quad (2.26)$$

where

$$\Delta_{i_1 \dots i_N a_1 \dots a_N} = E_0^{(0)} - \langle \Phi_{i_1 \dots i_N}^{a_1 \dots a_N} | H_0 | \Phi_{i_1 \dots i_N}^{a_1 \dots a_N} \rangle. \quad (2.27)$$

Similar analysis can be carried out for each order, but the cost of calculating diagrams even at fourth order scales similarly to much higher quality many-body methods.

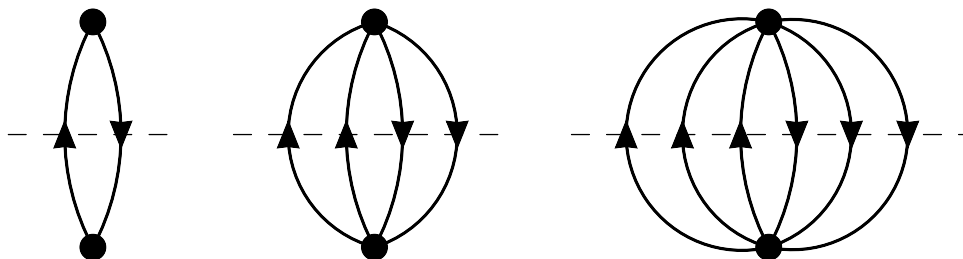


Figure 2.2: Diagram demonstrating the diagrammatic form of Eq. (2.26). The dashed line indicates the resolvent operator  $R_0$ .

## 2.4 Coupled Cluster Theory

As mentioned above, it is often impossible to arrive at a satisfactory energy or wavefunction from low-order perturbation theory, necessitating infinite-order partial resummations of Eq. (2.21) and (2.24). One such resummation is CC theory, which has a distinguished history in quantum chemistry, and is commonly regarded as the *ab initio* method with the optimal compromise between accuracy and computational cost. Although first contemplated by nuclear physicists, the “hardcore” inter-nucleon interactions used at that time made it difficult to apply CC theory to nuclei without performing a complicated rearrangement of the CC equations to adequately capture the strong short range correlations [48–50, 60]. In chemistry it has become a mature field, most notably because of its ease of use, and its ability to approximate more exact CC methods from less expensive ones without reverting to the more exact methods cost. These features will be briefly reviewed in the following sections.

### 2.4.1 Exponential Ansatz

CC theory relies first and foremost on the ability to parametrize the exact wavefunction as the result of an exponential operator acting on a reference Slater determinant  $|\Phi\rangle$ ,

$$|\Psi_{CC}\rangle = e^T |\Phi\rangle, \quad T = T_1 + T_2 + \dots, \quad (2.28)$$

with cluster operators

$$T_1 = \sum_{ai} t_{ai} :a_a^\dagger a_i:, \quad (2.29)$$

$$T_2 = \frac{1}{4} \sum_{abij} t_{abij} :a_a^\dagger a_b^\dagger a_j a_i: . \quad (2.30)$$

$\vdots$

It can be shown via the linked cluster theorem that  $|\Psi_{CC}\rangle$  is an exact reformulation of the MBPT wavefunction, and thus the CC ansatz is an exact reformulation of the Schrödinger equation if  $T$  is not truncated [16, 61]. The energy and coefficients of the cluster operators are determined by solving the algebraic system of equations

$$\langle \Phi | e^{-T} H e^T | \Phi \rangle = E_0, \quad (2.31)$$

$$\langle \Phi_i^a | e^{-T} H e^T | \Phi \rangle = 0, \quad (2.32)$$

$$\langle \Phi_{ij}^{ab} | e^{-T} H e^T | \Phi \rangle = 0, \quad (2.33)$$

$\vdots$

where  $|\Phi_i^a\rangle, |\Phi_{ij}^{ab}\rangle, \dots$ , are particle-hole excited Slater determinants. The full algebraic forms of Eqs. 2.31-2.33 can be found in Ref. [16]. It is clear that if these equations are satisfied, the similarity transformed hamiltonian  $\bar{H} = e^{-T} H e^T$  no longer connects  $|\Phi\rangle$  to excited Slater determinants. It is also important to note that the similarity transformation is non-unitary, which makes the similarity transformed Hamiltonian  $\bar{H}$  non-Hermitian.

Solving for the higher-body amplitudes like those found in Eq. 2.31-2.33 becomes increasingly more expensive for each higher-body cluster that is solved for. Thus it becomes necessary to truncate the cluster amplitudes, meaning the method becomes an approximate solution to the Schrödinger equation. It is most common then to solve these equations approximately for only  $T_n$  with  $n < m_A$  where  $m_A < A$ . Solving for up to  $T_1, T_2, T_3, \dots$  has commonly become known as singles (S), doubles (SD), triples(SDT), etc. Most commonly,  $T$  is approximated at the  $T_1 + T_2$  level, which is known as CC singles + doubles (CCSD), which has a cost of  $n_o^2 n_u^4$  where  $n_o$  and  $n_u$  are the number of occupied and unoccupied single particle orbitals in the calculation.

One of the most important implications of using the CC ansatz is that of relative insensitivity to the choice of reference. According to a theorem by Thouless [62], any two Slater determinants  $|\Phi_A\rangle, |\Phi_B\rangle$  that are non-orthogonal and therefore have non-vanishing overlap are related (up to a normalization constant and phase factor) by a similarity transformation:

$$|\Phi_B\rangle \sim \exp\left(\sum_{ai} t_{ai} :a_a^\dagger a_i:\right) |\Phi_A\rangle \equiv e^{T^{(1)}} |\Phi_A\rangle. \quad (2.34)$$

Since the  $T_i$  are only defined in terms of particle-hole *excitation* operators, it is easy to see

that cluster operators of different particle rank commute,

$$[T_i, T_j] = 0, \quad (2.35)$$

because contractions between particle creation and hole annihilation operators vanish. Consequently, the CCSD wave function can be written as

$$|\Psi_{\text{CCSD}}\rangle \approx e^{T_1+T_2} |\Phi\rangle = e^{T_2} e^{T_1} |\Phi\rangle, \quad (2.36)$$

and thus Thouless' theorem (2.34) is directly built into the CC formalism. The single Slater determinant mapped to by  $e^{T_1} |\Phi\rangle$  will in general be of the better Slater determinants that can be chosen, regardless of the original choice of  $|\Phi\rangle$ .

It has been shown that the CCSD approximation contains certain classes of perturbative diagrams like the so-called particle-particle ladders, and hole-hole ladders summed to infinite order [63]. Further, the particle-hole ladders, and their interference with particle-particle and hole-hole ladders are included as well. This separates it from more traditional resummation methods like the Brueckner Hartree-Fock formalism or the Random Phase Approximation [63, 64]. The perturbative content of the CCSD method is important to note now, as the approximations to triples that are forthcoming were originally motivated by a desire to increase the order by order accuracy of the method [16]. A close inspection of the CCSD energy shows that it is complete through third order in MBPT, and is incomplete with respect to MBPT beginning with connected triple excitations at fourth order.

## 2.5 Approximate Triples

Since full CCSDT is computationally expensive even when using just a two-body Hamiltonian, scaling at  $n_o^3 n_p^5$ , various approximations have been developed which take into account the leading effects of triples on CCSD. In this thesis, I will focus on the non-iterative triples correlations which are calculated using fully converged singles and doubles amplitudes in the absence of  $T_3$ . These approximations share strong parallels both in form and philosophy to the three-body IM-SRG approximations made in this thesis in Chapter 5.

### 2.5.1 CCSD(T)

The most commonly used CC method in quantum chemistry and nuclear physics is CC singles doubles plus perturbative triples, and denoted as CCSD(T) [65]. Here I will only present an earlier version of this approximation, referred to as CCSD[T] or CCSD+T. If starting with a Hartree-Fock reference state, the required diagrams to restore fourth order MBPT content are found in CCSD[T]. In this approximation,  $T_3$  is approximated correctly up to second order in MBPT. This allows for an energy correction correct through fourth order.  $T_3$  has the diagrammatic form found in Fig. 2.3, and algebraic form of

$$T_{abcijk} \approx \langle \Phi_{ijk}^{abc} | \{R_0 \Gamma T_2\}_C | \Phi \rangle. \quad (2.37)$$

It can be shown that all fourth order triple excitation diagrams found in Fig. 3.16 can be found in CC theory as

$$\Delta E_{CCSD[T]} = \frac{1}{3!^2} \sum_{abcijk} |T_{abcijk}|^2 \Delta_{ijkabc}, \quad (2.38)$$

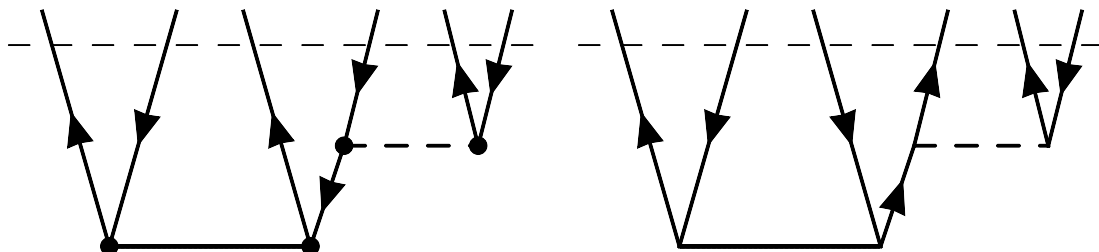


Figure 2.3: Diagrams demonstrating the approximate  $T_3$  constructed from converged  $T_2$  amplitudes in the CCSD[T] energy correction. The dashed line represents the resolvent operator  $R_0$  from perturbation theory.

where  $\Delta_{ijklabc} = \epsilon_i + \epsilon_j + \epsilon_k - \epsilon_a - \epsilon_a - \epsilon_b$ , and  $\epsilon_i = f_{ii}$ . It is important to note that  $T_{abcijk}$  must be made antisymmetric before use in (2.38). By inspecting the diagrams in Fig. 2.3 and counting the number of particle and hole lines, one arrives at the  $n_o^3 n_u^4$  scaling usually quoted by a perturbative triples calculation. This will be the same scaling for all non-iterative triples within CC theory. The addition of the  $\Delta E_{CCSD[T]}$  term to CCSD calculations improves agreement with exact results at equilibrium geometries of molecules dramatically, but usually begins to fail at stretched geometries even for single bond-breaking in chemistry results, and more generally any time the system exhibits a strong multi-reference character [66]. The situation is better, but still qualitatively similar for CCSD(T). For nuclear systems, it is expected that these corrections behave similarly, but the issue of explicit three-body forces makes the issue somewhat less transparent [67].

## 2.5.2 $\Lambda$ -CCSD[T]

One important development in CC theory is its recasting as the solution to a bi-variational minimization [16]. This involves identifying the right and left eigenvector of the similarity transformed Hamiltonian. The left eigenstate can be written as

$$\langle \Phi | (1 + \Lambda), \quad \Lambda = \lambda_1 + \lambda_2 + \dots, \quad (2.39)$$

where the different  $\lambda_n$  are different rank de-excitation operators defined as

$$\begin{aligned} \lambda_1 &= \sum_{ai} \lambda_{ia} : a_i^\dagger a_a : , \\ \lambda_2 &= \frac{1}{4} \sum_{ijab} \lambda_{ijab} : a_i^\dagger a_j^\dagger a_b a_a : \dots \end{aligned} \quad (2.40)$$

This yields the formal CC energy functional as

$$E_{\Lambda-CC} = \langle \Phi | (1 + \Lambda) (e^{-T} H e^T)_C | \Phi \rangle. \quad (2.41)$$

If the  $\Lambda$  and  $T$  are truncated at the same level, for example at the singles and doubles level, then the Eq. 2.31-2.33 result as the stationarity conditions for the functional as  $\lambda_{ia}$  and  $\lambda_{ijab}$  are varied. Additionally, one arrives at a set of  $\Lambda$  equations if  $T_{ia}$  and  $T_{ijab}$  are varied. This not only provides an avenue for generating observables, but also for further approximating the effect of higher order cluster and  $\Lambda$  amplitudes. Again, isolating the perturbative content to restore fourth order terms to a  $\Lambda$ -CCSD energy calculation,

$$\Delta E_{\Lambda-CCSD[T]} = \langle \Phi | \Lambda_2 (\Gamma T_3)_C | \Phi \rangle, \quad (2.42)$$

where  $T_3$  is approximated in the same way as it was for CCSD[T]. This correction allows for the inclusion of different diagrams than CCSD[T], and generally behaves better when describing bond breaking, but again breaks down for systems with a strong multi-reference character [16, 68, 69].

### 2.5.3 Completely Renormalized CC Methods

Arguably the most complete non-iterative method for approximating full CCSDT from CCSD methods is the recent formulation of completely renormalized CC commonly labelled as CR-CC $\mathcal{L}$  or just CR-CC from now on in this work [8]. CR-CC $\mathcal{L}$  improved upon earlier completely renormalized methods such as CR-CCSD(T) which performed much better than the non-iterative triples presented above, but were not rigorously size extensive [70–72]. We will follow the presentation found in Ref.[8]. Here we must define some notation for expedience. As mentioned before, the cluster amplitude is truncated at some excitation rank. If we denote this by the number  $m_A$ , then  $T(m_A) = \sum_{n=1}^{m_A} T_n$ , and  $\bar{H}(m_A) = e^{-T(m_A)} H e^{T(m_A)}$ . CR-CC methods dispense with purely perturbative arguments and instead use a moment expansion combined with a novel parametrization of the true full CI “bra” vector

$$\langle \Psi_0 | H = E_0 \langle \Psi_0 | = E_0 \langle \Phi | \mathcal{L} e^{-T(m_A)}. \quad (2.43)$$

It is important here to notice that although the  $\mathcal{L}$  is similar in form and function to  $1 + \Lambda$  from the previous section, they are not identical.  $\mathcal{L}$  is defined for higher-body components above  $m_A$ , whereas  $1 + \Lambda$  is only defined up to the same level of approximation as  $T$  in the  $\Lambda - CC$  theory. This would make it unfeasible to incorporate a residual three-body force in either of the previous approximate triples treatments. This parametrization leads to the

asymmetric expression for the true ground state energy

$$E_0 = \frac{\langle \Phi | \mathcal{L} e^{-T(m_A)} H e^{T(m_A)} | \Phi \rangle}{\langle \Phi | \mathcal{L} e^{-T(m_A)} e^{T(m_A)} | \Phi \rangle} = \langle \Phi | \mathcal{L} \bar{H}(m_A) | \Phi \rangle. \quad (2.44)$$

This allows for insertion of completeness in terms of excited Slater determinants to arrive at

$$E_0 = \sum_{n=0}^A \sum_{\substack{i_1 < \dots < i_n \\ a_1 < \dots < a_n}} \langle \Phi | \mathcal{L} | \Phi_{i_1 \dots i_n}^{a_1 \dots a_n} \rangle \langle \Phi_{i_1 \dots i_n}^{a_1 \dots a_n} | \bar{H}(m_A) | \Phi \rangle = E(m_A) + \delta(m_A, A). \quad (2.45)$$

The level of excitations inserted between  $\mathcal{L}$  and  $\bar{H}(m_A)$  can be truncated at another level  $m_B$ . If we also make the identification of the “moments” of the similarity transformed matrix element as  $\mathcal{M}_{i_1 \dots i_n}^{a_1 \dots a_n}(m_A) = \langle \Phi_{i_1 \dots i_n}^{a_1 \dots a_n} | \bar{H}(m_A) | \Phi \rangle$ . This allows the CR-CC energy correction to be written as a function of  $m_A$  and  $m_B$ ,

$$\delta(m_A, m_B) = \sum_{n=m_A+1}^{m_B} \sum_{\substack{i_1 < \dots < i_n \\ a_1 < \dots < a_n}} l_{i_1 \dots i_n}^{a_1 \dots a_n} \mathcal{M}_{i_1 \dots i_n}^{a_1 \dots a_n}(m_A). \quad (2.46)$$

Having given the formalism underpinning CR-CC methods, I now turn to the relevant CR-CC(2,3) method. That means that  $\mathcal{L} \approx 1 + \Lambda_{CCSD} + \mathcal{L}_3$ . The  $\mathcal{L}_3$  amplitudes are approximated by multiplying Eq. (2.43) on the right by  $e^{T(CCSD)} | \Phi_{ijk}^{abc} \rangle$ , yielding

$$\langle \Phi | (1 + \Lambda_{CCSD}) \bar{H}(CCSD) | \Phi_{ijk}^{abc} \rangle + \langle \Phi | \mathcal{L}_3 \bar{H}(CCSD) | \Phi_{ijk}^{abc} \rangle = E_0 l_{ijk}^{abc}. \quad (2.47)$$

If the further approximation is made that  $\langle \Phi_{lmn}^{def} | \bar{H}(CCSD) | \Phi_{ijk}^{abc} \rangle \approx 0$  unless  $ijk = lmn$  and  $abc = def$ , and that  $E_0 \approx E_{CCSD}$ , then the  $l_{ijk}^{abc}$  can be isolated using only known

quantities to yield

$$l_{ijk}^{abc}(CCSD) \approx \frac{\langle \Phi | (1 + \Lambda_{CCSD}) \bar{H}(CCSD) | \Phi_{ijk}^{abc} \rangle}{E_{CCSD} - \langle \Phi_{ijk}^{abc} | \bar{H}(CCSD) | \Phi_{ijk}^{abc} \rangle}. \quad (2.48)$$

Full CCSDT tends to track full CI results quite well even for systems with a moderately large multi-reference character. CR-CC(2,3) seems to give comparable accuracy to full CCSDT, while the previous two fail to qualitatively reproduce full CCSDT in these cases [8]. This ability of CR-CC(2,3) to mimic full CCSDT despite scaling in the same manner as CCSD(T) can be tracked down to two main features. The first improvement enters by updating the definition of “diagonal” than is used in the energy denominators of both CCSD(T) and  $\Lambda$ -CCSD(T) corrections. The denominator of the first two methods are just the Möller-Plesset denominators of the bare HF energies. In the completely renormalized theory presented, one instead uses the energy denominator associated with the full similarity transformed Hamiltonian, and diagonal two-body terms are included in the denominators. In Chapters 5 and 6, results will be presented with the label  $CCSD(2)_T$ , which is equivalent to CR-CC(2,3), where the denominator is made up of only one-body terms from the full similarity transformed Hamiltonian. Secondly, the three-body “moment” of the CR-CC(2,3) correction contains many more topologies not found in the previous methods, as they were only linear in the  $T_2$  amplitudes.

# Chapter 3

## In-Medium Similarity

## Renormalization Group

As discussed in Sec. 1.1, the rapid progress in *ab initio* nuclear structure in recent years has been driven in large part by the development of renormalization group methods to produce soft “low-momentum” interactions from underlying “hard” interactions without distorting low-energy observables. Soft potentials are highly advantageous for many-body methods that rely on expanding wave functions in a finite basis of localized single-particle orbitals, as the convergence of calculations with respect to basis size is dramatically improved. Moreover, since strong short-range correlations are smoothed out, Hartree-Fock becomes a reasonable zeroth order starting point for nuclei, making methods like MBPT and coupled cluster theory based on building correlations on top of a “simple” reference state attractive methods for nuclear structure calculations.

As will be shown in the following, the IM-SRG approach extends the RG notion of decoupling low- and high-momentum degrees of freedom to the many-body Hilbert space by formulating “in-medium” flow equations, the solution of which is equivalent to the partial diagonalization or block-diagonalization of the many-body Hamiltonian [11, 21, 24, 33, 39, 58]. Because of its favorable polynomial scaling with system size, and the flexibility to target ground and excited states of both closed- and open-shell systems, the IM-SRG provides a

powerful *ab initio* framework for calculating medium-mass nuclei from first principles.

In the present chapter, I present the basic IM-SRG formalism and review some of the successful applications to nuclei in recent years. After this introductory review and survey of previous results, I present a detailed analysis of the perturbative content of the IM-SRG in Sec. 3.5. While this section is rather technical, it provides crucial guidance for understanding the similarities and differences with coupled cluster theory. More importantly, the perturbative analysis in this chapter will play a key role in formulating the improved approximations to be discussed in Chapter 5.

## 3.1 IM-SRG Formalism

### 3.1.1 Overview of the SRG

The main idea of the Similarity Renormalization Group (SRG) is to drive the Hamiltonian  $H(s)$  towards a diagonal or block-diagonal form via a continuous unitary transformation [73]

$$H(s) = U^\dagger(s)H(0)U(s). \quad (3.1)$$

Taking the derivative of Eq. (3.1) with respect to the flow parameter  $s$ , we immediately obtain the operator flow equation

$$\frac{d}{ds}H(s) = [\eta(s), H(s)], \quad (3.2)$$

where the generator  $\eta(s)$  is related to the unitary transformation  $U(s)$  by

$$\eta(s) = \frac{dU^\dagger(s)}{ds}U(s) = -\eta^\dagger(s). \quad (3.3)$$

Note that the formal solution for  $U(s)$  is given by the *path-* or *S-ordered* exponential

$$U(s) = \mathcal{S} \exp \int_0^s ds' \eta(s'). \quad (3.4)$$

For now, the specific form of  $\eta(s)$  is unimportant; I will revisit possible choices in Section 3.2, and how they can be designed to drive certain parts of the transformed Hamiltonian to zero. In the original applications to nuclear physics, which we refer to as the free space SRG, the aim was to soften the Hamiltonian by choosing  $\eta$  to decouple high- and low- momentum modes, driving the Hamiltonian towards a band-diagonal form with increasing  $s$  in momentum representation, making the interactions more tractable for *ab initio* calculations [33, 52, 54, 55]. On the one hand, the free-space SRG is convenient, as it does not have to be performed for each different nucleus or nuclear matter density. On the other hand, it is necessary to consistently evolve three-nucleon (and possibly higher) interactions that are induced during the evolution to be able to soften the interactions significantly and maintain approximate  $s$ -independence of  $A \geq 3$  observables. The consistent SRG evolution of three-nucleon operators represents a significant technical challenge that has only recently been solved in recent years.

An interesting alternative is to perform the SRG evolution in-medium (IM-SRG) for each  $A$ -body system of interest by normal-ordering with respect to an appropriate  $A$ -body reference state [11, 21, 24, 33, 39, 58]. Unlike the free-space evolution, the IM-SRG has

the appealing feature that one can approximately evolve  $3, \dots, A$ -body operators using only two-body machinery thanks to the reshuffling of terms brought about by normal-ordering. Moreover, with a suitable definition of the off-diagonal part of the Hamiltonian to be driven to zero, the IM-SRG can be used as an ab-initio method in and of itself, rather than simply to soften the Hamiltonian as in the free-space SRG.

### 3.1.2 $M$ -Scheme Flow Equations for IM-SRG(2)

If the IM-SRG transformation is performed exactly for an  $A$ -body system, the transformed Hamiltonian will involve up to an  $A$ -body interactions regardless of the initial particle rank of the starting Hamiltonian. Within the second quantization formalism discussed above, it is simple to show how these induced many-body forces would occur via the following equation,

$$[: a_a^\dagger a_b^\dagger a_d a_c :, : a_i^\dagger a_j^\dagger a_l a_k :] = \delta_{ci} : a_a^\dagger a_b^\dagger a_j^\dagger a_l a_k a_d : + \dots \quad (3.5)$$

In the free space SRG, the coupling between the different particle rank operators is “one-way”. For instance, the two-body interactions feed into the flow equations for the three- and higher-body interactions, but higher-body operators don’t renormalize lower-rank operators. In contrast, for the IM-SRG these higher-body forces certainly feedback into evolution of the lower-body interactions. To control the proliferation of many-body interactions, practitioners of the IM-SRG method have typically performed a simple truncation in which only the normal-ordered zero-, one-, and two-body parts of  $\eta(s)$  and  $H(s)$  are kept, so that

$$H(s) \approx E(s) + f(s) + \Gamma(s), \quad (3.6)$$

$$\eta(s) \approx \eta^{(1)}(s) + \eta^{(2)}(s). \quad (3.7)$$

This is called the IM-SRG(2) truncation, and has been very successful in treating medium mass nuclei [39, 58, 74]. In this work, I will also discuss the IM-SRG(3), where the three-body forces are kept as well. The commutator expression with full three-body forces are given in Appendix B, but the full IM-SRG(3) method without approximations has never been implemented in physical systems due to its high computational cost. One of the main thrusts of my thesis is the development of computationally tractable approximate IM-SRG(3) calculations, see Chapter 5.

Evaluating Eq. 3.2 using the general commutator expressions found in Appendix A, one obtains the IM-SRG(2) equations

$$\frac{dE}{ds} = \sum_{ab} (n_a - n_b) \eta_{ab} f_{ba} + \frac{1}{2} \sum_{abcd} \eta_{abcd} \Gamma_{cdab} n_a n_b \bar{n}_c \bar{n}_d, \quad (3.8)$$

$$\begin{aligned} \frac{df_{12}}{ds} &= \sum_a (1 + P_{12}) \eta_{1a} f_{a2} + \sum_{ab} (n_a - n_b) (\eta_{ab} \Gamma_{b1a2} - f_{ab} \eta_{b1a2}) \\ &\quad + \frac{1}{2} \sum_{abc} (n_a n_b \bar{n}_c + \bar{n}_a \bar{n}_b n_c) (1 + P_{12}) \eta_{c1ab} \Gamma_{abc2}, \end{aligned} \quad (3.9)$$

$$\begin{aligned} \frac{d\Gamma_{1234}}{ds} &= \sum_a \{ (1 - P_{12}) (\eta_{1a} \Gamma_{a234} - f_{1a} \eta_{a234}) - (1 - P_{34}) (\eta_{a3} \Gamma_{12a4} - f_{a3} \eta_{12a4}) \} \\ &\quad + \frac{1}{2} \sum_{ab} (1 - n_a - n_b) (\eta_{12ab} \Gamma_{ab34} - \Gamma_{12ab} \eta_{ab34}) \\ &\quad - \sum_{ab} (n_a - n_b) (1 - P_{12}) (1 - P_{34}) \eta_{b2a4} \Gamma_{a1b3}, \end{aligned} \quad (3.10)$$

where  $\bar{n}_i = 1 - n_i$ , and the  $s$ -dependence has been suppressed. Note that permutation symbol  $P_{ij}$ , which represents the following interchange

$$P_{ij} g(\dots, i, \dots, j) \equiv g(\dots, j, \dots, i), \quad (3.11)$$

has been used to simplify the expressions.

The coupled differential equations in Eqs. (3.8)–(3.10) are integrated from  $s = 0$  until a suitable decoupling condition has been achieved, with the initial value condition

$$H(0) = E(0) + f(0) + \Gamma(0). \quad (3.12)$$

The perturbative content of Eqs. (3.8)–(3.10) will be analyzed in Section 3.5. In that presentation, it will become clear that, much like CCSD, the IM-SRG(2) includes infinite-order ladder sums in the  $pp$  and  $hh$  channels (i.e., Brueckner Hartree-Fock type correlations), infinite-order ring diagram sums in the  $ph$  channel (RPA type correlations), plus complicated “interference” terms between the various channels. Furthermore, like coupled cluster theory, the IM-SRG at any truncation level is based on a commutator expression. Consequently, the Hamiltonian contains only connected diagrams [16, 75] and one obtains size-extensive results. From Eqs. (3.8)–(3.10), the two-body flow equation which contains doubly contracted two-body operators dominates the cost. These terms scale polynomially as  $\mathcal{O}(N^6)$  with the single-particle basis size  $N$ . This is similar in cost to CCSD, the Self-Consistent Green’s Function Approach (SCGF) [19, 76, 77], or canonical transformation theory [78, 79].

### 3.1.3 Symmetries and the Flow Equations

It is often useful to impose explicit symmetries on a hamiltonian in order to reduce unneeded trivial effort. This is obviously true for the flow equations as well. Examples include spin symmetry in coulombic systems, translational invariance in a plane wave basis, and spherical symmetry with nuclear systems, all of which are utilized in this work. I will present only the spherically symmetric  $JJ$ -coupled flow equations, as they are the least trivial example.

If the single-particle indices are made to refer to radial, angular momentum, and isospin quantum numbers  $i = (k_i l_i j_i \tau_i)$ , then they do not depend on the angular momentum projection  $m_i$ . Then the only non-diagonal part of the one-body matrix elements become the radial quantum numbers, e.g.,

$$f_{12} = f_{k_1 k_2}^{l_1 j_1 \tau_1} \delta_{l_1 l_2} \delta_{j_1 j_2} \delta_{\tau_1 \tau_2}. \quad (3.13)$$

Additionally, the two-body matrix can be coupled to angular momentum  $J$  to yield the simplified (computationally) IM-SRG(2) flow equations

$$\frac{dE}{ds} = \sum_{ab} \hat{j}_a^2 \eta_{ab} f_{ba} (n_a - n_b) + \frac{1}{2} \sum_{abcdJ} \hat{J}^2 \eta_{abcd}^J \Gamma_{cdab}^J n_a n_b \bar{n}_c \bar{n}_d, \quad (3.14)$$

$$\begin{aligned} \frac{df_{12}}{ds} &= \sum_a (1 + P_{12}) \eta_{1a} f_{a2} + \frac{1}{\hat{j}_1^2} \sum_{abJ} \hat{J}^2 (n_a - n_b) \left( \eta_{ab} \Gamma_{b1a2}^J - f_{ab} \eta_{b1a2}^J \right) \\ &+ \frac{1}{2 \hat{j}_1^2} \sum_{abcJ} \hat{J}^2 (n_a n_b \bar{n}_c + \bar{n}_a \bar{n}_b n_c) (1 + P_{12}) \eta_{c1ab}^J \Gamma_{abc2}^J, \end{aligned} \quad (3.15)$$

$$\begin{aligned} \frac{d\Gamma_{1234}^J}{ds} &= \sum_a \left( \left( 1 - (-1)^{J-j_1-j_2} P_{12} \right) \left( \eta_{1a} \Gamma_{a234}^J - f_{1a} \eta_{a234}^J \right) \right. \\ &\quad \left. - \left( 1 - (-1)^{J-j_3-j_4} P_{34} \right) \left( \eta_{a3} \Gamma_{12a4}^J - f_{a3} \eta_{12a4}^J \right) \right) \\ &+ \frac{1}{2} \sum_{ab} \left( \eta_{12ab}^J \Gamma_{ab34}^J - \Gamma_{12ab}^J \eta_{ab34}^J \right) (1 - n_a - n_b) \\ &+ \sum_{abJ'} (n_a - n_b) \left( 1 - (-1)^{J-j_1-j_2} P_{12} \right) \\ &\quad \times \hat{J}'^2 \begin{Bmatrix} j_1 & j_2 & J \\ j_3 & j_4 & J' \end{Bmatrix} \left( \bar{\eta}_{1\bar{4}ab}^{J'} \bar{\Gamma}_{ab\bar{3}\bar{2}}^{J'} - \bar{\Gamma}_{1\bar{4}ab}^{J'} \bar{\eta}_{ab\bar{3}\bar{2}}^{J'} \right), \end{aligned} \quad (3.16)$$

where  $\hat{j} = \sqrt{2j+1}$ , indices with a bar indicate time-reversed states, and the  $\bar{\eta}$  and  $\bar{\Gamma}$  matrix elements in the last line of Eq. (3.16) are obtained by a generalized Pandya transform (see,

e.g., [80]),

$$\bar{O}_{1\bar{2}3\bar{4}}^J = - \sum_{J'} \hat{j}'^2 \begin{Bmatrix} j_1 & j_2 & J \\ j_3 & j_4 & J' \end{Bmatrix} O_{1432}^{J'}. \quad (3.17)$$

It has been shown that this angular momentum coupling process drops the  $N$  number of M-scheme orbitals down to roughly to roughly to  $N^{2/3}$  J-scheme orbitals [64]

### 3.1.4 General Observables

Within the IM-SRG framework, the consistent transformation of observables in addition to the Hamiltonian is conceptually very simple: The operator  $O(s)$  is normal ordered with respect to  $|\Phi\rangle$  and truncated to the same two-body level, and then subjected to exactly the same transformation via the same differential equation

$$\frac{d}{ds}O(s) = [\eta(s), O(s)], \quad (3.18)$$

This means that an additional set of flow equations for each  $O(s)$  need to be integrated concurrently with the hamiltonian, roughly doubling the size of the system of coupled differential equations. This means that the method scales linearly with each additional observable one wishes to calculate, rendering the IM-SRG (as presented) unsuitable for treating systems where more than a few additional observables are needed. In Chapter 4, a novel formulation of the IM-SRG using Magnus expansion techniques will be presented that bypasses this (and other related) computational limitation.

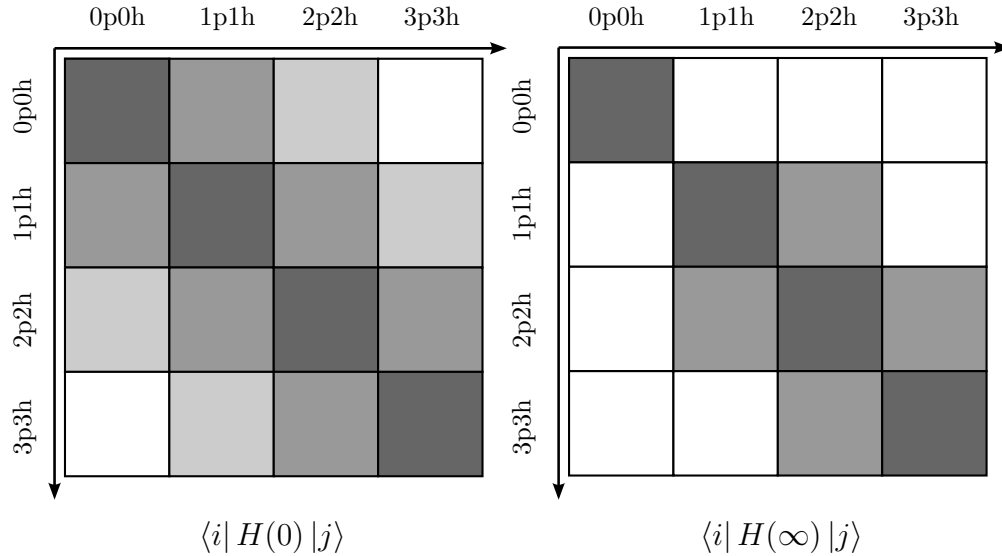


Figure 3.1: Schematic representation of the initial and final Hamiltonians,  $H(0)$  and  $H(\infty)$ , in the many-body Hilbert space spanned by particle-hole excitations of the reference state.

## 3.2 Choice of Generator

### 3.2.1 Decoupling

As mentioned previously, the IM-SRG transformation can be tailored to drive a suitably defined “off-diagonal” part of the Hamiltonian to zero. To see how this works, let us consider the case of a single reference system such as the ground state of a closed-shell nucleus. Fig. 3.1 shows a schematic representation of the  $s = 0$  normal ordered hamiltonian  $H(0)$  on the left, where the reference state  $|\Phi\rangle$  is the  $0p0h$  state at the top left. To isolate the ground state, we desire a transformation that drives the Hamiltonian towards the form shown in the right panel, where the  $0p0h$  reference is now an eigenstate of the transformed hamiltonian. Note that an initial three-body interaction would generate coupling between the  $nph$  and  $(n+3)p(n+3)h$  blocks, so the notation of Fig. 3.1 implicitly assumes we only have two-body interactions.

Clearly, the matrix elements that couple the  $0p0h$  reference state  $|\Phi\rangle$  to higher excitations

are

$$\langle \Phi | H(0) : a_p^\dagger a_h : | \Phi \rangle = f_{ph}, \quad (3.19)$$

$$\langle \Phi | H(0) : a_p^\dagger a_{p'}^\dagger a_{h'} a_h : | \Phi \rangle = \Gamma_{pp'hh'}, \quad (3.20)$$

and their Hermitian conjugates. So for this particular problem, a suitable definition for the “off-diagonal” parts of the hamiltonian to be driven to zero are

$$H^{od}(s) = \sum_{ph} f_{ph} : a_p^\dagger a_h : + \frac{1}{4} \sum_{pp'hh'} \Gamma_{pp'hh'} : a_p^\dagger a_{p'}^\dagger a_{h'} a_h : + \text{H.c.} \quad (3.21)$$

During the flow, coupling is induced between the  $0p0h$  and higher states, e.g.

$$\langle \Phi | H(s) : a_{p_1}^\dagger \dots a_{p_A}^\dagger a_{h_A} \dots a_{h_1} : | \Phi \rangle \neq 0. \quad (3.22)$$

These induced forces are forced to vanish by our truncation, thus the eigenvalue obtained in any truncated IM-SRG(n) type calculation is not variational. It is important that the size and effect of this truncation can be investigated for systematic checking and improvement. The matrix elements (3.19), (3.20) are approximately driven to zero, and the single zero-body part of the hamiltonian becomes the eigenvalue of the exact ground state. Alternatively, one could think of the final transformed hamiltonian as a unitarily equivalent hamiltonian in which the Hartree-Fock solution is exact.

### 3.2.2 White Generators

A generator must now be chosen, with the requirement that it will eliminate  $H^{od}$  as the hamiltonian is transformed via the IM-SRG flow equations. The class of generators which provides the biggest numerical benefits, and most transparent connection to MBPT is that found in the work of White on canonical transformation theory in quantum chemistry [58, 78]:

$$\eta^{\text{IA/B}}(s) \equiv \sum_{ph} \frac{f_{ph}(s)}{\Delta_{ph}^{\text{A/B}}(s)} :a_p^\dagger a_h: + \sum_{pp'hh'} \frac{\Gamma_{pp'hh'}(s)}{\Delta_{pp'hh'}^{\text{A/B}}(s)} :a_p^\dagger a_{p'}^\dagger a_{h'} a_h: - \text{H.c.} . \quad (3.23)$$

In future sections, I will appeal to the obvious three-body generalizations of this generator in order to move forward with approximations to IM-SRG(3). Anti-Hermiticity of  $\eta(s)$  is guaranteed by the sign change in the energy denominators under transposition in Eq. (3.23).

There are two different choices for the energy denominators employed in the White generators. These are differentiated by the superscripts in (3.23). They correspond to the Epstein-Nesbet and Møller-Plesset partitionings used in Many-Body Perturbation Theory (MBPT) (see, e.g., [16]). White's prescription in Ref. [78] leads to the Epstein-Nesbet case:

$$\Delta_{ph}^{\text{A}} \equiv \langle ph | H | ph \rangle - \langle \Phi | H | \Phi \rangle = f_p - f_h + \Gamma_{phph} = -\Delta_{hp}^{\text{A}}, \quad (3.24)$$

$$\Delta_{pp'hh'}^{\text{A}} \equiv \langle pp'hh' | H | pp'hh' \rangle - \langle \Phi | H | \Phi \rangle = f_p + f_{p'} - f_h - f_{h'} - A_{pp'hh'} \equiv -\Delta_{hh'pp'}^{\text{A}}, \quad (3.25)$$

where  $f_p = f_{pp}$ ,  $f_h = f_{hh}$ , and

$$A_{pp'hh'} \equiv \Gamma_{pp'pp'} + \Gamma_{hh'hh'} - \Gamma_{phph} - \Gamma_{p'h'p'h'} - \Gamma_{ph'p'h'} - \Gamma_{p'h'p'h}. \quad (3.26)$$

The Møller-Plesset case is simpler, yielding

$$\Delta_{ph}^B \equiv f_p - f_h \equiv -\Delta_{hp}^B, \quad (3.27)$$

$$\Delta_{pp'hh'}^B \equiv f_p + f_{p'} - f_h - f_{h'} \equiv -\Delta_{hh'pp'}^B. \quad (3.28)$$

These two choices give rise to almost no difference in practical calculations, but the connection to Møller-Plesset perturbation theory is easier to show with the Møller-Plesset type denominators. Almost all results presented in this work have been produced with Møller-Plesset type White generators.

If one wants to work with the  $J$ -scheme flow equations (3.14)–(3.16), it is not unambiguously clear how to treat the two-body matrix elements in the Epstein-Nesbet denominators (3.24), (3.25) in the angular momentum coupling process. Using the monopole matrix elements yield a straightforward solution to this problem, i.e.

$$\Gamma_{abcd}^{(0)} \equiv \frac{\sum_J (2J+1) \Gamma_{abcd}^J}{\sum_J (2J+1)} \quad (3.29)$$

in Eqs. (3.24)–(3.26).

The big advantage of White-type generators in practical calculations lies in the fact that it suppresses *all* off-diagonal matrix at roughly the same decay scale (see Section 3.2.5). Thus, the suppression rate is not a function of any energy or momentum scale, and it therefore does not represent a proper RG flow. This in contrast to the imaginary-time and Wegner generators, which will be discussed in the next Section 3.2.4. This RG distinction is unimportant in terms of final results, as any choice choice of generator that decouples the reference from excitations is producing an eigenstate regardless of the organization of order

of suppression.

The benefits of this uniform suppression of off-diagonal elements is difficult to understate. Because the White type generator's matrix elements are given by ratios of energies,  $f$  and  $\Gamma$  appear linearly of the right-hand side of the IM-SRG flow equations (3.8)–(3.10). This clearly would yield a much less stiff set of flow equations than the Wegner generator, where third powers of  $f$  and  $\Gamma$  appear (see below), or the imaginary time class, where second powers appear. Thus, for systems where the White type generator remains a well defined object throughout the transformation, the number of integration steps required to solve the IM-SRG flow equations are manifestly less than other generators. However, if one encounters a systems with vanishing energy denominators [21, 39], the White generators will be poorly defined. In this work, all systems presented can be approximated as closed-shell systems, and thus the White type generators are in general a well defined operator.

### 3.2.3 Imaginary-Time Generators

One can also motivate a second class of generator, by appealing to solutions of the imaginary-time Schrödinger equation. Using the off-diagonal Hamiltonian, Eq. (3.21), we define

$$\begin{aligned} \eta^{\text{IIA/B}}(s) \equiv & \sum_{ph} \text{sgn} \left( \Delta_{ph}^{\text{A/B}}(s) \right) f_{ph}(s) : a_p^\dagger a_h : \\ & + \sum_{pp'hh'} \text{sgn} \left( \Delta_{pp'hh'}^{\text{A/B}}(s) \right) \Gamma_{pp'hh'}(s) : a_p^\dagger a_{p'}^\dagger a_{h'} a_h : -\text{H.c.}, \end{aligned} \quad (3.30)$$

where  $\Delta^{\text{A/B}}$  are again the Epstein-Nesbet and Møller-Plesset energy denominators defined in Eqs. (3.24)–(3.28). The sign functions ensure that off-diagonal matrix elements are suppressed instead of enhanced during the flow. Solving the IM-SRG(2) equations for the

imaginary time generator shows that the decay scale for these matrix elements is approximately given by the diagonal energy difference between the reference and 1p1h or 2p2h excitations. This energy difference is just  $\Delta^{A/B}$ , depending on the definition chosen for diagonal. Thus  $\eta^{\text{IIA/B}}$  generates a proper RG flow, organized by energy differences in the choice for “diagonal”.

As mentioned, the quadratic dependence of the IM-SRG(2) equations on  $f$  and  $\Gamma$  creates a more stiff set of equations, and thus require more integration steps to solve. This generator is robustly defined even in the presence of vanishing energy denominators, and thus provides a good choice for systems where the White generator becomes a poorly defined object. This has been found to be very useful in the multi-reference IM-SRG(2) method of Hergert et al. [81].

### 3.2.4 Wegner Generators

The generator which has been most formally explored is the Wegner type generators [73]. These provide a robustly defined generator for any definition of “off-diagonal”, and not just ground state decoupling presented above. In the original work, Wegner proposed the following generator

$$\eta^{\text{III}}(s) = [H^d(s), H^{od}(s)]. \quad (3.31)$$

Using the definition of the off-diagonal Hamiltonian for this work, Eq. (3.21), and the commutators from Appendix A, one can arrive at the matrix elements of  $\eta(s)$ . In IM-SRG(2)

calculations, one keeps only two-body and lower operators, yielding

$$\begin{aligned} \eta_{12} = & \sum_a (1 - P_{12}) f_{1a}^d f_{a2}^{od} + \sum_{ab} (n_a - n_b) (f_{ab}^d \Gamma_{b1a2}^{od} - f_{ab}^{od} \Gamma_{b1a2}^d) \\ & + \frac{1}{2} \sum_{abc} (n_a n_b \bar{n}_c + \bar{n}_a \bar{n}_b n_c) (1 - P_{12}) \Gamma_{c1ab}^d \Gamma_{abc2}^{od}, \end{aligned} \quad (3.32)$$

$$\begin{aligned} \eta_{1234} = & \sum_a \left\{ (1 - P_{12}) (f_{1a}^d \Gamma_{a234}^{od} - f_{1a}^{od} \Gamma_{a234}^d) - (1 - P_{34}) (f_{a3}^d \Gamma_{12a4}^{od} - f_{a3}^{od} \Gamma_{12a4}^d) \right\} \\ & + \frac{1}{2} \sum_{ab} (1 - n_a - n_b) (\Gamma_{12ab}^d \Gamma_{ab34}^{od} - \Gamma_{12ab}^{od} \Gamma_{ab34}^d) \\ & - \sum_{ab} (n_a - n_b) (1 - P_{12}) (1 - P_{34}) \Gamma_{b2a4}^d \Gamma_{a1b3}^{od}. \end{aligned} \quad (3.33)$$

Clearly, the Wegner generator defined in Eqs. (3.32) and (3.33), and the flow equations (3.9) and (3.10) are nearly identical except for anti-hermiticity and hermiticity respectively. Thus the spherical  $J$ -scheme expressions for  $\eta^{\text{III}}(s)$  are easily obtained from Eqs. (3.15) and (3.16).

The IM-SRG equations reach a fixed point when  $\eta(s)$  vanishes, the transformation ceases. For the Wegner generator, a fixed point at  $s \rightarrow \infty$  exists if  $H^{od}(s)$  vanishes as required. It has been shown that [73, 82]

$$\frac{d}{ds} \text{tr} \left( H^{od}(s) \right)^2 = -2 \text{tr} \left( \eta^\dagger(s) \eta(s) \right) \leq 0 \quad (3.34)$$

since  $\eta^\dagger(s) \eta(s)$  is positive semi-definite. This implies that with this choice of generator,  $H^{od}(s)$  is increasingly suppressed and  $H(s)$  is rendered into a form of  $H^d(s)$ .

Similar, to the imaginary time generator, the Wegner generator creates a proper RG flow that suppresses matrix elements based on the diagonal energy difference between the reference and 1p1h or 2p2h excitations. While formally appealing, and robust to vanishing

energy denominators, this generator creates flow equations that depend on  $f$  and  $\Gamma$  in a cubic fashion. This leads to extremely stiff equations that require many, many steps to arrive at a decoupled reference. Additionally, the cost to construct  $\eta^{\text{III}}$  is as much as evaluating the flow equations, making each timestep approximately double the cost of the previous two generators.

### 3.2.5 Decay Scales

Let us examine in more detail how the generators give rise to the different decay scales we have claimed above, and thus create varying degrees of stiffness in solving the IM-SRG. As with everything assumed above, we identify a diagonal and off-diagonal part of the hamiltonian,

$$H(s) = H^d(s) + H^{od}(s), \quad (3.35)$$

where  $H^{od}(s)$  is to be suppressed as  $s \rightarrow \infty$ . It is then natural to work in the eigenbasis of  $H^d(0)$ . Since the form of  $H^d(s)$  doesn't change, it is possible to assume that its eigenbasis is invariant under  $s$ , so that at each step of the flow

$$H^d(s) |n\rangle = E_n(s) |n\rangle. \quad (3.36)$$

In this basis representation, Eq. (3.2) becomes

$$\begin{aligned} \frac{d}{ds} \langle i | H | j \rangle &= \sum_k (\langle i | \eta | k \rangle \langle k | H | j \rangle - \langle i | H | k \rangle \langle k | \eta | j \rangle) \\ &= - (E_i - E_j) \langle i | \eta | j \rangle + \sum_k \left( \langle i | \eta | k \rangle \langle k | H^{od} | j \rangle - \langle i | H^{od} | k \rangle \langle k | \eta | j \rangle \right), \quad (3.37) \end{aligned}$$

and  $\langle i | H^{od} | i \rangle = 0$ .

Consider now a White type generator, which can be written as

$$\langle i | \eta^I | j \rangle = \frac{\langle i | H^{od} | j \rangle}{E_i - E_j}, \quad (3.38)$$

and specifies Eq. (3.2) to the following

$$\frac{d}{ds} \langle i | H | j \rangle = -\langle i | H^{od} | j \rangle + \sum_k \frac{E_i + E_j - 2E_k}{(E_i - E_k)(E_j - E_k)} \langle i | H^{od} | k \rangle \langle k | H^{od} | j \rangle. \quad (3.39)$$

If the transformation generated by  $\eta$  truly suppresses  $H^{od}$ , and if it is assumed that  $H^{od}$  either begins small compared to  $H^d$ , or will become so during the flow, then we can neglect the second term quadratic in  $H^{od}$ . Then it is possible to just inspect the first term in the flow equations in order to illustrate how off-diagonal matrix elements are being suppressed.

In this case, Eq. (3.39) implies

$$\left. \frac{dE_i}{ds} \right|_{s=0} = 2 \sum_k \frac{\langle i | H^{od} | k \rangle \langle k | H^{od} | i \rangle}{(E_i - E_k)}. \approx 0, \quad (3.40)$$

and the energies stay (approximately) constant:

$$E_i(s) \approx E_i(0). \quad (3.41)$$

Consequently, Eq. (3.39) can be integrated, and one arrives at

$$\langle i | H^{od}(s) | j \rangle \approx \langle i | H^{od}(0) | j \rangle e^{-s}, \quad s > s_0, \quad (3.42)$$

as already mentioned in Section 3.2.2. This is not suggesting that the quadratic terms are unimportant, just that the first term is what sets the decay scale.

The imaginary-time generator can be written as

$$\langle i | \eta^{\text{II}} | j \rangle = \text{sgn} (E_i - E_j) \langle i | H^{\text{od}} | j \rangle, \quad (3.43)$$

and the flow equation

$$\begin{aligned} \frac{d}{ds} \langle i | H | j \rangle &= - |E_i - E_j| \langle i | H^{\text{od}} | j \rangle \\ &+ \sum_k (\text{sgn}(E_i - E_k) + \text{sgn}(E_j - E_k)) \langle i | H^{\text{od}} | k \rangle \langle k | H^{\text{od}} | j \rangle. \end{aligned} \quad (3.44)$$

Note that the sign function in the definition of  $\eta^{\text{II}}$  ensures that only the absolute value of the energy difference between the states  $|i\rangle$  and  $|k\rangle$  appears in the first term. Integration of Eq. (3.44) yields

$$\langle i | H^{\text{od}}(s) | j \rangle \approx \langle i | H^{\text{od}}(0) | j \rangle e^{-|E_i - E_j|s}, \quad (3.45)$$

and off-diagonal matrix elements are suppressed, with a decay scale set by  $|E_i - E_j|$ .

Finally, we perform the same kind of analysis for the Wegner generator

$$\langle i | \eta^{\text{III}} | j \rangle = \langle i | [H^d, H^{\text{od}}] | j \rangle = (E_i - E_j) \langle i | H^{\text{od}} | j \rangle. \quad (3.46)$$

The flow equation reads

$$\frac{d}{ds} \langle i | H | j \rangle = - (E_i - E_j)^2 \langle i | H^{\text{od}} | j \rangle + \sum_k (E_i + E_j - 2E_k) \langle i | H^{\text{od}} | k \rangle \langle k | H^{\text{od}} | j \rangle, \quad (3.47)$$

and we obtain

$$\langle i | H^{od}(s) | j \rangle \approx \langle i | H^{od}(s_0) | j \rangle e^{-(E_i - E_j)^2 (s - s_0)}. \quad (3.48)$$

Thus, the imaginary-time and Wegner generators yield proper RG transformations, in the sense that matrix elements between states with large energy differences  $\Delta E_{ij} = |E_i - E_j|$  decay at smaller flow parameters  $s$  than states with small  $\Delta E_{ij}$ . The White generator, on the other hand, acts on all matrix elements simultaneously. In Section 3.3, it will be shown that these different choices do not lead to large differences in the large  $s$  limit.

### 3.3 Numerical Explorations

In this section, we illustrate the general properties of the IM-SRG flow equations in numerical applications, with special emphasis on a comparison of the different generators that were introduced in the previous sections. To simplify matters, we only use a two-body interaction throughout this section (see 3.3.1 for details).

#### 3.3.1 Implementation

Barring a few cases, the IM-SRG has only really been implemented for nuclear systems, therefore in this review chapter of the method I only present details for typical nuclear calculations. The details that will be relevant for other systems will be introduced as the results appear in later chapters. For nuclear systems, the IM-SRG is implemented in harmonic oscillator (HO) configuration spaces. The principal advantage of this basis in nuclear systems is that one can factorize center-of-mass and relative degrees of freedom in the evaluation of matrix elements (see, e.g., for [83]). This is an invaluable property for self-bound systems like nuclei. For methods like the No-Core Shell Model, this property can be retained even at

the many-body level for a suitable choice of model space truncation [12]. For methods which use single-particle basis truncations, like the IM-SRG, coupled cluster, and self-consistent greens functions, this exact factorization of center-of-mass and intrinsic wave functions is analytically spoiled, although it is still observed empirically. We revisit this in chapter 4.

As mentioned before, the IM-SRG explicitly exploits spherical symmetry for nuclear applications by working with the  $J$ -scheme IM-SRG flow equations presented in Sec. 3.1.3. In these spherically symmetric basis sets, it is possible to achieve convergence for spherical nuclei of interest in reasonable calculations. This is true even for “bare” interactions from chiral EFT like the  $N^3\text{LO}$  interaction by Entem and Machleidt, with an initial cutoff  $\Lambda = 500 \text{ MeV}/c$  [1, 2]. This is the interaction used to produce most of the nuclear results presented in this thesis, both at its original resolution scale, indicated by  $\lambda = \infty$ , and at a lower resolution scale  $\lambda = 2.0 \text{ fm}^{-1}$ , which is generated by a free-space SRG evolution or softening [33, 53].

To obtain reference states for the IM-SRG calculation, the Hartree-Fock equations for the intrinsic Hamiltonian (2.2) are self consistently solved. The intrinsic Hamiltonian is then transformed to the Hartree-Fock basis and normal ordered with respect to the Hartree-Fock reference state, discarding the residual 3N part in the process (cf. Eq.(2.5)). Starting from the zero-, one-, and two-body matrix elements of the truncated normal-ordered Hamiltonian as initial values, the  $J$ -scheme flow equations (3.14)–(3.16) are integrated with the CVODE solver from the SUNDIALS package [84]. For White and imaginary-time generators, we choose the recommended Adams-Bashforth-Moulton predictor-corrector method for non-stiff systems, while the fifth-order backward-differentiation method is used for the stiff flow equations in the Wegner case.

In order to determine at what finite value of  $s$  sufficient decoupling is achieved, second-

Nucleus	$\lambda$ [fm $^{-1}$ ]	$E_{14}$ [MeV]	$E_{\text{ex}}$ [MeV]
$^4\text{He}$	$\infty$	-27.18	-27.26(3)
$^{16}\text{O}$	$\infty$	-126.01	-126.3(1)
$^{40}\text{Ca}$	$\infty$	-366.23	-369(1)
$^4\text{He}$	2.0	-28.27	-28.27
$^{16}\text{O}$	2.0	-165.68	-165.68
$^{40}\text{Ca}$	2.0	-595.98	-595.95(2)
$^{78}\text{Ni}$	2.0	-1319.41	-1319.4(1)
$^{100}\text{Sn}$	2.0	-1953.96	-1954.3(3)
$^{132}\text{Sn}$	2.0	-2752.03	-2753(2)

Table 3.1: IM-SRG(2) ground-state energies of selected closed-shell nuclei for the the chiral  $\text{N}^3\text{LO}$  interaction by Entem and Machleidt [1, 2], with  $\lambda = \infty$  and  $\lambda = 2.0 \text{ fm}^{-1}$  (cf. Fig. 3.2).  $E_{14}$  are the energies obtained for  $e_{\text{max}} = 14$  at optimal  $\hbar\omega$ , and  $E_{\text{ex}}$  are extrapolated to infinite basis size (see text), with extrapolation uncertainties indicated in parentheses.

order MBPT correction for the flowing Hamiltonian  $H(s)$  is used. This is a direct measure of the off-diagonal part of the Hamiltonian as defined in Eqs. (3.21). When the second order MBPT correction drops below  $10^{-6}$  MeV, the flow is stopped and the resulting zero-body energy is considered the full ground state energy.

### 3.3.2 Convergence

In Fig. 3.2, the convergence of the IM-SRG(2) ground-state energies of the closed-shell nuclei  $^4\text{He}$ ,  $^{16}\text{O}$ , and  $^{40}\text{Ca}$  with respect to the single-particle basis size  $e_{\text{max}}$  (see Appendix 3.3.1) is shown. All calculations shown use the White-Epstein-Nesbet generator  $\eta^C$ , Eq. (3.23), and it should be assumed unless otherwise stated that this is the generator being used. It should be noted that for the unevolved  $\text{N}^3\text{LO}$  interaction, the Hartree-Fock solutions for all three nuclei have positive energy. Nonetheless, the HF states still lead to reasonable and converged IM-SRG(2) energies as shown in Fig. 3.2.

We can correct for the effects of using a finite HO basis by using the methods described in Refs. [13, 14]. A HO basis with fixed  $e_{\text{max}}$  has ultraviolet and infrared cutoffs which are

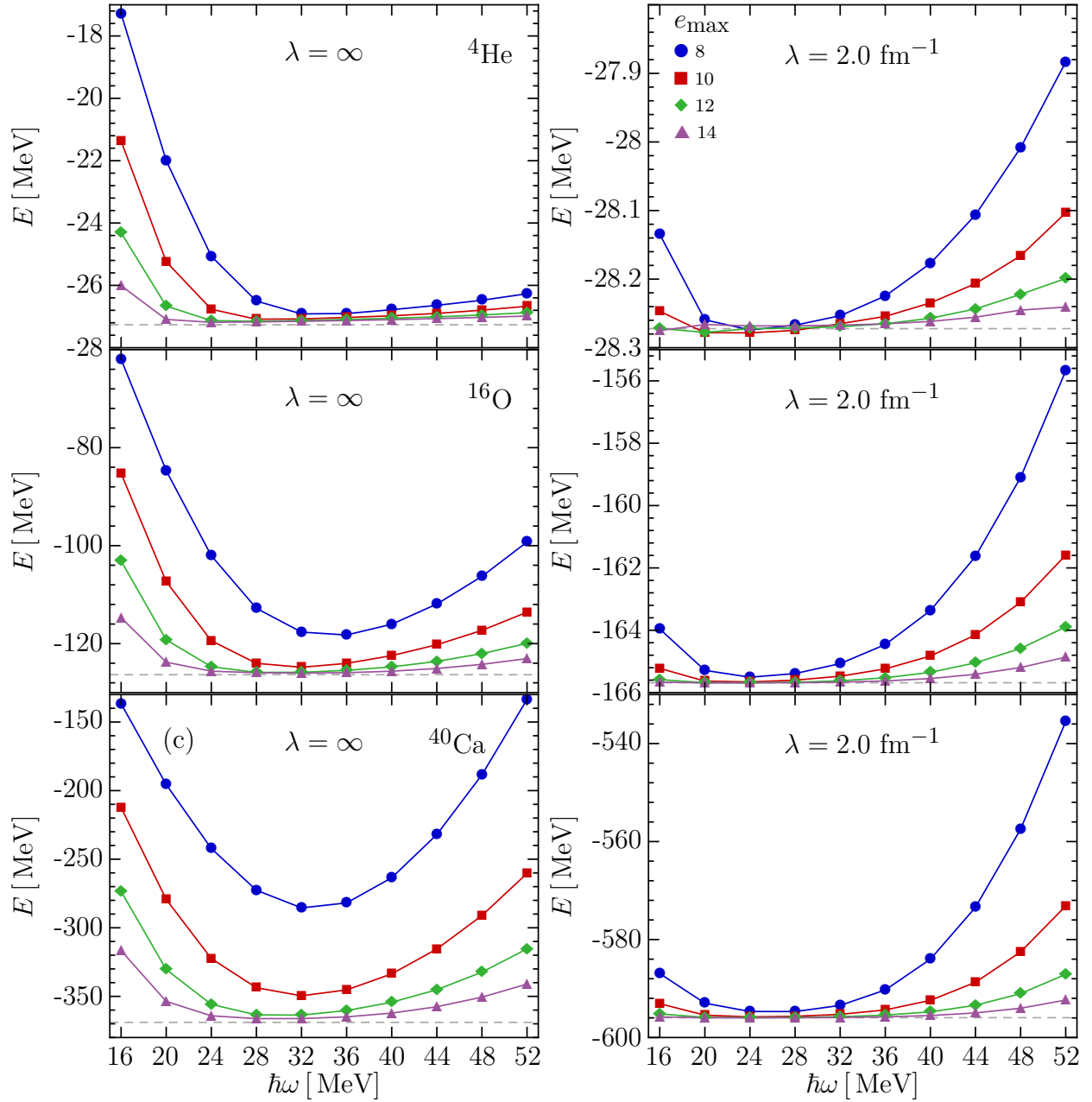


Figure 3.2: Convergence of  ${}^4\text{He}$ ,  ${}^{16}\text{O}$ , and  ${}^{40}\text{Ca}$  IM-SRG(2) ground-state energies w.r.t. single-particle basis size  $e_{\text{max}}$ , for a chiral  $\text{N}^3\text{LO}$   $NN$  interaction with  $\lambda = \infty$  (left panels) and  $\lambda = 2.0 \text{ fm}^{-1}$  (right panels). Notice the significant differences in the energy scales between the left and right panels. Gray dashed lines indicate energies from extrapolation the  $e_{\text{max}} \geq 10$  data sets to infinite basis size (see text and Refs. [13, 14]).

given by

$$\Lambda_{\text{UV}} \equiv \sqrt{2e_{\text{max}} + 7} \hbar/a_{\text{HO}}, \quad (3.49)$$

$$L_{\text{IR}} \equiv \sqrt{2e_{\text{max}} + 7} a_{\text{HO}}, \quad (3.50)$$

where  $a_{\text{HO}} = \sqrt{\hbar/m\omega}$  is the usual oscillator length, and  $m$  the nucleon mass. With these definitions, we can perform a simultaneous fit of the data for (almost) all pairs  $(e_{\text{max}}, \hbar\omega)$  to the expression

$$E(e_{\text{max}}, \hbar\omega) = E_{\infty} + A_0 e^{-\Lambda_{\text{UV}}^2/A_1^2} + A_2 e^{-2k_{\infty}L_{\text{IR}}}, \quad (3.51)$$

where the energy for infinite basis size  $E_{\infty}$ , the binding momentum  $k_{\infty}$ , and the  $A_i$  are treated as parameters. For the unevolved N<sup>3</sup>LO interaction, we found it necessary to exclude the  $e_{\text{max}} = 8$  data set to obtain stable fits for <sup>16</sup>O and <sup>40</sup>Ca, most likely because  $\Lambda_{\text{UV}}$  is close to the cutoff of the initial interaction for  $e_{\text{max}} = 8$  and the lower values of  $\hbar\omega$  we are considering. The resulting extrapolated energies are indicated by gray dashed lines in Fig. 3.2, and they fall within 1% or less of the energies for  $e_{\text{max}} = 14$ , the largest basis size which was used in actual calculations. Both energies are reported for each nucleus in Table 3.1.

For the light nuclei <sup>4</sup>He, the IM-SRG(2) ground-state energy is about 2 MeV below the exact result from a No-Core Shell Model (NCSM) calculation with the same chiral N<sup>3</sup>LO interaction (see, e.g., Ref. [54]). Further, IM-SRG(2) results can be compared to Coupled Cluster calculations with the same interaction [64, 85] (also see Ref. [74]). The IM-SRG(2) energies are significantly lower than the CCSD energies, lower even than the  $\Lambda$ -CCSD(T)

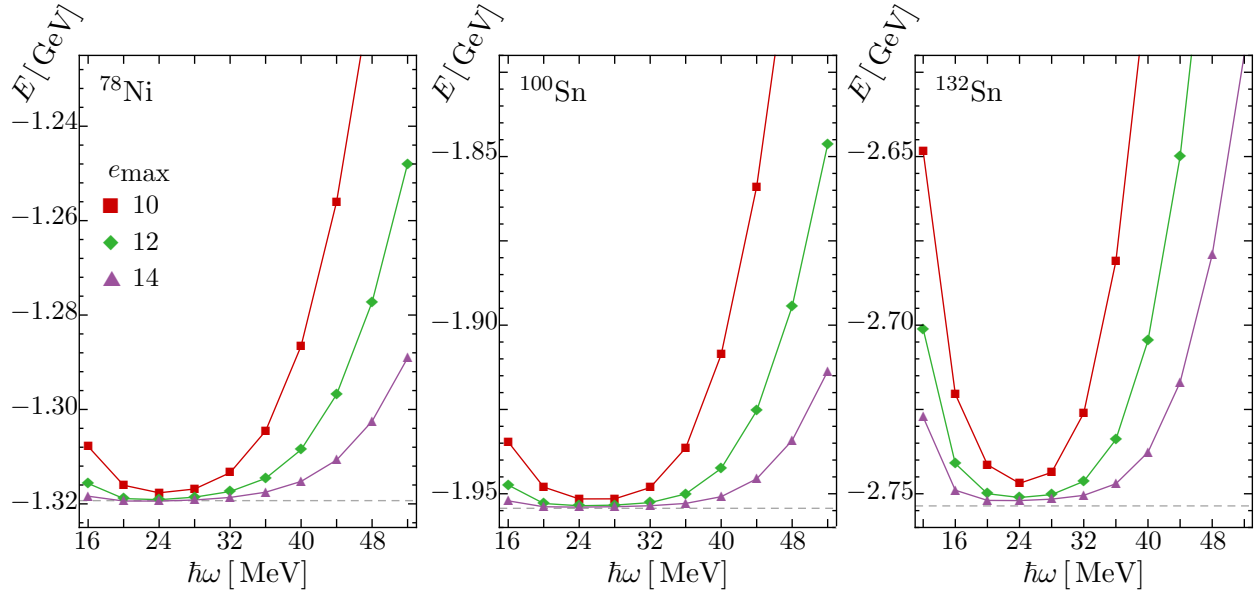


Figure 3.3: Convergence of  $^{78}\text{Ni}$ ,  $^{100}\text{Sn}$ , and  $^{132}\text{Sn}$  IM-SRG(2) ground-state energies w.r.t. single-particle basis size  $e_{\text{max}}$ , for the chiral  $\text{N}^3\text{LO}$   $NN$  interaction with  $\lambda = 2.0 \text{ fm}^{-1}$ . Gray dashed lines indicate energies from extrapolation the  $e_{\text{max}} \geq 10$  data sets to infinite basis size (see text and Refs. [13, 14]).

results, a CC method which takes perturbative triples corrections into account. I will soon present a perturbative analysis of the IM-SRG in Sec. 3.5, which shows the origin of the the difference between IM-SRG(2) and CCSD. This overbinding can be explained by a systematic undercounting of certain repulsive fourth-order terms in the IM-SRG(2) truncation, which simulates the additional attraction that is otherwise gained from including triples correction. For the (comparably) hard initial interaction, the IM-SRG(2) overshoots the  $\Lambda$ -CCSD(T) results, while the reduced importance of higher-order MBPT corrections for soft interactions causes the IM-SRG(2) results to fall in between the CCSD and  $\Lambda$ -CCSD(T) results (see Secs. 3.5 and Refs. [58, 74]).

In the right panels of Fig. 3.2, we show the same kind of convergence plots for the chiral  $\text{N}^3\text{LO}$  interaction at the reduced resolution scale  $\lambda = 2.0 \text{ fm}^{-1}$ . As expected, the speed of the convergence is greatly enhanced by using a softer interaction [33], which is evident

from the significantly smaller energy scales in the lower panels. In Tab. 3.1, we can see that the extrapolated energies agree with the  $e_{\max} = 14$  results within 0.01-0.1%. For  ${}^4\text{He}$ , there appear to be some deviations from the otherwise variational convergence pattern in the other cases. Of course, the IM-SRG is not strictly variational because of the truncations in the flow equations (3.8)–(3.10). In the present case, however, these deviations are on the order of a 10 keV or less, and are most likely dominated by numerical artifacts from integrating the flow equations.

For a soft interaction, the large single-particle basis sizes we have used here are sufficient to converge nuclei which are much heavier than  ${}^{40}\text{Ca}$ . This is demonstrated in Fig. 3.3, where we show the convergence of the IM-SRG(2) ground-state energies of the proton- or neutron-rich exotic nuclei  ${}^{78}\text{Ni}$ ,  ${}^{100}\text{Sn}$ , and  ${}^{132}\text{Sn}$ . The corresponding energies are included in Tab. 3.1. Using only a softened chiral  $\text{N}^3\text{LO}$  interaction, the binding energy of these nuclei is overestimated significantly, continuing a trend which was already noticeable for  ${}^{16}\text{O}$  in Fig. 3.2. This overbinding is caused by the shift of repulsive strength from the off-shell two-body interaction to induced three- and higher many-body forces as the resolution scale is lowered, of course, and fixed by including at least the induced three-nucleon forces [21, 74]. While the inclusion of three-body operators comes with computational challenges, we stress that these induced terms have low resolution scales as well, and do not affect the rate of convergence of the IM-SRG ground-state energies adversely. While computational issues pertaining to the storage of  $3N$  matrix elements present a challenge, converged calculations with  $NN + 3N$  interactions for the  $A \sim 100$  region and beyond have now become possible [74, 86, 87].

### 3.3.3 Choice of Generator

Let us now study the effect of our choice of generator on the IM-SRG(2) ground-state energies. In Fig. 3.4, we show the IM-SRG(2) ground-state energies for the five different generators discussed in Sec. 3.2. Note that the panels for the White and imaginary-time generators show curves for *both* the Epstein-Nesbet and Møller-Plesset choices for the energy denominators and sign functions, respectively. The resulting ground-state energies for  $^{40}\text{Ca}$  agree within 15 keV, which amounts to relative differences from  $10^{-6}$  to  $10^{-4}$ . Remarkably, this agreement holds for both the softened and bare  $\text{N}^3\text{LO}$  interactions, and irrespective of the used basis parameters  $e_{\text{max}}$  and  $\hbar\omega$ . The extrapolated energies therefore also only differ by equally small amounts.

It is evident from Fig. 3.4 that the White and imaginary-time generators give very similar results. For the bare  $\text{N}^3\text{LO}$  interaction, the extrapolated  $^{40}\text{Ca}$  ground-state energies are  $-368.9$  MeV and  $-367.7$  MeV, respectively, which is a difference of about 0.3%. For any  $\hbar\omega$  in the studied range, the energy differences between the two types of generators drop below 1% from  $e_{\text{max}} = 8$  onward. As expected, the differences become smaller when the resolution scale of the interaction is lowered to  $\lambda = 2.0 \text{ fm}^{-1}$ . The extrapolated energies are  $-596.0$  MeV and  $-595.6$  MeV for the White and imaginary-time generators, respectively, which amounts to a relative difference of order  $10^{-4}$ . The extrapolated values are affected by slightly larger differences for small and large  $\hbar\omega$ . Near the energy minima with respect to  $\hbar\omega$ , where the results are better converged, absolute differences are typically below 10 keV.

For the soft interaction, the results for the Wegner generator agree very well with those for the other generators: The extrapolated  $^{40}\text{Ca}$  ground-state energy is  $-595.4$  MeV. The situation is quite different for the bare interaction, though. To understand what we see, we

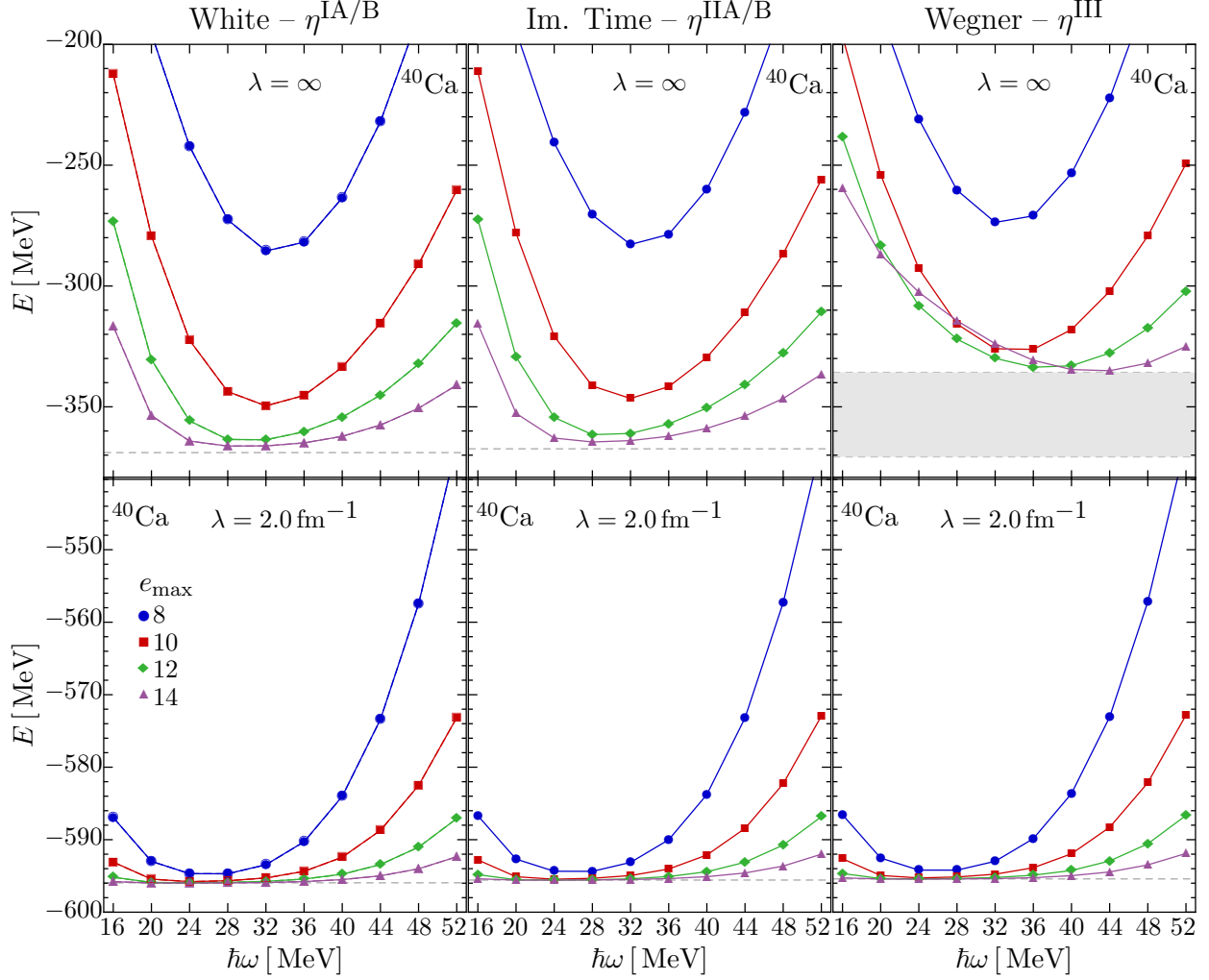


Figure 3.4: IM-SRG(2) ground-state energies of  $^{40}\text{Ca}$  obtained with different choices of the generator, as a function of  $\hbar\omega$  and the single-particle basis size  $e_{\text{max}}$ . The interaction is the chiral  $\text{N}^3\text{LO}$  potential with  $\lambda = \infty$  (top panels) and  $\lambda = 2.0 \text{ fm}^{-1}$  (bottom panels), respectively. The dashed lines indicate extrapolated energies. For the Wegner generator, the shaded area indicates the variation from using different data sets for the extrapolation (see text).

first consider the convergence pattern that is predicted for a (quasi)-variational theory by the extrapolation formula (3.51) [13, 14]. At fixed  $e_{\text{max}}$ , the derivative of Eq. (3.51) with respect to the oscillator parameter  $\hbar\omega$  indicates that the ultraviolet (UV) and infrared (IR) correction terms are minimized at large and small  $\hbar\omega$ , respectively. The exponents of the UV and IR terms behave like  $\Lambda_{\text{UV}}^2 \sim -e_{\text{max}}$  and  $L_{\text{IR}} \sim \sqrt{e_{\text{max}}}$  as  $e_{\text{max}}$  increases, hence we

expect IR corrections to dominate eventually. Consequently, we can infer that the minimum of the energy with respect to the oscillator parameter should move to larger  $\hbar\omega$  first until UV convergence is achieved, and then to smaller  $\hbar\omega$  for IR convergence.

In Fig. 3.4, we only see the energy minimum move towards IR convergence at small  $\hbar\omega$ , which suggests that the calculation is sufficiently converged in the UV regime already for  $e_{\max} = 8$ , the smallest basis shown in the figure. For the Wegner generator, the minimum is still moving to larger  $\hbar\omega$  values, which suggests that the calculation is not yet converged in the UV regime, and a slower convergence with basis in general. If we use the data for  $e_{\max} = 8, 10, 12$ , which behave variationally, an extrapolation to infinite basis using Eq. (3.51), yields  $-370.7$  MeV, which is compatible with the extrapolated results for the White and imaginary-time generators within uncertainties.

Going to  $e_{\max} = 14$ , we face a complication: while the energy minimum moves to larger  $\hbar\omega$ , the curve intersects those for smaller  $e_{\max}$ . This is not ruled out a priori, because the IM-SRG is a non-variational approach, but makes the assumptions underlying the extrapolation formula (3.51) questionable. Setting aside the fundamental issue of applicability, we have extrapolated the energy using different subsets of our calculated data, and thereby obtain the shaded band in Fig. 3.4, which represents a 10% variation of the extrapolated energy.

To better understand the behavior of the IM-SRG flow for the Wegner generator, we have to consider how its structure differs from our other choices for  $\eta$ . The definition of the off-diagonal Hamiltonian  $H^{od}(s)$ , Eq. (3.21), is the same in all three cases, so we aim for the same (or at least similar) fixed points of the flow, where  $\eta(\infty) = 0$ . However, we know that the White and imaginary-time generators are directly proportional to  $H^{od}$ , i.e., the only non-vanishing matrix elements are of the types  $\eta_{ph/hp}$  and  $\eta_{pp'hh'/hh'pp'}$ . The Wegner generator, on the other hand, has many additional non-zero matrix elements coming from the evaluation

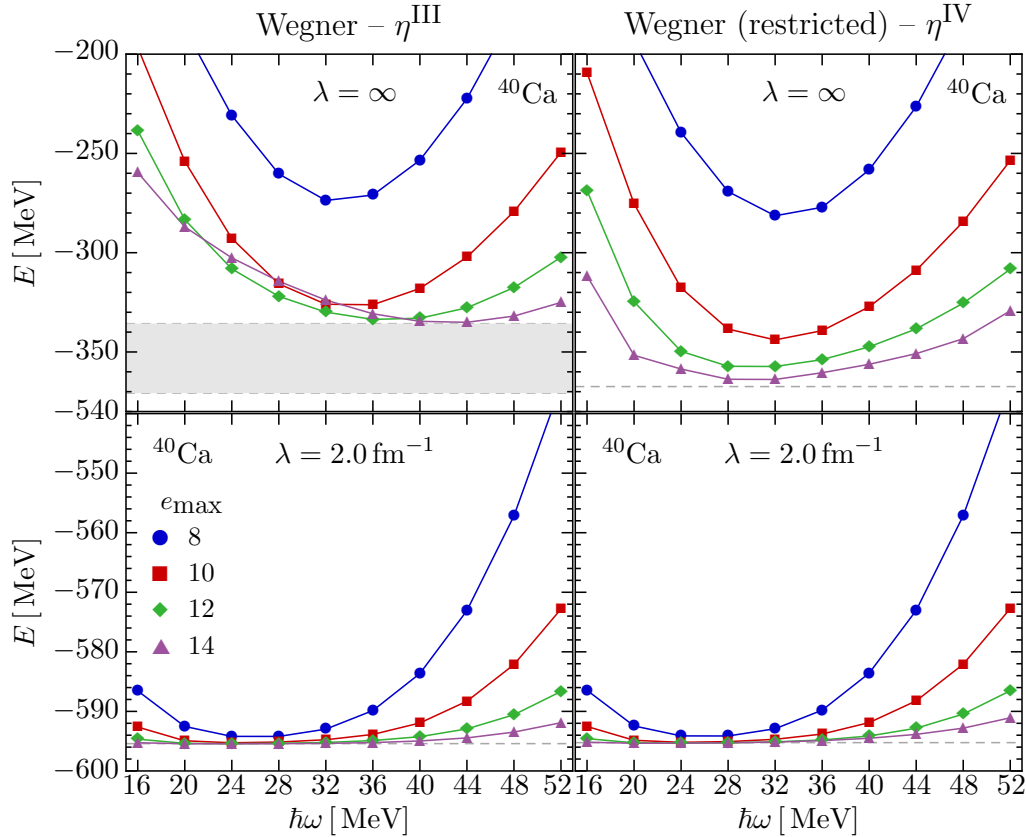


Figure 3.5: IM-SRG(2) ground-state energies of  $^{40}\text{Ca}$  for the regular (left, as in Fig. 3.4) and restricted Wegner generators (right, see text), as a function of  $\hbar\omega$  and the single-particle basis size  $e_{\text{max}}$ . The interaction is the chiral  $\text{N}^3\text{LO}$  potential with  $\lambda = \infty$  (top panels) and  $\lambda = 2.0 \text{ fm}^{-1}$  (bottom panels), respectively. The dashed lines indicate extrapolated energies.

of the commutator, analogous to the IM-SRG flow equation itself (cf. Eqs. (3.32),(3.33)).

It does not come as a surprise, then, that the generators differ in the way they build correlation effects from the many-body perturbation series into the flowing Hamiltonian — a difference that will be enhanced for interactions for which order-by-order convergence of the Many-Body Perturbation series cannot be guaranteed (cf. Secs. 3.3.4 and 3.5). For illustration, Fig. 3.5 compares results for the regular Wegner generator with those for a

restricted version defined by

$$\eta_{ij}^{\text{IV}} = \eta_{ij}^{\text{III}}, \quad \eta_{ijkl}^{\text{IV}} = \begin{cases} \eta_{ijkl}^{\text{III}} & \text{for } i j k l = p p' h h', h h' p p', \\ 0 & \text{else,} \end{cases} \quad (3.52)$$

matching the structure of the White and imaginary-time generators. We have explored restrictions of the one-body part as well, but they cause no noticeable differences while the impact of the restriction in the two-body part is significant.

The convergence pattern of the restricted  $\eta^{\text{IV}}$  is quasi-variational for both the bare and softened N<sup>3</sup>LO interactions, and has the energy minimum moving towards smaller  $\hbar\omega$ , suggesting that the calculation is converged in the UV regime, and now converging in the IR regime. The extrapolated <sup>40</sup>Ca g.s. energies are  $-367.4$  MeV and  $-595.3$  MeV, respectively, in very good agreement with the White and imaginary-time generators, as well as the unrestricted Wegner generator  $\eta^{\text{III}}$  in the case of the soft interaction (also cf. Fig. 3.5). This strongly suggests that our hypothesis was correct, and it is indeed the additional non-zero matrix elements in  $\eta^{\text{III}}$  which introduce uncontrolled behavior. It remains to be seen whether we can reach a deeper understanding of the underlying mechanism. A likely explanation is that the truncation of the commutator (3.31) to one- and two-body contributions only (Eqs. (3.32), (3.33)) causes an imbalance in the infinite-order resummation of the Many-Body Perturbation series. For the time being, we have to advise against the use of the Wegner generator in IM-SRG calculations with (comparably) “hard” interactions that exhibit poor order-by-order convergence of the perturbation series.

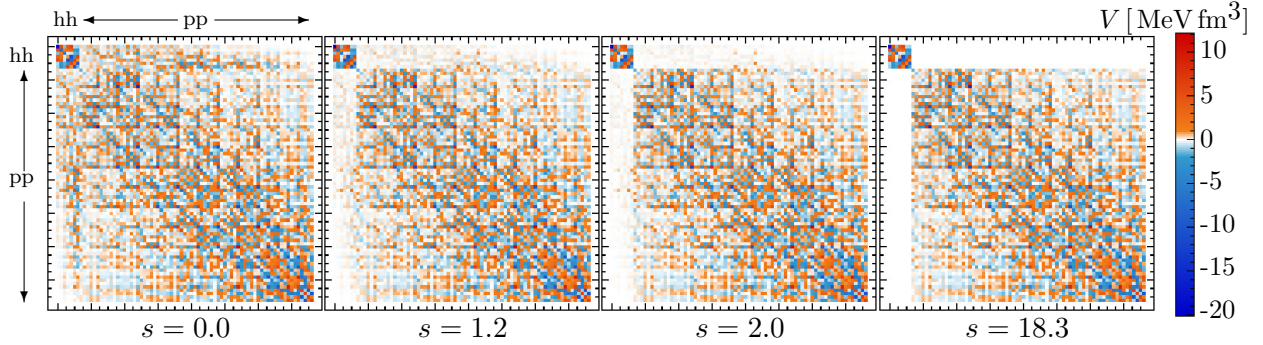


Figure 3.6: Decoupling for the White generator, Eq. (3.23), in the  $J^\pi = 0^+$  neutron-neutron interaction matrix elements of  $^{40}\text{Ca}$  ( $e_{\text{max}} = 8$ ,  $\hbar\omega = 20$  MeV, Entem-Machleidt N<sup>3</sup>LO(500) evolved to  $\lambda = 2.0$  fm<sup>-1</sup>). Only  $hhhh$ ,  $hhpp$ ,  $pphh$ , and  $pppp$  blocks of the matrix are shown.

### 3.3.4 Decoupling

As discussed in Sec. 3.2.1, the IM-SRG is built around the concept of decoupling the reference state from excitations, and thereby mapping it onto the fully interacting ground state of the many-body system within truncation errors. Let us now demonstrate that the decoupling occurs as intended in a sample calculation for  $^{40}\text{Ca}$  with our standard chiral N<sup>3</sup>LO interaction at  $\lambda = 2.0$  fm<sup>-1</sup>. Fig. 3.6 shows the rapid suppression of the off-diagonal matrix elements in the  $J^\pi = 0^+$  neutron-neutron matrix elements as we integrate the IM-SRG(2) flow equations. At  $s = 2.0$ , after only 20–30 integration steps with the White generator, the  $\Gamma_{pp'hh'}(s)$  have been weakened significantly, and when we reach the stopping criterion for the flow at  $s = 18.3$ , these matrix elements have vanished to the desired accuracy. While the details depend on the specific choice of generator, the decoupling seen in Fig. 3.6 is representative for other cases.

With the suppression of the off-diagonal matrix elements, the many-body Hamiltonian is driven to the simplified form indicated in Fig. 3.6. The IM-SRG evolution does not only decouple the ground state from excitations, but reduces the coupling between excitations as well. This coupling is an indicator of strong correlations in the many-body system,

which usually require high- or even infinite-order treatments in approaches based on the Goldstone expansion. As we have discussed in Sec. 3.1, the IM-SRG can also be understood as such a non-perturbative, infinite-order resummation of the Many-Body Perturbation series, which builds the effects of correlations into the flowing Hamiltonian. To illustrate this, we show results from using the final IM-SRG Hamiltonian  $H(\infty)$  in Hartree-Fock and post-HF methods in Fig. 3.7.

After the same 20–30 integration steps that lead to a strong suppression of the off-diagonal matrix elements (cf. Fig. 3.11), the energies of all methods collapse to the same result, which is the IM-SRG(2) ground-state energy. By construction, this is the result that would be obtained in a Hartree-Fock calculation with the IM-SRG Hamiltonian. Energy corrections due to correlations have been re-summed into the zero-body part of  $H(\infty)$ , and therefore MBPT(2) or either of the CC resummations do not contribute additional correlation energy. The collapse of the ground-state energies occurs in the same fashion for all  $(e_{\max}, \hbar\omega)$ , although the rate and magnitude of the change in g.s. energy with the flow parameter  $s$  may be quite different for each method.

Let us take a more detailed look at Fig. 3.7. For the bare N<sup>3</sup>LO interaction, the  $e_{\max} = 10$  results are not yet sufficiently converged with respect to either the single-particle basis and many-body expansions, hence the ground-state energy changes quite significantly with  $s$  (cf. Fig. 3.2). For the soft N<sup>3</sup>LO interaction with  $\lambda = 2.0 \text{ fm}^{-1}$ , on the other hand, convergence w.r.t. basis size is already quite satisfactory at  $e_{\max} = 10$ . Because this interaction is more perturbative, the small energy differences between the different many-body methods, in particular the second-order and infinite-order CC and IM-SRG resummations, indicates good convergence of the many-body expansion<sup>1</sup> [33, 51]. We will return to this subject in

---

<sup>1</sup>As discussed in Sec. 3.4, there is a caveat attached to this statement, namely that order-by-order pertur-

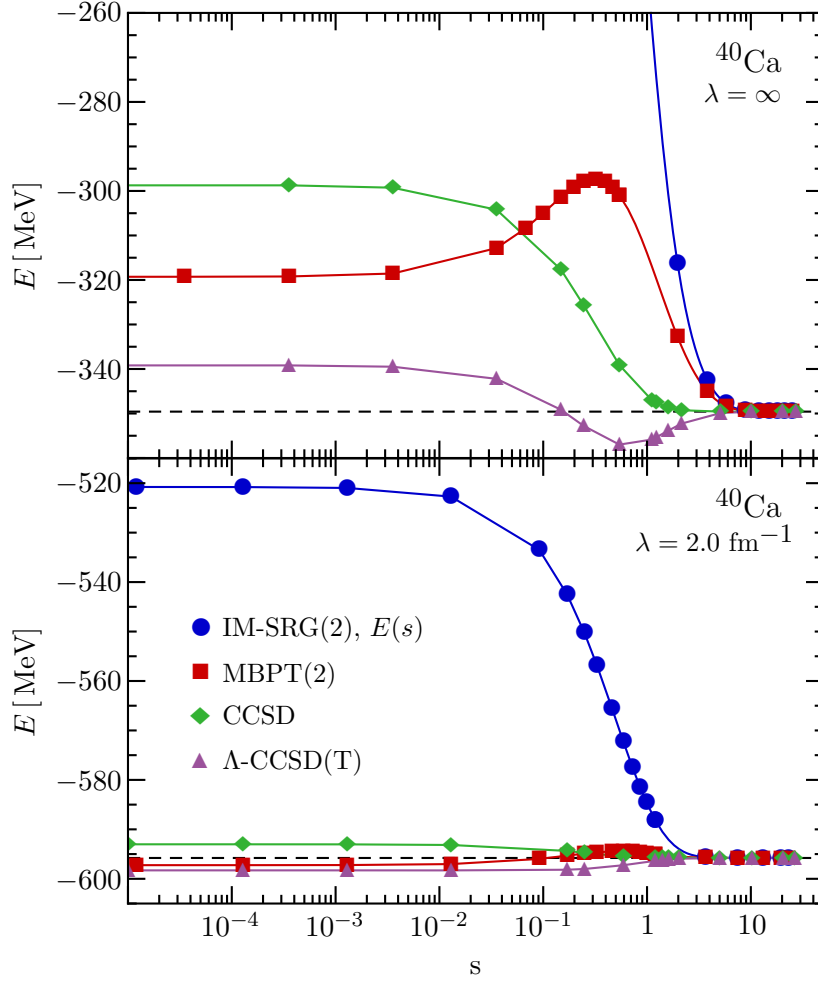


Figure 3.7: IM-SRG(2) ground-state energy of  $^{40}\text{Ca}$  as a function of the flow parameter  $s$ , compared to MBPT(2), CCSD, and  $\Lambda$ -CCSD(T) energies with the IM-SRG-evolved Hamiltonian  $H(s)$ . We only show part of the data points to avoid clutter. Calculations were done for  $e_{\text{max}} = 10$  and optimal  $\hbar\omega = 32$  MeV (top) and  $\hbar\omega = 24$  MeV (bottom), respectively, using the chiral NN interaction at different resolution scales. The dashed lines indicate the final IM-SRG(2) energies.

Sec. 3.5.

To conclude this section, we want to briefly discuss the four main scenarios that can occur when we use IM-SRG Hamiltonians as input for other many-body methods. We assume that calculations are converged w.r.t. basis size, etc.

1. *Full IM-SRG, exact many-body method:* For exact methods like the No-Core Shell
- 
- bative convergence strongly depends around which reference state the perturbation expansion is constructed.

Model or No-Core Full Configuration, the ground-state energy would be flat as a function of  $s$ . By performing an untruncated IM-SRG calculation, we essentially split the diagonalization of the many-body Hamiltonian into a part that is obtained by solving the IM-SRG flow equation, and a part that is obtained with traditional eigenvalue methods, with  $s$  serving as an arbitrary separation point.

2. *Full IM-SRG, approximate many-body method:* The ground-state energy varies with  $s$ , but for  $s \rightarrow \infty$ , the approximate many-body method yields the *exact* eigenvalue due to the untruncated IM-SRG transformation. Here we see how the IM-SRG can be used to improve the input Hamiltonian for other many-body approaches.
3. *Truncated IM-SRG, exact many-body method:* Again, the ground-state energy varies with  $s$ , and the overall variation is a measure of the extent to which the IM-SRG truncation violates exact unitarity.
4. *Truncated IM-SRG, approximate many-body method:* This is the most common, and most complicated case. Because of the IM-SRG truncation, the IM-SRG will reproduce the exact ground-state energy only approximately in the limit  $s \rightarrow \infty$ . If the approximate many-body method contains content *beyond* the truncated IM-SRG, then the result may actually degrade to some extent, whereas the IM-SRG still improves the result in the opposite scenario, but the uncertainty of  $E(\infty)$  is hard to quantify unless one also uses exact many-body methods for comparison. Both of these scenarios are realized in Fig. 3.7: MBPT(2) is less complete than the IM-SRG(2), so the MBPT(2) energy is improved towards the exact energy. Note that this improvement can come in the form of attractive or repulsive corrections, because MBPT(2) typically underestimates the g.s. energy for the bare interaction, but overshoots with soft interactions [33, 58, 88–

92]. Both CCSD and  $\Lambda$ -CCSD(T) differ from the IM-SRG(2) at fourth order in MBPT (see Sec. 3.5). CCSD typically underpredicts the nuclear binding energy, hence the additional correlation energy provided by the IM-SRG improvement should improve agreement with exact methods.  $\Lambda$ -CCSD(T) contains fourth-order 3p3h (triples) correlations, which are typically attractive, and missing in the IM-SRG(2) (cf. Sec. 3.5). This explains why the CCSD(T) ground-state energy actually increases (i.e., the binding energy *decreases*) with IM-SRG(2) input Hamiltonians as  $s \rightarrow \infty$  for the soft interaction. As mentioned above,  $e_{\max} = 10$  is not yet sufficiently converged in the case of the ground-state energies shown in the top panel. For larger bases, the IM-SRG(2) again increases the  $\Lambda$ -CCSD(T) ground-state energy Ref. [74]. Part of this increase is benign, because  $\Lambda$ -CCSD(T) is known to overestimate ground-state energies [16, 64, 67, 93–95].

### 3.3.5 Radii

In Sec. 3.1.4, we have discussed the evaluation of observables other than the ground-state energy, by solving additional sets of flow equations along with those for the Hamiltonian. As an example, we show the convergence of the charge radii of  ${}^4\text{He}$ ,  ${}^{16}\text{O}$ , and  ${}^{40}\text{Ca}$  in Fig. 3.8. The results are obtained by normal-ordering and evolving the intrinsic proton mean-square radius operator,

$$R_p^2 \equiv \sum_i \frac{1}{2} \left( 1 + \tau_3^{(i)} \right) (\mathbf{r}_i - \mathbf{R})^2, \quad (3.53)$$

where the isospin operator projects on protons, and  $\mathbf{R}$  is the center of mass. We obtain the charge radii by applying the corrections due to the mean-square charge radii of proton and

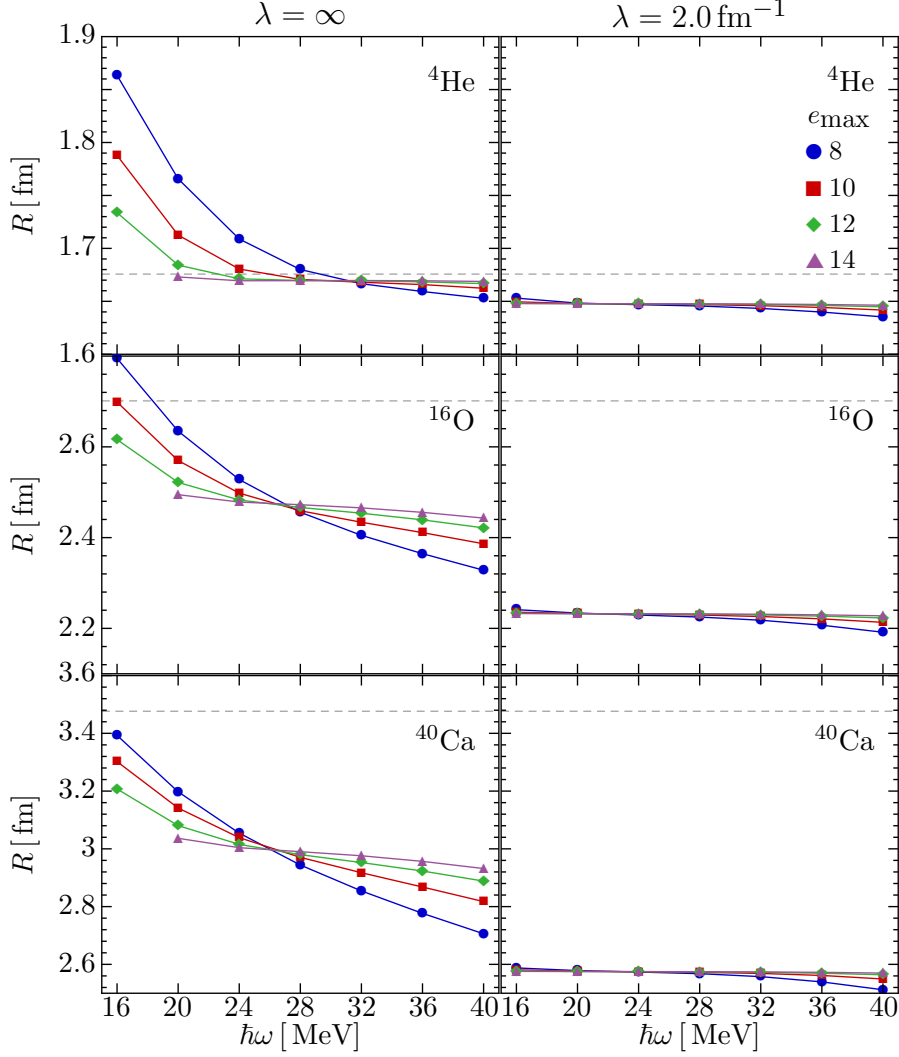


Figure 3.8: Convergence of  ${}^4\text{He}$ ,  ${}^{16}\text{O}$ , and  ${}^{40}\text{Ca}$  IM-SRG(2) charge radii w.r.t. single-particle basis size  $e_{\text{max}}$ , for a chiral  $\text{N}^3\text{LO}$  NN interaction with  $\lambda = \infty$  (left panels) and  $\lambda = 2.0 \text{ fm}^{-1}$  (right panels). The gray dashed lines indicate experimental charge radii from [15].

neutron (see, e.g., [96]):

$$R_{\text{ch}} \equiv \sqrt{R_p^2 + r_p^2 + \frac{N}{Z} r_n^2} = \sqrt{R_p^2 + (0.8775 \text{ fm})^2 - 0.1161 \text{ fm}^2}, \quad (3.54)$$

with values of  $r_p^2$  and  $r_n^2$  taken from [97].

Focusing on the results for the bare  $\text{N}^3\text{LO}$  interaction first, we find satisfactory conver-

gence of the charge radii to the level of 1% over a wide region of basis parameters  $\hbar\omega$ . For different  $e_{\max}$ , the curves intersect in the vicinity of the  $\hbar\omega$  that minimizes the ground-state energies (cf. Fig. 3.2). The IM-SRG(2) result for the charge radius of  ${}^4\text{He}$  is quite close to the experimental value. It is somewhat counter-intuitive, however, that the radius is slightly underpredicted, while about 1 MeV binding energy is missing (see Tab. 3.1). For  ${}^{16}\text{O}$ , the binding energy is similarly close to the experimental one, but the charge radius is already too small by almost 10%, while overbinding and underestimation of the radius are consistent on a superficial level with  ${}^{40}\text{Ca}$ .

Using the softened  $\text{N}^3\text{LO}$  interaction with  $\lambda = 2.0 \text{ fm}^{-1}$  as input, convergence of the radii improves dramatically over the bare  $\text{N}^3\text{LO}$  case. On the scales shown in Fig. 3.8, results from  $e_{\max} = 10$  onwards are all but indistinguishable. At the same time, the underestimation of the radii becomes worse, which is consistent with the increased binding energies that are reported in Sec. 3.3.2. Part of the problem is that the change of the resolution scale of the  $\text{N}^3\text{LO}$  interaction induces  $3N, \dots$  interactions which have not been taken into account. These induced interactions give repulsive contributions to the g.s. energy, and are therefore also expected to increase the radii to some extent Refs. [19, 21, 42, 74, 86, 87, 98–100].

Under a change of resolution scale  $\lambda$ , the radius operator (or any other observable) should be transformed consistently with the Hamiltonian, causing it to gain induced many-body contributions. Since RG transformations like the free-space SRG, and related methods like Lee-Suzuki, are designed to deal with high-momentum/short-distance physics, their effect on the radius and other long-ranged operators, and therefore the size of induced contributions, was expected to be small [101–103]. A recent free-space SRG study suggests that induced contributions may be small but not negligible in view of the discrepancies between experimental and calculated radii from state-of-the-art *ab initio* many-body calculations [104].

A related issue is the use of simple one-body ansätze like (3.53) for the mean-square proton radius and other radius or transition operators. These specific forms neglect two- and higher many-body contributions which are generated by exchange currents, for instance, and should be included in the “bare” operator in the first place. Chiral EFT provides a consistent framework to treat these effects on a similar footing as the interaction itself [105–114], but the exploration of these structurally richer operators in nuclear many-body calculations is still in its infancy [115].

## 3.4 Choice of Reference State

### 3.4.1 Overview

As explained in Sec. 3.2.1, the IM-SRG generates a mapping between an *arbitrary* reference state  $|\Phi\rangle$  and an eigenstate  $|\Psi\rangle$  of the Hamiltonian. In a finite system, i.e., in absence of phase transitions, and without symmetry constraints on the basis, such a mapping *always exists*, because we can diagonalize the Hamiltonian and construct a unitary transformation as the dyadic product of the exact ground state and the reference state, plus suitable additional states to complete the basis. Performing an evolution with the untruncated IM-SRG flow equations is equivalent to such a (partial) diagonalization<sup>2</sup>.

### 3.4.2 Harmonic Oscillator vs. Hartree-Fock Slater Determinants

In previous sections, we have explained that the ground-state energies of the untruncated IM-SRG flow equations do not depend on the choice of reference state. In practice, the IM-SRG(2) truncation of the flow equation system (Eqs. (3.8)–(3.10)) introduces an artificial

---

<sup>2</sup>Problems could only occur if we used a pathological generator.

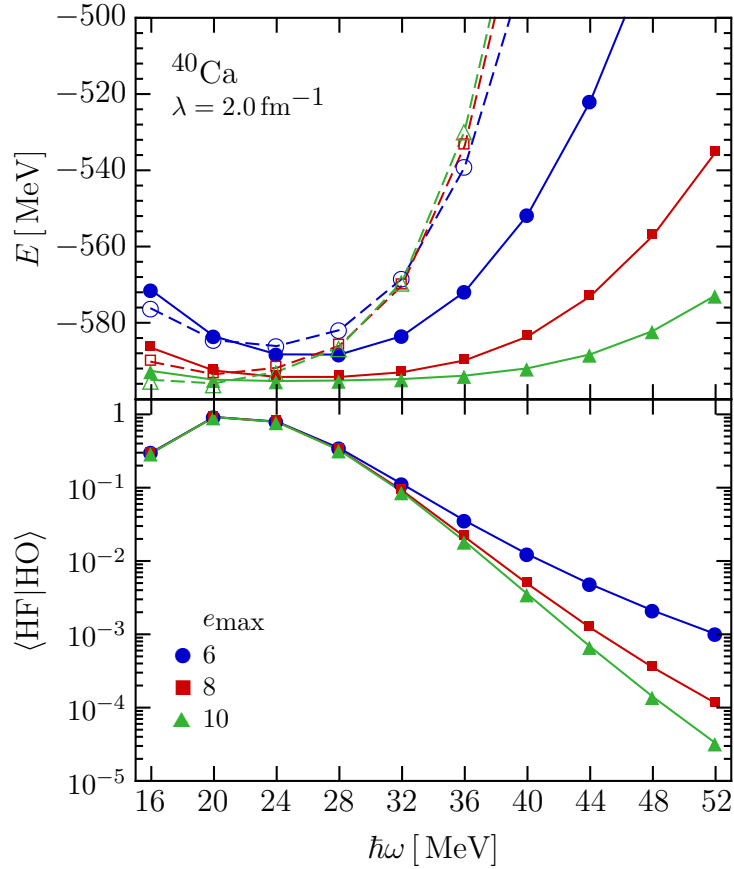


Figure 3.9: Top panel: IM-SRG(2) energy of  $^{40}\text{Ca}$  with a HF (solid lines and symbols) and a HO reference state (dashed lines, open symbols), obtained with the Wegner generator. Bottom panel: Overlap of the HF and HO reference states.

reference-state dependence.

In Fig. 3.9, we compare ground-state energies for  $^{40}\text{Ca}$  that were obtained with a naive HO Slater determinant and a HF Slater determinant, respectively. For oscillator parameters  $16 \leq \hbar\omega \leq 24$  MeV, the two types of calculations essentially converge to the same ground-state energies. In this range, the HO and HF determinants have their largest overlap, as shown in the lower panel of Fig. 3.9. Outside of this window, the overlap drops off steeply, which suggests that the HF single-particle wave functions differ appreciably from the plain HO single-particle wave functions. Of course, we have to keep in mind that these differences

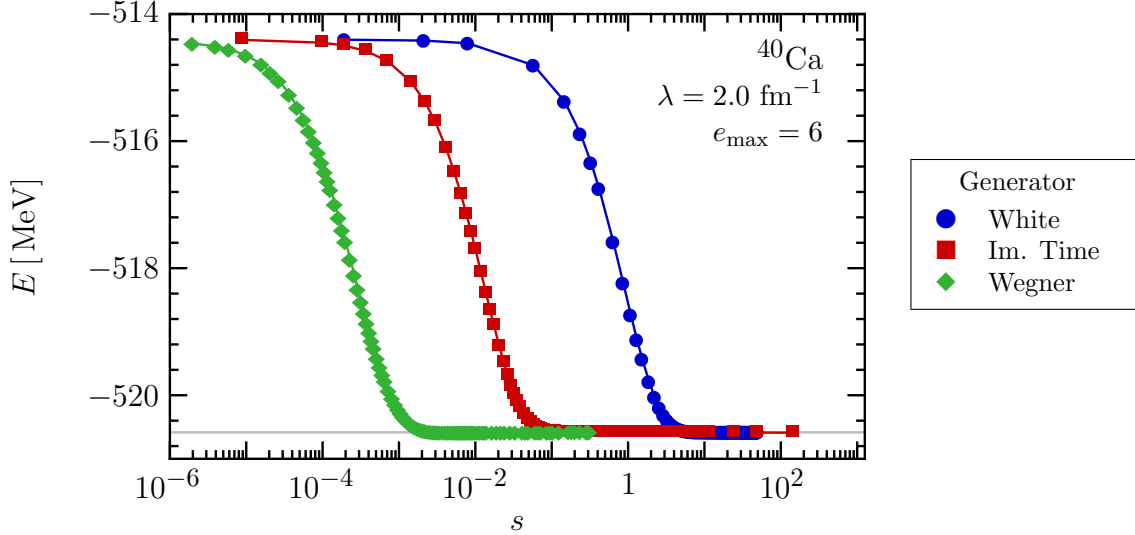


Figure 3.10: IM-SRG decoupling of 1p1h excitations for different generator choices, starting from a HO reference state. The figure shows the  $^{40}\text{Ca}$  ground-state energy as a function of the value of the flow parameter  $s$ . The unit of  $s$  is suppressed because it differs with the choice of generator. The gray line indicates the result of the Hartree-Fock calculation with the same interaction and basis parameters.

are amplified exponentially when the many-body overlap is calculated as the product of single-particle overlaps.

Beyond  $\hbar\omega = 28 \text{ MeV}$ , the IM-SRG(2) energies obtained with a HO reference state actually grow with the basis size  $e_{\text{max}}$ , which suggests that the IM-SRG is no longer targeting the Hamiltonian's ground state in those cases. This conclusion is supported by our inability to obtain converged results with White-type generators (see Eq. (3.23)) for the larger  $\hbar\omega$  values. The IM-SRG flow stalls because of divergences in the generator matrix elements that are caused by small energy denominators, which can be viewed as indicators of level crossings in the spectrum of the evolving many-body Hamiltonian.

So we see that unlike CC theory, truncated IM-SRG calculations are sensitive to the quality of the starting reference. This can be easily explained if the unitary transformation generated by the IM-SRG(2) is inspected. In order to have this insensitivity to reference choice, we would need to be able to take advantage of the unitary version of Thouless' thm

found in (2.34), proven by Rowe, Ryman, and Rosensteel in Ref. [116], relating any two non-orthogonal normalized Slater determinants  $|\Phi_A\rangle, |\Phi_B\rangle$  via

$$|\Phi_B\rangle = \exp\left(\sum_{ph} X_{ph} :a_p^\dagger a_h : - X_{ph}^* :a_h^\dagger a_p :\right) |\Phi_A\rangle. \quad (3.55)$$

Unfortunately, Eq. (3.55) does not apply to the IM-SRG in a straightforward fashion.

As mentioned in Sec. 3.1.1, the unitary transformation generated by the IM-SRG is formally given by the  $\mathcal{S}$ -ordered exponential

$$U(s) = \mathcal{S} \exp \int_0^s ds' \eta(s'), \quad (3.56)$$

because the generator dynamically changes during the flow. It can be defined as a product of infinitesimal unitary transformations,

$$U(s) = \lim_{N \rightarrow \infty} \prod_{i=0}^N e^{\eta(s_i) \delta s_i}, \quad \sum_i s_i = s, \quad (3.57)$$

or the series expansion

$$U(s) = \sum_n \frac{1}{n!} \int_0^s ds_1 \int_0^{s_1} ds_2 \dots \int_0^{s_{n-1}} ds_n \mathcal{S}\{\eta(s_1) \dots \eta(s_n)\}. \quad (3.58)$$

Here,  $\mathcal{S}$  ensures that the flow parameters in the operator products appearing in the integrands are always in descending order. Unlike the cluster operator of the CC method, the generator  $\eta(s)$  necessarily contains particle-hole de-excitation operators, or else it would not be anti-Hermitian as required for a unitary transformation. Thus, it is possible to have non-vanishing contractions between generator components of different particle rank, and commutators of

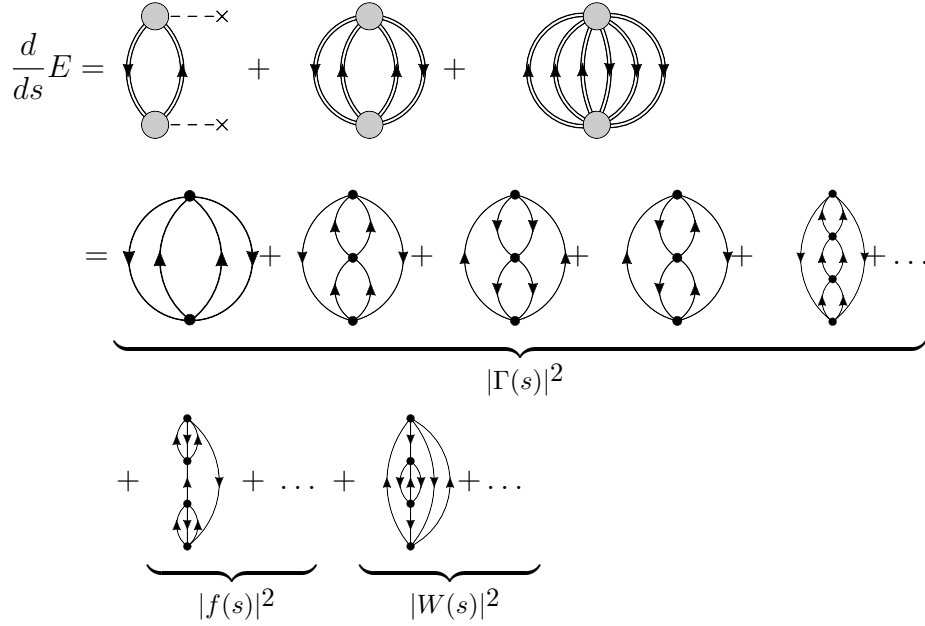


Figure 3.11: Schematic illustration of the energy flow equation (3.61) for the White generator with Møller-Plesset energy denominators (Eq. (3.23)) in terms of Hugenholtz diagrams (see text). The grey vertices represent  $H(s)$ , and the double lines indicate energy denominators calculated with  $f(s)$ . On the second line, the flow equation is expanded in terms of  $H(s - \delta s)$  (simple black vertices) and the corresponding energy denominators from  $f(s - \delta s)$  (single lines). The braces indicate which term of  $H(s)$  is expanded, and dots represent higher order diagrams generated by the integration step  $s - \delta s \rightarrow s$ .

such components do not vanish in general:

$$[\eta^{(i)}(s), \eta^{(j)}(s')] \neq 0. \quad (3.59)$$

As a result,  $U(s)$  does not factorize automatically, and it is this lack of factorization that makes the IM-SRG(2) method sensitive to reference states. We will revisit this sensitivity to reference state in the context of chemistry systems in Sec. 6.1.

## 3.5 Perturbative Analysis of the Flow Equations

### 3.5.1 Overview

The expressions for the White-type generators discussed in Sec. 3.2.2 are a manifest link between the IM-SRG and Many-Body Perturbation Theory. For the sake of discussion, we focus on the White generator with Møller-Plesset energy denominators, keeping the short-hands  $\Delta_{ph}$ ,  $\Delta_{pp'hh'}$ , etc., but dropping the superscript  $B$ . The generator with Epstein-Nesbet energy denominators can always be connected to this case by series expansion, e.g.,

$$\frac{1}{f_p - f_h + \Gamma_{phph}} = \frac{1}{f_p - f_h} \sum_k \left( \frac{\Gamma_{phph}}{f_p - f_h} \right)^k. \quad (3.60)$$

Let us now consider the flow equation for the ground-state energy (3.8), but broaden our perspective beyond the IM-SRG(2) truncation to keep track of the induced three-body contribution (cf. Eq. (B.2) and the discussion in Sec. 3.2.1). Plugging in the White-Møller-Plesset generator with explicit three-body contribution, we obtain

$$\frac{dE}{ds} = 2 \sum_{ph} \frac{|f_{ph}|^2}{\Delta_{ph}} + \frac{1}{2} \sum_{pp'hh'} \frac{|\Gamma_{pp'hh'}|^2}{\Delta_{pp'hh'}} + \frac{1}{18} \sum_{pp'hh'} \frac{|W_{pp'p''hh'h''}|^2}{\Delta_{pp'p''hh'h''}}. \quad (3.61)$$

The right-hand side of Eq. (3.61) has the structure of the second-order MBPT correction to the ground-state energy, but the matrix elements and energy denominators depend on the flow parameter  $s$ . Thus, Eq. (3.61) implies that the ground-state energy  $E(s)$  is RG-improved with contributions from higher orders of MBPT during the flow.

In the following discussion, we characterize all operators in terms of the same dimensionless book-keeping parameter  $g$ . We also assume that the initial Hamiltonian satisfies

the hierarchy  $f^d > \Gamma > W$  throughout the flow. The hierarchy of  $\Gamma$  and  $W$ , in particular, is compatible with the natural hierarchy of chiral two- and three-nucleon forces [32, 33]. Initially,

$$E(0) = \mathcal{O}(g^0), \quad f^d(0) = \mathcal{O}(g^0), \quad \Gamma(0) = \mathcal{O}(g). \quad (3.62)$$

If we do not include an initial three-body term, and choose a HF Slater determinant ( $f^{od} = \{f_{ph}, f_{hp}\}$ ) as the IM-SRG reference state, we also have

$$f^{od}(0) = 0, \quad W(0) = 0. \quad (3.63)$$

From the flow equations (3.8)–(3.10) (or (B.2)–(B.5)), we can conclude that corrections to  $\Gamma(s)$  are of order  $\mathcal{O}(g)$ . Corrections to  $f(s)$  are  $\mathcal{O}(g^2)$  because they are generated by terms which are quadratic in  $\Gamma(s)$ , and the same reasoning holds for the induced off-diagonal and three-body matrix elements,

$$f^{od}(s) = \mathcal{O}(g^2), \quad W(s) = \mathcal{O}(g^2), \quad \text{for } s > 0 \quad (3.64)$$

(also cf. Sec. 3.2.5). This establishes that the three terms in the flow equation (3.61) are of order  $\mathcal{O}(g^4)$ ,  $\mathcal{O}(g^2)$ , and  $\mathcal{O}(g^4)$ , respectively.

In Fig. 3.11, the effect of integrating Eq. (3.61) by a single step  $s - \delta s \rightarrow s$  is illustrated schematically in terms of Hugenholtz diagrams (see, e.g., [16, 117]). Expanding the  $H(s)$  vertices in terms of  $H(s - \delta s)$  vertices, we see that the  $\Gamma(s)$  term has contributions from  $\mathcal{O}(g^2)$  through  $\mathcal{O}(g^4)$ . Expanding in  $H(s - 2\delta s)$  instead, we would get additional higher order diagrams, and so forth. Thus, we perform a (partial)re-summation of the many-body

perturbation series by integrating the IM-SRG flow equations from  $s = 0$  to  $\infty$ .

Fig. 3.11 shows that all topologies for second- and third-order energy diagrams are generated, and we will demonstrate below that we build up to the complete energy through  $\mathcal{O}(g^3)$  when we integrate Eq. (3.61). The  $\Gamma(s)$  term also generates fourth-order diagrams with up to 4p4h/quadruples excitations, but  $f(s)$  and  $W(s)$  terms clearly contribute at fourth order as well. The former are included in the IM-SRG(2), which is therefore third-order correct, similar to Coupled Cluster with singles and doubles (CCSD). To obtain a formally correct fourth-order energy, we need to keep the induced three-body terms, e.g., use the IM-SRG(3) truncation or some appropriate approximation, as, for instance, in CC with singles, doubles, and perturbative triples (CCSD(T)).

We stress, however, that the perturbative analysis will *not* provide us with a means to judge the IM-SRG truncation error in nuclear physics applications, aside from a guaranteed linear scaling of the error with the particle number  $A$  due to size extensivity [16, 118].

In the remainder of this section, we will analyze the IM-SRG in greater detail. The main goal of this analysis is to provide an understanding of how the IM-SRG relates to other diagrammatic methods like finite-order MBPT, the Self-Consistent Green's Function approach [19, 76, 119], or the Coupled Cluster method, which can be analyzed diagrammatically along the same lines as the IM-SRG (see, e.g., [16]).

As mentioned above, we choose a HF Slater determinant as the reference state  $|\Phi\rangle$  for the IM-SRG and the MBPT expansion. Then  $f_{ph}(s)$  vanishes for  $s = 0$  (because of the HF equations) and  $s \rightarrow \infty$  (because of the IM-SRG decoupling condition), and we will only have to discuss canonical HF MBPT diagrams in the language of [16]. The inclusion of non-HF (where  $f_{ph} \neq 0$ ) and non-canonical HF diagrams (where  $f_{pp'}, f_{hh'}$  are non-diagonal) is straightforward but tedious because their number grows much more rapidly than the number

of canonical HF diagrams [16].

### 3.5.2 Power Counting

In the following discussion, we will use superscripts to indicate the order of individual terms in the IM-SRG flow equations. Let us first address the subtleties in the power counting that was defined in Eqs. (3.62) and (3.64). The natural orbitals for a HF Slater determinat  $|\Phi\rangle$  are the HF orbitals, which means that  $f(0)$  is diagonal in the particle and hole blocks of the s.p. basis, and  $f_{ph}(0) = f_{hp}(0) = 0$ . Since these are the off-diagonal matrix elements defining the one-body part of the generator (3.23),  $\eta_{ab}$  vanishes as well, and the one-body flow equation at  $s = 0$  becomes

$$\left. \frac{df_{12}}{ds} \right|_{s=0} = \sum_{abc} (n_a n_b \bar{n}_c + \bar{n}_a \bar{n}_b n_c) (1 + P_{12}) \eta_{c1ab}^{[1]} \Gamma_{abc2}^{[1]} + \dots \quad (3.65)$$

Thus, corrections to  $f$  start at  $\mathcal{O}(g^2)$  (cf. Sec. 3.2.5), and we have

$$f_{pp'}(s) = \bar{f}_p^{[0]} \delta_{pp'} + f_{pp'}^{[2]}(s) + \dots, \quad (3.66)$$

$$f_{hh'}(s) = \bar{f}_h^{[0]} \delta_{hh'} + f_{hh'}^{[2]}(s) + \dots, \quad (3.67)$$

$$f_{ph}(s) = f_{ph}^{[2]}(s) + \dots, \quad (3.68)$$

where the notation  $\bar{f}^{[0]}$  indicates that the term does not depend on  $s$ . It immediately follows that corrections and  $s$ -dependence of the Møller-Plesset energy denominators also appear at

$\mathcal{O}(g^2)$ ,

$$\Delta_{ab}(s) = \overline{\Delta}_{ab}^{[0]} + \overline{\Delta}_{ab}^{[2]} + \dots, \quad (3.69)$$

$$\Delta_{abcd}(s) = \overline{\Delta}_{abcd}^{[0]} + \overline{\Delta}_{abcd}^{[2]} + \dots. \quad (3.70)$$

Consequently, the generator matrix elements are given by

$$\eta_{ph} = \frac{f_{ph}^{[2]}}{\overline{\Delta}_{ph}^{[0]}} + \frac{f_{ph}^{[3]}}{\overline{\Delta}_{ph}^{[0]}} + \frac{f_{ph}^{[4]}}{\overline{\Delta}_{ph}^{[0]}} + \frac{f_{ph}^{[2]} \overline{\Delta}_{ph}^{[2]}}{(\overline{\Delta}_{ph}^{[0]})^2} + \mathcal{O}(g^5), \quad (3.71)$$

$$\eta_{pp'hh'} = \frac{\Gamma_{pp'hh'}^{[1]}}{\overline{\Delta}_{pp'hh'}^{[0]}} + \frac{\Gamma_{pp'hh'}^{[2]}}{\overline{\Delta}_{pp'hh'}^{[0]}} + \frac{\Gamma_{pp'hh'}^{[3]}}{\overline{\Delta}_{pp'hh'}^{[0]}} + \frac{\Gamma_{pp'hh'}^{[1]} \overline{\Delta}_{pp'hh'}^{[2]}}{(\overline{\Delta}_{pp'hh'}^{[0]})^2} + \mathcal{O}(g^4), \quad (3.72)$$

and their Hermitian conjugates. Based on these considerations, we will proceed to discuss the one- and two-body flow equations at increasing orders  $\mathcal{O}(g^n)$ . Since the energy flow equation does not feed back into the flow for  $f$  and  $\Gamma$ , we will discuss it separately afterwards.

### 3.5.3 $\mathcal{O}(g)$ Flow

As shown in the previous section, corrections to the one-body Hamiltonian  $f$  only begin to contribute at  $\mathcal{O}(g^2)$ , hence

$$\dot{f}_{12}^{[1]} = 0 \quad \Rightarrow \quad f_{12}^{[1]}(s) = 0, \quad (3.73)$$

where the dot indicates the derivative with respect to  $s$ . The first-order contribution to the two-body flow comes from the first line of Eq. (3.10):

$$\dot{\Gamma}_{1234}^{[1]} = - \sum_a \left\{ (1 - P_{12}) (\overline{f}_{1a}^{[0]} \eta_{a234}^{[1]}) - (1 - P_{34}) (\overline{f}_{a3}^{[0]} \eta_{12a4}^{[1]}) \right\}, \quad (3.74)$$

where we have used Eqs. (3.71) and (3.72), and  $f^{[1]} = 0$ . Since  $\eta$  only has pphh and hhpp matrix elements and  $f^{[0]}$  is diagonal, we have

$$\begin{aligned}\dot{\Gamma}_{pp'hh'}^{[1]} &= -\left(\bar{f}_p^{[0]} + \bar{f}_{p'}^{[0]} - \bar{f}_h^{[0]} - \bar{f}_{h'}^{[0]}\right)\eta_{pp'hh'}^{[1]} \\ &= -\bar{\Delta}_{pphh'}^{[0]}\eta_{pp'hh'}^{[1]},\end{aligned}\tag{3.75}$$

and an analogous equation for the Hermitian conjugate, while  $\dot{\Gamma}_{1234}^{[1]} = 0$  otherwise. Thus, the flow equations can be integrated easily, and we obtain

$$\Gamma_{abcd}^{[1]}(s) = \bar{\Gamma}_{abcd}^{[1]} \times \begin{cases} e^{-s} & \text{for } abcd = pp'hh', hh'pp', \\ 1 & \text{otherwise,} \end{cases}\tag{3.76}$$

with

$$\bar{\Gamma}_{abcd}^{[1]} \equiv \Gamma_{abcd}(0).\tag{3.77}$$

### 3.5.4 $\mathcal{O}(g^2)$ Flow

We begin our discussion with the second-order contribution to  $f$ . Using Eq. (3.76), the IM-SRG flow equation (3.9) yields

$$\begin{aligned}\dot{f}_{pp'}^{[2]} &= \frac{1}{2} \sum_{p''hh'} \left( \eta_{p''phh'}^{[1]} \Gamma_{hh'p''p'}^{[1]} + \eta_{p''p'hh'}^{[1]} \Gamma_{hh'p''p}^{[1]} \right) \\ &= \frac{1}{2} \sum_{p''hh'} \bar{\Gamma}_{p''phh'}^{[1]} \bar{\Gamma}_{hh'p''p'}^{[1]} \left( \frac{e^{-2s}}{\bar{\Delta}_{p''ph'hh'}^{[0]}} + \frac{e^{-2s}}{\bar{\Delta}_{p''p'h'hh'}^{[0]}} \right) \\ &\equiv 2\bar{f}_{pp'}^{[2]} e^{-2s}.\end{aligned}\tag{3.78}$$

The flow equations for the other matrix elements of  $f^{[2]}(s)$  have the same structure, consisting of an  $s$ -independent amplitude and a function containing a decaying exponential in  $s$ . With the initial value condition  $f^{[2]}(0) = 0$ , we obtain

$$f_{ab}^{[2]}(s) = \bar{f}_{ab}^{[2]} \times \begin{cases} (1 - e^{-2s}) & \text{for } ab = pp', hh', \\ se^{-s} & \text{for } ab = ph, hp. \end{cases} \quad (3.79)$$

For  $s \rightarrow \infty$ , the IM-SRG builds up and adds the amplitudes  $\bar{f}_{pp'}^{[2]}$  and  $\bar{f}_{hh'}^{[2]}$  to the effective one-body Hamiltonian, which precisely correspond to the second-order contributions from MBPT. We can express them succinctly in terms of the antisymmetrized Goldstone diagrams shown in Fig. 3.12:

$$\bar{f}_{pp'}^{[2]} = \frac{1}{2} \left( (f_1)_{pp'} + (p \leftrightarrow p') \right), \quad (3.80)$$

$$\bar{f}_{hh'}^{[2]} = \frac{1}{2} \left( (f_2)_{hh'} + (h \leftrightarrow h') \right), \quad (3.81)$$

$$\bar{f}_{ph}^{[2]} = (f_3)_{ph} + (f_4)_{hp}. \quad (3.82)$$

The rules for interpreting such diagrams are derived in most many-body texts, so we only summarize them in Appendix C for convenience. For the particle-hole matrix elements, we have

$$f_{ph}^{[2]}(0) = f_{ph}^{[2]}(\infty) = 0, \quad (3.83)$$

because we start with a HF Slater determinant and demand that the reference state is again decoupled from 1p1h excitations for  $s \rightarrow \infty$ . At intermediate stages of the flow, the amplitudes  $\bar{f}_{ph}^{[2]}$  and  $\bar{f}_{hp}^{[2]}$  contribute to the build-up of higher-order MBPT diagrams.

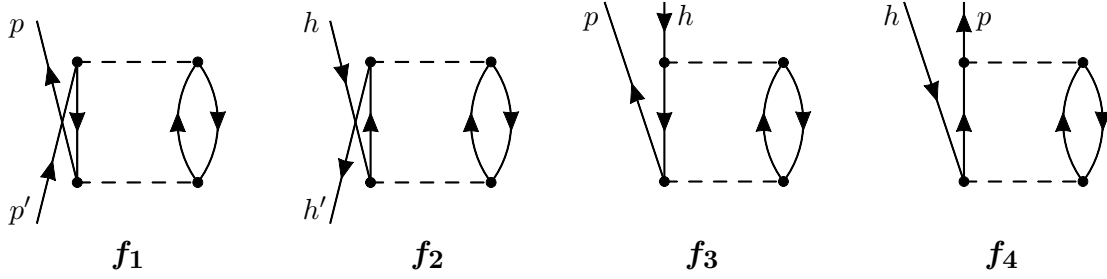


Figure 3.12: Antisymmetrized Goldstone diagrams for the  $\mathcal{O}(g^2)$  effective one-body Hamiltonian (see text). Interpretation rules are summarized in Appendix C.

For the second-order two-body vertex  $\Gamma^{[2]}$ , the same kind of analysis yields

$$\Gamma_{abcd}^{[2]}(s) = \bar{\Gamma}_{abcd}^{[2]} \times \left\{ \begin{array}{ll} (1 - e^{-2s}) & \text{for } abcd = p_1 p_2 p_3 p_4, \\ & h_1 h_2 h_3 h_4, \\ & p_1 h_1 p_2 h_2, \dots, \\ (1 - e^{-s}) & \text{for } abcd = p_1 p_2 p_3 h, \\ & h_1 h_2 h_3 p, \dots, \\ s e^{-s} & \text{for } abcd = p_1 p_2 h_1 h_2, \\ & \dots, \end{array} \right. \quad (3.84)$$

where the dots indicate all allowed permutations and Hermitian conjugates of the explicitly

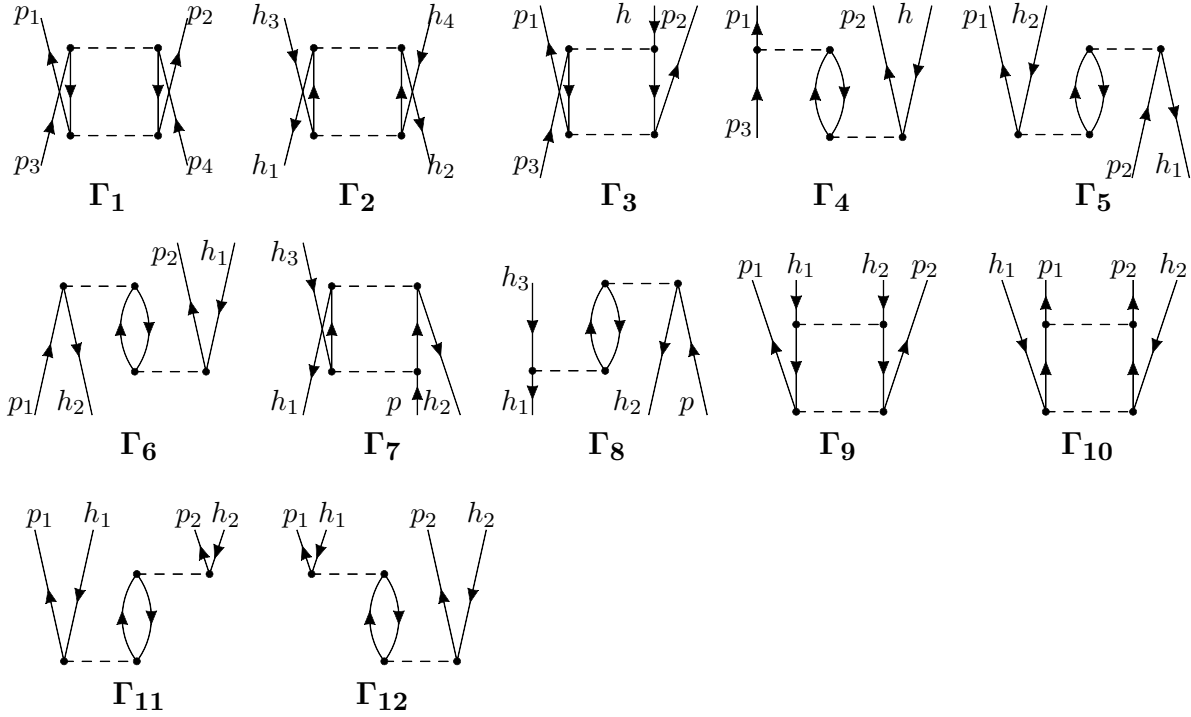


Figure 3.13: Antisymmetrized Goldstone diagrams for the  $\mathcal{O}(g^2)$  effective two-body vertex  $\Gamma$  (see text). Interpretation rules are summarized in Appendix C.

given indices. The corresponding amplitudes are

$$\bar{\Gamma}_{p_1 p_2 p_3 p_4}^{[2]} = \frac{1}{2} \left( (\Gamma_1)_{p_1 p_2 p_3 p_4} + (\Gamma_1)_{p_3 p_4 p_1 p_2} \right), \quad (3.85)$$

$$\bar{\Gamma}_{h_1 h_2 h_3 h_4}^{[2]} = \frac{1}{2} \left( (\Gamma_2)_{h_1 h_2 h_3 h_4} + (\Gamma_2)_{h_3 h_4 h_1 h_2} \right), \quad (3.86)$$

$$\bar{\Gamma}_{p_1 p_2 p_3 h}^{[2]} = (\Gamma_3)_{p_1 p_2 p_3 h} + (1 - P_{p_1 p_2}) (\Gamma_4)_{p_1 p_2 p_3 h}, \quad (3.87)$$

$$\bar{\Gamma}_{p_1 h_1 p_2 h_2}^{[2]} = \frac{1}{2} \left( (\Gamma_5)_{p_1 h_1 h_2 p_2} + (\Gamma_6)_{h_2 p_2 p_1 h_1} \right), \quad (3.88)$$

$$\bar{\Gamma}_{h_1 h_2 h_3 p}^{[2]} = (\Gamma_7)_{h_1 h_2 h_3 p} + (1 - P_{h_1 h_2}) (\Gamma_8)_{h_1 h_2 h_3 p}, \quad (3.89)$$

$$\bar{\Gamma}_{p_1 p_2 h_1 h_2}^{[2]} = (\Gamma_9)_{p_1 p_2 h_1 h_2} + (\Gamma_{10})_{h_1 h_2 p_1 p_2} + (1 - P_{p_1 p_2}) (\Gamma_{11} + \Gamma_{12})_{p_1 p_2 h_1 h_2}, \quad (3.90)$$

where we refer to the diagrams in Fig. 3.13. Expressions for the remaining combinations

of indices can be obtained by using the antisymmetry and Hermiticity of  $\bar{\Gamma}_{abcd}^{[2]}$ . Equations (3.85)–(3.90) are given in a hybrid form, i.e., they contain explicit Hermitian conjugates and line permutations of the diagrams. This allows us to express our analytic expressions for the amplitudes in terms of the minimal set of diagrams in Fig. 3.13. If one envisions the inverse problem of constructing the IM-SRG flow equations from diagrams, one would of course include all possible diagram topologies, and express the amplitudes purely as sums of diagrams before deriving analytic expressions.

As in the schematic discussion of the energy flow equation in Sec. 3.5.1, we also want to keep track of induced three-body terms. The IM-SRG(3) flow equation for the three-body vertex, Eq. (B.5), reveals that there are  $\mathcal{O}(g^2)$  contributions from products of  $\eta_{abcd}^{[1]}(s)$  and  $\Gamma_{abcd}^{[1]}(s)$ , hence we have to analyze  $W^{[2]}$ . However, we will limit the discussion to the matrix elements of  $W^{[2]}$  which can actually contribute to the fourth-order corrections to the ground-state energy (see Fig. 3.1 and the discussion Sec. 3.5.1). Integrating the  $\mathcal{O}(g^2)$  three-body flow equation, we obtain

$$W_{abcdef}^{[2]}(s) = \bar{W}_{abcdef}^{[2]} \times \left\{ \begin{array}{ll} (1 - e^{-2s}) & \text{for } abcdef = \\ & p_1 p_2 h_1 h_2 p_3 p_4, \\ & h_1 h_2 p_1 p_2 h_3 h_4, \\ & \dots, \\ se^{-s} & \text{for } abcdef = \\ & p_1 p_2 p_3 h_1 h_2 h_3, \\ & \dots, \end{array} \right. \quad (3.91)$$

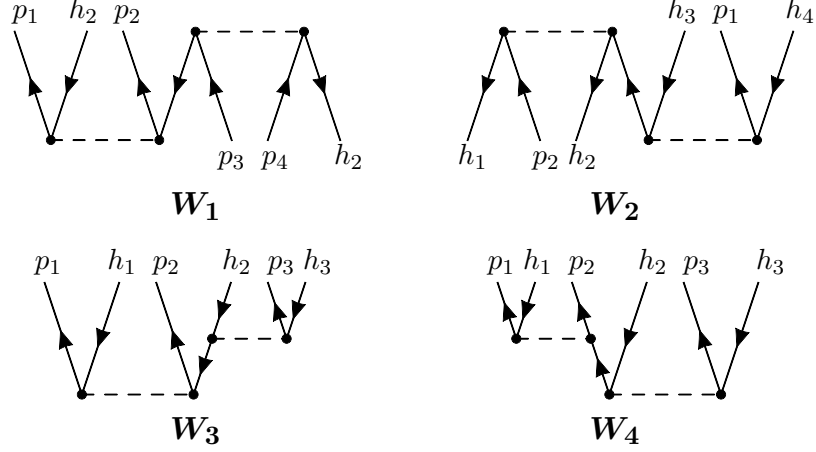


Figure 3.14: Antisymmetrized Goldstone diagrams for the  $\mathcal{O}(g^2)$  effective three-body vertex  $W$  (see text). Interpretation rules are summarized in Appendix C.

where the dots again indicate allowed Hermitian conjugates and permutations of indices. In terms of the diagrams shown in Fig. 3.14, the amplitudes are

$$\overline{W}_{p_1 p_2 h_1 h_2 p_3 p_4}^{[2]} = \frac{1}{2} \left( (W_1)_{p_1 p_2 h_1 h_2 p_3 p_4} + (W_1)_{h_2 p_3 p_4 p_1 p_2 h_1} \right), \quad (3.92)$$

$$\overline{W}_{h_1 h_2 p_1 p_2 h_3 h_4}^{[2]} = \frac{1}{2} \left( (W_2)_{h_1 h_2 p_1 p_2 h_3 h_4} + (W_2)_{p_2 h_3 p_4 h_1 h_2 p_1} \right), \quad (3.93)$$

$$\overline{W}_{p_1 p_2 p_3 h_1 h_2 h_3}^{[2]} = P(p_1 p_2 / p_3) P(h_1 h_2 / h_3) (W_3 + W_4)_{p_1 p_2 p_3 h_1 h_2 h_3}, \quad (3.94)$$

where we have defined the three-body permutation symbols

$$P(ij/k) \equiv 1 - P_{ik} - P_{jk}, \quad (3.95)$$

$$P(i/jk) \equiv 1 - P_{ij} - P_{ik}. \quad (3.96)$$

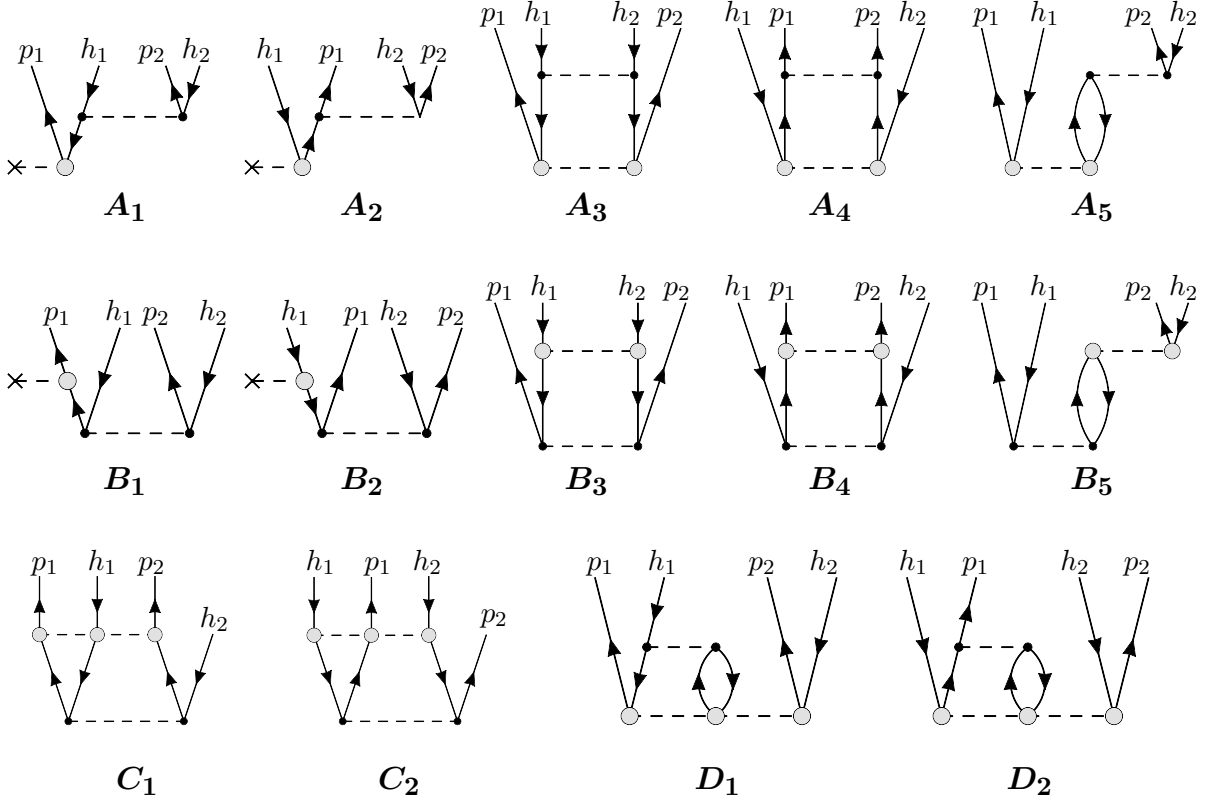


Figure 3.15: Antisymmetrized Goldstone diagrams for the  $\mathcal{O}(g^3)$  effective two-body vertex  $\Gamma$  (see text). Black ( $\bullet$ ) and gray vertices ( $\odot$ ) correspond to  $\bar{\Gamma}^{[1]}$  (Eq. (3.77)),  $\bar{f}^{[2]}$  (Eqs. (3.80)–(3.82)),  $\bar{\Gamma}^{[2]}$  (Eqs. (3.85)–(3.90)), and  $\bar{W}^{[2]}$  (Eqs. (3.92)–(3.94)), respectively. Interpretation rules are summarized in Appendix C.

### 3.5.5 $\mathcal{O}(g^3)$ Flow

The analysis of the third-order one- and two-body flow equations is straightforward, but the number of terms (or diagrams) we have to consider increases significantly. Here, we content ourselves with analyzing  $\Gamma_{pp'hh'}^{[3]}(s)$ , the only missing ingredient for the discussion of the energy flow equation through  $\mathcal{O}(g^4)$ , as in the overview presented in Sec. 3.5.1. Using our

results from the previous sections, the two-body flow equation can be written as

$$\dot{\Gamma}_{p_1 p_2 h_1 h_2}^{[3]} \equiv -\Gamma_{p_1 p_2 h_1 h_2}^{[3]} + (\bar{A} + \bar{D})_{p_1 p_2 h_1 h_2} s e^{-s} + (\bar{B} + \bar{C})_{p_1 p_2 h_1 h_2} (e^{-3s} - e^{-s}) , \quad (3.97)$$

which is solved by

$$\Gamma_{p_1 p_2 h_1 h_2}^{[3]}(s) = (\bar{A} + \bar{D})_{p_1 p_2 h_1 h_2} \frac{s^2}{2} e^{-s} - (\bar{B} + \bar{C})_{p_1 p_2 h_1 h_2} \left( \frac{e^{-3s} - e^{-s}}{2} + s e^{-s} \right) . \quad (3.98)$$

The amplitudes  $\bar{A}$  to  $\bar{D}$  are given by the diagrams shown in Fig. 3.15, where black and grey indices indicate the first- and second-order vertices, respectively:

$$\begin{aligned} \bar{A}_{p_1 p_2 h_1 h_2} &= (1 - P_{p_1 p_2}) (A_1)_{p_1 p_2 h_1 h_2} + (1 - P_{h_1 h_2}) (A_2)_{p_1 p_2 h_1 h_2} \\ &\quad + (A_3 + A_4)_{p_1 p_2 h_1 h_2} + (1 - P_{p_1 p_2}) (1 - P_{h_1 h_2}) (A_5)_{p_1 p_2 h_1 h_2} , \end{aligned} \quad (3.99)$$

$$\begin{aligned} \bar{B}_{p_1 p_2 h_1 h_2} &= -\bar{\eta}_{p_1 p_2 h_1 h_2}^{[2]} \bar{\Delta}_{p_1 p_2 h_1 h_2}^{[2]} \\ &\quad + (1 - P_{p_1 p_2}) (B_1)_{p_1 p_2 h_1 h_2} + (1 - P_{h_1 h_2}) (B_2)_{p_1 p_2 h_1 h_2} \\ &\quad + (B_3 + B_4)_{p_1 p_2 h_1 h_2} + (1 - P_{p_1 p_2}) (1 - P_{h_1 h_2}) (B_5)_{p_1 p_2 h_1 h_2} , \end{aligned} \quad (3.100)$$

$$\bar{C}_{p_1 p_2 h_1 h_2} = (1 - P_{h_1 h_2}) (C_1)_{p_1 p_2 h_1 h_2} + (1 - P_{p_1 p_2}) (C_2)_{p_1 p_2 h_1 h_2} , \quad (3.101)$$

$$\bar{D}_{p_1 p_2 h_1 h_2} = (1 - P_{h_1 h_2}) (D_1)_{p_1 p_2 h_1 h_2} + (1 - P_{p_1 p_2}) (D_2)_{p_1 p_2 h_1 h_2} . \quad (3.102)$$

$\bar{A}$  and  $\bar{B}$  are contained in the standard IM-SRG(2) truncation, whereas  $\bar{C}$  and  $\bar{D}$  are leading-order induced three-body terms. In particular, the former is a product of  $\bar{W}^{[2]}$  and the

two-body generator,

$$\begin{aligned} \bar{C}_{p_1 p_2 h_1 h_2} &= \frac{1}{2}(1 - P_{h_1 h_2}) \sum_{p' p'' h'} \bar{W}_{p_1 h' p_2 p' h_1 p''}^{[2]} \bar{\eta}_{p' p'' h'}^{[1]} \\ &+ \frac{1}{2}(1 - P_{p_1 p_2}) \sum_{h' h'' p'} \bar{W}_{h_1 p' h_2 h' p_1 h''}^{[2]} \bar{\eta}_{h' h'' p'}^{[1]}, \end{aligned} \quad (3.103)$$

while the latter is a product of  $\bar{\Gamma}^{[1]}$  and the three-body generator instead:

$$\begin{aligned} \bar{D}_{p_1 p_2 h_1 h_2} &= \frac{1}{2}(1 - P_{h_1 h_2}) \sum_{h' h'' p'} \bar{\eta}_{h' h_2 h'' p_1 p_2 p'}^{[2]} \bar{\Gamma}_{h_1 p'' h' h''}^{[1]} \\ &+ \frac{1}{2}(1 - P_{p_1 p_2}) \sum_{p' p'' h'} \bar{\eta}_{p' p'' p_2 h_1 h' h_2}^{[2]} \bar{\Gamma}_{p_1 h' p' p''}^{[1]}. \end{aligned} \quad (3.104)$$

This distinction is of little consequence in the present analysis, but may become important if the Hamiltonian and the generator are not truncated to the same particle rank. Note, however, that the diagrams for  $\bar{C}$  and  $\bar{D}$  have different topologies: The former couples the reference state to an excited 2p2h state via intermediate 2p2h excitations, whereas the latter has intermediate 3p3h states.

By expanding the grey  $\bar{\Gamma}^{[2]}$  vertices in Fig. 3.15 in terms of  $\bar{\Gamma}^{[1]}$ , we can also see how the IM-SRG flow performs a non-perturbative resummation of the MBPT series, as indicated in Sec. 3.5.1. The diagram  $A_3$ , for instance, is expanded as

$$= \text{Diagram 1} + \text{Diagram 2} + \text{Diagram 3} + \dots, \quad (3.105)$$

and contains ladder diagrams (first row), as well as diagrams where ladder and polarization configurations interfere (second row). Such interference diagrams set the IM-SRG apart from the traditional  $G$ -matrix and RPA approaches, which only resum ladders and polarization diagrams, respectively [120].

### 3.5.6 Energy through $\mathcal{O}(g^4)$

Let us now consider the energy flow equation. At  $\mathcal{O}(g^2)$ , we have

$$\begin{aligned}\dot{E}^{[2]} &= \frac{1}{2} \sum_{h_1 h_2 p_1 p_2} \eta_{h_1 h_2 p_1 p_2}^{[1]} \Gamma_{p_1 p_2 h_1 h_2}^{[1]} \\ &= \frac{1}{2} \sum_{h_1 h_2 p_1 p_2} \bar{\eta}_{h_1 h_2 p_1 p_2}^{[1]} \bar{\Gamma}_{p_1 p_2 h_1 h_2}^{[1]} e^{-2s}.\end{aligned}\tag{3.106}$$

Integrating this equation with  $E^{[2]}(0) = 0$ , we obtain

$$E^{[2]}(s) = \frac{1}{4} \left(1 - e^{-2s}\right) \sum_{h_1 h_2 p_1 p_2} \frac{\bar{\Gamma}_{h_1 h_2 p_1 p_2}^{[1]} \bar{\Gamma}_{p_1 p_2 h_1 h_2}^{[1]}}{\bar{\Delta}_{h_1 h_2 p_1 p_2}^{[0]}},\tag{3.107}$$

i.e.,  $E^{[2]}(\infty)$  is just the standard second-order MBPT correction to the energy of the reference state (cf. Fig. 3.11).

Likewise, the flow equation for the  $\mathcal{O}(g^3)$  energy reads

$$\begin{aligned}\dot{E}^{[3]} &= \frac{1}{2} \sum_{h_1 h_2 p_1 p_2} \left( \eta_{h_1 h_2 p_1 p_2}^{[1]} \Gamma_{p_1 p_2 h_1 h_2}^{[2]} + \eta_{h_1 h_2 p_1 p_2}^{[2]} \Gamma_{p_1 p_2 h_1 h_2}^{[1]} \right) \\ &= \sum_{h_1 h_2 p_1 p_2} \frac{\bar{\Gamma}_{h_1 h_2 p_1 p_2}^{[1]} \bar{\Gamma}_{p_1 p_2 h_1 h_2}^{[2]}}{\bar{\Delta}_{h_1 h_2 p_1 p_2}^{[0]}} e^{-2s}\end{aligned}\tag{3.108}$$

and integration yields

$$E^{[3]}(s) = \frac{1}{4} \left( 1 - (2s + 1)e^{-2s} \right) \sum_{h_1 h_2 p_1 p_2} \frac{\bar{\Gamma}_{h_1 h_2 p_1 p_2}^{[1]} \bar{\Gamma}_{p_1 p_2 h_1 h_2}^{[2]}}{\bar{\Delta}_{h_1 h_2 p_1 p_2}^{[0]}}. \quad (3.109)$$

For  $s \rightarrow \infty$ ,

$$E^{[3]}(\infty) = \frac{1}{4} \sum_{h_1 h_2 p_1 p_2} \frac{\bar{\Gamma}_{h_1 h_2 p_1 p_2}^{[1]} \bar{\Gamma}_{p_1 p_2 h_1 h_2}^{[2]}}{\bar{\Delta}_{h_1 h_2 p_1 p_2}^{[0]}}, \quad (3.110)$$

and plugging in  $\bar{\Gamma}^{[2]}$  from Eq. (3.90), this immediately becomes

$$E^{[3]}(\infty) = \begin{array}{c} \text{Diagram 1} \\ \text{Diagram 2} \\ \text{Diagram 3} \end{array} + \begin{array}{c} \text{Diagram 4} \\ \text{Diagram 5} \\ \text{Diagram 6} \end{array} + \begin{array}{c} \text{Diagram 7} \\ \text{Diagram 8} \\ \text{Diagram 9} \end{array}, \quad (3.111)$$

the standard third order energy correction.

At  $\mathcal{O}(g^4)$ , we have to consider products of  $\eta^{[2]}$  and the second-order Hamiltonian contributions  $f^{[2]}$ ,  $\Gamma^{[2]}$ , and  $W^{[2]}$  (cf. Fig. 3.11), as well as the cross terms

$$\begin{aligned} E_{3-1}^{[4]} &= \frac{1}{2} \sum_{p_1 p_2 h_1 h_2} \left( \eta_{h_1 h_2 p_1 p_2}^{[3]} \Gamma_{p_1 p_2 h_1 h_2}^{[1]} + [\eta \leftrightarrow \Gamma] \right) \\ &= \frac{1}{2} \sum_{p_1 p_2 h_1 h_2} \left( -\Gamma_{h_1 h_2 p_1 p_2}^{[1]} \frac{\Delta_{h_1 h_2 p_1 p_2}^{[2]}}{\bar{\Delta}_{h_1 h_2 p_1 p_2}^{[0]}} + 2\Gamma_{h_1 h_2 p_1 p_2}^{[3]} \right) \times \frac{\Gamma_{p_1 p_2 h_1 h_2}^{[1]}}{\bar{\Delta}_{h_1 h_2 p_1 p_2}^{[0]}}. \end{aligned} \quad (3.112)$$

The first term is due to the expansion of the energy denominator in  $\eta^{[3]}$  to second order (cf. Sec. 3.5.2). However, it is easy to see that contributions from this term cancel in the sum, because  $\Delta_{pp'hh'}^{[0/2]}$  is antisymmetric under transposition while  $\Gamma_{pp'hh'}^{[1]}$  is symmetric. Thus,

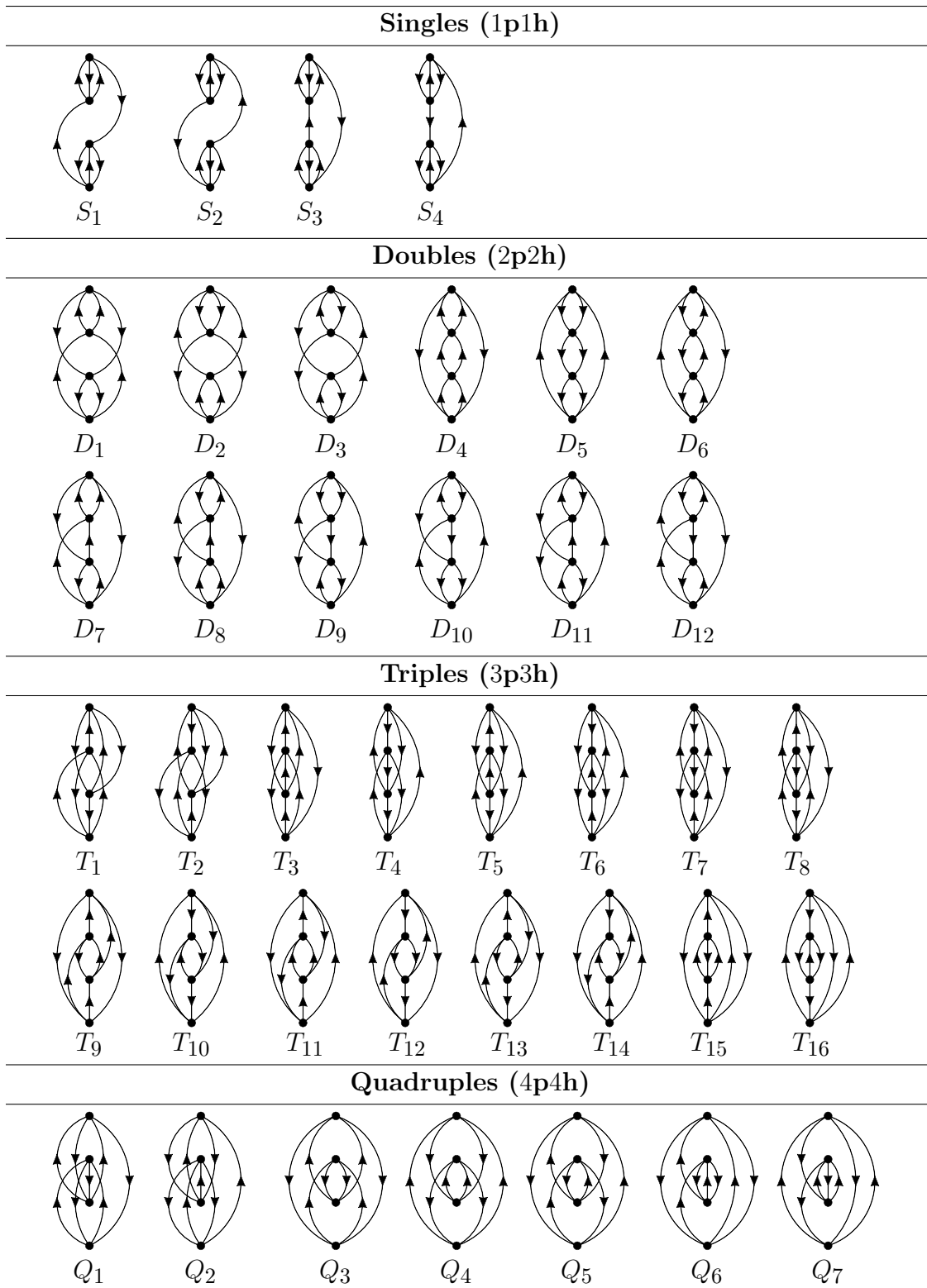


Figure 3.16: Connected Hugenholtz diagrams for the fourth-order energy correction  $E^{(4)}$  (Ref. [16]).

the energy flow equation becomes

$$\begin{aligned}
\dot{E}^{[4]} &= 2s^2 e^{-2s} \sum_{ph} \bar{\eta}_{hp}^{[2]} \bar{f}_{ph}^{[2]} + \frac{s^2}{2} e^{-2s} \sum_{p_1 p_2 h_1 h_2} \bar{\eta}_{h_1 h_2 p_1 p_2}^{[2]} \bar{\Gamma}_{p_1 p_2 h_1 h_2}^{[2]} \\
&+ \frac{s^2}{18} e^{-2s} \sum_{p_1 p_2 p_3 h_1 h_2 h_3} \bar{\eta}_{h_1 h_2 h_3 p_1 p_2 p_3}^{[2]} \bar{W}_{p_1 p_2 p_3 h_1 h_2 h_3}^{[2]} \\
&+ \frac{s^2}{2} e^{-2s} \sum_{p_1 p_2 h_1 h_2} (\bar{A} + \bar{D})_{h_1 h_2 p_1 p_2} \frac{\bar{\Gamma}_{p_1 p_2 h_1 h_2}^{[1]}}{\Delta_{h_1 h_2 p_1 p_2}} \\
&- \left( \frac{e^{-4s} - e^{-2s}}{2} + s e^{-s} \right) \sum_{p_1 p_2 h_1 h_2} (\bar{B} + \bar{C})_{h_1 h_2 p_1 p_2} \frac{\bar{\Gamma}_{p_1 p_2 h_1 h_2}^{[1]}}{\Delta_{h_1 h_2 p_1 p_2}}. \tag{3.113}
\end{aligned}$$

Integrating and taking the limit  $s \rightarrow \infty$ , we obtain the fourth-order energy correction

$$\begin{aligned}
E^{[4]}(\infty) &= \frac{1}{2} \sum_{ph} \bar{\eta}_{hp}^{[2]} \bar{f}_{ph}^{[2]} + \frac{1}{8} \sum_{p_1 p_2 h_1 h_2} \bar{\eta}_{h_1 h_2 p_1 p_2}^{[2]} \bar{\Gamma}_{p_1 p_2 h_1 h_2}^{[2]} \\
&+ \frac{1}{72} \sum_{p_1 p_2 p_3 h_1 h_2 h_3} \bar{\eta}_{h_1 h_2 h_3 p_1 p_2 p_3}^{[2]} \bar{W}_{p_1 p_2 p_3 h_1 h_2 h_3}^{[2]} \\
&+ \frac{1}{8} \sum_{p_1 p_2 h_1 h_2} \left[ (\bar{A} - \bar{B})_{h_1 h_2 p_1 p_2} + (\bar{D} - \bar{C})_{h_1 h_2 p_1 p_2} \right] \frac{\bar{\Gamma}_{p_1 p_2 h_1 h_2}^{[1]}}{\Delta_{h_1 h_2 p_1 p_2}} \\
&\equiv E_f^{[4]} + E_\Gamma^{[4]} + E_W^{[4]} + E_A^{[4]} + E_B^{[4]} + E_C^{[4]} + E_D^{[4]}. \tag{3.114}
\end{aligned}$$

In Fig. 3.16, we show all fourth-order Hugenholtz energy diagrams for the canonical HF case (see Sec. 3.5.1 and Ref. [16]). It is a straightforward but arduous task to identify the diagrammatic content of the individual contributions to  $E^{[4]}$  by plugging the expressions for

the amplitudes from the previous sections into (3.114). We find

$$E_f^{[4]} = \frac{1}{2} \sum_{i=1}^4 S_i, \quad (3.115)$$

$$E_\Gamma^{[4]} = \frac{1}{2} \sum_{i=1}^{12} D_i, \quad (3.116)$$

$$E_W^{[4]} = \frac{1}{2} \sum_{i=1}^{16} T_i, \quad (3.117)$$

$$E_A^{[4]} = \frac{1}{2} \left( \sum_{i=1}^4 S_i + \sum_{i=1}^{12} D_i \right), \quad (3.118)$$

$$E_B^{[4]} = Q_3 + Q_4 + Q_5 + \frac{1}{2} (Q_1 + Q_2 + Q_6 + Q_7), \quad (3.119)$$

$$E_C^{[4]} = \frac{1}{2} (Q_1 + Q_2 + Q_6 + Q_7), \quad (3.120)$$

$$E_D^{[4]} = \frac{1}{2} \sum_{i=1}^{16} T_i, \quad (3.121)$$

so  $E^{[4]}(\infty)$  contains all required diagrams, and is indeed the complete fourth-order energy.

### 3.5.7 Discussion

As concluded on general grounds in Sec. 3.5.1, the IM-SRG(2) energy is complete to third order in MBPT, but misses certain contributions in fourth order. Our detailed analysis shows that

$$\begin{aligned} E_{\text{IM-SRG}(2)}^{[4]} &= E_f^{[4]} + E_\Gamma^{[4]} + E_A^{[4]} + E_B^{[4]} \\ &= \sum_{i=1}^4 S_i + \sum_{i=1}^{12} D_i + Q_3 + Q_4 + Q_5 + \frac{1}{2} (Q_1 + Q_2 + Q_6 + Q_7), \end{aligned} \quad (3.122)$$

i.e., IM-SRG(2) contains the complete fourth-order singles and doubles contributions, as well as the symmetric and *half* of the antisymmetric quadruples diagrams shown in Fig. 3.16.

In the discussion of Fig. 3.7 in Sec. 3.3.4, we have observed that the IM-SRG(2) ground-state energy of  $^{40}\text{Ca}$  for the chiral NN Hamiltonian with  $\lambda = 2.0 \text{ fm}^{-1}$  lies between Coupled Cluster results at the CCSD and  $\Lambda\text{-CCSD(T)}$  level [16, 93, 94]. Overall, the three methods agree within a few percent of the total ground-state energy. This pattern has consistently emerged in all our IM-SRG calculations for finite nuclei with softened chiral interactions (resolution scales  $\lambda \sim 2 \text{ fm}^{-1}$ ), both with and without 3N forces [21, 23, 58, 74]. The diagrammatic content of these methods through fourth order explains this behavior, at least qualitatively. In terms of the quantities (3.115)–(3.121) defined in the previous subsection, the fourth-order energy contributions to CCSD and  $\Lambda\text{-CCSD(T)}$  are

$$\begin{aligned} E_{\text{CCSD}}^{[4]} &= E_f^{[4]} + E_\Gamma^{[4]} + E_A^{[4]} + E_B^{[4]} + E_C^{[4]} \\ &= \sum_{i=1}^4 S_i + \sum_{i=1}^{12} D_i + \sum_{i=1}^7 Q_i, \end{aligned} \quad (3.123)$$

and

$$\begin{aligned} E_{\Lambda\text{-CCSD(T)}}^{[4]} &= E_f^{[4]} + E_\Gamma^{[4]} + E_W^{[4]} + E_A^{[4]} + E_B^{[4]} + E_C^{[4]} + E_D^{[4]} \\ &= \sum_{i=1}^4 S_i + \sum_{i=1}^{12} D_i + \sum_{i=1}^{16} T_i + \sum_{i=1}^7 Q_i, \end{aligned} \quad (3.124)$$

respectively. In a typical calculation, CCSD ground-state energies are too high due to missing correlation energy from attractive fourth-order 3p3h (triples) configurations that are included in  $\Lambda\text{-CCSD(T)}$  through  $E_{W,D}^{[4]}$ . In all our calculations, the asymmetric quadruples diagrams  $Q_{1,2,6,7}$  (cf. Fig. 3.16) are repulsive. The IM-SRG(2) misses half of this repulsion, namely

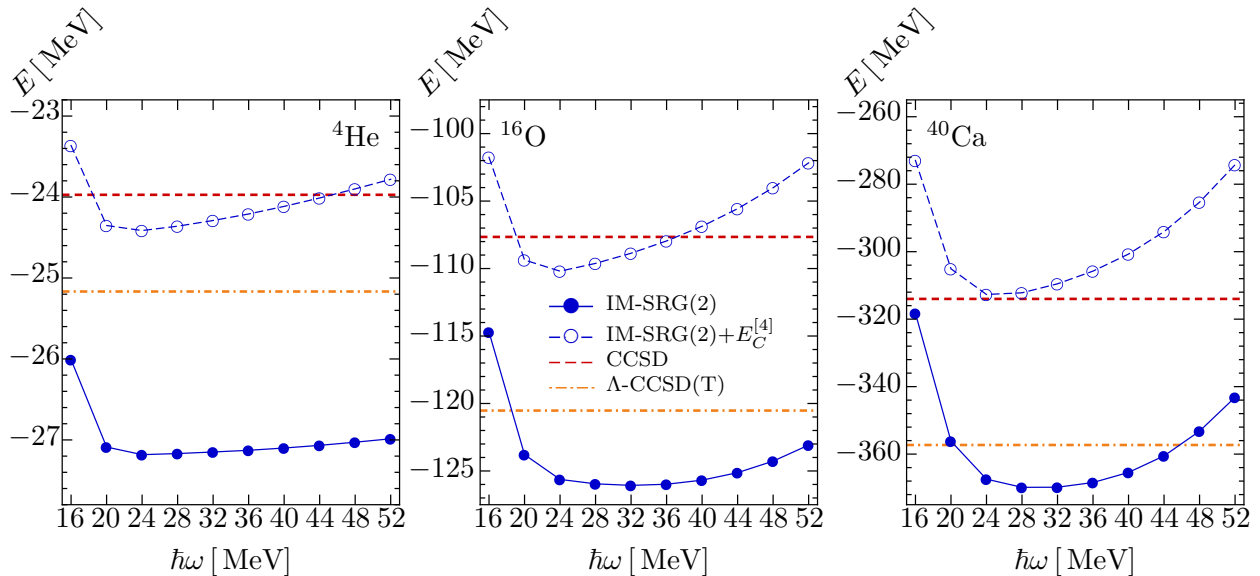


Figure 3.17: Effect of fourth-order quadruples (4p4h) contribution  $E_C^{[4]}$ , Eq. (3.120) on the ground-state energies of  ${}^4\text{He}$ ,  ${}^{16}\text{O}$ , and  ${}^{40}\text{Ca}$  (see text): Comparison of IM-SRG(2) with and without  $E_C^{[4]}$ , calculated with the initial Hamiltonian  $H(0)$ , to CCSD and  $\Lambda$ -CCSD(T). All calculations used the chiral  $\text{N}^3\text{LO}$  Hamiltonian with  $\lambda = \infty$  in an  $e_{\text{max}} = 14$  single-particle basis. The shown CC values were taken at optimal  $\hbar\omega$ .

the  $E_C^{[4]}$  term, and mocks up missing attraction from the triples terms  $E_{W,D}^{[4]}$  in this way.

Let us now consider the implications of our analysis for calculations with the unevolved chiral  $\text{N}^3\text{LO}$  Hamiltonian. Referring back to Fig. 3.7 again, there is a larger variation between the  ${}^{40}\text{Ca}$  ground-state energies from IM-SRG(2), CCSD, and  $\Lambda$ -CCSD(T). This is expected because of the Hamiltonian's higher resolution scale, which adversely affects the many-body convergence. We find an IM-SRG(2) ground-state energy that is lower than that of  $\Lambda$ -CCSD(T), which contains the complete fourth-order energy and is therefore expected to be a better approximation to the exact result from the MBPT point of view. A similar observation was made for  ${}^4\text{He}$  in the first published IM-SRG study [58], where the IM-SRG(2) ground-state energy of  $-27.6$  MeV was found to be about 2 MeV lower than the  $\Lambda$ -CCSD(T) and exact NCSM results. This motivated the development of a perturbative truncation scheme that is discussed in Sec. 3.5.8, but no longer used in practice.

In Fig. 3.17, we show the effect of adding the fourth-order quadruples term  $E_C^{[4]}$  to the IM-SRG(2) ground-state energies of  ${}^4\text{He}$ ,  ${}^{16}\text{O}$ , and  ${}^{40}\text{Ca}$ . In light of our perturbative analysis, especially Eqs.(3.122) and (3.123), it is not surprising that the repulsive contributions from this term shift the ground-state energies in close proximity to the the CCSD results, which are shown for reference. The agreement is not exact due to fifth- and higher-order differences in the perturbative content of IM-SRG(2) and CCSD.

Finally, we want to remark on the different origins of the induced three-body vertices which contribute to  $E_C^{[4]}$  and  $E_D^{[4]}$ , as pointed out in the discussion of Eqs. (3.103) and (3.104) in Sec. 3.5.5. This is relevant for asymmetric truncations of  $H$  and  $\eta$  at different particle rank, and the development of approximations to the full IM-SRG(3) scheme by the selective addition of terms to the IM-SRG(2) flow equations.  $E_C^{[4]}$  is a product of  $\overline{W}^{[2]}$  and the two-body generator, while  $E_D^{[4]}$  is a product of  $\overline{\Gamma}^{[2]}$  and the three-body generator. Thus, it is sufficient to consider only the induced three-body interaction  $W$  to fully include the fourth-order quadruples<sup>3</sup>. A full inclusion of fourth-order triples requires the induced three-body interaction as well as the use of a three-body generator.

### 3.5.8 Perturbative Truncations

As discussed repeatedly throughout this work (see, e.g., Secs. 3.3.4, 3.5.1), order-by-order convergence of a many-body perturbation expansion strongly depends on the resolution scale of the Hamiltonian, and the choice of reference state on which the perturbation series is constructed. This is particularly true for the case of nuclear Hamiltonians [33, 51, 92, 122,

---

<sup>3</sup>In Ref. [121], Evangelista and Gauss have demonstrated that  $E_C^{[4]}$  is not included in a modified CCSD scheme if intermediate terms in the nested commutators are only expanded up to two-body operators. These intermediates correspond to the pieces of  $W$  that are induced by the commutator of two-body operators, hence the mechanism for generating  $E_C^{[4]}$  is very similar in CC and IM-SRG.

123]. Nevertheless, it is worthwhile to attempt and organize the right-hand side of the IM-SRG flow equation — essentially, the  $\beta$  function of the IM-SRG flow (see, e.g., [124, 125]) — in terms of a perturbative expansion, which is a common feature of RG approaches throughout all fields of physics.

Based on the power counting from Eqs. (3.62) and (3.64), an earlier work [58] introduced a perturbative truncation which eliminates terms of  $\mathcal{O}(g^3)$  from the flow equations (3.8)–(3.10):

$$\frac{dE}{ds} = \frac{1}{2} \sum_{abcd} \eta_{abcd} \Gamma_{cdab} n_a n_b \bar{n}_c \bar{n}_d, \quad (3.125)$$

$$\begin{aligned} \frac{df_{12}}{ds} &= \sum_a (1 + P_{12}) \eta_{1a} f_{a2} \\ &+ \sum_{abc} (n_a n_b \bar{n}_c + \bar{n}_a \bar{n}_b n_c) (1 + P_{12}) \eta_{c1ab} \Gamma_{abc2}, \end{aligned} \quad (3.126)$$

$$\begin{aligned} \frac{d\Gamma_{1234}}{ds} &= - \sum_a \{ (1 - P_{12}) f_{1a} \eta_{a234} - (1 - P_{34}) f_{a3} \eta_{12a4} \} \\ &+ \frac{1}{2} \sum_{ab} (1 - n_a - n_b) (\eta_{12ab} \Gamma_{ab34} - \Gamma_{12ab} \eta_{ab34}) \\ &- \sum_{ab} (n_a - n_b) (1 - P_{12}) (1 - P_{34}) \eta_{b2a4} \Gamma_{a1b3}. \end{aligned} \quad (3.127)$$

We will refer to this truncation scheme as IM-SRG(2') in the following<sup>4</sup>.

The integration of the IM-SRG(2') flow equation yields a third-order complete energy, while certain contributions from fourth order onward are missing. Using the same definitions

---

<sup>4</sup> (Note that the labeling was reversed in Ref. [58], which primarily used this perturbative truncation scheme for numerical calculations.)

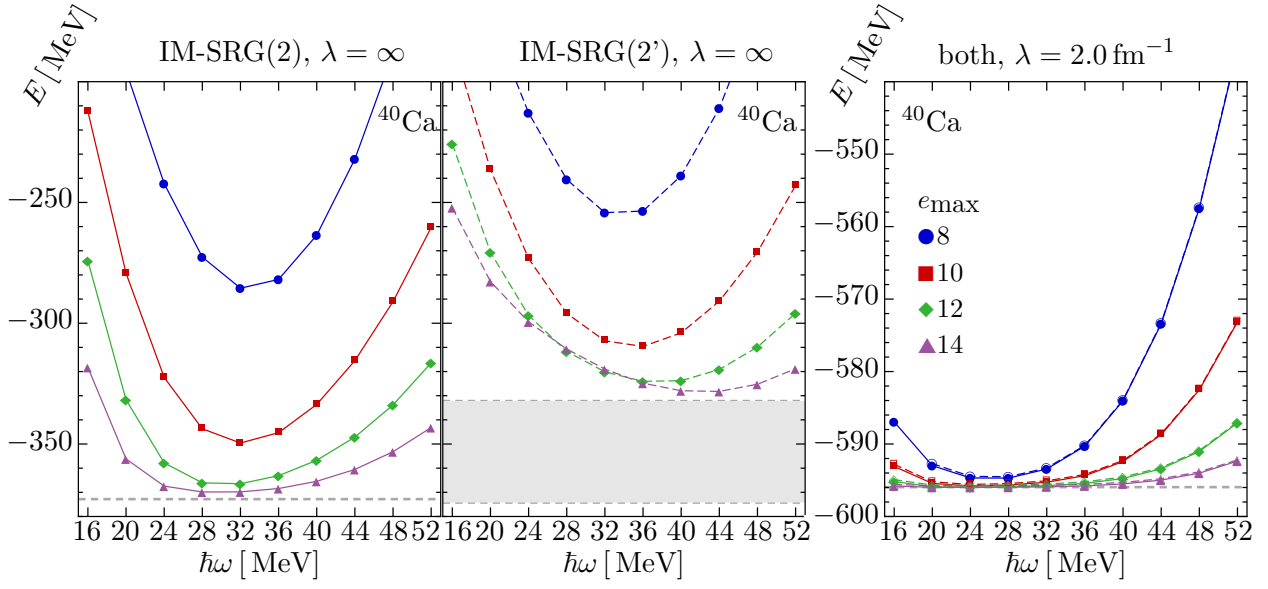


Figure 3.18: Comparison of  $^{40}\text{Ca}$  ground-state energies of the regular IM-SRG(2) (solid lines) and perturbative IM-SRG(2') truncations (dashed lines). The default White generator  $\eta^{\text{IA}}$ , Eq. (3.23), was used in both cases. The interaction is the chiral  $\text{N}^3\text{LO}$  potential with  $\lambda = \infty$  (left and center panels) and  $\lambda = 2.0 \text{ fm}^{-1}$  (right panel), respectively. The dashed lines indicate extrapolated energies. For the IM-SRG(2') truncation, the shaded area indicates the variation from using different data sets for the extrapolation (see text).

as in Eq. (3.114), we find that

$$\begin{aligned}
 E_{\text{IM-SRG}(2')}^{[4]} &= E_{\Gamma}^{[4]} + (E_A^{[4]} - E_f^{[4]}) + E_B^{[4]} \\
 &= \sum_{i=1}^{12} D_i + Q_3 + Q_4 + Q_5 + \frac{1}{2} (Q_1 + Q_2 + Q_6 + Q_7), \quad (3.128)
 \end{aligned}$$

i.e., the IM-SRG(2') does not contain the fourth-order singles contribution. This is caused by the absence of the single-particle term in the energy flow equation (3.125), and the diagrams  $A_1$  and  $A_2$  from the amplitude  $\bar{A}$  (see Fig. 3.15 and Eq. (3.99)).

In Fig. 3.18, we compare  $^{40}\text{Ca}$  ground-state energies obtained with the regular and perturbative truncations. For the soft  $\text{N}^3\text{LO}$  interaction with  $\lambda = 2.0 \text{ fm}^{-1}$ , shown in the right panel, the two truncations give almost identical results. The agreement between ground-state energies is on the level of  $10^{-4}$  or better, with extrapolated energies for  $^{40}\text{Ca}$  differing

by only 2 keV.

For the bare interaction, on the other hand, the truncation schemes behave quite differently. The IM-SRG(2) ground-state energy has a quasi-variational convergence pattern, which allows us a stable extrapolation to infinite HO basis size. The IM-SRG(2') truncation's ground-state energy minimum is still moving to larger  $\hbar\omega$  for the considered bases, indicating a lack of UV convergence, and the variational pattern breaks down as we increase  $e_{\max}$  from 12 to 14. Extrapolation from different subsets of the calculated energies using Eq. (3.51) produces large uncertainties which are indicated by the shaded band in Fig. 3.18.

As discussed above, the IM-SRG(2') ground-state energy, Eq. (3.128), does not contain the fourth-order singles. In Fig. 3.19, we demonstrate that the omission of this contribution accounts for the bulk of the energy difference between IM-SRG(2) and IM-SRG(2'), using  $^{40}\text{Ca}$  as an example. Moreover, the addition of the fourth-order singles restores the variational behavior of the ground-state energy as a function of the single-particle basis size  $e_{\max}$ . Compared to the regular IM-SRG(2), the IM-SRG(2') flow equations lack  $\mathcal{O}(g^3)$  contractions of  $f$  and  $\Gamma$  with the two- and one-body parts of  $\eta$ , respectively. The effect of this omission on the two-body matrix element is hard to analyze in greater detail, in part due to their sheer number. To test the impact of the missing terms on the flowing one-body Hamiltonian, we calculate the Baranger effective single-particle energies (ESPEs) by diagonalizing the final  $f(\infty)$  in both truncations (see [126–128]). The neutron and proton  $sd$ - and  $pf$ -shell ESPEs in  $^{40}\text{Ca}$  are shown in Fig. 3.20, and we find that the results obtained with IM-SRG(2) and IM-SRG(2') are practically indistinguishable.

We conclude by following up on the perturbative analysis of the difference between IM-SRG(2) and CC results with the unevolved chiral  $\text{N}^3\text{LO}$  Hamiltonian that was begun in Sec. 3.5.7. In Ref. [58], the overestimation of the  $^4\text{He}$  ground-state energy in IM-SRG(2) cal-

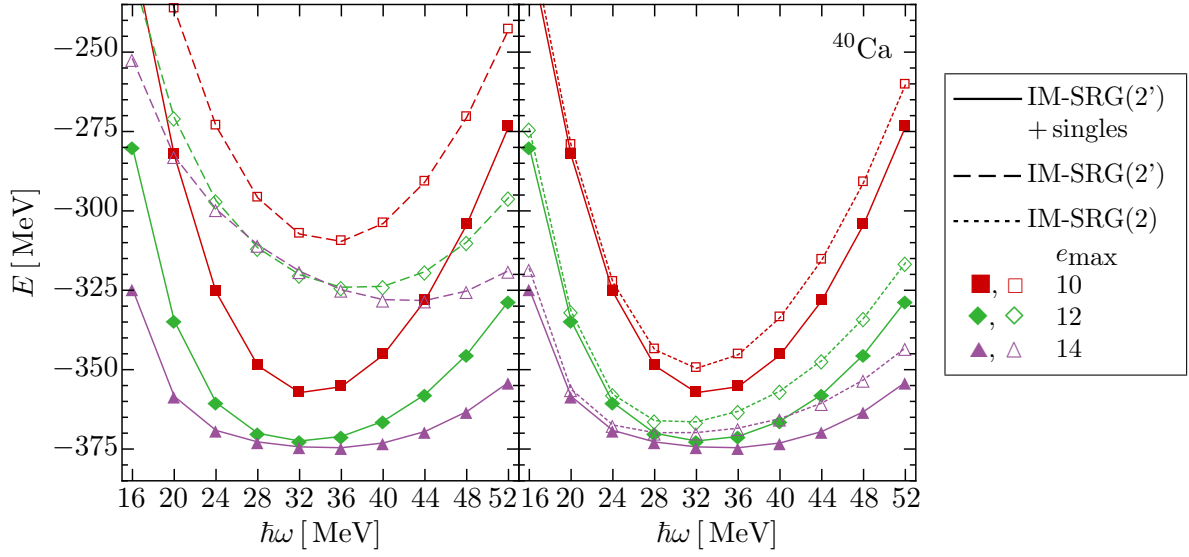


Figure 3.19: Effect of adding the fourth-order singles (1p1h) contribution (cf. Eqs. (3.115), (3.118) and (3.128)) to the IM-SRG(2') ground-state energy of  $^{40}\text{Ca}$  (see text). The singles contributions for different  $\hbar\omega$  were calculated with the initial Hamiltonian  $H(0)$ . All shown results were obtained for the chiral  $\text{N}^3\text{LO}$  Hamiltonian with  $\lambda = \infty$ .

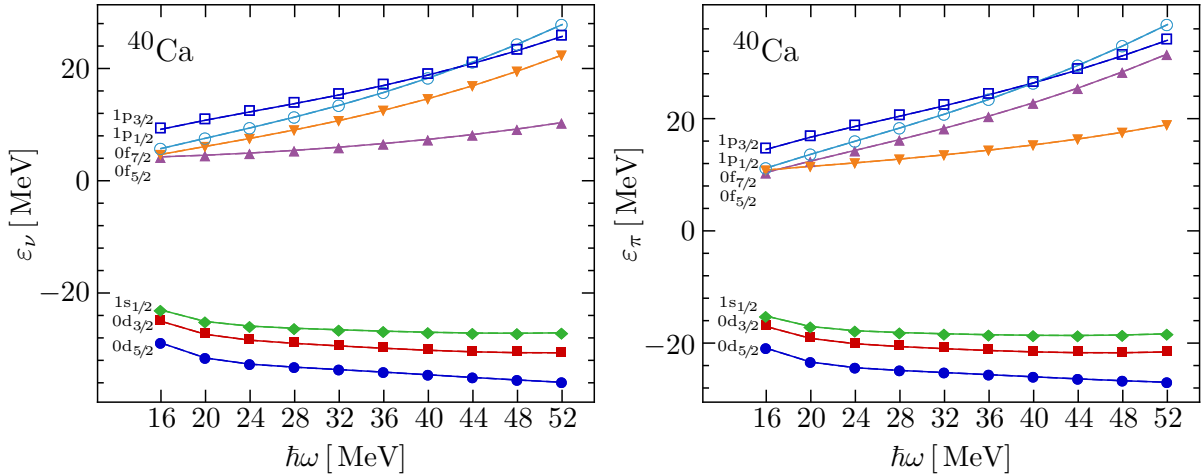


Figure 3.20: Effective neutron (left panel) and proton (right panel) single-particle energies of  $^{40}\text{Ca}$  from IM-SRG(2) (solid lines) and IM-SRG(2') (dashed lines) calculations using the chiral  $\text{N}^3\text{LO}$  interaction with  $\lambda = \infty$  in an  $e_{\text{max}} = 14$  single-particle basis.

culations when compared to  $\Lambda$ -CCSD(T) and exact NCSM results was the main motivation for the investigation of the IM-SRG(2') truncation. The IM-SRG(2') result closely matches

the CCSD result for  ${}^4\text{He}$ ,  $-23.98$  MeV, but the present discussion reveals this agreement as accidental, an artifact of the omission of attractive fourth-order singles producing a similar change in the ground-state energy as the addition of the repulsive quadruples term  $E_C^{[4]}$  (see the discussion in Sec. 3.5.7). While both truncations work equally well for sufficiently soft, perturbative nuclear Hamiltonians, the IM-SRG(2) truncation remains well-behaved at higher resolution scales, at the same computational cost, which is why we favor this truncation scheme in practical applications.

# Chapter 4

## Magnus Formulation

### 4.1 Introduction

Chapter 3 demonstrated the effectiveness of the IM-SRG(2) method for ground state calculations of nuclei at (sub)shell closures. However, we now need to address the primary computational limitations of the method as it was presented. The IM-SRG calculations presented in chapter 3 typically use ODE solvers based on high-order Runge-Kutta or predictor-corrector methods to solve Eq. 3.2. The use of these high-order methods is essential as the accumulation of time-step errors will destroy the unitary equivalence between  $H(s)$  and  $H(0)$ , even if no truncations are made in the flow equations. State-of-the-art solvers can require the storage of 15-20 copies of the solution vector in memory, which becomes problematic for large model spaces. For example, a typical Oxygen calculation in a basis set corresponding to an  $e_{max}$  of 12, IM-SRG(2) calculations require around 30 GB to run. This large memory footprint is exacerbated if one wants to calculate additional observables, roughly doubling the memory requirements assuming the same NO2B truncation as for the Hamiltonian. Moreover, the additional flow equations for each observable can evolve with rather different timescales than the Hamiltonian, which increase the likelihood of the ODEs becoming stiff. In this chapter, we will demonstrate that these difficulties can be circumvented by recasting Eq. (3.2) with the Magnus expansion[129]. The new formulation is convenient for establishing improved truncations to be discussed in chapter 5. The presentation follows a recent publication in

Ref. [130].

## 4.2 Formalism

In the notation of our present problem, our starting point is the differential equation obeyed by the unitary transformation,

$$\frac{dU(s)}{ds} = -\eta(s)U(s), \quad (4.1)$$

where  $U(0) = 1$  and  $U^\dagger(s)U(s) = U(s)U^\dagger(s) = 1$ . This can be formally integrated and written as the time-ordered exponential

$$U(s) = T_s \left\{ e^{-\int_0^s \eta(s') ds'} \right\} \quad (4.2)$$

$$\equiv 1 - \int_0^s ds' \eta(s') + \int_0^s ds' \int_0^{s'} ds'' \eta(s') \eta(s'') + \dots \quad (4.3)$$

Eq. 4.3 is not very useful in practical calculations since i) there is no guidance on how the series should be truncated, ii) one would need to store  $\eta$  for multiple  $s$ -values, and iii) it is not obvious how to consistently transform the Hamiltonian and other observables in a fully linked, size-extensive manner with the truncated series.

The essence of the Magnus expansion is that, given a few technical requirements on  $\eta(s)$ , a solution to Eq. 4.1 of the form

$$U(s) = e^{\Omega(s)} \quad (4.4)$$

exists, where  $\Omega^\dagger(s) = -\Omega(s)$  and  $\Omega(0) = 0$  [131]. In most previous applications of the

Magnus expansion, one typically expands  $\Omega(s)$  in powers of  $\eta(s)$  as

$$\Omega = \sum_{n=1}^{\infty} \Omega_n. \quad (4.5)$$

Combining this with the exact derivative

$$\begin{aligned} \frac{d\Omega}{ds} &= \sum_{k=0}^{\infty} \frac{B_k}{k!} ad_{\Omega}^k(\eta) \\ ad_{\Omega}^0(\eta) &= \eta \\ ad_{\Omega}^k(\eta) &= [\Omega, ad_{\Omega}^{k-1}(\eta)], \end{aligned} \quad (4.6)$$

where  $B_k$  are the Bernoulli numbers and  $ad_{\Omega}^k(\eta)$  the recursively defined nested commutators, one can obtain explicit expressions for the  $\Omega_n(s)$ ,

$$\begin{aligned} \Omega_1(s) &= - \int_0^s ds_1 \eta(s_1) \\ \Omega_2(s) &= \frac{1}{2} \int_0^s ds_1 \int_0^{s_1} ds_2 [\eta(s_1), \eta(s_2)] \\ &\vdots \end{aligned} \quad (4.7)$$

As expected, rewriting the time-ordered exponential as a true matrix exponential moves the complications of time ordering into the expression for  $\Omega(s)$ . The utility of the Magnus expansion lies in the fact that, even if  $\Omega$  is truncated to low-orders in  $\eta$ , the resulting transformation in Eq. 4.4 using the approximate  $\Omega$  is unitary, in contrast to any truncated version of Eq. 4.2.

For large-scale IM-SRG calculations, the expressions in Eq. 4.7 are of limited value since they require the storage of  $\eta(s)$  over a range of  $s$ -values. Therefore, in the present work we

instead construct  $\Omega(s)$  by numerically integrating Eq. 4.6, subject to certain approximations discussed below. The transformed Hamiltonian, and any other operator of interest, can then be constructed by applying the Baker-Cambell-Hausdorff (BCH) formula,

$$H(s) = e^{\Omega} H e^{-\Omega} = \sum_{k=0}^{\infty} \frac{1}{k!} ad_{\Omega}^k(H) \quad (4.8)$$

$$O(s) = e^{\Omega} O e^{-\Omega} = \sum_{k=0}^{\infty} \frac{1}{k!} ad_{\Omega}^k(O). \quad (4.9)$$

### 4.3 Analytical Model

Before discussing how we truncate Eqs. 4.6 and 4.8 in practical calculations, it is instructive to study a simple matrix model that can be solved without any truncations. Consider the initial Hamiltonian

$$H = T + V = \begin{pmatrix} 1 & 1 \\ 1 & -1 \end{pmatrix}, \quad (4.10)$$

where the diagonal “kinetic energy” term is

$$T = \begin{pmatrix} 1 & 0 \\ 0 & -1 \end{pmatrix}. \quad (4.11)$$

Let us now try to diagonalize  $H$  using the Wegner generator presented in chapter 3, making  $\eta(s) = [T, H(s)]$ , solving the SRG equations using the Magnus expansion and by direct integration of Eq. 3.2. Note that for this choice of initial  $H$ , both  $\eta(s)$  and  $\Omega(s)$  are real,

antisymmetric matrices throughout the flow

$$\eta(s) = ig_\eta(s)\sigma_2 \quad (4.12)$$

$$\Omega(s) = ig_\Omega(s)\sigma_2, \quad (4.13)$$

where  $\sigma_2$  is the Pauli matrix. Consequently, Eq. 4.6 terminates at the first term and Eq. 4.8 can be summed up to all orders using the well-known properties of Pauli matrices. This simplicity also allows for an analytical solution for  $H(s) = g_T(s)T + g_V(s)V$ , where

$$g_T(s) = \sqrt{2}\tanh(\sqrt{32}s + \operatorname{arcsinh}(1)) \quad (4.14)$$

$$g_V(s) = \sqrt{2}\operatorname{sech}(\sqrt{32}s + \operatorname{arcsinh}(1)). \quad (4.15)$$

The large memory footprint of high-order adaptive solvers is the main computational challenge in large-scale SRG calculations, so in addition to using a Gordon-Shampine integrator to solve Eqs. 3.2, we demonstrate what happens when a naive first-order Euler method is used to integrate Eqs. 3.2 and 4.6. The results are shown in Fig. 4.1, where we plot  $|H_{11}(s) - E_{gs}|$  – which should go to zero at large  $s$  – versus  $s$  for different Euler step sizes  $\delta s$ . Unsurprisingly, we see that the direct integration of Eq. 3.2 accumulates large time-step errors, with the plateaus at large  $s$  displaying a strong dependence on the Euler step size. Even when Eq. 3.2 is integrated with a high-order method with very conservative absolute and relative tolerances of  $1e-12$ , the solution fails to produce the exact answer. The Magnus solution, on the other hand, converges to a final answer at large  $s$  that is independent of step size and agrees with the exact result to within machine precision. Even more, the naive Euler step with  $\delta s = .001$  is indistinguishable from the analytical result. The insensitivity

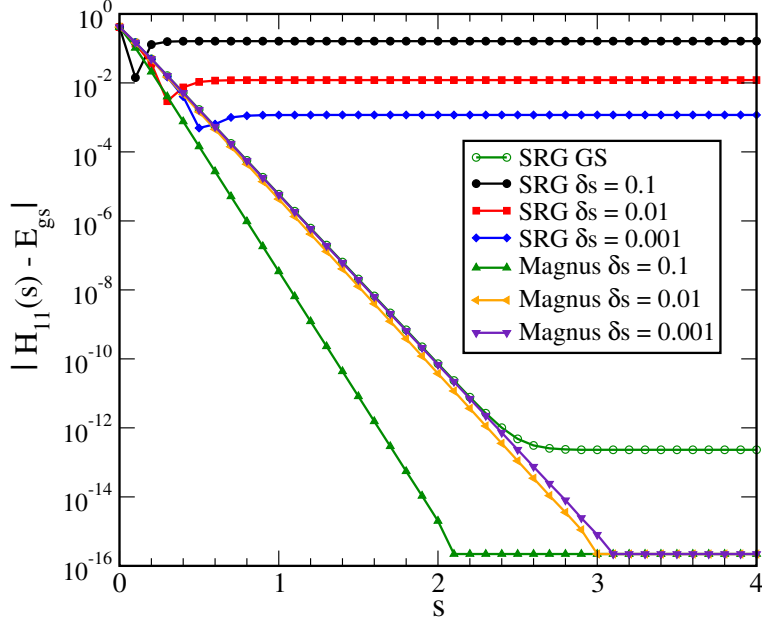


Figure 4.1:  $|H_{11}(s) - E_{gs}|$  versus  $s$  for different Euler step sizes calculated via direct integration of the SRG flow equation, Eq. 3.2, and using the Magnus expansion, Eqs. 4.6 and 4.8. Also plotted is the integration of Eq. 3.2 with the Gordon-Shampine integrator.

to the time step size is due to the fact that while each Euler step in Eq. 4.6 gives an error of order  $\mathcal{O}(\delta s^2)$ , the exponentiated operator at the end of the evolution is still unitary. This is the primary advantage of the Magnus expansion; by reformulating the problem to solve flow equations for  $\Omega(s)$  instead of  $H(s)$ , one can use a simple first-order Euler method and dramatically reduce memory usage. Once  $\Omega(s)$  is in hand, the transformation of  $H(s)$  and any other observables of interest immediately follows from Eq. 4.8. Note that in contrast to the direct integration of Eq. 3.2, the dimensionality of the flow equations does not increase when one evolves additional observables.

## 4.4 MAGNUS(2) Approximation

Having illustrated the advantages of the Magnus expansion in a simple model, we would now like to apply it large-scale many-body calculations. Before going into necessary approximations, it is instructive to highlight how the Magnus formulation of the IM-SRG makes the connection to coupled cluster theory more tangible. We recall from chapter 2 that closed shell coupled cluster theory is centered in the philosophy of decoupling a single reference from higher excitations via a non-hermitian similarity transformed Hamiltonian  $\bar{H} = e^{-T} H e^T$ . The IM-SRG is also based on this same philosophy, but within the Magnus approach, the means of doing so become more transparent. We are now solving the hermitian  $H(s) = e^{\Omega(s)} H e^{-\Omega(s)}$ , which bears more than passing similarity to  $\bar{H}$ .

Unlike in coupled cluster theory where the BCH formula for the similarity transformed Hamiltonian terminates at finite order, both Eqs. 4.6 and 4.8 involve an infinite-order series of nested commutators that generate up to  $A$ -body operators. Thus, to make progress, we introduce the MAGNUS(2) truncation in which all commutators (as well as  $\Omega(s)$ ,  $\eta(s)$  and  $H(s)$ ) are truncated to the NO2B level. Even with this approximation, the expressions for  $d\Omega/ds$  and  $H(s)$  involve an infinite number of terms. However, for both Eqs. 4.6 and 4.8 at the NO2B level, we empirically find that the magnitude of terms decreases monotonically in  $k$  for all systems studied thus far. Therefore, we numerically truncate Eqs. 4.6 at the  $k^{\text{th}}$  term if

$$\left| \frac{B_k \|ad_{\Omega}^k(\eta)\|}{k! \|\Omega\|} \right| < \epsilon_{\text{deriv}}. \quad (4.16)$$

For the truncation of (4.8), we could use a similar criteria as for the derivative expression. However, since we are interested in the ground-state energy, we use a simpler condition where

the series is truncated when the zero-body piece of the  $k^{\text{th}}$  term falls below some threshold,

$$\left| \frac{\{ad_{\Omega}^k(H)\}_{0b}}{k!} \right| < \epsilon_{\text{BCH}}. \quad (4.17)$$

In the calculations presented below, we will find that the final results are insensitive to large variations in  $\epsilon_{\text{deriv}}$  and  $\epsilon_{\text{BCH}}$ , which we take as an *a posteriori* justification for our truncations.

## 4.5 Hamiltonians and Implementation

Before presenting the results of IM-SRG(2) and MAGNUS(2) calculations of the homogeneous electron gas (HEG) and  $^{16}\text{O}$ , we review some details of our implementations for both systems. For the homogeneous electron gas, we perform our calculations for the closed-shell configuration of  $N = 14$  electrons in a cubic box with periodic boundary conditions. Note that if one is interested in extrapolating to the thermodynamic limit, calculations should be done for a larger closed-shell configurations of  $N = 38, 54, 66, \dots$  electrons, with finite-size corrections for the kinetic and potential energy taken into account. Here we neglect these corrections since our primary purpose is to demonstrate the effectiveness of the Magnus expansion, and the quasi-exact Full Configuration Interaction Quantum Monte Carlo (FCIQMC) results we compare against also neglect these corrections [3]. The relevant single particle orbitals are plane waves with quantized momenta

$$\psi_{\mathbf{k}\sigma}(\mathbf{r}) = \frac{1}{\sqrt{L^3}} e^{i\mathbf{k}\cdot\mathbf{r}} \chi_{\sigma}, \quad (4.18)$$

where  $L^3$  is the box volume,  $\chi_\sigma$  is a spin eigenfunction, and  $\mathbf{k} = \frac{2\pi}{L}(n_x, n_y, n_z)$  where  $n_x, n_y$ , and  $n_z$  are integers. We follow common practice and use the Wigner-Seitz radius to characterize the density of the HEG,

$$r_s = \frac{r_0}{a_0}, \quad (4.19)$$

where  $a_0$  is the Bohr radius and  $r_0$  is defined in terms of the density as

$$\frac{4}{3}\pi r_0^3 = \frac{N}{L^3}. \quad (4.20)$$

We use a basis set truncation which keeps  $M$  single particle states with energy less than some cutoff  $E_c$ , although other choices are possible [132].

In the plane wave basis, the kinetic energy matrix elements are diagonal

$$T_{i,j} = \frac{1}{2}\mathbf{k}_i^2 \delta_{ij}, \quad (4.21)$$

and the Coulomb matrix elements are given by

$$V_{ijkl} = \frac{1}{L^3} \frac{1}{q^2} \delta_{\sigma_i, \sigma_k} \delta_{\sigma_j, \sigma_l} \delta_{\mathbf{q}, \mathbf{k}_i - \mathbf{k}_k} \delta_{\mathbf{q}, \mathbf{k}_l - \mathbf{k}_j}. \quad (4.22)$$

Note that the  $\mathbf{q} = 0$  term is omitted due to its cancellation against the inert, uniform positively charged background that is needed to make the system charge neutral [133]. Since we are interested primarily in the correlation energy, we have omitted the Madelung term in all of our calculations.

For the calculations of  $^{16}\text{O}$ , our starting point is the intrinsic nuclear  $A$ -body Hamiltonian

$$H = \left(1 - \frac{1}{A}\right)T + T^{(2)} + V^{(2)}, \quad (4.23)$$

where  $T^{(2)}$  is the two-body part of the intrinsic kinetic energy, and we restrict our attention to two-nucleon interactions only. Results are presented for input NN interactions derived from the  $\text{N}^3\text{LO}$  (500 MeV) potential of Entem and Machleidt [17] at several different free-space SRG resolution scales,  $\lambda = 2.0, 2.7,$  and  $3.0 \text{ fm}^{-1}$ .

In both MAGNUS(2) and IM-SRG(2) calculations, we start by normal ordering the Hamiltonian with respect to the HF ground state. In the case of the HEG, translational invariance implies the HF orbitals are plane waves. Therefore, the HF reference state is just a Slater determinant comprised of the lowest energy doubly occupied plane wave states for  $N = 14$  electrons. For  $^{16}\text{O}$ , we must self-consistently solve the Hartree-Fock equations by expanding the unknown HF orbitals in a harmonic oscillator basis truncated to oscillator states obeying  $2n + l \leq e_{\text{max}}$ , where  $e_{\text{max}}$  is sufficiently large so that the results are approximately independent of the  $\hbar\omega$  value of the underlying oscillator basis. For the NN interactions used in the present calculations, a cutoff of  $e_{\text{max}} = 8$  is sufficiently large for most purposes. Once a converged HF ground-state is obtained, the Hamiltonian is normal-ordered w.r.t. to this solution, and the resulting in-medium zero-, one-, and two-body operators serve as the initial values for the MAGNUS(2) and IM-SRG(2) flow equations. These are subsequently integrated until sufficient decoupling is achieved, as determined by the size of the second-order many-body perturbation theory MBPT(2) contribution of the flowing Hamiltonian  $H(s)$  to the ground state energy. We use a threshold of  $10^{-6}$  Hartree (MeV) for the HEG ( $^{16}\text{O}$ ) calculations, respectively, which corresponds to relative changes in the flowing ground-state

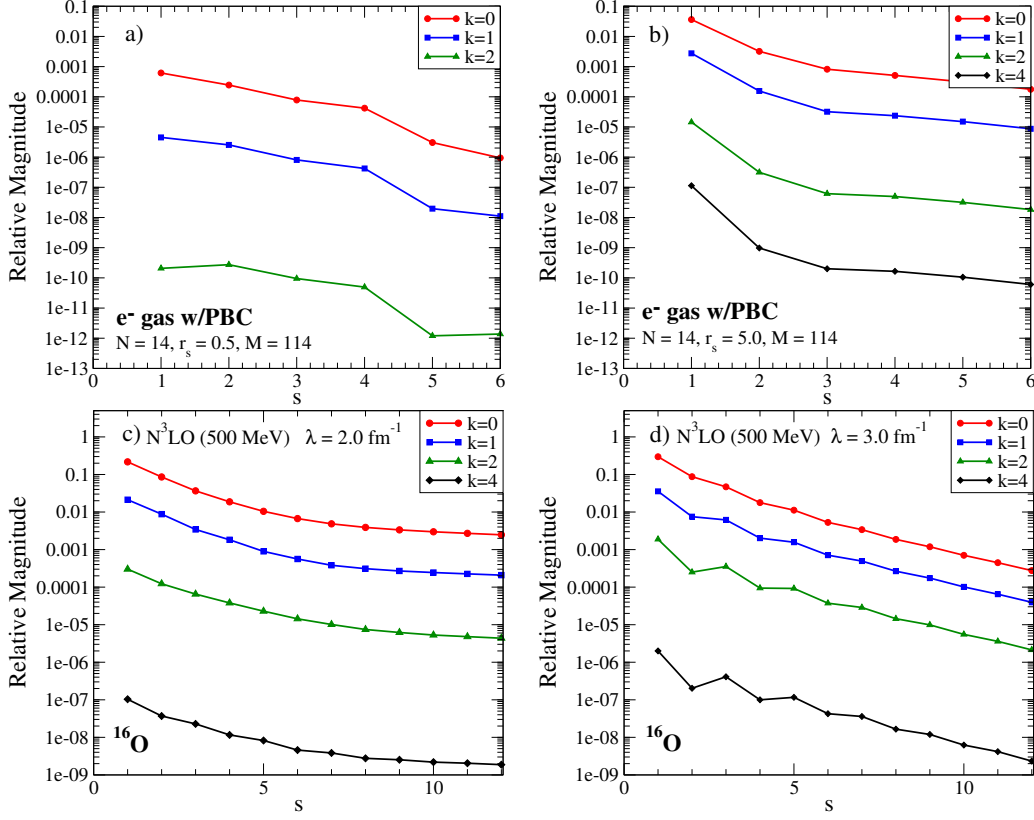


Figure 4.2: Relative importance of the  $k^{\text{th}}$  term in the Magnus derivative as defined by the lefthand side of Eq. 4.16 evaluated in the NO2B approximation. The top row is for the homogeneous electron gas at Wigner-Seitz radii of a)  $r_s = 0.5$  and b)  $r_s = 5.0$ . The bottom row is for  $^{16}\text{O}$ , starting from the chiral NN potential of Entem and Machleidt [17], softened by a free-space SRG evolution to (c)  $\lambda = 2.0 \text{ fm}^{-1}$  and (d)  $\lambda = 3.0 \text{ fm}^{-1}$ . The electron gas calculations were done for  $N = 14$  electrons in a periodic box with  $M = 114$  single particle orbitals. The  $^{16}\text{O}$  calculations were done in an  $e_{max} = 8$  model space, with  $\hbar\omega = 24 \text{ MeV}$  for the underlying harmonic oscillator basis.

energy of  $10^{-7}$  or less for both systems.

## 4.6 Results

We begin by examining the numerical evidence for truncating Eqs. 4.6 and 4.8 by hand. In Figure 4.2, we plot the lefthand side of Eq. 4.16 for the HEG (top row) and  $^{16}\text{O}$  (bottom row) as a function of the flow parameter. To assess the role of correlations, the HEG calculations were performed at two different Wigner-Seitz radii,  $r_s = 0.5$  and  $r_s = 5.0$ , and the  $^{16}\text{O}$

calculations were done using NN interactions at two different resolution scales,  $\lambda = 2.0 \text{ fm}^{-1}$  and  $\lambda = 3.0 \text{ fm}^{-1}$ . For the HEG, the  $r_s = 0.5$  contributions are completely negligible by the  $k = 2$  term, which is not surprising since the kinetic energy dominates in this weakly correlated high-density regime [133]. Even for the  $r_s = 5.0$  case, where correlations and non-perturbative effects start to become sizable, one finds that the successive terms in Eq. 4.6 decrease monotonically, though the individual terms are substantially larger than for the  $r_s = 0.5$  case. Analogous results are found for  $^{16}\text{O}$ ; the individual terms are larger for the harder  $\lambda = 3.0 \text{ fm}^{-1}$  interaction since the system is more strongly correlated, but they systematically decrease with increasing order  $k$ .

Figure 4.3 tells a similar story for the BCH formula, where the lefthand side of Eq. 4.17 is plotted as a function of the flow parameter. In all cases, we see the importance of successive terms decreases monotonically. Reassuringly, we find that the final results in our calculations are essentially independent of the convergence criteria provided  $\epsilon_{\text{deriv}} \lesssim 10^{-4}$  and  $\epsilon_{\text{BCH}} \lesssim 10^{-4}$ , where the latter is in units of Hartree (MeV) for the HEG ( $^{16}\text{O}$ ) calculations, respectively. For instance, raising both convergence criteria from  $10^{-8}$  to  $10^{-4}$  changes the ground state energy at the 1 eV ( $10^{-7}$  Hartree) level in the  $^{16}\text{O}$  (HEG) calculations, respectively.

As was illustrated for the toy model in Sec. 4.2, the key advantage of the Magnus expansion is that one can use a first-order Euler method to accurately solve the flow equations. We now demonstrate that the same conclusion holds for realistic IM-SRG calculations. Referring to Figs. 4.4 and 4.5, we show the 0-body part of the flowing Hamiltonian  $H(s)$  versus the flow parameter for the electron gas<sup>1</sup> and  $^{16}\text{O}$ . The black solid lines denote the results of a standard IM-SRG(2) calculation using the adaptive ODE solver of Shampine and Gordon,

---

<sup>1</sup>For the HEG, we plot  $E_0(s) - E_{HF}$ , which approaches the correlation energy at large  $s$ .

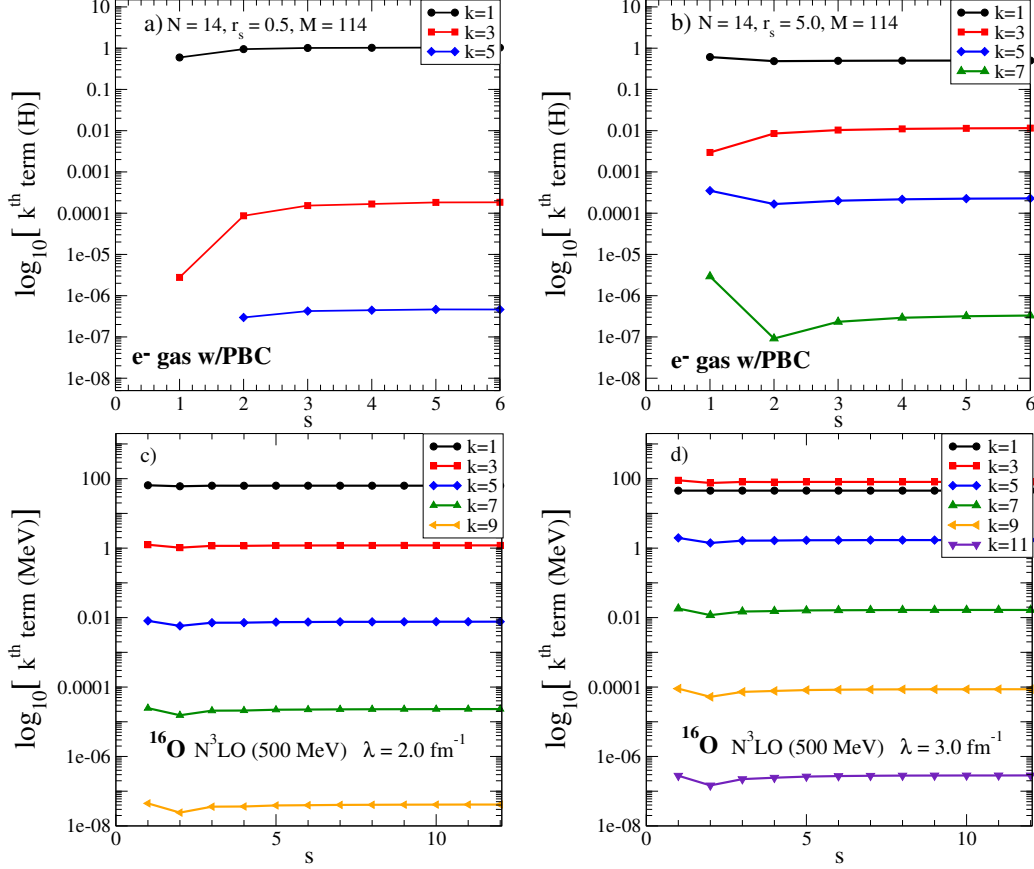


Figure 4.3: Magnitude of the 0-body contributions of the  $k^{\text{th}}$  term in Eq. 4.8 evaluated in the NO2B approximation. The top row is for the electron gas at Wigner-Seitz radii of (a)  $r_s = 0.5$  and (b)  $r_s = 5.0$ . The bottom row is for  $^{16}\text{O}$ , starting from the chiral NN potential of Entem and Machleidt [17], softened by a free-space SRG evolution to (c)  $\lambda = 2.0 \text{ fm}^{-1}$  and (d)  $\lambda = 3.0 \text{ fm}^{-1}$ . The electron gas calculations were done for  $N = 14$  electrons in a periodic box with  $M = 114$  single particle orbitals. The  $^{16}\text{O}$  calculations were done in an  $e_{max} = 8$  model space, with  $\hbar\omega = 24 \text{ MeV}$  for the underlying harmonic oscillator basis.

while the other curves denote IM-SRG(2) and MAGNUS(2) calculations using a first-order Euler method with different step sizes  $\delta s$ . For the electron gas, the exact FCIQMC results [3] are shown for reference. Unsurprisingly, the IM-SRG(2) Euler calculations are very poor, with the various step sizes converging to different large- $s$  limits. The MAGNUS(2) calculations, on the other hand, converge to the same large- $s$  limit in excellent agreement with the standard IM-SRG(2) results. The insensitivity to step size is due to the fact that the time step errors accumulate in  $\Omega(s)$  as opposed to  $H(s)$ . At the end of the flow,  $\Omega(s)$  is still

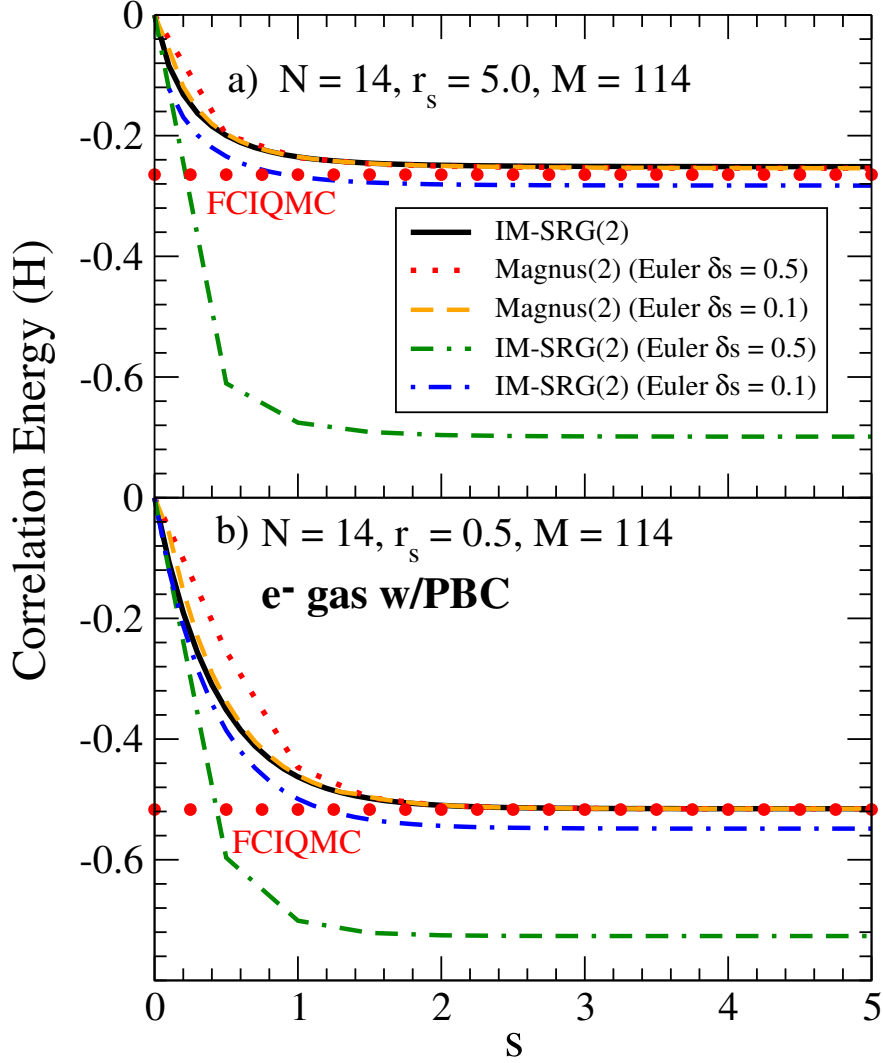


Figure 4.4: Flowing IM-SRG(2) and MAGNUS(2) HEG correlation energy,  $E_0(s) - E_{\text{HF}}$ , for Wigner-Seitz radii of a)  $r_s = 5.0$  and b)  $r_s = 0.5$ . The solid black line corresponds to IM-SRG(2) results using an adaptive solver based on the Adams-Bashforth method, while the other lines correspond to MAGNUS(2) and IM-SRG(2) results using different Euler step sizes. The red circles denote the quasi-exact FCIQMC results of Ref. [3].

an anti-hermitian operator, and the transformation in Eq. 4.8 is unitary, up to truncation errors in the NO2B approximation.

Given that the MAGNUS(2) results are independent of step size over the range considered, one might try to keep increasing the step size to reach the ground state in fewer steps. This unfortunately is not possible, as the flow tends to diverge with too large of a time

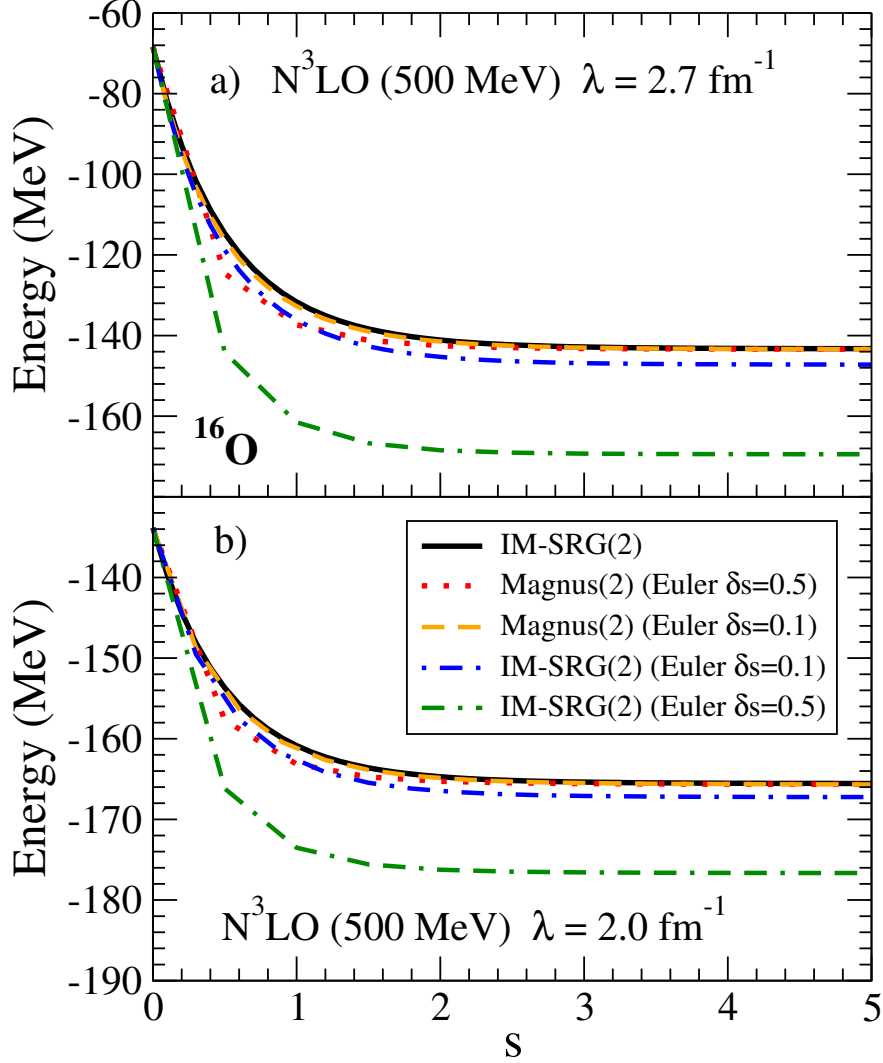


Figure 4.5: Flowing IM-SRG(2) and MAGNUS(2) ground state energy,  $E_0(s)$ , for  $^{16}\text{O}$  starting from the  $\text{N}^3\text{LO}$  NN interaction of Entem and Machleidt [17] evolved by the free-space SRG to a)  $\lambda = 2.7 \text{ fm}^{-1}$  and  $\lambda = 2.0 \text{ fm}^{-1}$ . The solid black line corresponds to IM-SRG(2) results using an adaptive solver based on the Adams-Bashforth method, while the other lines correspond to MAGNUS(2) and IM-SRG(2) results using different Euler step sizes. The calculations were done in an  $e_{max} = 8$  model space, with  $\hbar\omega = 24 \text{ MeV}$  for the underlying harmonic oscillator basis.

step. One of the strengths of the SRG approach is that the transformation is adapted as the Hamiltonian is transformed. With too large of a time step, we rob the method of this flexibility and run the risk of applying a “large rotation” of the Hamiltonian that induces large three- and higher-body components. This would not be a problem if we evaluated the

BCH and Magnus derivative expressions without approximation; the method would find its way back since the large rotation is still unitary if no truncations are made. However, in the MAGNUS(2) approximation we make, the neglect of the induced three- and higher-body terms can lead to a lack of convergence. Empirically, we find that this difficulty is avoided by enforcing that at each time step the “off-diagonal” matrix norm  $\|H^{\text{od}}\|$  is decreasing. This can be implemented by using a simple mid-point integrator algorithm and decreasing the time step if  $\|H^{\text{od}}\|$  has increased between the first and second half of a step.

As a final demonstration of the utility of the Magnus expansion, we turn to the evolution of operators other than the Hamiltonian. In the conventional approach based on the direct integration of Eq. 3.2, the dimensionality of the flow equations increases with each additional operator to be evolved. In contrast, in the Magnus expansion the dimensionality of the flow equations does not change; the additional computational expense shows up only in the evaluation of the BCH formula for the transformed operator, Eq. 4.9. For a given operator  $O$ , we have

$$\langle \Psi_0 | O | \Psi_0 \rangle = \lim_{s \rightarrow \infty} \langle \Phi | e^{\Omega(s)} O e^{-\Omega(s)} | \Phi \rangle, \quad (4.24)$$

where  $|\Phi\rangle$  is the reference state. Therefore, the 0-body piece of the transformed operator approaches the interacting ground state expectation value in the large- $s$  limit.

As a proof-of-principle, we perform a MAGNUS(2) evolution to evaluate the ground state expectation value of the momentum distribution operator  $\hat{n}_{\mathbf{k}} \equiv a_{\mathbf{k}}^\dagger a_{\mathbf{k}}$  for the HEG, and the generalized center of mass (COM) Hamiltonian for the  $^{16}\text{O}$  nucleus,

$$H_{\text{cm}}(\tilde{\omega}) = T_{\text{cm}} + \frac{1}{2} m A \tilde{\omega}^2 R_{\text{cm}}^2 - \frac{3}{2} \hbar \tilde{\omega}. \quad (4.25)$$

Figure 4.6 shows the MAGNUS(2) ground state momentum distribution for a system of  $N =$

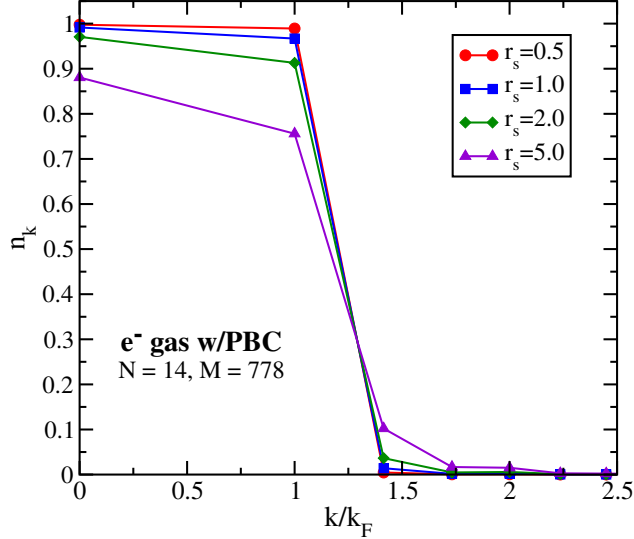


Figure 4.6: Electron gas momentum distributions calculated in the MAGNUS(2) approximation. The calculations were done for  $N = 14$  electrons in a periodic box with  $M = 778$  single particle orbitals.

14 electrons in a periodic box for several different Wigner-Seitz radii. Even with the neglect of finite size corrections and the extremely coarse momentum grid due to the small box sizes considered, the qualitative behavior agrees with expectations for the electron gas; correlations become more important at larger  $r_s$ , leading to a stronger depletion of modes with  $k < k_F$  and smaller discontinuity at the Fermi surface. We note that the MAGNUS(2) results are in good agreement with the IM-SRG(2) calculations based on Eq. 3.2 as well as results generated by the Feynman-Hellman theorem, but at a fraction of the cost. In addition to providing a memory-efficient means for evolving operators beyond the Hamiltonian, Fig. 4.7 shows that the MAGNUS(2) approximation gives a small but robust computational speedup for a range of basis sets, even including the additional effort of generating the momentum distributions, which were not computed in the IM-SRG(2) timings.

For our second illustration of operator evolution, we consider the generalized COM Hamiltonian, Eq. 4.25. In calculations of nuclei, the ground state expectation value of this quan-

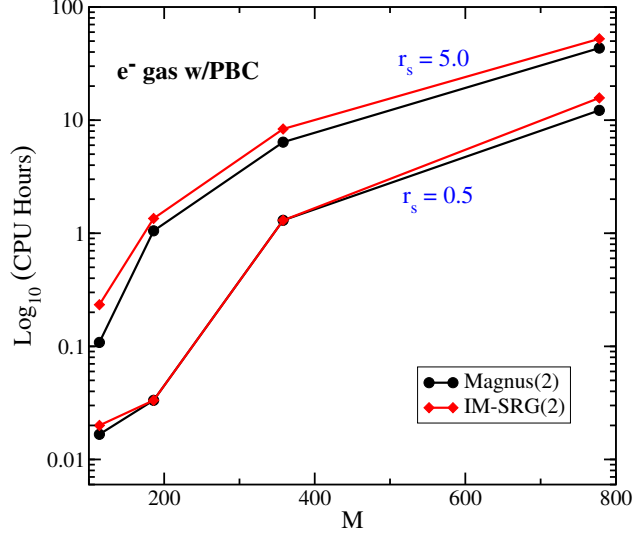


Figure 4.7: Timing for MAGNUS(2) and IM-SRG(2) HEG calculations as the single particle basis is increased. The two bottom curves are for  $r_s = .5$  and the top for  $r_s = 5$ . For the MAGNUS(2) timing, this includes the calculations of the momentum distributions.

tity is useful to diagnose whether approximate solutions of the Schrödinger equation are contaminated by spurious COM motion. Since nuclei are self-bound objects governed by a translationally-invariant Hamiltonian, an exact solution of the Schrödinger equation must factorize into the product of a wave function for the physically relevant intrinsic motion times a wave function for the COM coordinate,

$$|\Psi\rangle = |\psi\rangle_{\text{in}} \otimes |\psi\rangle_{\text{cm}}. \quad (4.26)$$

As is well known, there are two strategies to rigorously guarantee this factorization; one can work in a translationally-invariant basis from the outset, or one can work in a so-called full  $N\hbar\omega$  model space comprised of all  $A$ -particle harmonic oscillator Slater determinants with excitations up to and including  $N\hbar\omega$ . Neither choice is optimal since the former is limited to light nuclei due to the factorial scaling of the required antisymmetrization, while

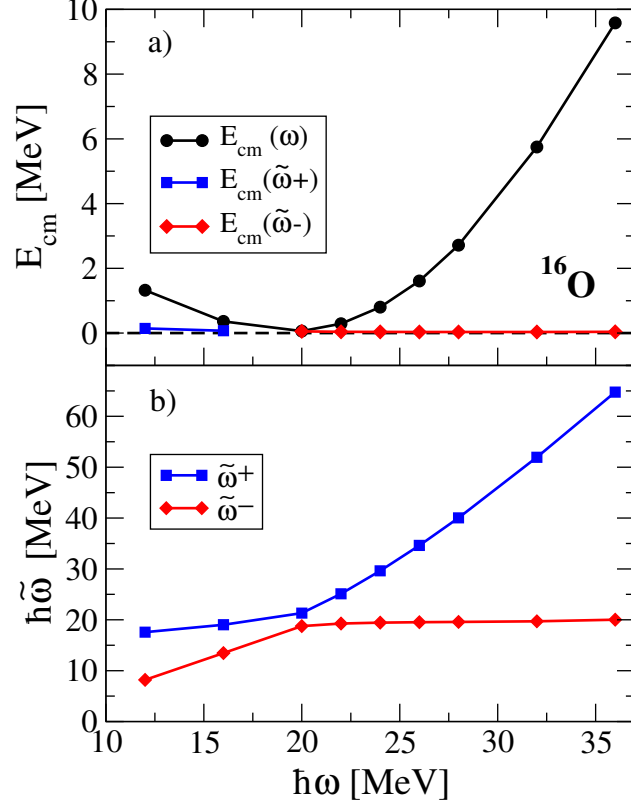


Figure 4.8: Center of mass diagnostics for MAGNUS(2) calculations of  $^{16}\text{O}$  starting from the  $\text{N}^3\text{LO}$  NN interaction of Entem and Machleidt [17] evolved by the free-space SRG to  $\lambda = 2.0 \text{ fm}^{-1}$ . See the text for details. The calculations were done in an  $e_{\text{max}} = 9$  model space.

the latter limits the choice of the single particle orbitals to the harmonic oscillator basis and does not carry over to methods that are capable of reaching heavier nuclei, such as coupled cluster theory and the IM-SRG where it is more natural to define the model space via an energy cutoff (e.g.,  $2n + 1 \leq e_{\text{max}}$ ) on the single particle states. In the case of calculations with an  $e_{\text{max}}$  cutoff, there is no analytical guarantee that the COM and intrinsic wave functions factorize.

In Ref. [18], Hagen and collaborators gave an ingenious prescription to diagnose whether or not Eq. 4.26 is satisfied in such calculations. The basic idea is to assume that the factorized COM wave function is in the ground state of  $H_{\text{cm}}(\tilde{\omega})$  with lowest eigenvalue. Note that  $\tilde{\omega} \neq \omega$

in general, where  $\omega$  is the frequency of the underlying oscillator basis. The prescription to find  $\tilde{\omega}$  involves solving a quadratic equation

$$\hbar\tilde{\omega} = \hbar\omega + \frac{2}{3}E_{\text{cm}}(\omega) \pm \sqrt{\frac{4}{9}(E_{\text{cm}}(\omega))^2 + \frac{4}{3}\hbar\omega E_{\text{cm}}(\omega)}, \quad (4.27)$$

where

$$E_{\text{cm}}(\omega) \equiv \langle \Psi | H_{\text{cm}}(\omega) | \Psi \rangle \quad (4.28)$$

$$= \lim_{s \rightarrow \infty} \langle \Phi | e^{\Omega(s)} H_{\text{cm}}(\omega) e^{-\Omega(s)} | \Phi \rangle \quad (4.29)$$

$$= \lim_{s \rightarrow \infty} \{ e^{\Omega(s)} H_{\text{cm}}(\omega) e^{-\Omega(s)} \}_{0\text{b}}. \quad (4.30)$$

Since there are two roots of Eq. 4.27, we choose the one that gives a smaller value for  $E_{\text{cm}}(\tilde{\omega})$ . Applying this prescription to our calculations of  $^{16}\text{O}$ , we obtain the results shown in Fig. 4.8. In the top panel, we see that the expectation value of the COM Hamiltonian  $H_{\text{cm}}(\omega)$  is approximately zero for  $\omega \approx 20$  MeV, but varies parabolically and becomes rather large away from this point. This suggests that if Eq. 4.26 is satisfied, the frequency of the factorized COM Gaussian should have  $\tilde{\omega} \approx 20$  MeV. This is born out in the bottom panel, where the two roots of Eq. 4.27 are plotted as a function of  $\hbar\omega$ . Picking the root that minimizes  $E_{\text{cm}}(\tilde{\omega})$ , we find that indeed  $\tilde{\omega} \approx 20$  MeV over a wide range of  $\omega$ , and that  $E_{\text{cm}}(\tilde{\omega}) \approx 0$ . Since the excitation energy for the first spurious COM mode is  $\hbar\tilde{\omega} \approx 20$  MeV, while  $E_{\text{cm}}(\tilde{\omega})$  ranges between 0.03-0.14 MeV over the entire range of  $\hbar\omega$ , we conclude that the factorization of COM/intrinsic motion is satisfied to an excellent approximation.

## 4.7 MAGNUS(2) Conclusion

In these simple systems, we have shown that all the utility of IM-SRG(2) calculations in Chapter 3 is available now at significantly decreased cost, with the option of investigating any observable without conducting the full IM-SRG(2) calculation again. We have thus circumvented two of the largest weaknesses of the method, the already mentioned need to solve a large set of differential equations with small errors, and the linear scaling in desired observables. We would now like to address the undercounting of a certain class of diagrams mentioned in 3.5. Within the MAGNUS(2) formulation, we have a fairly straightforward way to proceed with this, which will be presented in Chapter 5.

# Chapter 5

## Approximating the IM-SRG(3)

Having established that the exact solution of the vast majority of many-body problems is beyond the reach of even the most advanced methods in chapter 2, practitioners instead set their aim on finding systematic approximations that, in some limit, approach the complete solution. This philosophy is evident in coupled cluster theory, where one can truncate the cluster operator  $T$  at increasing excitation rank, giving a hierarchy of improved approximations (CCD, CCSD, CCSDT, etc.). Moreover, since truncations beyond the CCSD level can become extremely expensive for larger systems, much effort has gone into the development of computationally cheap non-iterative approximations to these higher truncations. The central aim of the present chapter is to describe how analogous approximations can be constructed in the IM-SRG.

In Chapter 4, we argued that the direct integration of the IM-SRG(2) flow equations in Eq. (3.2) is limited by the large memory demands of the high-order ODE solvers that are needed to control the accumulation of numerical errors. One of the major themes of my thesis is the use of the Magnus expansion to eliminate these difficulties by reformulating the problem so that the set of flow equations to be solved is given by Eq. (4.6). As discussed in Chapter 4, this reformulation, which in the NO2B approximation is deemed MAGNUS(2), can be solved with a simple first-order Euler method and yields a nearly identical transformation as the IM-SRG(2), but with much smaller memory requirements. As a result, the MAGNUS(2) makes it feasible to extend calculations to heavier systems and, more importantly, perform

calculations of other properties besides spectra.

In addition to providing substantial computational improvements, the Magnus formulation provides a particularly transparent path towards developing approximate MAGNUS(3) calculations from converged MAGNUS(2) calculations. The development of such *approximate* NO3B calculations is essential, as the full IM-SRG(3)/MAGNUS(3) methods naively scale as  $n^9$ , which makes them intractable for large-scale calculations. In the present chapter, we will first delve into quantum chemistry type systems to demonstrate the shortcomings of IM-SRG(2) type calculations even with respect to CCSD, despite the fact that they should be naively related to each other. From there, guided by the perturbative analysis of Section 3.5, we will introduce computationally feasible approximations to mitigate these shortcomings. And then finally, we will introduce a family of methods that are analagous to CCSD plus non-iterative approximate triples.

## 5.1 Deficiencies of the IM-SRG(2) in Chemistry

The first application of the IM-SRG(2) to ab-initio many-body calculations, though couched in somewhat different terminology and notation, was carried out by White in treating an H<sub>2</sub>O molecule in a DZP basis set [78]. While the method was more or less abandoned in chemistry systems, though see the related work of Evangelista and collaborators [134] and Chan et al. [79]. An important finding in that first seminal work was that, unlike CCSD which generally underbinds with respect to FCI, IM-SRG(2) produced results that were dramatically overbound at equilibrium and not convergent at even modest bond lengths. This was peculiar, as the scaling and philosophy of the methods are similar.

Pinpointing the failure of the IM-SRG(2) and MAGNUS(2) to produce converged results

in  $\text{H}_2\text{O}$  and other stretched molecules can be guided most easily by the perturbative analysis found in Sec. 3.5. As we have already pointed out, diagrams making up those (3.120) are undercounted by a factor of two in both IM-SRG(2) and MAGNUS(2). These are properly accounted for in CCSD calculations, so initial attempts to resolve non-convergence centered around restoring this content to the transformed Hamiltonian. Evangelista et al. had similar findings when the BCH of traditional coupled cluster is applied via one- and two-body intermediates, as opposed to the full diagrammatic content of the cluster amplitudes found in (2.31)-(2.33) [121]. The lack of these diagrams caused dramatic overbinding with respect to full CCSD in  $\text{H}_2\text{O}$  and similar molecular systems. As discussed in the following and in 3.5, this is also the reason IM-SRG(2)/MAGNUS(2) results track in between CCSD and CCSD(T) calculations for a wide range of closed-shell nuclei, 2D quantum dots, and the homogenous electron gas.

## 5.2 The IM-SRG(2\*) Approximation

In the traditional IM-SRG formalism, it is not straightforward how one might restore the above undercounted terms without storing a full three-body operator, which is a six-index tensor. This is certainly something we wish to avoid, as calculations are often memory limited even with the 15-20 copies of a two-body Hamiltonian. Since these diagrams are found in the IM-SRG(2), but with the wrong weight, maybe it is possible to find a way to re-weight the effect of what is already included without changing the computational cost too much. Indeed, this can be done. Figure 5.1 and Figure 5.2 both show similar third-order contributions to the transformed Hamiltonian, both of which lead to identical fourth order energy contributions. The first is found in IM-SRG(2) calculations, while the second

enters via an intermediate three-body force that one would naively need the IM-SRG(3) to include. A similar attempt at mocking up twice the total effect of diagrams found in Figure 5.1 was made recently by Evangelista in Ref. [134], simply by doubling the prefactor of the derivative to flowing one-body Hamiltonian in Eq. (3.2). While this brought results into good agreement with CCSD at equilibrium, and stabilized convergence for some bond-lengths, it obviously distorts the single-particle spectra. This ad-hoc distortion has some undesirable consequences, particularly if the resulting transformed Hamiltonian is to be used for subsequent applications (e.g., the computation of excited states or a valence shell model Hamiltonian). In the present work, we describe an alternative fix in which, rather than doubling “by hand” the prefactor of the single-particle spectra flow equation, we store the change to the single particle Hamiltonian separately from the transformed Hamiltonian itself. This can be easily accomplished by introducing an auxiliary one-body operator  $\chi$  with the following flow equation,

$$\frac{d\chi_{qr}}{ds} = \frac{1}{2} \sum_{stu} (n_q n_r + \bar{n}_q \bar{n}_r) (n_s n_t \bar{n}_u + \bar{n}_s \bar{n}_t n_u) (1 + P_{qr}) \eta_{uqst} \Gamma_{stur} \quad (5.1)$$

subject to the boundary conditions

$$\chi_{qr}(0) = 0. \quad (5.2)$$

It is then possible to amend the flow equations in the following way

$$\frac{dH(s)}{ds} = [\eta(s), H(s) + \chi(s)]. \quad (5.3)$$

This allows for a direct solution of (3.2) that correctly accounts for all (non-triples) fourth order energy content. We note now, that although the inclusion of  $\chi$  corrects the asymmetric fourth order quadruples diagrams correctly, it is not technically incorrect in the way it corrects the flowing two-body vertex. This can be seen by comparing the resulting contributions to the third-order vertex in Fig. 5.1 and Fig. 5.2, since one has triple contractions between first order generators, and one does not. We will revisit whether this is an advantage or not in Sec. 5.3. Despite this slight discrepancy, this inclusion stabilizes the flow away from equilibrium geometries compared to the naive re-weighting correction in [134]. Since this is not a true three-body IM-SRG, and still scales in the same way as IM-SRG(2), we refer to it as IM-SRG(2\*). Unfortunately, we have not yet discerned a way to keep track of the induced three-body force required to account for a triples type calculation in the direct solution of (3.2). Fortunately though, the main thrust of my thesis work has been the development of the Magnus formulation of the IM-SRG, which offers a more transparent path towards approximating the neglected induced three-body interactions. For this reason, we will not actually present any IM-SRG(2\*) results in this work.

### 5.3 The MAGNUS(2\*) Approximation

The MAGNUS(2) method has the same undercounting of the fourth-order quadruple-excitation diagrams mentioned above, and therefore exhibits the same overbinding and lack of stability for stretched bonds. We now present the analogous MAGNUS(2\*) method that corrects for these undercounted terms. As we will see, it is more natural in the Magnus formulation to approximately correct for terms that are missing or undercounted in the MAGNUS(2) level of truncation.

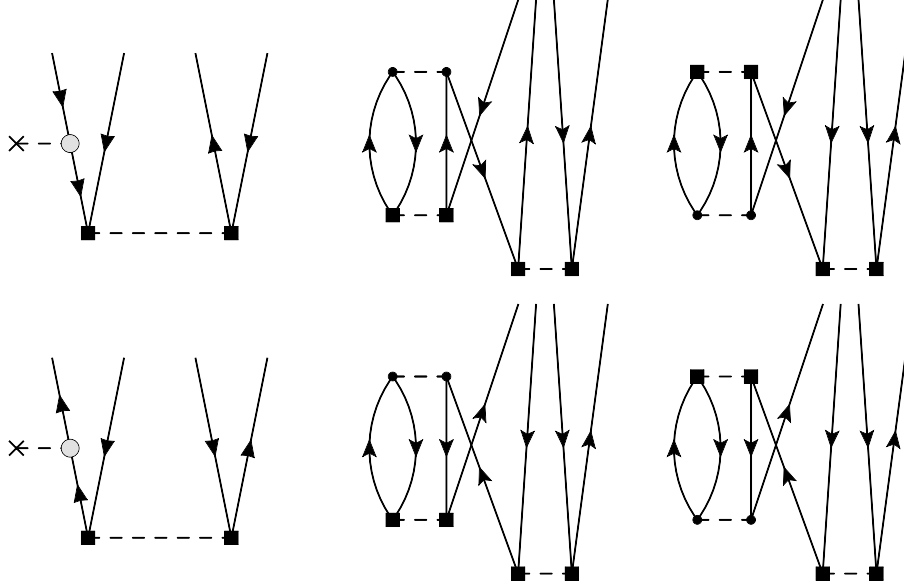


Figure 5.1: The dark circle and square represent the bare Hamiltonian and generator respectively. The light circles in the first column represent the second order 1-body Hamiltonian originating from  $[\eta, H]_{1B}$ . If the second order 1-body vertex is expanded in terms of bare quantities, the 4 asymmetric Goldstone diagrams on the right are the result.

We start by recalling that the Magnus formulation centers around the application of an exponent  $\Omega$  via the Baker-Cambell-Hausdorff expansion in Eq. (4.8). In the MAGNUS(2) approximation, every internal commutator is truncated at the NO2B level. In the diagrams of Figs. 5.1 and 5.2, we can replace the generator  $\eta$  with  $\Omega$ , which shows that the diagrams from internal one- and three- body terms arise from BCH terms  $[\Omega, [\Omega, H]_{1B}]_{2B}$  and  $[\Omega, [\Omega, H]_{3B}]_{2B}$  respectively. We have attempted to restore the diagrams in Fig. 5.2 as they are, but it appears that the effective one-body operator arising from the triple contraction of  $\Omega$  with itself, which appears in the second column of expanded diagrams, generally causes problems at stretched geometries of molecules. In contrast, for nuclear systems we include them as they are, and see no problems with convergence, which was never a problem for these systems even in the IM-SRG(2)/MAGNUS(2) calculations.

In keeping with the same philosophy as the IM-SRG(2\*) method, we modify the ex-

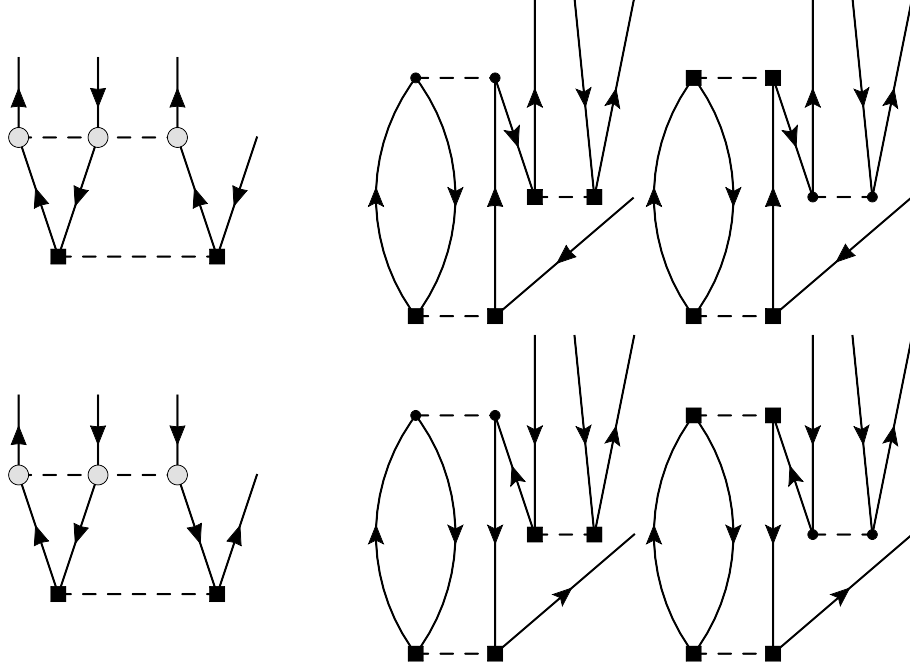


Figure 5.2: The dark circle and square represent the bare Hamiltonian and generator respectively. The light circles in the first column represent the second order 3-body Hamiltonian originating from  $[\eta, H]_{3B}$ . If the second order induced 3-body vertex is expanded in terms of bare quantities, the 4 asymmetric Goldstone diagrams on the right are the result.

pression for each adjoint operator in the BCH formula with a one-body operator  $\tilde{\chi}^k$  in the following way,

$$H(s) = e^{\Omega} H e^{-\Omega} = \sum_{k=0}^{\infty} \frac{1}{k!} \tilde{ad}_{\Omega}^k(H) \quad (5.4)$$

$$\tilde{ad}_{\Omega}^k(H) = ad_{\Omega}^k(H) \quad \text{for } k=0,1, \quad (5.5)$$

$$\tilde{ad}_{\Omega}^k(H) = [\Omega, \tilde{ad}_{\Omega}^{k-1}(H) + \tilde{\chi}^{k-1}] \quad \text{for } k>1, \quad (5.6)$$

where the one-body operator  $\tilde{\chi}^k$  is defined as

$$\tilde{\chi}_{qr}^k = \frac{1}{2} \sum_{stu} (n_q n_r + \bar{n}_q \bar{n}_r) (n_s n_t \bar{n}_u + \bar{n}_s \bar{n}_t n_u) (1 + P_{qr}) \Omega_{uqst} X_{stur}^{k-1} \quad (5.7)$$

$$(5.8)$$

and  $X^k = \widetilde{ad}_\Omega^k(H)_{2B}$ . Although this corrected BCH expression was motivated by perturbative considerations, it appears that this general topology of terms, i.e, the diagrams of Figs. 5.1 and 5.2, but with the full flowing vertices (which themselves are non-perturbative resummations), are very important. To clarify, every piece of this diagram involves “off-diagonal” components of the Hamiltonian, and feeds directly back into the flow of the same “off-diagonal” vertices. This seems to promote its importance beyond a naive perturbative counting of terms. For instance, the third such modified nested commutator, which contributes to energy at fifth order, changes answers by .1-.5 mH for the molecules we present results for. Therefore, we keep all such nested commutators in our calculations. This might raise concerns that other neglected topologies arising from  $[\Omega, [\Omega, H]_{3B}]_{1B,2B}$  are not negligible. To check this, I have implemented all terms arising from expressions of internal three-body commutators that immediately are triply contracted with the two-body  $\Omega$ , as they can all be factorized into an  $N^6$  evaluations. However, these terms typically affect the final answer (at equilibrium) by a negligible amount of around .1 mH or less. We are not claiming that higher-body terms in further nested commutators are also negligible, but generating them will cause the method to scale the same as the full IM-SRG(3), and therefore they are not considered in this work. This question will be explored more in future work, at least for sufficiently small systems so that the full calculations can be carried out, to verify that they are not sizeable.

This modified truncation of the BCH commutators provides a robust convergence pattern, which agrees with CCSD results at equilibrium geometries for every molecule and basis set we have investigated in this work. As bonds are stretched, the results from MAGNUS(2\*) begin to underbind with respect to CCSD results. However, this underbinding may prove to be a good thing, given that three-body effects (which should be attractive) have not yet

been fully accounted for in the above method. We should also mention that here, there is nothing that is more or less valid when applying this corrected BCH expression for any observable we are dealing with. In other words, it should be generally applicable for any operator dominated by its NO2B and lower components.

In spirit, this approximation captures much *more* than the three-body Mukherjee decomposition found in canonical transformation theory [79]. The difference is that there, they are decoupling an “active space”, and that their tensor decomposition introduces a state specificity to the transformation. It would be interesting to go back and use our approximation presented in a complete active space calculation to see how it compares. For now, that is beyond the scope of this work.

## 5.4 Approximations to MAGNUS(3)

In Chapter 2 we reviewed the main non-iterative CCSD plus some non-iterative approximate inclusion of three-body cluster amplitudes. We present here the various ways that similar approximations can be included our framework. Having just summarized how the effect of certain three-body operators that are internal to the BCH can be included, we now turn to approximate the leading effects of including all NO3B effects as well, termed the MAGNUS(3). Like CC methods presented earlier, we are only interested in non-iterative methods that are just slightly more costly than the MAGNUS(2\*) calculation they are based upon.

All of our methods are reminiscent of CC theory, but given that they are framed in terms of a transformed Hamiltonian that is Hermitian, they are more intuitive. For the remainder of this section, any non-subscripted  $\Omega$  is the converged operator of a MAGNUS(2\*)

decoupling. We denote  $\bar{H} = H(\infty) = e^{\Omega}H(0)e^{-\Omega}$  in order to simplify equations. If we want to incorporate physics beyond the NO2B Hamiltonian, then we need to allow for a three-body interaction  $\bar{W}$  in the following way,

$$\bar{H} \approx \{\bar{E} + \bar{f} + \bar{\Gamma}\}_{MAGNUS(2^*)} + \bar{W}. \quad (5.9)$$

The contents of the brackets contain the final Hamiltonian we generate in our fully converged MAGNUS(2\*) transformation, and as such, it is completely “diagonal.” The  $\bar{W}$  part of the interaction, on the other hand, can connect our reference  $\Phi$  to triply excited Slater determinants. For now, we will leave the form of  $\bar{W}$  unspecified. Given that it is possible to generate it, the most straightforward way to immediately give an energy correction due to  $\bar{W}$  is just second order perturbation theory. We have already given the form of this in Eq. (2.26), but for the reader’s ease we reproduce it here. The energy correction  $\Delta E_{[3]}$  can be written as

$$\Delta E_{[3]} = \frac{1}{3!^2} \sum_{ijkabc} \frac{\bar{W}_{ijkabc}\bar{W}_{abcijk}}{\bar{\Delta}_{ijkabc}} = \frac{1}{3!^2} \sum_{ijkabc} \bar{\Omega}_{ijkabc}\bar{\Omega}_{abcijk}\bar{\Delta}_{abcijk}. \quad (5.10)$$

Although this energy correction was motivated by perturbation theory with the transformed Hamiltonian, there is an alternate derivation in which it arises in another way. We also take a moment to note that the denominator  $\bar{\Delta}_{ijkabc}$  can be made from the bare or transformed Hamiltonian, and can be chosen freely to be Möller-Plesset or Epstein-Nesbett type. If we introduce a second transformation  $e^{\bar{\Omega}}$ , with elements of the following form,

$$\bar{\Omega}_{abcijk} = \frac{\bar{W}_{abcijk}}{\bar{\Delta}_{abcijk}}, \quad (5.11)$$

then we can transform the final MAGNUS(2\*) Hamiltonian as

$$\bar{\bar{H}} = e^{\bar{\Omega}} \bar{H} e^{-\bar{\Omega}}. \quad (5.12)$$

If we assume that this second transformation's BCH expansion follows the same pattern of monotonically decreasing terms as shown in Fig.4.3, then the brunt of the energy correction will come from the first few terms. Isolating the first few terms, we arrive at

$$\Delta E_{[3]} = [\bar{\Omega}, \bar{H}]_{0B} + \frac{1}{2} [\bar{\Omega}, [\bar{\Omega}, \bar{H}]]_{0B}. \quad (5.13)$$

Here we will have to restrict the Hamiltonian  $\bar{H}$  appearing in the second commutator to only have the diagonal form used to define  $\bar{\Delta}$ , else the numerical scaling to establish  $\Delta E_{[3]}$  will rise from its cheapest  $n_o^3 n_u^4$  to at least  $n_o^3 n_u^6$  or higher depending on how much of  $\bar{H}$  is included in this commutator. But keeping the prescription as presented, the two formulas yield identical results as designed. The reason for demonstrating the same energy correction arises from BCH formalism, is that it allows for the straightforward inclusion of observables at the same level of accuracy, and in future work with other applications of the MAGNUS(2) to valence space and multireference methods, we will will not need to appeal to a more complicated perturbation theory to proceed.

We now turn to how we approximate  $\bar{W}$ , and it is here that we begin to really draw analogies with the CC methods presented earlier. If we recall how the triples energy correction to CCSD[T] was established,  $T_3$  was approximated as linear in the converged  $T_2$  amplitudes, with the bare resolvent. We can form a similar approximation,  $\bar{W} = [\Omega, H]_{3B}$ , and also using only the bare HF energies in the denominator to establish  $\bar{\Omega}$ . In order to do

this we need only elements of the form  $\bar{W}_{abcijk} = [\Omega, H]_{abcijk}$ .

$$[\Omega, H]_{abcijk} = (1 - P_{ab} - P_{bc})(1 - P_{ij} - P_{ik}) \left( \sum_l \Omega_{abil} \Gamma_{lcjk} - \sum_d \Gamma_{abid} \Omega_{dcjk} - (\Omega \leftrightarrow \Gamma) \right). \quad (5.14)$$

Not surprisingly, this is the term that dictates the  $n_o^3 n_u^4$  scaling already mentioned, and is exactly the same expression that appears in coupled cluster theory in Eq. (2.37) and Fig. 2.3. Once established,  $\Delta E_{[3]}$  corrects the  $E_{MAGNUS(2^*)}$  energy to fourth order in MBPT with regards to the original reference. It is important to notice that this energy only goes beyond fourth order via the use of an infinite order two-body  $\Omega$ . This will be the crudest approximation we can make in this formalism, and we denote it MAGNUS(2\*)[3]-A, with energy correction  $\Delta E_{[3]-A}$ .

For next level of approximation, instead of using the original bare Hamiltonian for usage in our denominators, we can use the fully transformed one-body Hamiltonian resulting from a MAGNUS(2\*) calculation. Thus the resolvent is updated by the fact that our single Slater determinant is a much better approximation after the MAGNUS(2\*) transformation. This type of correction will be denoted by MAGNUS(2\*)[3]-B to make the connection to renormalized coupled cluster theory.

We can go one step further by not limiting ourselves to induced three-body interactions that are only linear in  $\Omega$ . This is accomplished by using an “internal BCH” to establish the two-body piece that is contracted with  $\Omega$  to form  $\bar{W}_C$ . This is motivated by returning to the matrix adjoint expression of  $\bar{H}$  from Eq. 5.4, which only begins at  $k = 1$  for an induced three-body force

$$\bar{W} = \sum_{k=1}^{\infty} \frac{1}{k!} \tilde{a} d_{\Omega}^k (H)_{3B} = [\Omega, H]_{3B} + \frac{1}{2} [\Omega, [\Omega, H]]_{3B} + \dots \quad (5.15)$$

If we want to approximate this as fully as possible without increasing the single  $n_o^3 n_u^4$  iteration, it is easy to form a fully renormalized internal vertex by rewriting

$$\bar{W} = [\Omega, H + \frac{1}{2}[\Omega, H] + \dots]_{3B} = [\Omega, \sum_{k=1} \frac{1}{(k+1)!} \tilde{ad}_{\Omega}^k(H)_{2B}]_{3B} = [\Omega, \tilde{H}]_{3B}. \quad (5.16)$$

This makes it possible to use Eq. 5.14, just by replacing  $H$  with  $\tilde{H}$ . We suggest that this replacement makes connects philosophically with the completely renormalized coupled cluster CR-CC(2,3), as everything that goes into the triples matrix elements is consistently transformed. We call the method arising from these choices MAGNUS(2\*)[3]-C. All topologies of terms found in the three-body  $\mathcal{M}$  of CR-CC(2,3) can also be found in  $\bar{W}_C$ , although admittedly some of them will be under counted. This can be seen as identical terms can arise identically from  $[\Omega, [\Omega, H]_{3B}]_{3B}$ , which will be omitted in our truncation scheme. These should be further investigated to see how large they are. It has been found that using Epstein-Nesbett type denominators in the analogous denominators of CR-CC(2,3) lead to results that track much more closely to full CCSD[T] [8]. We will also explore another scheme, where the denominator from MAGNUS(2\*)[3]-C is made to include diagonal elements from the fully transformed two-body Hamiltonian resulting from a MAGNUS(2\*). We will denote this as MAGNUS(2\*)[3]-D.

## 5.5 Applications

Despite the fact that these corrections have been motivated by the failure of the IM-SRG(2) methods in chemistry systems, it is fitting that we start elsewhere, as the story of the success of these methods in chemistry systems is still nuanced. We will first investigate

Method	$\bar{W}$	$\bar{\Delta}_{ijklabc}$
MAGNUS(2*)[3]-A	$[\Omega, H]_{3B}$	$\langle \Phi_{ijk}^{abc}   f   \Phi_{ijk}^{abc} \rangle$
MAGNUS(2*)[3]-B	$[\Omega, H]_{3B}$	$\langle \Phi_{ijk}^{abc}   \bar{f}   \Phi_{ijk}^{abc} \rangle$
MAGNUS(2*)[3]-C	$[\Omega, \tilde{H}]_{3B}$	$\langle \Phi_{ijk}^{abc}   \bar{f}   \Phi_{ijk}^{abc} \rangle$
MAGNUS(2*)[3]-D	$[\Omega, \tilde{H}]_{3B}$	$\langle \Phi_{ijk}^{abc}   \bar{f} + \bar{\Gamma}   \Phi_{ijk}^{abc} \rangle$

Table 5.1: Approximations made in the various MAGNUS(2\*)[3] variants.

the ability of the corrections presented above to dramatically improve calculations of the electron gas. Then we will present some simple, but realistic nuclear calculations for  ${}^4\text{He}$  and  ${}^{16}\text{O}$ , that show generally expected results. Finally we will show results for a handful of chemistry results, with varying level of success. We will then use some of the failures in chemistry systems to highlight another tool that the MAGNUS(2\*) class of methods can add to treating difficult systems where Hartree-Fock is not an adequate starting point.

### 5.5.1 Electron Gas Results

In Chapter 4, we examined the ability of the Magnus formulation to reproduce IM-SRG(2) calculations for both the electron gas and finite nuclei. In figure 5.3, we benchmark results of MAGNUS(2) to quasi-exact calculations at a variety of densities and basis set sizes. When compared to CCD calculations, MAGNUS(2) (and IM-SRG(2)) results are always between the exact FCIQMC and CCD calculations. A similar pattern is found in the vast majority of nuclear calculations, where the naive IM-SRG(2) and MAGNUS(2) results fall between CCSD and CCSD(T) calculations, see the discussion in Chapter 3. When we now apply the MAGNUS(2\*) to the electron gas, we find answers that are virtually indistinguishable from

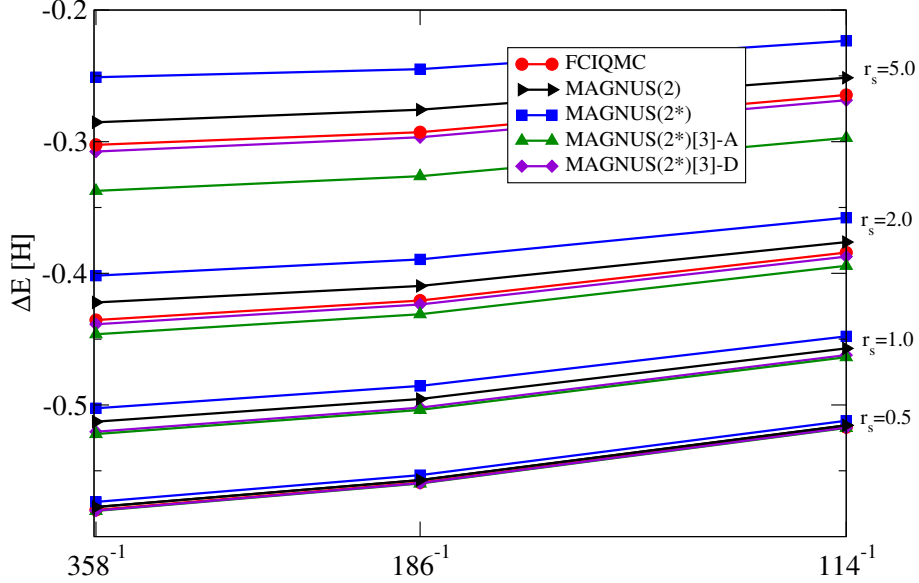


Figure 5.3: Ground state calculations for 14 electrons confined to a box at densities of  $r_s/a_0$  of .5, 1, 2, and 5 and performed at 3 basis set sizes of 114, 186, and 358 with various methods. Although CCSD results are not plotted, correcting the MAGNUS(2) commutator expressions as shown in Eq. (5.4) makes MAGNUS(2\*) indistinguishable from CCSD on these scales. Further, the triples correction due to the MAGNUS(2\*)[3]-D binds the result back down to agree very well with FCIQMC results from Ref. [3], while the bare denominators found in variant A of MAGNUS(2\*)[3] overbind dramatically.

CCD. This indicates that the apparent higher quality of the IM-SRG(2)/MAGNUS(2) results (relative to the analogous CCD and CCSD results) is generally a result of cancellation of two classes of errors, one repulsive omission that is fixed by including the MAGNUS(2\*) terms of Eq. (5.4), and one attractive omission that is fixed with the inclusion of approximate triples. We now turn to the different variants of MAGNUS(2\*)[3], and as a visual guide to what approximation is being made, we refer the reader to Table 5.1. Variants A and D of the MAGNUS(2\*)[3] correction are plotted in Fig. 5.3, the others are not shown for clarity. The success of the MAGNUS(2\*)[3] approximations is fairly astonishing, even given the simplicity of this system. The most naive approximation  $\Delta E_{[3]-A}$  causes slight overbinding at a  $r_s/a_0 = .5$ , to fairly dramatic over binding at  $r_s/a_0 = 5$ . This is not surprising as the system is exceedingly non-perturbative at  $r_s/a_0 = 5$ . At this density even the plane wave HF energy

Method	$r_s/a_0 = .5$	$r_s/a_0 = 1.0$	$r_s/a_0 = 2.0$	$r_s/a_0 = 5.0$
Hartree-Fock <sup>a</sup>	58.5927	13.6036	2.8786	.2099
FCIQMC <sup>a</sup>	-.5169	-0.4611	-0.3842	-0.2645
CCD <sup>b</sup>	0.9906	0.9714	0.9313	0.8445
CCDT <sup>b</sup>	1.0007	1.0032	1.0152	
MAGNUS(2)	0.9972	0.9912	0.9802	0.9617
MAGNUS(2*)	0.9905	0.9714	0.9311	0.8434
MAGNUS(2*)[3]-A	1.0011	1.0056	1.0263	1.1234
MAGNUS(2*)[3]-B	1.0010	1.0043	1.0162	1.0401
MAGNUS(2*)[3]-C	1.0006	1.0021	1.0081	1.0151
MAGNUS(2*)[3]-D	1.0005	1.0016	1.0061	1.0107

Table 5.2:

<sup>a</sup> FCIQMC results from Ref. [3].

<sup>b</sup> CCD and CCDT results from Ref. [4].

Ground state of 14 electrons calculated in a basis set of M=114 plane waves with various approximations. The Full Configuration Quantum Monte Carlo correlation energy is reported in Hartree. All other energies are reported as a fraction of the correlation energy recovered with respect to quasi-exact FCIQMC results.

is bound, so it is surprising that we achieve satisfactory results at that density. The fourth order MBPT triple excitations for  $r_s/a_0 = 5$  produce results that are over bound by a little under a full Hartree. The triples energy gap approximately doubles when using transformed instead of untransformed energy denominators, that is  $\bar{\Delta}_{ijkabc} \approx 2\Delta_{ijkabc}$ . This benefit of using transformed denominators can be seen in the drastic improvement from A to B in Table 5.2. The inclusion of the internally transformed  $\tilde{H}$  makes another large improvement from B to C. And finally C to D, where the transformed Möller-Plesset denominators are replaced with Epstein-Nesbet type, creates a small, but measurable difference that makes  $\Delta E_{[3]-D}$  shows very good agreement with FCIQMC results. A recent publication produced full triples results for the smallest of these basis set sizes, and the comparison of all methods to the FCIQMC are shown in Table 5.2[4]. Most interesting is that methods C and D outperform even full CCDT results for this system. There is no reason to expect that this pattern would

hold for all basis set sizes. Unfortunately, this clear and systematic improvement that is seen in the periodic electron gas is much more complicated to see in more realistic systems like nuclei and molecules.

### 5.5.2 Nuclear Results

For nuclear systems, where the IM-SRG(2) method has found great success in treating medium mass nuclei, there have been fewer problems with convergence, but the open question of why IM-SRG(2) methods, which scale as CCSD, generally tracks  $\Lambda$ -CCSD(T) type results. For the results we are about present, we use a NN-only chiral  $N^3$ LO chiral interaction by Entem and Machleidt [1, 2] softened to  $\lambda = 2.0 \text{ fm}^{-1}$ . Figure 5.4 shows the same conclusion that was drawn from the electron gas, that is, it appears that when corrected MAGNUS(2\*) results agree very closely with CCSD. For  $^4\text{He}$ , MAGNUS(2\*) comes from being overbound with respect to  $\Lambda$ -CCSD(T) results to being in very close agreement with CCSD. When the  $\Delta E_{[3]-C}$  correction is added to it, it is in very close agreement with the  $\Lambda$ -CCSD(T) results. This can be seen again similarly in  $^{16}\text{O}$  calculations, shown in Fig. 5.5. This has been coded up by Nathan Parzuchowski in his large scale spherical nuclear code, and he has performed the spherical coupling of the  $\bar{W}$  operators so that it can be scaled up to treat heavier nuclei. The details of this process, which is exactly the same as recent  $\Lambda$ -CCSD calculations can be found in the appendix of [64]. It will be fruitful to explore these new approximations, and investigate how they behave and can be extended in the presence of a full residual three-body force, in the same spirit as recent works which analyze  $\Lambda$ -CCSD methods with chiral three-nucleon potentials.

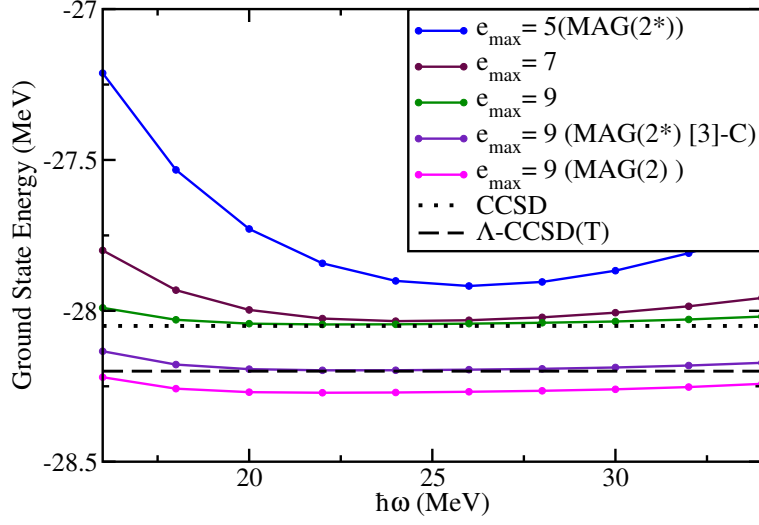


Figure 5.4: MAGNUS(2\*) results, with final MAGNUS(2\*)[3]-C for the largest basis set for  ${}^4\text{He}$  with the chiral  $\text{N}^3\text{LO}$  chiral interaction by Entem and Machleidt [1, 2] softened to  $\lambda = 2.0 \text{ fm}^{-1}$ . We notice that correcting the commutator as shown in Eq. (5.4) provides repulsion that brings MAGNUS(2\*) up to CCSD. Further, the triples correction due to the MAGNUS(2\*)[3]-C binds the result back down to agree with  $\Delta\text{CCSD}[\text{T}]$ . CC results from Ref. [18]

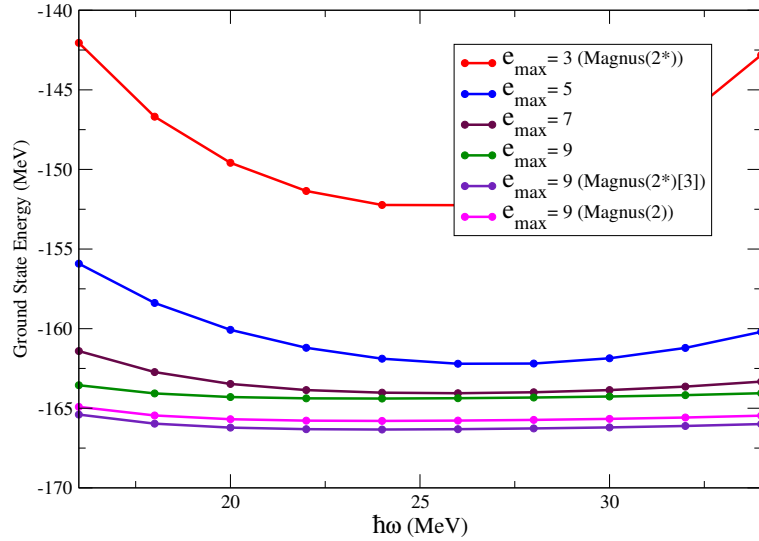


Figure 5.5: MAGNUS(2\*) results, with final MAGNUS(2\*)[3]-C for the largest basis set for  ${}^{16}\text{O}$  with the chiral  $\text{N}^3\text{LO}$  chiral interaction by Entem and Machleidt [1, 2] softened to  $\lambda = 2.0 \text{ fm}^{-1}$ .

### 5.5.3 H<sub>2</sub>O Results

We finally turn to chemistry systems, where the efficiency of the approximations is more difficult to gauge. We have spent much of this work explaining first in 3.5.7 of Chapter 3 how IM-SRG(2) is missing diagrams that CCSD keeps, and then discussing how this led to the catastrophic failure of the IM-SRG(2) in chemistry systems. In Table 5.3, we plot the results of several CC vs our calculated magnus results for H<sub>2</sub>O in a cc-pVDZ basis set[135], at equilibrium bond ( $R_e = 1.84345$  bohr) and HOH angle fixed at 110.6 for several symmetrical stretchings of the molecule. Although this is not an easy system to treat since it involves double bond breaking, we present it first to address the issue of convergence. The first and most important finding is that in this typical double bond breaking test system, where White’s seminal work on the IM-SRG(2) failed, the MAGNUS(2\*) calculations are robustly convergent[78] except at an O-H bond length of  $3R_e$ , which we will show in 6.1 is an artifact of MAGNUS(2\*) sensitivity to reference states. We see that as the O-H bond is stretched, MAGNUS(2\*) is generally underbound with respect to CCSD. This may actually be beneficial, as it offsets the large triples correction that will be added to it, to give reasonable results. We see that MAGNUS(2\*)-A,B,C give results that are underbound with respect to FCI by a few mH, while the D variant remains quite close even in the face of failing CCSDT results. This is a very interesting finding, as we will see in treating Hydrogen Flouride, that the MAGNUS(2\*)[3] methods fail while CCSDT remains within chemical accuracy.

Method	$R_e$	$1.50R_e$	$2R_e$	$2.5R_e$	$3.0R_e$
Full CI <sup>a</sup>	-76.241 860	-76.072 348	-75.951 665	-75.917 991	-75.911 946
CCSD <sup>b</sup>	3.744	10.043	22.032	20.307	10.849
CCSDT <sup>a</sup>	0.493	1.423	-1.405	-24.752	-40.126
CCSD(T) <sup>b</sup>	0.658	1.631	-3.820	-42.564	-90.512
CCSD(2) <sub>T</sub> <sup>c</sup>	0.906	2.825	3.805	-15.830	-33.035
CR-CC(2,3) <sup>d</sup>	0.344	1.142	-0.551	-23.100	-40.556
MAGNUS(2)	-0.897	N.C.	N.C.	N.C.	N.C.
MAGNUS(2*)	3.797	10.384	25.162	36.554	N.C.
MAGNUS(2*)-A	0.688	2.195	4.131	-1.646	
MAGNUS(2*)-B	0.794	2.735	6.725	4.865	
MAGNUS(2*)-C	0.982	3.342	8.952	8.825	
MAGNUS(2*)-D	0.299	0.994	1.531	-4.497	

Table 5.3:

<sup>a</sup>From Ref. [5].

<sup>b</sup>CCSD and CCSD(T) results obtained with PSI4[6].

<sup>c</sup>From Ref.[7]

<sup>d</sup>From Ref. [8]

A comparison of various CC ground-state energies obtained for the cc-pVDZ H<sub>2</sub>O molecule at the equilibrium OH bond length  $R_e = 1.84345$  bohr and several nonequilibrium geometries obtained by stretching the OH bonds, while keeping the HOH angle fixed at 110.6. The spherical components of the d orbitals were used. In post-RHF calculations, all electrons were correlated. The full CI total energies are given in hartree. The remaining energies are reported in millihartree relative to the corresponding full CI energies.

### 5.5.4 Neon Results

We now turn to a simplified atomic system of the closed shell system Ne in a cc-pVDZ basis set[135]. This is just to show that the extremely accurate reproduction of FCI found in the homogenous electron gas of Table 5.2 was not accidental given that there are not pressing issues of reference state dependence in this system, or extremely difficult to capture static correlation. We observe that again, MAGNUS(2\*) reproduces CCSD quite well, with the approximate MAGNUS(3) methods performing as well or better than full CCSDT with respect to full CI. It should be observed, that in the publication that the CC results were taken from, the unitary variants of CC had similar performance in the cc-pVDZ basis set,

Method	Full CI <sup>a</sup>	CCSD <sup>a</sup>	CCSDT <sup>a</sup>	CCSD(T) <sup>a</sup>	
Energy	-128.679 025	0.9935	0.9992	0.9990	
Method	MAG(2*)	MAG(2*)[3]-A	MAG(2*)[3]-B	MAG(2*)[3]-C	MAG(2*)[3]-D
Energy	0.9936	0.9996	0.9994	0.9989	1.0004

Table 5.4:

<sup>a</sup>From Ref. [9].

A comparison of CC and Magnus IM-SRG ground-state energies obtained for a Neon atom in a cc-pVDZ basis set. In these post-HF calculations, the 1s orbital was frozen. The full CI total energy is given in Hartree. The remaining energies are reported as a fraction of the correlation energy recovered relative to  $\Delta E = E_{HF} - E_{FCI}$ .

and then recovered slightly less energy than full CCSDT in the larger cc-pVTZ basis set[9].

### 5.5.5 C<sub>2</sub> Results

I must highlight now that my implementation of the IM-SRG and MAGNUS equations was implemented inside a plug-in for the chemistry suite PSI4 [6], but certainly not at a production level. Given that the understanding of how point-group symmetries was not understood when writing the plug-in, that symmetry has not been exploited. That makes typical calculations for  $r_e, \omega_e$ , and other energy dependent quantities like that infeasible for even modest basis sets. It is a goal of the writers to rewrite a production level plug-in for PSI4. This introduction was needed to explain why only the energies are being compared here for C<sub>2</sub>, a system we choose to treat because it has large multi-configurational content even at equilibrium[9, 136]. In this system, we observe that again, MAGNUS(2\*) reproduces CCSD quite well, with the approximate MAGNUS(3) methods performing similarly to CC methods.

Method	Full CI <sup>a</sup>	CCSD <sup>a</sup>	CCSDT <sup>a</sup>	CCSD(T) <sup>a</sup>	
Energy	75.729 853	29.957	3.371	2.042	
Method	MAG(2*)	MAG(2*)[3]-A	MAG(2*)[3]-B	MAG(2*)[3]-C	MAG(2*)[3]-D
Energy	31.234	3.671	6.634	9.420	-2.448

Table 5.5:

<sup>a</sup>From Ref. [9].

A comparison of CC and Magnus IM-SRG ground-state energies obtained for C<sub>2</sub> at the equilibrium FCI bond length of  $r_e = 1.27273$  Å in a cc-pVDZ basis set, taken from Ref. [9]. In these post-HF calculations, the 1s orbitals was frozen on the C atoms. The full CI total energy is given in Hartree. The remaining energies are reported correlation energy recovered relative to  $\Delta E = E_{HF} - E_{FCI}$ .

### 5.5.6 HF Results

In Table 5.6, we demonstrate the outcomes when HF in a DZP basis[137] is treated with MAGNUS(2\*) methods. We find generally much worse results than we found in any of the previous systems. With regards to full CC methods, CCSDT provides chemical accuracy across the whole potential energy surface, and CR-CC(2,3) approximates this very well. CCSD(T) fails badly, The only place where satisfactory results compared to either CCSD(T), CR-CC(2,3) is achieved is at equilibrium H-F bond length. Everywhere else, we find dramatically overbound results, and non-systematic results even for the MAGNUS(2\*) base method, where it becomes very close to full CI results at  $3R_e$  and then unbound at  $5R_e$ . We suggest that this, like the failure to converge at large bond lengths for H<sub>2</sub>O, is a results of reference state dependence and the fact that Hartree-Fock references become much less accurate starting points during bond breaking.

Method	$R_e$	$2R_e$	$3R_e$	$5R_e$
Full CI <sup>a</sup>	-100.160 300	-100.021 733	-99.985 281	-99.983 293
CCSD <sup>b</sup>	1.634	6.047	11.596	12.291
CCSDT <sup>a</sup>	1.0007	1.0032	1.0152	0.431
CCSD(T) <sup>b</sup>	0.325	0.038	-24.480	-53.183
CCSD(2) <sub>T</sub> <sup>c</sup>	0.229	1.45	2.177	1.443
CR-CC(2,3) <sup>c</sup>	-0.119	0.062	-0.096	-1.005
MAGNUS(2)	-0.897	N.C.	N.C	N.C.
MAGNUS(2*)	1.581	4.495	0.988	14.249
MAGNUS(2*)[3]-A	-0.115	-3.170	-29.319	-24.377
MAGNUS(2*)[3]-B	-0.056	-2.167	-20.846	-10.924
MAGNUS(2*)[3]-C	0.121	-0.723	-12.437	-3.252
MAGNUS(2*)[3]-D	-0.324	-4.080	-28.661	-31.390

Table 5.6:

<sup>a</sup>From Ref. [10].

<sup>b</sup>CCSD and CCSD(T) results from [6].

<sup>c</sup>From Ref. [8]

A comparison of CC and Magnus IMSRG ground-state energies obtained for the equilibrium geometry of  $R_e = 1.7328$  bohr and other nuclear separations of HF with a DZ basis set. In these post-HF calculations all electrons were correlated. The full CI total energies are given in hartree. The remaining energies are reported in millihartree relative to the corresponding full CI energy values.

## 5.6 Summary

We find that for the electron gas, nuclear systems, and the very simple chemistry systems, that the MAGNUS(2\*)[3] methods do a very good job of reproducing full CI results where available, and perform as expected where they are not. This represents a huge step forward for the ability of the IM-SRG to deal with these systems cheaply at higher accuracy, and to get a handle on the expected contributions from higher order methods. For more complicated chemistry systems like H<sub>2</sub>O and HF, there are other open questions. We have shown that the truncated IM-SRG(2) method is in general sensitive to the quality of starting reference states. It is believable that the failure of the method in these systems is due to this, in the next section, we will explore this possibility.

# Chapter 6

## Other Work

The majority of this thesis has been focused on establishing the Magnus formulation of the IM-SRG equations as an effective way to move forward in treating the shortcomings of the traditional solution both in the generation of observables, computational effort, and the ability to approximate the inclusion of three-body forces . We have shown that the exponential formalism that underpins the new formulation offers the possibility of further advances. Here we will present a few areas where work is current and promising, but full conclusions are not yet ready to be drawn. The first of these will be informed again by coupled cluster methods based on finding the best single reference by approximating Brueckner orbitals; this is something that is even more natural in the context of Magnus IM-SRG as we will demonstrate. We will also take the opportunity here to present the possibility of generalizing our approximate three-body inclusion methods in the context of excited state methods being pursued by other practitioners of the IM-SRG method. Finally, we will present how the IM-SRG can also be used to motivate multiconfiguration wavefunction methods in the spirit of CIPSI.

### 6.1 Improving the Reference

In Chapter 2 and 3, we showed how a reference plays a crucial role as the starting point of the IM-SRG,CC, and MBPT type methods. For the IM-SRG, we have shown that results are sensitive to the choice of reference. We have also shown why CC methods are generally

not sensitive to starting reference. The quality of approximate triples, even in CC theory, generally depends on the quality of the reference. Thus chemistry literature is full of attempts to choose the best reference; one of the most interesting is by using a Slater determinant composed of natural, or Brueckner Orbitals. This Brueckner reference  $|\Phi_{BR}\rangle$  can be defined as meeting one of two equivalent criteria. The first is that the overlap of the Brueckner reference with the true ground state is maximized, that is,  $\langle\Phi|\Psi_0\rangle$  is largest when  $|\Phi\rangle = |\Phi_{BR}\rangle$  [16]. A second commonly stated condition for this state is that the full CC ground state built on a Brueckner reference has the following property,

$$|\Psi_{CC}\rangle = e^{T_A+\dots+T_2+T_1} |\Phi_{BR}\rangle = e^{T_A+\dots+T_2} |\Phi_{BR}\rangle, \quad (6.1)$$

or that  $T_1$  vanishes in the fully converged solution [16]. To restate one more time, this means the Hamiltonian needs no single particle change of basis and the ground state  $|\Psi_0\rangle$  contains no single particle excitations when expressed in Brueckner orbitals. This ideal set of orbitals are fairly easy to grasp philosophically, but are often as expensive to pursue as a fully correlated solution itself. Although there are several ways to accomplish this, it has been pursued in depth within CC methods [16, 138, 139]. The one we will present here is the one that will bring insight to our method, and the one that is implemented in the PSI4[6] software suite under the name BCCD or Brueckner CCD. In it, full CCSD calculations are conducted, and then the resulting  $T_1$  amplitudes are used to generate a new set of orthonormal orbitals. These are then used to transform the Hamiltonian into this new basis. A CCSD calculation is carried out again, and this procedure is iterated until the  $T_1$  amplitudes are vanishingly small. In this way, they approximate the Brueckner reference within approximated CC theory. One can see that this is a very expensive procedure, and generally these so called

BCCD energies, and CCSD energies are very close for normal systems precisely because of Thouless theorem (2.34). However, when the effects of  $T_3$  are approximately included instead of exactly included, the starting reference becomes influential. There is also some evidence that in the case of symmetry breaking, BCCD calculations can provide some large benefits as well[139].

The same requirement is more tricky to observe in the Magnus formulation of the IM-SRG, since as we have mentioned several times,  $e^{-\Omega_{2B}-\Omega_{1B}} \neq e^{-\Omega_{2B}}e^{-\Omega_{1B}}$ , or any different rank operators for that matter. It is however evident that even in the IM-SRG formalism,

$$|\Psi_{IM-SRG}\rangle = e^{-\Omega_{AB}\dots-\Omega_{2B}-\Omega_{1B}} |\Phi_{BR}\rangle = e^{-\Omega_{AB}\dots-\Omega_{2B}} |\Phi_{BR}\rangle, \quad (6.2)$$

since any  $\Omega(1)$  will still create 1p1h excitation from  $|\Phi_{BR}\rangle$  which by definition do not belong. The Magnus formulation has shown that we do not need to solve a differential equation perfectly in order to arrive at our desired decoupled Hamiltonian. It turns out that the MAGNUS formalism still works if freed entirely from the differential equation. If we force the transformation to instead take the form of

$$|\Psi_{BMAGNUS(2^*)}\rangle = e^{-\Omega_{1B}}e^{-\Omega_{2B}} |\Phi\rangle, \quad (6.3)$$

and we can still accomplish decoupling in our formalism, then  $|\Phi\rangle \rightarrow |\Phi_{BR}\rangle$ , at least again within our MAGNUS(2<sup>\*</sup>) approximation, which should be similar to the BCCD. We also dispense with the additional matrix adjoint terms in Eq. (4.6) besides just operator  $\eta$  itself, since we are no longer trying to follow the differential equation. If we now look at how this

is practically carried out,

$$H(s) = e^{\Omega_2} e^{\Omega_1} H e^{-\Omega_1} e^{\Omega_2} = \sum_{k=0}^{\infty} \frac{1}{k!} ad_{\Omega_2}^k (e^{\Omega_1} H e^{-\Omega_1}) \quad (6.4)$$

$$e^{\Omega_1} H e^{-\Omega_1} = \sum_{k=0}^{\infty} \frac{1}{k!} ad_{\Omega_1}^k (H). \quad (6.5)$$

So we apply the transformation in two steps, first applying the one-body  $\Omega_{1B}$ , and then the  $\Omega_{2B}$  to the resulting Hamiltonian. Because there is no error in applying a one-body  $\Omega_{1B}$  within our method, this represents a perfect change of basis without approximation. This is in contrast to applying both the one- and two-body pieces together, as  $\Omega_{1B}$  then appears in three-body intermediates that are truncated. In this way we establish a new method, which we name Brueckner IM-SRG, or for this work and its established truncation scheme, BMAGNUS(2\*). Further, all the same approximate MAGNUS(2\*)[3] methods can be carried over with no necessary generalization, thus we will also present the BMAGNUS(2\*)[3] methods where their interpretations are obvious with the exception of where the bare Hartree-Fock energies were used in variant A. For BMAGNUS(2\*)-A, the diagonal energies from the one-body diagonal Hamiltonian of  $e^{\Omega_1} H e^{-\Omega_1}$  are used to make the denominators.

## 6.2 Brueckner IM-SRG Results

For this section, we will present most of the chemistry systems treated from Chapter 5, but now with the analogous BMAGNUS(2\*)[3] methods. I will not be presenting anything for the electron gas, as momentum conservation makes the plane waves the only basis set one can work with without dramatically increasing the computational effort. I will also not present any Brueckner results for nuclear systems. This is mostly a result of not having any nuclear

BCCD results to draw comparisons with, but a future work centered on this BMAGNUS(2\*) methods in nuclear systems should be forthcoming very soon. Alongside the chemistry results, I will present the BCCD(T) results from PSI4. For these methods, it is also interesting to output the BCCD and BMAGNUS(2\*) reference energies in order to compare the character of the orbitals produced from the two approximations, and affirm that BMAGNUS(2\*) is a similar approximation as BCCD. We will present these  $BMAGNUS(2*)_{ref}$  in most of the systems. Given more time and understanding, it would also be beneficial for understanding to actually produce the overlap of the two references, but coaxing PSI4 to output its BCCD orbitals proved beyond our ability in the time available.

We begin again with the results from the very simple system of a cc-pVDZ neon system at equilibrium. Even though this a very simple system, we can begin to characterize some benefits of the Brueckner procedure.

### 6.2.1 BMAGNUS(2\*) Results for Neon and C<sub>2</sub>

We begin to see a pattern here for what happens with both BMAGNUS(2\*) type results. Almost universally, the Brueckner results are underbound versus the Magnus results based on Hartree-Fock references. We see this is particularly helpful in bringing the BMAGNUS(2\*)[D] method, the most complete method, back to agreement with exact values. This appears to be a general finding. Because of this we will choose to only present the BMAGNUS(2\*)-D method for these results. Unless otherwise mentioned, the other results are further underbound with respect to presented results. Similarly, we see an overbound result for MAGNUS(2\*)[3]-D rise up to BMAGNUS(2\*)[3]-D and become very, very close to FCI results for C<sub>2</sub> in Table 6.2. From these results, it is reasonable to believe that in the absence of strong static correlation, BMAGNUS(2\*)[3]-D collects a larger fraction of

Method	Full CI <sup>a</sup>	CCSD <sup>a</sup>	CCSDT <sup>a</sup>	CCSD(T) <sup>a</sup>	
Energy	-128.679 025	0.9935	0.9992	0.9990	
Method	MAG(2*)	MAG(2*)[3]-A	MAG(2*)[3]-B	MAG(2*)[3]-C	MAG(2*)[3]-D
Energy	0.9936	0.9996	0.9994	0.9989	1.0004
Method	BCCD <sub>ref</sub>	BCCD(T)	BMAG(2*) <sub>ref</sub>	BMAG(2*)[3]-D	
Energy	-0.0013	0.9991	-0.0010	0.9998	

Table 6.1:

<sup>a</sup>From Ref. [9].

A comparison of CC and Magnus IMSRG ground-state energies obtained for a Neon atom. In these post-HF calculations, the 1s orbital was frozen. The full CI total energy is given in Hartree. The remaining energies are reported as a fraction of the correlation energy recovered relative to FCI in mH.

Method	Full CI <sup>a</sup>	CCSD <sup>a</sup>	CCSDT <sup>a</sup>	CCSD(T) <sup>a</sup>	
Energy	75.729 853	29.957	3.371	2.042	
Method	MAG(2*)	MAG(2*)[3]-A	MAG(2*)[3]-B	MAG(2*)[3]-C	MAG(2*)[3]-D
Energy	31.234	3.671	6.634	9.420	-2.448
Method	SCF	BCCD <sub>ref</sub>	BCCD(T)	BMAG(2*) <sub>ref</sub>	BMAG(2*)[3]-D
Energy	343.396	364.157	1.665	357.704	0.516

Table 6.2:

<sup>a</sup> From Ref. [9].

A comparison of CC and Magnus IMSRG ground-state energies obtained for C<sub>2</sub> at the equilibrium FCI bond length of  $r_e = 1.27273$  Å. In these post-HF calculations, the 1s orbitals was frozen on the C atoms. The full CI total energy is given in Hartree. The remaining energies are reported in millihartree relative to the full CI energy.

correlation energy even compared to full CCSDT. It is imperative though to take time to write a production level code in which symmetry is exploited in order to benchmark against full IMSRG(3) results in reasonable basis sets.

### 6.2.2 BMAGNUS(2\*) Results for HF and H<sub>2</sub>O

In the treatment of HF in the DZ basis, and H<sub>2</sub>O, we see that where BCCD results are available, that the reference energy of BMAGNUS(2\*)<sub>ref</sub> and BCCD<sub>ref</sub> are very close to

each other. Further, in bond breaking of HF, where MAGNUS(2\*)[3]-D results become dramatically overbound as at  $3R_e$  and above, the Brueckner BMAGNUS(2\*)[3]-D is stable and reasonably close to FCI answers. These results still are not nearly as well behaved as CR-CC(2,3) for this system. But if we instead look at H<sub>2</sub>O, not only do we still get convergence at  $3R_e$ , but we continue to get reasonable results even while CCSDT is extremely overbound for double bond stretching.

### 6.2.3 Brueckner Summary

In conclusion, we see that BMAGNUS(2\*)[3] results are reasonable, and almost always outperform CCSD(T) results, but may not be competitive CR-CC(2,3) results for every molecule. Rather generally, the Brueckner results appear to be producing a reference that is similar in quality to BCCD references, which is most interesting as production of these references has a computational cost very similar to a single MAGNUS(2\*) calculation, while these BCCD calculations required about 10-50 full CCSD iterations before the effects of  $T_1$  are small enough to be neglected. Even if old  $T_1$  and  $T_2$  are used as the starting point of each iteration, this results in a BCCD calculation that is one the order of 10 times the effort of a single CCSD calculation. Further, since we force  $\Omega_{2B}$  to keep the structure of  $\Omega = T^\dagger - T$  for BMAGNUS(2\*) results, it can be set to scale exactly as CCSD,  $n_o^2 n_u^4$  over the  $n^6$  of MAGNUS(2\*) with a general  $\Omega$ .

## 6.3 Extensions to MR-IM-SRG

The IM-SRG formalism and applications presented so far use a single Slater determinant as the reference state. In nuclear physics, these approaches are only appropriate for the

Method	$R_e$	$1.50R_e$	$2R_e$	$2.5R_e$	$3.0R_e$
Full CI <sup>a</sup>	-76.241 860	-76.072 348	-75.951 665	-75.917 991	-75.911 946
CCSD <sup>b</sup>	3.744	10.043	22.032	20.307	10.849
CCSDT <sup>a</sup>	0.493	1.423	-1.405	-24.752	-40.126
CCSD(T) <sup>b</sup>	0.658	1.631	-3.820	-42.564	-90.512
CCSD(2) <sub>T</sub> <sup>c</sup>	0.906	2.825	3.805	-15.830	-33.035
CR-CC(2,3) <sup>d</sup>	0.344	1.142	-0.551	-23.100	-40.556
SCF	217.834	269.982	363.967	476.756	573.585
MAGNUS(2*)	3.797	10.384	25.162	36.554	N.C.
MAGNUS(2*)-D	0.299	0.994	1.531	-4.497	N.C.
BCCD <sub>ref</sub>	218.758	276.328	383.342	515.316	*
BCCD	3.887	10.668	22.126	16.988	*
BCCD(T)	0.682	1.803	-3.753	-46.317	*
BMAGNUS(2*) <sub>ref</sub>	218.621	275.693	383.154	519.876	634.684
BMAGNUS(2*)	3.874	10.829	26.836	42.469	47.968
BMAGNUS(2*)-D	0.385	1.600	4.597	3.615	-3.583

Table 6.3:

<sup>a</sup>From Ref. [5].

<sup>b</sup>CCSD and CCSD(T) results obtained with PSI4[6].

<sup>c</sup>From Ref.[7]

<sup>d</sup>From Ref. [8]

A comparison of various CC ground-state energies obtained for the cc-pVDZ H<sub>2</sub>O molecule at the equilibrium OH bond length  $R_e = 1.84345$  bohr and several nonequilibrium geometries obtained by stretching the OH bonds, while keeping the HOH angle fixed at 110.6. The spherical components of the d orbitals were used. In post-RHF calculations, all electrons were correlated. The full CI total energies are given in hartree. The remaining energies are reported in millihartree relative to the corresponding full CI energies. In Ref. [10], the authors noticed that there are two SCF solutions, one of which poorly describes the weak H-O bonding. In the chemistry suite, PSI4[6], we could not force the CCSD routine, and thus the BCCD routine to use the correct SCF starting reference. This is why there are no results reported for  $3.0R_e$

description of nuclei around (sub-)shell closures.

In open-shell nuclei, correlations cause the emergence of phenomena like nuclear superfluidity or intrinsic deformation. With reference-state constructions, one can attempt to capture these effects at the mean-field level to some extent, by breaking symmetries either spontaneously or explicitly. Pairing correlations can be treated in the Hartree-Fock-Bogoliubov

Method	$R_e$	$2R_e$	$3R_e$	$5R_e$
Full CI <sup>a</sup>	-100.160 300	-100.021 733	-99.985 281	-99.983 293
CCSD <sup>b</sup>	1.634	6.047	11.596	12.291
CCSDT <sup>a</sup>	1.0007	1.0032	1.0152	0.431
CCSD(T) <sup>b</sup>	0.325	0.038	-24.480	-53.183
CCSD(2) <sub>T</sub> <sup>c</sup>	0.229	1.45	2.177	1.443
CR-CC(2,3) <sup>c</sup>	-0.119	0.062	-0.096	-1.005
MAGNUS(2*)	1.581	4.495	0.988	14.249
MAGNUS(2*)[3]-D	-0.324	-4.080	-28.661	-31.390
SCF	138.329	206.485	299.388	375.354
BCCD <sub>ref</sub>	139.775	221.576	344.157	454.695*
BCCD	2.012	6.622	10.696	318.710*
BCCD(T)	0.261	0.844	-4.339	317.288*
BMAGNUS(2*) <sub>ref</sub>	139.475	222.492	355.615	445.704
BMAGNUS(2*)	1.920	7.170	16.971	22.019
BMAGNUS(2*)[3]-D	0.090	1.071	4.659	6.505

Table 6.4:

<sup>a</sup> From Ref. [10].

<sup>b</sup> CCSD and CCSD(T) results obtained with PSI4[6].

<sup>c</sup> From Ref. [8]

A comparison of CC and Magnus IMSRG ground-state energies obtained for the equilibrium geometry of  $R_e = 1.7328$  bohr and other nuclear separations of HF with a DZ basis set. In these post-HF calculations all electrons were correlated. The full CI total energies are given in hartree. The remaining energies are reported in millihartree relative to the corresponding full CI energy values.

(HFB) formalism, which is formulated in terms of Slater determinants of fermionic quasi-particles that are superpositions of particles and holes. Intrinsic deformation will develop if the single-particle basis is not symmetry restricted, e.g., in an  $m$ -scheme formalism, and rotational symmetry breaking is energetically favored.

An  $m$ -scheme IM-SRG or CC calculation may be able to converge to a solution if the excitation spectrum of the symmetry-broken reference state has a sufficiently large gap, i.e., a single dominant configuration. If such a solution is found, one must eventually restore the broken symmetries through the application of projection methods, which have a long track record in nuclear physics (see, e.g., [140–151]). At this point, one is no longer dealing with

a single-reference problem, although the projected states retain an imprint of the original symmetry-broken (single-)reference states that simplifies practical implementations.

In the domain of exotic neutron-rich nuclei, the single-reference paradigm may also break down. The complex interplay of nuclear interactions, many-body correlations, and, in the dripline region, continuum effects, can cause strong competition between configurations with different intrinsic structures. This manifests in phenomena like the erosion and emergence of shell closures [22, 23, 44, 152], or the appearance of the so-called islands of inversion (see, e.g., [153]). Their description requires a true multi-reference treatment.

The Multi-Reference IM-SRG (MR-IM-SRG) is capable of dealing with the aforementioned scenarios [21, 23, 45]. It generalizes the IM-SRG formalism discussed in this work to arbitrary correlated reference states, using the multi-reference normal ordering and Wick's theorem developed by Kutzelnigg and Mukherjee [154, 155]. The idea of decoupling the ground state from excitations readily carries over, except that excited states are given by

$$:a_i^\dagger a_j: |\Phi\rangle, :a_i^\dagger a_j^\dagger a_l a_k: |\Phi\rangle, \dots,$$

and the single-particle states are no longer of pure particle or hole character. The flow equation formulation of the MR-IM-SRG makes it possible to avoid complications due to the non-orthogonality and possible linear dependency of these general excitations (see [45] for more details).

While only one-body density matrices appear in the contractions of the standard Wick's theorem, additional contractions that involve two- and higher-body density matrices enter that encode the correlation content of the reference state. In the MR-IM-SRG framework, correlations that are hard to capture as few-body excitations of the reference state can be

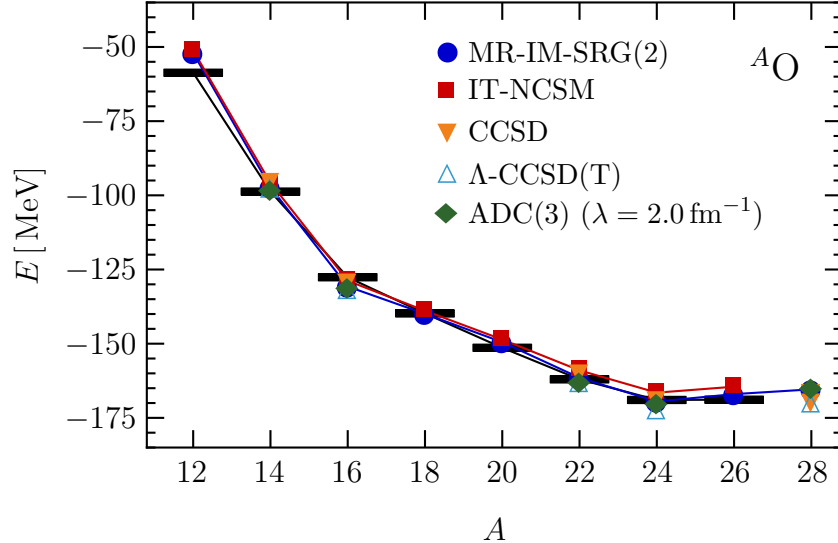


Figure 6.1: Ground-state energies of the oxygen isotopes from MR-IM-SRG and other many-body approaches, based on the NN+3N-full interaction with  $\Lambda_{3N} = 400$  MeV, evolved to the resolution scale  $\lambda = 1.88$  fm $^{-1}$  ( $\lambda = 2.0$  fm $^{-1}$  for the Green's Function ADC(3) results, cf. [19]). Black bars indicate experimental data [20]. See Ref. [21] for additional details.

built directly into the reference state.

In a first applications of the MR-IM-SRG framework, spherical, particle-number projected HFB vacua have been used to compute the ground-state energies of the even oxygen isotopes, starting from chiral NN+3N forces [21]. This work improved on previous Shell Model [25, 156] and CC studies [99], that included NN+3N interactions in MBPT or for the latter with 3N forces in a more phenomenological, nuclear-matter based normal ordering. Based on a Hamiltonian that is entirely fixed in the  $A = 3, 4$  system and consistently evolved to lower resolution, we found that MR-IM-SRG, various CC methods, and the importance-truncated NCSM consistently predict the neutron dripline in  $^{24}\text{O}$  if chiral 3N forces are included (see Fig. 6.1), as pointed out in the context of the Shell Model in Ref. [156].

Encouraged by this success, we moved on to the calcium and nickel isotopic chains [23], where importance-truncated NCSM calculations are no longer feasible. The same family of chiral NN+3N Hamiltonians that successfully reproduce the oxygen ground-state energies

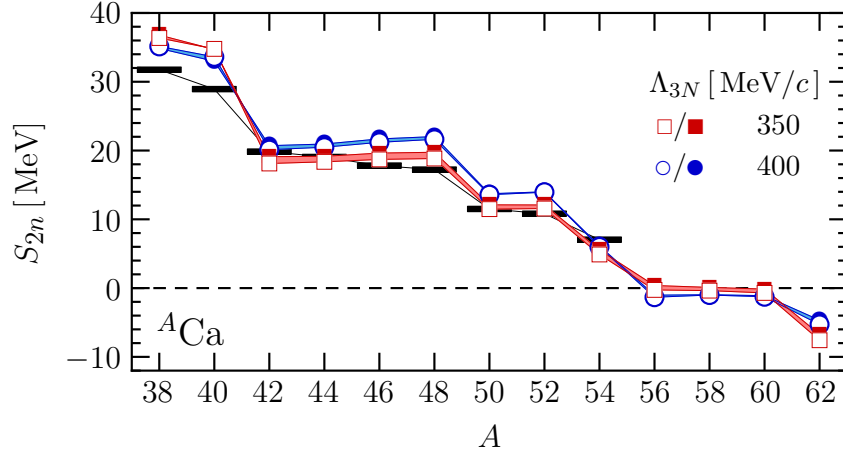


Figure 6.2: MR-IM-SRG results for Ca two-neutron separation energies, for chiral NN+3N interactions with different cutoffs in the 3N sector, and a range of resolution scales from  $\lambda = 1.88 \text{ fm}^{-1}$  (open symbols) to  $2.24 \text{ fm}^{-1}$  (solid symbols). Black bars indicate experimental data [20, 22]. See Ref. [23] for additional details.

overestimate the binding energies in these isotopes by several hundred keV per nucleon, in MR-IM-SRG and CC (also see [86, 87, 98]), as well as the second-order Gor’kov Green’s Function approach [44]. The revelation of these deficiencies has led to a variety of efforts to improve on the chiral interactions [47, 157–165].

Contrary to the ground-state energies, chiral NN+3N forces reproduce relative quantities like the two-neutron separation energies quite well, aside from the exaggerated  $N = 20$  shell closure (Fig. 6.2). In particular, they show signals of sub-shell closures in  $^{52,54}\text{Ca}$ , in agreement with Shell Model calculations based on NN+3N interactions in MBPT [22, 152]. These observations indicate which terms in the chiral input Hamiltonian may be deficient, and this information can be used in future optimizations.

Ongoing work within MR-IM-SRG relevant to this thesis focuses on overcoming the same shortcomings the traditional IM-SRG faced, and that the Magnus formulation circumvented in the single reference IM-SRG methods. Initial inspection indicates that multi-reference MAGNUS(2) calculations will faithfully reproduce their MR-IM-SRG(2) calculations as it

did with single reference IM-SRG(2). Further, it appears that one might expect that the largest missed corrections to MR-MAGNUS(2) would be completely analogous to the MAGNUS(2\*) and MAGNUS(2\*)[3] type corrections. This is of course conjecture and will need full inspection to verify. One reason we presented  $\Delta E_{[3]}$  in terms of commutators is that it avoids the appeal to perturbation theory, which becomes very expensive with a multi-reference type state. As mentioned above the MR-IM-SRG avoids complications due to the non-orthogonality and possible linear dependency of excitations through this usage of generalized normal ordering. Thus, it would be expected that we could come up with an analogous  $\Delta E_{[3]}$  based on leading expression from the multi-reference BCH. This would be in the same spirit of recent multi-reference perturbation theory based on the driven similarity renormalization group motivated perturbation theory found in [166]. Further, using the factorization scheme of [167], it would be possible to factorize these expressions in Eq. 5.13 to  $n^6$  scaling. This is only helpful for the multi-reference formalism where there is no distinction between particle and hole states, as the most expensive term for a closed shell system scales as  $n_o n_u^5$  which is generally larger than  $n_o^3 n_u^4$ . Thus it might be possible to correct the MR-IMSRG(2) to the MR-MAGNUS(2\*)[3] without affecting scaling, yielding around CCSD(T) accuracy even for open shell nuclei.

## 6.4 Extensions to Excited State Formalism

For open-shell systems, rather than solving the full  $A$ -body problem, it is profitable to follow the Shell Model paradigm by constructing and diagonalizing an effective Hamiltonian in which the active degrees of freedom are  $A_v$  valence nucleons confined to a few orbitals near the Fermi level. Both phenomenological and microscopic implementations of the Shell

Model have been used with success to understand and predict the evolution of shell structure, properties of ground and excited states, and electroweak transitions [168–170].

Recent microscopic Shell-Model studies have revealed the impact of 3N forces in predicting ground- and excited-state properties in neutron- and proton-rich nuclei [22, 25, 152, 156, 171–174]. Despite the novel insights gained from these studies, they make approximations that are difficult to benchmark. The microscopic derivation of the effective valence-space Hamiltonian relies on MBPT [175], where order-by-order convergence is unclear. Even with efforts to calculate particular classes of diagrams nonperturbatively [176], results are sensitive to the HO frequency  $\hbar\omega$  (due to the core), and the choice of valence space [25, 171, 172]. A nonperturbative method to address these issues was developed in [177–179], which generates valence-space interactions and operators by projecting their full NCSM counterparts into a given valence space.

To overcome these limitations in heavier systems, the IM-SRG can be extended to derive effective valence-space Hamiltonians and operators nonperturbatively. Calculations without initial 3N forces [39] indicated that an *ab initio* description of ground and excited states for open-shell nuclei may be possible with this approach.

The utility of the IM-SRG lies in the freedom to tailor the definition of  $H^{\text{od}}$  to a specific problem. For instance, to construct a Shell Model Hamiltonian for a nucleus comprised of  $A_v$  valence nucleons outside a closed core, we define a HF reference state  $|\Phi\rangle$  for the core with  $A_c$  particles, and split the single-particle basis into hole ( $h$ ), valence ( $v$ ), and non-valence ( $q$ ) particle states. Treating all  $A$  nucleons as active, i.e., without a core approximation, we eliminate matrix elements which couple  $|\Phi\rangle$  to excitations, just as in IM-SRG ground-state calculations [21, 58, 74]. In addition, we decouple states with  $A_v$  particles in the valence space,  $:a_{v_1}^\dagger \dots a_{v_{A_v}}^\dagger :|\Phi\rangle$ , from states containing non-valence states.

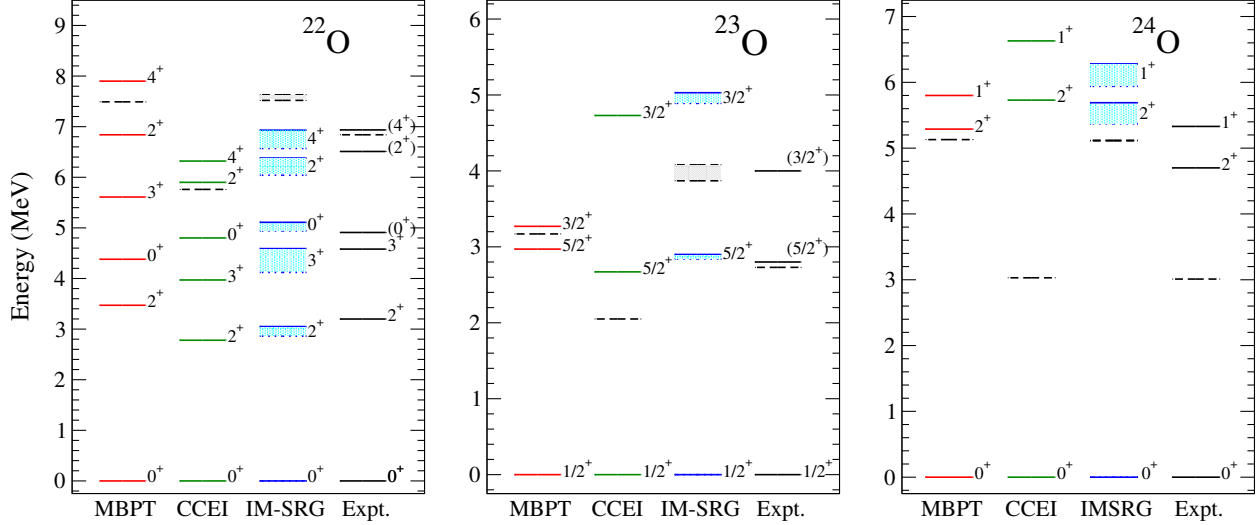


Figure 6.3: Excited-state spectra of  $^{22,23,24}\text{O}$  based on chiral NN+3N interactions and compared with experiment. Figures adapted from Ref. [24]. The MBPT results are performed in an extended  $sd_{7/2}p_{3/2}$  space [25] based on low-momentum NN+3N interactions, while the IM-SRG [24] and CC effective interaction (CCEI) [26] results are in the  $sd$  shell from the SRG-evolved NN+3N-full Hamiltonian with  $\hbar\omega = 20$  MeV (CCEI and dotted IM-SRG) and  $\hbar\omega = 24$  MeV (solid IM-SRG). The dashed lines show the neutron separation energy. Figure taken from Ref. [27].

After the IM-SRG derivation of the valence-space Hamiltonian, the  $A$ -dependent Hamiltonian is diagonalized in the valence space to obtain the ground and excited states. For the oxygen isotopes, a good description of the experimental spectra is found (Fig. 6.3). Recently, these calculations were extended to nearby F, Ne, and Mg isotopes showing excellent agreement with new measurements in  $^{24}\text{F}$  [180] and that deformation can emerge from these *ab initio* calculations [41]. Future directions include extending the valence space, which will give access to the island-of-inversion region and potentially the full  $sd$ -shell (and higher) neutron dripline.

The results being produced by Stroberg and collaborators [41] are already reliant on the Magnus formulation of the IM-SRG described here; and quickly it is becoming clear that effective valence space observables will be readily available because of it. This could help

to answer long-standing questions about a whole host of shell-model phenomenology from first principles. It is imperative that we inspect the effect of three-body forces, induced and otherwise, in these effective valence spaces interactions. The generalization of this work's findings for ground state decouplings will not generalize easily to the new non-trivial definition of off-diagonal used to decouple valence spaces, but the path forward is straightforward and needs to be inspected.

# Chapter 7

## Summary and Conclusions

This work investigated the IM-SRG method, which has seen increasing recent use in nuclear physics due to its flexibility and relatively gentle scaling with system size. Despite its amazing success in nuclear physics, its initial failure to successfully treat even fairly simple chemical systems was more than a little puzzling. As a first step towards solving this puzzle, I investigated the truncated IM-SRG(2)'s perturbative content. It was found that it undercounted a class of fourth order quadrupole excitation diagrams that CCSD theory includes correctly. Being that the two methods seem to have a similar machinery, computational cost and philosophy, it became one of my goals to find a way to restore this content to the method so that it would be possible to bring the success of the IM-SRG to chemical systems as well. Incidentally, the outstanding performance of the IM-SRG(2) in nuclear calculations is related to this undercounting of 4th-order terms, as it mimics the partial cancellations that occur between these repulsive contributions and attractive triples correlations in CCSD and CCSDT calculations. In other words, the undercounting of this class of diagrams mimics the effects of triples correlations for nuclei, which is why the IM-SRG(2) results fall in between CCSD and CCSDT calculations for all nuclei studied.

It was during this quest to find a way to restore the full counting of these terms that it was found that the IM-SRG flow equations could be recast using the Magnus expansion. This led to formulation of the IM-SRG equations which not only alleviated the need for solving the flow equations with expensive high-order ODE solvers, but also allowed for the generation

of observables at no additional cost. The first calculations showing these benefits have been conducted for nuclei and the electron gas, with very promising results. As mentioned, this formalism has already found its way to several other independent practitioners of the IM-SRG formalism, particularly those developing valence space interactions, to great success.

With the Magnus formulation in hand, it was then possible to revisit these missing terms that caused the naive IM-SRG(2) and MAGNUS(2) truncations to fail for chemical systems. Not only was it possible to restore these terms, yielding the MAGNUS(2\*) method, but it also became possible to borrow insight from CC theory to engineer approximate corrections that would be due to IM-SRG(3). We have shown that the class of approximations to IM-SRG(3) dubbed MAGNUS(2\*)[3] treats the electron gas, nuclei, and simple chemistry systems extraordinarily well. With more complicated chemistry systems, these methods do as well as some approximate non-iterative triples methods in CC theory, but not all. It seems that the methods ability to map the fully correlated ground state to a mean field picture is compromised as the correlations become more complicated. It is likely that more nuanced approximations of IM-SRG(3) or higher may be needed. Regardless, for first results of the method, the quality of MAGNUS(2\*)[3] results seem very promising indeed.

Thus this work has shown how the IM-SRG method has been augmented with the Magnus formulation to be faster, more accurate, more robust, and more versatile in the treatment of observables. The outlook for future developments, both in nuclear and chemical systems is promising, be they in the Brueckner formulation, the multi-reference formulation, or pursuing new approximations to the IM-SRG(3) when deriving valence interactions within the IM-SRG. We expect that not only are these endeavors now possible, but they will likely be accomplished soon.

## APPENDICES

# Appendix A

## Fundamental Commutators

For convenience, we collect the expressions for the fundamental commutators which are required for the derivation of the IM-SRG flow equations and Wegner-type generators. We write one-, two-, and three-body operators as

$$A^{(1)} = \sum_{ij} A_{ij} : a_i^\dagger a_j : , \quad (\text{A.1})$$

$$A^{(2)} = \frac{1}{(2!)^2} \sum_{ijkl} A_{ijkl} : a_i^\dagger a_j^\dagger a_l a_k : , \quad (\text{A.2})$$

$$A^{(3)} = \frac{1}{(3!)^2} \sum_{ijklmn} A_{ijklmn} : a_i^\dagger a_j^\dagger a_k^\dagger a_n a_m a_l : , \quad (\text{A.3})$$

where the two- and three-body matrix elements are assumed to be fully anti-symmetrized. Single-particle indices refer to natural orbitals, so that occupation numbers are  $n_i = 0, 1$ , and we use the notation  $\bar{n}_a = 1 - n_a$ . We also recall that the commutator of two operators of rank  $M$  and  $N$  can only have contributions of rank  $|M - N|, \dots, M + N - 1$ ,

$$[A^{(M)}, B^{(N)}] = \sum_{k=|M-N|}^{M+N-1} C^{(k)} . \quad (\text{A.4})$$

$[A^{(1)}, \circ]$

$$[A^{(1)}, B^{(1)}]^{(1)} = \sum_{ij} \sum_a :a_i^\dagger a_j : (A_{ia} B_{aj} - B_{ia} A_{aj}) \quad (\text{A.5})$$

$$[A^{(1)}, B^{(1)}]^{(0)} = \sum_{ij} A_{ij} B_{ji} (n_i - n_j) \quad (\text{A.6})$$

$$[A^{(1)}, B^{(2)}]^{(2)} = \frac{1}{4} \sum_{ijkl} \sum_a :a_i^\dagger a_j^\dagger a_l a_k : \{ (1 - P_{ij}) A_{ia} B_{ajkl} - (1 - P_{kl}) A_{ak} B_{ijal} \} \quad (\text{A.7})$$

$$[A^{(1)}, B^{(2)}]^{(1)} = \sum_{ij} \sum_{ab} :a_i^\dagger a_j : \{ (n_a - n_b) A_{ab} B_{biaj} \} \quad (\text{A.8})$$

$$[A^{(1)}, B^{(3)}]^{(3)} = \frac{1}{36} \sum_{ijklmn} \sum_a :a_i^\dagger a_j^\dagger a_k^\dagger a_n a_m a_l : \\ \times \{ (1 - P_{ij} - P_{ik}) A_{ia} B_{ajklmn} - (1 - P_{lm} - P_{ln}) A_{al} B_{ijkamn} \} \quad (\text{A.9})$$

$$[A^{(1)}, B^{(3)}]^{(2)} = \sum_{ijkl} \sum_{ab} :a_i^\dagger a_j^\dagger a_l a_k : (n_a - n_b) A_{ab} B_{bijakl} \quad (\text{A.10})$$

$[A^{(2)}, \circ]$

$$[A^{(2)}, B^{(2)}]^{(3)} = \frac{1}{36} \sum_{ijklmn} \sum_a : a_i^\dagger a_j^\dagger a_k^\dagger a_n a_m a_l : \\ \times P(ij/k)P(l/mn) (A_{ijla}B_{akmn} - B_{ijla}A_{akmn}) \quad (\text{A.11})$$

$$[A^{(2)}, B^{(2)}]^{(2)} = \frac{1}{4} \sum_{ijkl} \sum_{ab} : a_i^\dagger a_j^\dagger a_l a_k : \left\{ \frac{1}{2} (A_{ijab}B_{abkl} - B_{ijab}A_{abkl})(1 - n_a - n_b) \right. \\ \left. + (n_a - n_b)(1 - P_{ij} - P_{kl} + P_{ij}P_{kl})A_{aibk}B_{bjal} \right\} \quad (\text{A.12})$$

$$[A^{(2)}, B^{(2)}]^{(1)} = \frac{1}{2} \sum_{ij} \sum_{abc} : a_i^\dagger a_j^\dagger : (A_{ciab}B_{abcj} - B_{ciab}A_{abcj}) (\bar{n}_a \bar{n}_b n_c + n_a n_b \bar{n}_c) \quad (\text{A.13})$$

$$[A^{(2)}, B^{(2)}]^{(0)} = \frac{1}{4} \sum_{ijkl} n_i n_j \bar{n}_k \bar{n}_l (A_{ijkl}B_{klij} - B_{ijkl}A_{klij}) \quad (\text{A.14})$$

$$[A^{(2)}, B^{(3)}]^{(3)} = \frac{1}{72} \sum_{ijklmn} \sum_{ab} : a_i^\dagger a_j^\dagger a_k^\dagger a_n a_m a_l : (1 - n_a - n_b) \\ \times (P(ij/k)A_{ijab}B_{abklmn} - P(l/mn)A_{abmn}B_{ijklab}) \quad (\text{A.15})$$

$$[A^{(2)}, B^{(3)}]^{(2)} = -\frac{1}{8} \sum_{ijkl} \sum_{abc} : a_i^\dagger a_j^\dagger a_l a_k : (n_a \bar{n}_b \bar{n}_c + \bar{n}_a n_b n_c) \\ \times (1 - P_{ij}P_{ik}P_{jl} - P_{kl} + P_{ik}P_{jl}) A_{bcak}B_{aijbcl} \quad (\text{A.16})$$

$$[A^{(2)}, B^{(3)}]^{(1)} = -\frac{1}{4} \sum_{ij} \sum_{abcd} : a_i^\dagger a_j : (n_a n_b \bar{n}_c \bar{n}_d - \bar{n}_a \bar{n}_b n_c n_d) A_{cdab}B_{abijcd} \quad (\text{A.17})$$

$[A^{(3)}, \circ]$

$$\begin{aligned}
& [A^{(3)}, B^{(3)}]^{(3)} \\
&= \frac{1}{36} \sum_{ijklmn} \sum_{abc} :a_i^\dagger a_j^\dagger a_k^\dagger a_n a_m a_l : \\
&\quad \times \left\{ \frac{1}{6} (n_a n_b n_c + \bar{n}_a \bar{n}_b \bar{n}_c) (A_{ijkabc} B_{abclmn} - B_{ijkabc} A_{abclmn}) \right. \\
&\quad \left. + \frac{1}{2} (n_a n_b \bar{n}_c + \bar{n}_a \bar{n}_b n_c) P(ij/k) P(l/mn) (A_{abkcmn} B_{cijabl} - A_{ckjabc} B_{iablmc}) \right\}
\end{aligned} \tag{A.18}$$

$$\begin{aligned}
& [A^{(3)}, B^{(3)}]^{(2)} \\
&= \frac{1}{4} \sum_{ijkl} \sum_{abcd} :a_i^\dagger a_j^\dagger a_l a_k : \\
&\quad \times \left\{ \frac{1}{6} (n_a \bar{n}_b \bar{n}_c \bar{n}_d - \bar{n}_a n_b n_c n_d) (A_{aijbcd} B_{bcdakl} - A_{bcdakl} B_{aijbcd}) \right. \\
&\quad \left. + \frac{1}{4} (\bar{n}_a \bar{n}_b n_c n_d - n_a n_b \bar{n}_c \bar{n}_d) (1 - P_{ij})(1 - P_{kl}) A_{abidcl} B_{cdjabk} \right\}
\end{aligned} \tag{A.19}$$

$$\begin{aligned}
& [A^{(3)}, B^{(3)}]^{(1)} \\
&= \frac{1}{12} \sum_{ij} \sum_{acde} :a_i^\dagger a_j : (n_a n_b \bar{n}_c \bar{n}_d \bar{n}_e + \bar{n}_a \bar{n}_b n_c n_d n_e) (A_{abicde} B_{cdeabj} - B_{abicde} A_{cdeabj})
\end{aligned} \tag{A.20}$$

$$\begin{aligned}
& [A^{(3)}, B^{(3)}]^{(0)} \\
&= \frac{1}{36} \sum_{ijklmn} (n_i n_j n_k \bar{n}_l \bar{n}_m \bar{n}_n - \bar{n}_i \bar{n}_j \bar{n}_k n_l n_m n_n) A_{ijklmn} B_{lmnijk}
\end{aligned} \tag{A.21}$$

# Appendix B

## IM-SRG(3) Flow Equations

The IM-SRG(3) flow equations can be derived using the fundamental commutators from Appendix A. The permutation symbols  $P_{ij}$ ,  $P(ij/k)$ , and  $P(i/jk)$  have been defined in Eqs. (3.11), (3.95), and (3.96). The normal-ordered Hamiltonian is given by

$$H(s) \approx E(s) + f(s) + \Gamma(s) + W(s). \quad (\text{B.1})$$

The particle ranks of the individual contributions of  $H$  and the generator  $\eta$  are obvious from the indices of the associated matrix elements.

$$\begin{aligned} \frac{d}{ds}E &= \sum_{ab} (n_a - n_b) \eta_{ab} f_{ba} + \frac{1}{2} \sum_{abcd} \eta_{abcd} \Gamma_{cdab} n_a n_b \bar{n}_c \bar{n}_d \\ &+ \frac{1}{18} \sum_{abcdef} \eta_{abcdef} W_{defabc} n_a n_b n_c \bar{n}_d \bar{n}_e \bar{n}_f \end{aligned} \quad (\text{B.2})$$

$$\begin{aligned}
\frac{d}{ds}f_{ij} &= \sum_a (1 + P_{ij})\eta_{ia}f_{aj} + \sum_{ab} (n_a - n_b)(\eta_{ab}\Gamma_{biaj} - f_{ab}\eta_{biaj}) \\
&+ \frac{1}{2} \sum_{abc} (n_a n_b \bar{n}_c + \bar{n}_a \bar{n}_b n_c)(1 + P_{ij})\eta_{ciab}\Gamma_{abcj} \\
&+ \frac{1}{4} \sum_{abcd} (n_a n_b \bar{n}_c \bar{n}_d)(\eta_{abcdj}\Gamma_{cdab} - W_{abcdj}\eta_{cdab}) \\
&+ \frac{1}{12} \sum_{abcde} (n_a n_b \bar{n}_c \bar{n}_d \bar{n}_e + \bar{n}_a \bar{n}_b n_c n_d n_e)(\eta_{abcde}W_{cdeabj} - W_{abcde}\eta_{cdeabj}) \quad (B.3)
\end{aligned}$$

$$\begin{aligned}
\frac{d}{ds}\Gamma_{ijkl} &= \sum_a \left\{ (1 - P_{ij})(\eta_{ia}\Gamma_{ajkl} - f_{ia}\eta_{ajkl}) - (1 - P_{kl})(\eta_{ak}\Gamma_{ijal} - f_{ak}\eta_{ijal}) \right\} \\
&+ \frac{1}{2} \sum_{ab} (1 - n_a - n_b)(\eta_{ijab}\Gamma_{abkl} - \Gamma_{ijab}\eta_{abkl}) \\
&- \sum_{ab} (n_a - n_b)(1 - P_{ij})(1 - P_{kl})\eta_{bjal}\Gamma_{aibk} \\
&+ \sum_{ab} (n_a - n_b) (\eta_{aijbkl}f_{ba} - W_{aijbkl}\eta_{ba}) \\
&+ \frac{1}{2} \sum_{abc} (n_a \bar{n}_b \bar{n}_c + \bar{n}_a n_b n_c)(1 - P_{ik}P_{jl}P_{ij} - P_{kl} + P_{ik}P_{jl}) \\
&\quad \times (\eta_{aijbcl}\Gamma_{bcak} - W_{aijbcl}\eta_{bcak}) \\
&+ \frac{1}{6} \sum_{abcd} (n_a \bar{n}_b \bar{n}_c \bar{n}_d - \bar{n}_a n_b n_c n_d)(\eta_{aijbcd}W_{bcdakl} - \eta_{bcdakl}W_{aijbcd}) \\
&+ \frac{1}{4} \sum_{abcd} (\bar{n}_a \bar{n}_b n_c n_d - n_a n_b \bar{n}_c \bar{n}_d)(1 - P_{ij})(1 - P_{kl})\eta_{abcdl}W_{cdjabk} \quad (B.4)
\end{aligned}$$

$$\begin{aligned}
\frac{d}{ds}W_{ijklmn} = & \sum_a \left\{ P(i/jk)\eta_{ia}W_{ajklmn} - P(l/mn)\eta_{al}W_{ijkamn} \right\} \\
& - \sum_a \left\{ P(i/jk)f_{ia}\eta_{ajklmn} - P(l/mn)f_{al}\eta_{ijkamn} \right\} \\
& + \sum_a P(ij/k)P(l/mn)(\eta_{ijla}\Gamma_{akmn} - \Gamma_{ijla}\eta_{akmn}) \\
& + \frac{1}{2} \sum_{ab} (1 - n_a - n_b)(P(i/jk))(\eta_{ijab}W_{abklmn} - \Gamma_{ijab}\eta_{abklmn}) \\
& - \frac{1}{2} \sum_{ab} (1 - n_a - n_b)(P(lm/n))(\eta_{ablm}W_{ijkabn} - \Gamma_{ablm}\eta_{ijkabn}) \\
& - \sum_{ab} (n_a - n_b)P(i/jk)p(l/mn)(\eta_{bial}W_{ajkbmn} - \Gamma_{bial}\eta_{ajkbmn}) \\
& + \frac{1}{6} \sum_{abc} (n_a n_b n_c + \bar{n}_a \bar{n}_b \bar{n}_c)(\eta_{ijkabc}W_{abclmn} - W_{ijkabc}\eta_{abclmn}) \\
& + \frac{1}{2} \sum_{abc} (n_a n_b \bar{n}_c + \bar{n}_a \bar{n}_b n_c)P(ij/k)P(l/mn) \\
& \quad \times (\eta_{abkcmn}W_{cijabl} - \eta_{cjkabn}W_{iablmc})
\end{aligned} \tag{B.5}$$

# Appendix C

## Diagram Rules

For convenience, we briefly summarize the rules for interpreting the antisymmetrized Goldstone and Hugenholtz diagrams that appear in the perturbative discussion of the IM-SRG in Sec. 3.5. Detailed derivations can be found in standard texts on many-body theory, e.g., in Ref. [16, 117, 120], as well as in Refs. [175, 181, 182], which are particularly useful for diagrammatic treatments of effective nuclear Hamiltonians.

1. Solid lines represent single-particle states (indices), with up- and downward pointing arrows indicating particle ( $\varepsilon > \varepsilon_F$ ) and hole states ( $\varepsilon \leq \varepsilon_F$ ), respectively.
2. Interaction vertices are represented as dots in Hugenholtz diagrams,

$$\langle i|f|j\rangle = \begin{array}{c} i \\ | \\ \bullet \\ | \\ j \end{array} \text{---} \times, \quad \langle ij|\Gamma|kl\rangle = \begin{array}{c} i \quad j \\ \diagdown \quad \diagup \\ \bullet \\ \diagup \quad \diagdown \\ k \quad l \end{array}, \quad \langle ijk|W|lmn\rangle = \begin{array}{c} i \quad j \quad k \\ \diagdown \quad | \quad \diagup \\ \bullet \\ \diagup \quad | \quad \diagdown \\ l \quad m \quad n \end{array}, \quad (\text{C.1})$$

where the two- and three-body matrix elements are fully antisymmetrized. Throughout this work, we will also use the short-hand notation  $f_{ij} = \langle i|f|j\rangle$ ,  $\Gamma_{ijkl} = \langle ij|\Gamma|kl\rangle$ , etc.

For the discussion of the effective one- and two-body Hamiltonians, we switch from Hugenholtz diagrams to antisymmetrized Goldstone diagrams for clarity (see, e.g., Ref. [16]). To this end, the Hugenholtz point vertices are stretched into dashed inter-

action lines,

$$\langle i | f | j \rangle = \begin{array}{c} i \\ | \\ \bullet \\ | \\ j \end{array} \text{---} \times, \quad \langle ij | \Gamma | kl \rangle = \begin{array}{cc} i & j \\ | & | \\ \bullet & \bullet \\ | & | \\ k & l \end{array}, \quad \langle ijk | W | lmn \rangle = \begin{array}{ccc} i & j & k \\ | & | & | \\ \bullet & \bullet & \bullet \\ | & | & | \\ l & m & n \end{array}. \quad (\text{C.2})$$

Note that the matrix elements are still antisymmetrized: Each of the diagrams shown here represents all allowed exchanges of single-particle lines/indices in the bra and ket. This is reflected in the rules for prefactors that we adopt in the following [16].

3. Assign a factor  $1/2^{n_d}$  for  $n_d$  equivalent pairs, i.e., pairs of particle or hole lines that start at the same interaction vertex and end at the same interaction vertex. Likewise, assign  $1/6^{n_t}$  for  $n_t$  equivalent triples connecting the same interaction vertices.
4. Assign a phase factor  $(-1)^{n_l+n_h+n_c+n_{exh}}$  to each diagram, where  $n_l$  is the number of closed fermion loops,  $n_h$  the total number of hole lines,  $n_c$  is the number of crossings of distinct external lines, and  $n_{exh}$  the number of hole lines continuously passing through the whole diagram (i.e.,  $n_{exh} = 0$  for energy diagrams).
5. For each interval between interactions with particle lines  $p_1, \dots, p_M$  and hole lines  $h_1, \dots, h_N$  multiply the expression with the energy denominator

$$\frac{1}{\Omega + \sum_{i=1}^N \varepsilon_{h_i} - \sum_{i=1}^M \varepsilon_{p_i}}, \quad (\text{C.3})$$

where  $\Omega$  is the unperturbed energy of the state entering the diagram relative to the reference state, reading from bottom to top (e.g.,  $\Omega = 0$  for energy diagrams). Throughout this work, the energies are given by the diagonal matrix elements of the one-body

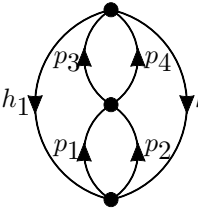
part of the Hamiltonian  $\varepsilon_i = f_{ii}$ ; for Hartree-Fock reference states,  $f$  is diagonal, of course. The sum over intermediate particle and hole lines in the denominator is the unperturbed energy of the excited  $MpNh$  state in a Møller-Plesset type perturbation theory with respect to the reference state. In the Epstein-Nesbet case, it is replaced with the diagonal matrix element of the Hamiltonian in the same state, i.e.,

$$\begin{aligned} & \langle \Phi | : a_{h_N}^\dagger \dots a_{h_1}^\dagger a_{p_M} \dots a_{p_1} : H : a_{p_1}^\dagger \dots a_{p_M}^\dagger a_{h_1} \dots a_{h_N} : | \Phi \rangle - E_0 \\ &= \sum_{i=1}^M \varepsilon_{p_i} - \sum_{i=1}^N \varepsilon_{h_i} + \text{additional terms}, \end{aligned} \quad (\text{C.4})$$

where  $E_0 = \langle \Phi | H | \Phi \rangle$ .

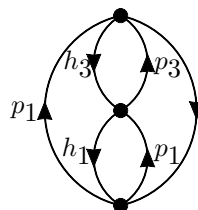
## 6. Sum freely over all internal single-particle indices.

Let us demonstrate the use of the diagram rules for a few examples. For the third-order particle-ladder diagram,



$$= \frac{1}{8} \sum_{\substack{p_1 p_2 p_3 p_4 \\ h_1 h_2}} \frac{\Gamma_{h_1 h_2 p_3 p_4} \Gamma_{p_3 p_4 p_1 p_2} \Gamma_{p_1 p_2 h_1 h_2}}{(\varepsilon_{h_1} + \varepsilon_{h_2} - \varepsilon_{p_1} - \varepsilon_{p_2})(\varepsilon_{h_1} + \varepsilon_{h_2} - \varepsilon_{p_3} - \varepsilon_{p_4})}. \quad (\text{C.5})$$

Here  $n_c = n_{exh} = 0$ ,  $n_h = 2$ , and the number of closed fermion loops is  $n_l = 2$ , namely  $p_1 \rightarrow p_3 \rightarrow h_1 \rightarrow p_1$  and  $p_2 \rightarrow p_4 \rightarrow h_2 \rightarrow p_2$ . For the particle-hole diagram, we have



$$= - \sum_{\substack{p_1 p_2 p_3 \\ h_1 h_2 h_3}} \frac{\Gamma_{h_3 h_2 p_1 p_3} \Gamma_{h_1 p_3 h_3 p_2} \Gamma_{p_1 p_2 h_1 h_2}}{(\varepsilon_{h_1} + \varepsilon_{h_2} - \varepsilon_{p_1} - \varepsilon_{p_2})(\varepsilon_{h_2} + \varepsilon_{h_3} - \varepsilon_{p_1} - \varepsilon_{p_3})}, \quad (\text{C.6})$$

with  $n_c = n_{exh} = 0$ ,  $n_h = 3$ , and two closed loops ( $n_l = 2$ ),  $p_1 \rightarrow h_3 \rightarrow h_1 \rightarrow p_1$  and  $p_2 \rightarrow p_3 \rightarrow h_2$ , giving a negative sign. Since the interaction vertices are connected by one particle and one hole line each,  $n_d = 0$ , and the pre-factor is 1.

For the second-order effective Hamiltonian, diagram  $f_4$  in Fig. 3.12 translates into

$$= \frac{1}{2} \sum_{p'p''h'} \frac{\Gamma_{ph'p'p''}\Gamma_{p'p''hh'}}{\varepsilon_h + \varepsilon_{h'} - \varepsilon_{p'} - \varepsilon_{p''}}. \quad (\text{C.7})$$

Reading from bottom to top, we have  $\Omega = 0$  just like in an energy diagram. To determine the phase, we note that there is one fermion loop ( $p'' \rightarrow h' \rightarrow p''$ ), there are two hole lines, one of which is external and passing through the diagram via  $h \rightarrow p' \rightarrow p$ . Thus  $n_l = 1, n_h = 2, n_{exh} = 1$ , and  $n_c = 0$ , so the phase factor is  $+1$ . There is one pair of equivalent particle lines,  $n_d = 1$ , giving rise to the pre-factor  $\frac{1}{2}$ .

As an example for a second-order two-body interaction, we consider diagram  $\Gamma_3$  in Fig. 3.13:

$$= \frac{1}{2} \sum_{h'h''} \frac{\Gamma_{p_1p_2h'h''}\Gamma_{h'h''p_3h}}{\varepsilon_{h'} + \varepsilon_{h''} - \varepsilon_{p_1} - \varepsilon_{p_2}}, \quad (\text{C.8})$$

where  $n_l = n_c = 0, n_h = 3$ , and there is one external hole line ( $n_{exh} = 1$ ) passing through the diagram,  $h \rightarrow h'' \rightarrow p$ , giving a phase factor  $+1$ . There is one pair of equivalent hole lines ( $n_d = 1$ ), and the starting energy is  $\Omega = p_3$ , which explains the symmetry pre-factor and energy denominator, respectively.

Our final example is an induced three-body interaction, diagram  $W_3$  in Fig. 3.14. The expression is

The diagram shows a sequence of vertices connected by dashed lines. The first vertex has two incoming lines labeled  $p_1$  and  $h_1$ . The second vertex has two outgoing lines labeled  $p_2$  and  $h'$ . The third vertex has two incoming lines labeled  $h_2$  and  $h'$ . The fourth vertex has two outgoing lines labeled  $p_3$  and  $h_3$ . A dashed line connects the first and second vertices, and another dashed line connects the second and third vertices. The diagram is equated to the following mathematical expression:

$$= - \sum_{h'} \frac{\Gamma_{p_1 p_2 h_1 h'} \Gamma_{h' p_3 h_3 h_3}}{\varepsilon_{h_1} + \varepsilon_{h'} - \varepsilon_{p_1} - \varepsilon_{p_2}}, \quad (\text{C.9})$$

where  $\Omega = 0$ , the phase factor is  $-1$  because  $n_l = n_c = 0, n_h = 4, n_{exh} = 3$ . Due to the lack of equivalent lines, the overall pre-factor of the diagram is 1.

## REFERENCES

## REFERENCES

- [1] D. R. Entem and R. Machleidt, Phys. Rev. C **68**, 041001 (2003).
- [2] R. Machleidt and D. Entem, Phys. Rept. **503**, 1 (2011).
- [3] J. J. Shepherd, G. H. Booth, and A. Alavi, Chem. Phys. **136**, 244101 (2012).
- [4] A. S. Hansen, *Coupled cluster studies of infinite systems*, Master's thesis, University of Oslo, Oslo, Norway (2015).
- [5] J. Olsen, P. Jorgensen, H. Koch, A. Balkova, and R. J. Bartlett, Chem. Phys. **104** (1996).
- [6] J. M. Turney, A. C. Simmonett, R. M. Parrish, E. G. Hohenstein, F. A. Evangelista, J. T. Fermann, B. J. Mintz, L. A. Burns, J. J. Wilke, M. L. Abrams, N. J. Russ, M. L. Leininger, C. L. Janssen, E. T. Seidl, W. D. Allen, H. F. Schaefer, R. A. King, E. F. Valeev, C. D. Sherrill, and T. D. Crawford, Wiley Interdiscip. Rev. Comput. Mol. Sci. **2**, 556 (2012).
- [7] S. Hirata, P.-D. Fan, A. A. Auer, M. Nooijen, and P. Piecuch, Chem. Phys. **121** (2004).
- [8] P. Piecuch and M. Wloch, Chem. Phys. **123**, 224105 (2005), 10.1063/1.2137318.
- [9] F. A. Evangelista, Chem. Phys. **134**, 224102 (2011), 10.1063/1.3598471.
- [10] K. B. Ghose, P. Piecuch, and L. Adamowicz, Chem. Phys. **103** (1995).
- [11] H. Hergert, S. K. Bogner, T. D. Morris, A. Schwenk, and K. Tsukiyama, Phys. Rept. **621**, 165 (2016).
- [12] B. R. Barrett, P. Navrátil, and J. P. Vary, Prog. Part. Nucl. Phys. **69**, 131 (2013).
- [13] R. J. Furnstahl, G. Hagen, and T. Papenbrock, Phys. Rev. C **86**, 031301 (2012).
- [14] S. N. More, A. Ekström, R. J. Furnstahl, G. Hagen, and T. Papenbrock, Phys. Rev. C **87**, 044326 (2013).
- [15] I. Angeli, At. Data Nucl. Data Tables **87**, 185 (2004).
- [16] I. Shavitt and R. J. Bartlett, *Many-Body Methods in Chemistry and Physics: MBPT and Coupled-Cluster Theory* (Cambridge University Press, 2009).
- [17] D. Entem and R. Machleidt, Phys.Rev. **C68**, 041001 (2003).
- [18] G. Hagen, T. Papenbrock, M. Hjorth-Jensen, and D. J. Dean, Rep. Prog. Phys. **77**, 096302 (2014).

- [19] A. Cipollone, C. Barbieri, and P. Navrátil, *Phys. Rev. Lett.* **111**, 062501 (2013).
- [20] M. Wang, G. Audi, A. Wapstra, F. Kondev, M. MacCormick, X. Xu, and B. Pfeiffer, *Chin. Phys. C* **36**, 1603 (2012).
- [21] H. Hergert, S. Binder, A. Calci, J. Langhammer, and R. Roth, *Phys. Rev. Lett.* **110**, 242501 (2013).
- [22] F. Wienholtz, D. Beck, K. Blaum, C. Borgmann, M. Breitenfeldt, R. B. Cakirli, S. George, F. Herfurth, J. D. Holt, M. Kowalska, S. Kreim, D. Lunney, V. Manea, J. Menendez, D. Neidherr, M. Rosenbusch, L. Schweikhard, A. Schwenk, J. Simonis, J. Stanja, R. N. Wolf, and K. Zuber, *Nature* **498**, 346 (2013).
- [23] H. Hergert, S. K. Bogner, T. D. Morris, S. Binder, A. Calci, J. Langhammer, and R. Roth, *Phys. Rev. C* **90**, 041302 (2014).
- [24] S. K. Bogner, H. Hergert, J. D. Holt, A. Schwenk, S. Binder, A. Calci, J. Langhammer, and R. Roth, *Phys. Rev. Lett.* **113**, 142501 (2014).
- [25] J. Holt, J. Menéndez, and A. Schwenk, *Eur. Phys. J. A* **49**, 1 (2013).
- [26] G. R. Jansen, J. Engel, G. Hagen, P. Navratil, and A. Signoracci, *Phys. Rev. Lett.* **113**, 142502 (2014).
- [27] K. Hebeler, J. D. Holt, J. Menéndez, and A. Schwenk, *Annual Review of Nuclear and Particle Science*, *Ann. Rev. Nucl. Part. Sci.* (2015).
- [28] K. A. Brueckner and C. A. Levinson, *Phys. Rev.* **97**, 1344 (1955).
- [29] H. A. Bethe, *Phys. Rev.* **103**, 1353 (1956).
- [30] J. Goldstone, *Proc. Roy. Soc. Lond. A Math. Phys. Eng. Sci.* **239**, 267 (1957).
- [31] H. F. S. III, *Quantum Chemistry: The Development of Ab-Initio Methods in Molecular Electronic Structure Theory* (Dover Publications Inc., 2004).
- [32] E. Epelbaum, H.-W. Hammer, and U.-G. Meißner, *Rev. Mod. Phys.* **81**, 1773 (2009).
- [33] S. K. Bogner, R. J. Furnstahl, and A. Schwenk, *Prog. Part. Nucl. Phys.* **65**, 94 (2010).
- [34] H.-W. Hammer, A. Nogga, and A. Schwenk, *Rev. Mod. Phys.* **85**, 197 (2013).
- [35] A. B. Balantekin, J. Carlson, D. J. Dean, G. M. Fuller, R. J. Furnstahl, M. Hjorth-Jensen, R. V. F. Janssens, B.-A. Li, W. Nazarewicz, F. M. Nunes, W. E. Ormand, S. Reddy, and B. M. Sherrill, *Mod. Phys. Lett. A* **29**, 1430010 (2014).
- [36] J. Carlson, S. Gandolfi, F. Pederiva, S. C. Pieper, R. Schiavilla, K. E. Schmidt, and R. B. Wiringa, *Rev. Mod. Phys.* **87**, 1067 (2015).
- [37] R. Roth, J. Langhammer, A. Calci, S. Binder, and P. Navrátil, *Phys. Rev. Lett.* **107**, 072501 (2011).

- [38] T. A. Lähde, E. Epelbaum, H. Krebs, D. Lee, U.-G. Meißner, and G. Rupak, *Phys. Lett. B* **732**, 110 (2014).
- [39] K. Tsukiyama, S. K. Bogner, and A. Schwenk, *Phys. Rev. C* **85**, 061304 (2012).
- [40] G. R. Jansen, A. Signoracci, G. Hagen, and P. Navrátil, (2015), arXiv:1511.00757 [nucl-th] .
- [41] J. D. H. S. K. B. S. R. Stroberg, H. Hergert and A. Schwenk, arXiv:1511.02802 [nucl-th] .
- [42] V. Somà, C. Barbieri, and T. Duguet, *Phys. Rev. C* **87**, 011303 (2013).
- [43] V. Somà, C. Barbieri, and T. Duguet, *Phys. Rev. C* **89**, 024323 (2014).
- [44] V. Somà, A. Cipollone, C. Barbieri, P. Navrátil, and T. Duguet, *Phys. Rev. C* **89**, 061301 (2014).
- [45] H. Hergert, in preparation (2015).
- [46] S. Gandolfi, A. Lovato, J. Carlson, and K. E. Schmidt, *Phys. Rev. C* **90**, 061306 (2014), arXiv:1406.3388 [nucl-th] .
- [47] G. Hagen, A. Ekstrom, C. Forssen, G. R. Jansen, W. Nazarewicz, T. Papenbrock, K. A. Wendt, S. Bacca, N. Barnea, B. Carlsson, C. Drischler, K. Hebeler, M. Hjorth-Jensen, M. Miorelli, G. Orlandini, A. Schwenk, and J. Simonis, *Nature Phys.* **advance online publication**, (2015).
- [48] F. Coester, *Nucl. Phys.* **7**, 421 (1958).
- [49] F. Coester and H. Kümmel, *Nucl. Phys.* **17**, 477 (1960).
- [50] J. Cizek and J. Paldus, *Int. J. Quant. Chem.* **5**, 359 (1971).
- [51] S. K. Bogner, R. J. Furnstahl, S. Ramanan, and A. Schwenk, *Nucl. Phys. A* **773**, 203 (2006).
- [52] S. K. Bogner, R. J. Furnstahl, S. Ramanan, and A. Schwenk, *Nucl. Phys. A* **784**, 79 (2007), arXiv:nucl-th/0609003 .
- [53] S. K. Bogner, R. J. Furnstahl, and R. J. Perry, *Phys. Rev. C* **75**, 061001(R) (2007).
- [54] E. D. Jurgenson, P. Navrátil, and R. J. Furnstahl, *Phys. Rev. Lett.* **103**, 082501 (2009).
- [55] K. Hebeler, *Phys. Rev. C* **85**, 021002 (2012).
- [56] R. J. Furnstahl, *Nucl. Phys. Proc. Suppl.* **228**, 139 (2012).
- [57] R. J. Furnstahl and K. Hebeler, *Rept. Prog. Phys.* **76**, 126301 (2013).

- [58] K. Tsukiyama, S. K. Bogner, and A. Schwenk, Phys. Rev. Lett. **106**, 222502 (2011).
- [59] K. A. Brueckner, Phys. Rev. **100**, 36 (1955).
- [60] J. Cizek, Chem. Phys. **45**, 4256 (1966).
- [61] J. Goldstone, Proc. R. Soc. A **239**, 267 (1957).
- [62] D. J. Thouless, Nucl. Phys. **21**, 225 (1960).
- [63] G. E. Scuseria, T. M. Henderson, and I. W. Bulik, Chem. Phys. **139**, 104113 (2013), <http://dx.doi.org/10.1063/1.4820557>.
- [64] G. Hagen, T. Papenbrock, D. J. Dean, and M. Hjorth-Jensen, Phys. Rev. C **82**, 034330 (2010).
- [65] K. Raghavachari, G. W. Trucks, J. A. Pople, and M. Head-Gordon, Chem. Phys. Lett. **157**, 479 (1989).
- [66] P. Piecuch, K. Kowalski, I. S. O. Pimienta, and M. J. McGuire, Int. Rev. Phys. Chem. **21**, 527 (2002).
- [67] S. Binder, P. Piecuch, A. Calci, J. Langhammer, P. Navrátil, and R. Roth, Phys. Rev. C **88**, 054319 (2013).
- [68] S. A. Kucharski and R. J. Bartlett, Chem. Phys. **108** (1998).
- [69] T. D. Crawford and J. F. Stanton, Int. J. Quant. Chem. **70**, 601 (1998).
- [70] K. Kowalski and P. Piecuch, Chem. Phys. **113** (2000).
- [71] K. Kowalski and P. Piecuch, Chem. Phys. **113** (2000).
- [72] K. Kowalski and P. Piecuch, Chem. Phys. **122**, 074107 (2005), 10.1063/1.1848093.
- [73] F. Wegner, Ann. Phys. (Leipzig) **3**, 77 (1994).
- [74] H. Hergert, S. K. Bogner, S. Binder, A. Calci, J. Langhammer, R. Roth, and A. Schwenk, Phys. Rev. C **87**, 034307 (2013).
- [75] B. H. Brandow, Rev. Mod. Phys. **39**, 771 (1967).
- [76] W. Dickhoff and C. Barbieri, Prog. Part. Nucl. Phys. **52**, 377 (2004).
- [77] C. Barbieri, D. Van Neck, and W. H. Dickhoff, Phys. Rev. A **76**, 052503 (2007).
- [78] S. R. White, J. Chem. Phys. **117**, 7472 (2002).
- [79] T. Yanai and G. K.-L. Chan, J. Chem. Phys. **124**, 194106 (2006).
- [80] J. Suhonen, *From Nucleons to Nucleus. Concepts of Microscopic Nuclear Theory*, 1st ed. (Springer, Berlin, 2007).

- [81] H. Hergert, S. Bogner, T. Morris, S. Binder, A. Calci, *et al.*, Phys.Rev. **C90**, 041302 (2014).
- [82] S. Kehrein, *The Flow Equation Approach to Many-Particle Systems*, Springer Tracts in Modern Physics, Vol. 237 (Springer Berlin / Heidelberg, 2006).
- [83] G. P. Kamuntavicius, R. K. Kalinauskas, B. R. Barrett, S. Mickevicius, and D. Germanas, Nucl. Phys. A **695**, 191 (2001), nucl-th/0105009 .
- [84] A. C. Hindmarsh, P. N. Brown, K. E. Grant, S. L. Lee, R. Serban, D. E. Shumaker, and C. S. Woodward, ACM Trans. Math. Softw. **31**, 363 (2005).
- [85] G. Hagen, private communication.
- [86] S. Binder, J. Langhammer, A. Calci, P. Navrátil, and R. Roth, Phys. Rev. C **87**, 021303 (2013).
- [87] S. Binder, J. Langhammer, A. Calci, and R. Roth, Phys. Lett. B **736**, 119 (2014).
- [88] R. Roth, P. Papakonstantinou, N. Paar, H. Hergert, T. Neff, and H. Feldmeier, Phys. Rev. C **73**, 044312 (2006), nucl-th/0510036 .
- [89] A. Günther, R. Roth, H. Hergert, and S. Reinhardt, Phys. Rev. C **82**, 024319 (2010), 1005.1599 .
- [90] R. Roth and J. Langhammer, Phys. Lett. B **683**, 272 (2010).
- [91] K. Hebeler, S. K. Bogner, R. J. Furnstahl, A. Nogga, and A. Schwenk, Phys. Rev. C **83**, 031301 (2011).
- [92] J. Langhammer, R. Roth, and C. Stumpf, Phys. Rev. C **86**, 054315 (2012).
- [93] A. G. Taube and R. J. Bartlett, J. Chem. Phys. **128**, 044110 (2008).
- [94] A. G. Taube and R. J. Bartlett, J. Chem. Phys. **128**, 044111 (2008).
- [95] G. Hagen, T. Papenbrock, M. Hjorth-Jensen, and D. J. Dean, Rept. Prog. Phys. **77**, 096302 (2014).
- [96] G. P. Kamuntavicius, Phys. Rev. C **56**, 191 (1997).
- [97] J. Beringer *et al.* (Particle Data Group), Phys. Rev. D **86**, 010001 (2012).
- [98] R. Roth, S. Binder, K. Vobig, A. Calci, J. Langhammer, and P. Navrátil, Phys. Rev. Lett. **109**, 052501 (2012).
- [99] G. Hagen, M. Hjorth-Jensen, G. R. Jansen, R. Machleidt, and T. Papenbrock, Phys. Rev. Lett. **108**, 242501 (2012).
- [100] G. Hagen, M. Hjorth-Jensen, G. R. Jansen, R. Machleidt, and T. Papenbrock, Phys. Rev. Lett. **109**, 032502 (2012).

- [101] I. Stetcu, B. R. Barrett, P. Navrátil, and J. P. Vary, Phys. Rev. C **71**, 044325 (2005), nucl-th/0412004 .
- [102] N. Paar, P. Papakonstantinou, H. Hergert, and R. Roth, Phys. Rev. C **74**, 014318 (2006), nucl-th/0601026 .
- [103] E. R. Anderson, S. K. Bogner, R. J. Furnstahl, and R. J. Perry, Phys. Rev. C **82**, 054001 (2010).
- [104] M. D. Schuster, S. Quaglioni, C. W. Johnson, E. D. Jurgenson, and P. Navrátil, Phys. Rev. C **90**, 011301 (2014).
- [105] S. Pastore, R. Schiavilla, and J. L. Goity, Phys. Rev. C **78**, 064002 (2008).
- [106] S. Pastore, L. Girlanda, R. Schiavilla, M. Viviani, and R. B. Wiringa, Phys. Rev. C **80**, 034004 (2009).
- [107] S. Kölling, E. Epelbaum, H. Krebs, and U. G. Meißner, Phys. Rev. C **80**, 045502 (2009).
- [108] Y.-H. Song, R. Lazauskas, and T.-S. Park, Phys. Rev. C **79**, 064002 (2009).
- [109] S. Pastore, L. Girlanda, R. Schiavilla, and M. Viviani, Phys. Rev. C **84**, 024001 (2011).
- [110] S. Kölling, E. Epelbaum, H. Krebs, and U.-G. Meißner, Phys. Rev. C **84**, 054008 (2011).
- [111] D. Rozpedzik, J. Golak, S. Kölling, E. Epelbaum, R. Skibiński, H. Witała, and H. Krebs, Phys. Rev. C **83**, 064004 (2011).
- [112] S. Kölling, E. Epelbaum, and D. R. Phillips, Phys. Rev. C **86**, 047001 (2012).
- [113] M. Piarulli, L. Girlanda, L. E. Marcucci, S. Pastore, R. Schiavilla, and M. Viviani, Phys. Rev. C **87**, 014006 (2013).
- [114] G. Orlandini, Eur. Phys. J. Spec. Top. **198**, 239 (2011).
- [115] S. Pastore, S. C. Pieper, R. Schiavilla, and R. B. Wiringa, Phys. Rev. C **87**, 035503 (2013).
- [116] D. J. Rowe, A. Ryman, and G. Rosensteel, Phys. Rev. A **22**, 2362 (1980).
- [117] J. W. Negele and H. Orland, *Quantum Many-Particle Systems*, Advanced Book Classics (Westview Press, 1998).
- [118] R. J. Bartlett, Annu. Rev. Phys. Chem. **32**, 359 (1981).
- [119] V. Somà, T. Duguet, and C. Barbieri, Phys. Rev. C **84**, 064317 (2011).
- [120] A. Fetter and J. Walecka, *Quantum Theory of Many-particle Systems*, Dover Books on Physics (Dover Publications, 2003).

- [121] F. A. Evangelista and J. Gauss, Chem. Phys. **401**, 27 (2012), [Recent advances in electron correlation methods and applications](#).
- [122] S. Ramanan, S. Bogner, and R. Furnstahl, Nucl. Phys. A **797**, 81 (2007).
- [123] J. Langhammer, *Consistent Chiral Three-Nucleon Interactions in Nuclear Structure*, Master's thesis, TU Darmstadt (2010).
- [124] M. E. Peskin and D. V. Schroeder, *An Introduction to Quantum Field Theory*, 5th ed. (Addison-Wesley, Reading, USA, 1997).
- [125] J. Zinn-Justin, *Phase Transitions and Renormalisation Group* (Oxford University Press, 2007).
- [126] M. Baranger, Nucl. Phys. A **149**, 225 (1970).
- [127] T. Duguet and G. Hagen, Phys. Rev. C **85**, 034330 (2012).
- [128] T. Duguet, H. Hergert, J. D. Holt, and V. Somà, Phys. Rev. C **92**, 034313 (2015).
- [129] W. Magnus, Comm. Pure Appl. Math. **7**, 649 (1954).
- [130] T. D. Morris, N. M. Parzuchowski, and S. K. Bogner, Phys. Rev. C **92**, 034331 (2015).
- [131] S. Blanes, F. Casas, J. Oteo, and J. Ros, Phys. Rept. **470**, 151 (2009).
- [132] G. Hagen, T. Papenbrock, A. Ekström, K. Wendt, G. Baardsen, *et al.*, Phys. Rev. C **89**, 014319 (2014).
- [133] A. L. Fetter and J. D. Walecka, *Quantum theory of many-particle systems*, International series in pure and applied physics (McGraw-Hill, San Francisco, 1971).
- [134] F. A. Evangelista, Chem. Phys. **141**, 054109 (2014).
- [135] T. H. Dunning, Chem. Phys. **90** (1989).
- [136] M. L. Abrams and C. D. Sherrill, J. Chem. Phys. **121**, 9211 (2004).
- [137] T. H. Dunning, Chem. Phys. **53** (1970).
- [138] J. D. Watts and R. J. Bartlett, Int. J. Quant. Chem. **52**, 195 (1994).
- [139] T. D. Crawford, T. J. Lee, N. C. Handy, and H. F. Schaefer, Chem. Phys. **107** (1997).
- [140] R. E. Peierls, Proc. R. Soc. London A **333**, 157 (1973).
- [141] P. Ring and P. Schuck, *The Nuclear Many-Body Problem*, 1st ed. (Springer, 1980).
- [142] J. L. Egido and P. Ring, Nucl. Phys. A **383**, 189 (1982).
- [143] L. M. Robledo, Phys. Rev. C **50**, 2874 (1994).

- [144] H. Flocard and N. Onishi, *Ann. Phys.* **254**, 275 (1997).
- [145] J. A. Sheikh and P. Ring, *Nucl. Phys. A* **665**, 71 (2000).
- [146] J. Dobaczewski, M. V. Stoitsov, W. Nazarewicz, and P. G. Reinhard, *Phys. Rev. C* **76**, 054315 (2007).
- [147] M. Bender, T. Duguet, and D. Lacroix, *Phys. Rev. C* **79**, 044319 (2009), arXiv:0809.2045 [nucl-th] .
- [148] T. Duguet, M. Bender, K. Bennaceur, D. Lacroix, and T. Lesinski, *Phys. Rev. C* **79**, 044320 (2009).
- [149] D. Lacroix, T. Duguet, and M. Bender, *Phys. Rev. C* **79**, 044318 (2009), arXiv:0809.2041 [nucl-th] .
- [150] D. Lacroix and D. Gambacurta, *Phys. Rev. C* **86**, 014306 (2012).
- [151] T. Duguet, *J. Phys. G* **42**, 025107 (2015).
- [152] J. D. Holt, J. Menéndez, J. Simonis, and A. Schwenk, *Phys. Rev. C* **90**, 024312 (2014).
- [153] B. A. Brown, *Physics* **3**, 104 (2010).
- [154] W. Kutzelnigg and D. Mukherjee, *J. Chem. Phys.* **107**, 432 (1997).
- [155] D. Mukherjee, *Chem. Phys. Lett.* **274**, 561 (1997).
- [156] T. Otsuka, T. Suzuki, J. D. Holt, A. Schwenk, and Y. Akaishi, *Phys. Rev. Lett.* **105**, 032501 (2010).
- [157] A. Ekström, G. R. Jansen, K. A. Wendt, G. Hagen, T. Papenbrock, B. D. Carlsson, C. Forssén, M. Hjorth-Jensen, P. Navrátil, and W. Nazarewicz, *Phys. Rev. C* **91**, 051301 (2015).
- [158] E. Epelbaum, H. Krebs, and U. G. Meißner, *Eur.Phys.J.A*, *Eur. Phys. J. A* **51**, 1 (2015).
- [159] E. Epelbaum, H. Krebs, and U.-G. Meißner, *Phys. Rev. Lett.* **115**, 122301 (2015).
- [160] D. R. Entem, N. Kaiser, R. Machleidt, and Y. Nosyk, (2015), arXiv:1505.03562 [nucl-th] .
- [161] D. R. Entem, N. Kaiser, R. Machleidt, and Y. Nosyk, *Phys. Rev. C* **91**, 014002 (2015).
- [162] B. D. Carlsson, A. Ekström, C. Forssén, D. F. Strömberg, O. Lilja, M. Lindby, B. A. Mattsson, and K. A. Wendt, (2015), arXiv:1506.02466 [nucl-th] .
- [163] A. Gezerlis, I. Tews, E. Epelbaum, M. Freunek, S. Gandolfi, K. Hebeler, A. Nogga, and A. Schwenk, *Phys. Rev. C* **90**, 054323 (2014).

- [164] M. Piarulli, L. Girlanda, R. Schiavilla, R. N. Pérez, J. E. Amaro, and E. R. Arriola, *Phys. Rev. C* **91**, 024003 (2015).
- [165] J. E. Lynn, I. Tews, J. Carlson, S. Gandolfi, A. Gezerlis, K. E. Schmidt, and A. Schwenk, (2015), arXiv:1509.03470 [nucl-th] .
- [166] C. Li and F. A. Evangelista, *J. Chem. Theory Comput.* **11**, 2097 (2015), pMID: 26574413.
- [167] P. Constans, P. Y. Ayala, and G. E. Scuseria, *Chem. Phys.* **113** (2000).
- [168] B. A. Brown, *Prog. Part. Nucl. Phys.* **47**, 517 (2001).
- [169] E. Caurier, G. Martínez-Pinedo, F. Nowacki, A. Poves, and A. P. Zuker, *Rev. Mod. Phys.* **77**, 427 (2005).
- [170] T. Otsuka, *Phys. Scripta* **2013**, 014007 (2013).
- [171] J. D. Holt, T. Otsuka, A. Schwenk, and T. Suzuki, *J. Phys. G* **39**, 085111 (2012).
- [172] J. D. Holt, J. Menéndez, and A. Schwenk, *Phys. Rev. Lett.* **110**, 022502 (2013).
- [173] J. D. Holt, J. Menéndez, and A. Schwenk, *J. Phys. G* **40**, 075105 (2013).
- [174] A. T. Gallant, J. C. Bale, T. Brunner, U. Chowdhury, S. Ettenauer, A. Lennarz, D. Robertson, V. V. Simon, A. Chaudhuri, J. D. Holt, A. A. Kwiatkowski, E. Mané, J. Menéndez, B. E. Schultz, M. C. Simon, C. Andreoiu, P. Delheij, M. R. Pearson, H. Savajols, A. Schwenk, and J. Dilling, *Phys. Rev. Lett.* **109**, 032506 (2012).
- [175] M. Hjorth-Jensen, T. T. S. Kuo, and E. Osnes, *Phys. Rept.* **261**, 125 (1995).
- [176] J. D. Holt, J. W. Holt, T. T. S. Kuo, G. E. Brown, and S. K. Bogner, *Phys. Rev. C* **72**, 041304 (2005).
- [177] A. F. Lisetskiy, B. R. Barrett, M. K. G. Kruse, P. Navrátil, I. Stetcu, and J. P. Vary, *Phys. Rev. C* **78**, 044302 (2008).
- [178] A. F. Lisetskiy, M. K. G. Kruse, B. R. Barrett, P. Navrátil, I. Stetcu, and J. P. Vary, *Phys. Rev. C* **80**, 024315 (2009).
- [179] E. Dikmen, A. F. Lisetskiy, B. R. Barrett, P. Maris, A. M. Shirokov, and J. P. Vary, *Phys. Rev. C* **91**, 064301 (2015).
- [180] L. Cáceres, A. Lepailleur, O. Sorlin, M. Stanoiu, D. Sohler, Z. Dombrádi, S. K. Bogner, B. A. Brown, H. Hergert, J. D. Holt, A. Schwenk, F. Azaiez, B. Bastin, C. Borcea, R. Borcea, C. Bourgeois, Z. Elekes, Z. Fülöp, S. Grévy, L. Gaudefroy, G. F. Grinyer, D. Guillemaud-Mueller, F. Ibrahim, A. Kerek, A. Krasznahorkay, M. Lewitowicz, S. M. Lukyanov, J. Mrázek, F. Negoita, F. de Oliveira, Y.-E. Penionzhkevich, Z. Podolyák, M. G. Porquet, F. Rotaru, P. Roussel-Chomaz, M. G. Saint-Laurent, H. Savajols, G. Sletten, J. C. Thomas, J. Timàr, C. Timis, and Z. Vajta, *Phys. Rev. C* **92**, 014327 (2015).

- [181] T. T. S. Kuo and E. Osnes, *Folded-Diagram Theory of the Effective Interaction in Nuclei, Atoms and Molecules*, Lecture Notes in Physics, Vol. 364 (Springer Berlin Heidelberg, 1990) pp. 1–170.
- [182] T. T. S. Kuo, J. Shurpin, K. C. Tam, E. Osnes, and P. J. Ellis, *Ann. Phys.* **132**, 237 (1981).